



Norwegian University of
Science and Technology

Development of a Solution Strategy for Non-Linear Finite Element Modelling of Reinforced Concrete Beams with Web Openings

Line Nilsson

Erlend André Ursin Nygårdsvoll

Kristine Reutz Nøttveit

Civil and Environmental Engineering

Submission date: June 2018

Supervisor: Max Hendriks, KT

Co-supervisor: Morten Engen, Multiconsult

Norwegian University of Science and Technology
Department of Structural Engineering



Norwegian University of
Science and Technology

Development of a Solution Strategy for Non-Linear Finite Element Modelling of Reinforced Concrete Beams with Web Openings

Line Nilsson
Kristine Nøttveit
Erlend Nygårdsvoll

June 2018

Department of Structural Engineering
Norwegian University of Science and Technology

Supervisors: Max A. N. Hendriks and Morten Engen



MASTER THESIS 2018

SUBJECT AREA: Design of Concrete Structures	DATE: 09.06.2018	NO. OF PAGES: 198
------------------------------------------------	---------------------	----------------------

TITLE:

Development of a Solution Strategy for Non-Linear Finite Element Modelling of Reinforced Concrete Beams with Web Openings

Utvikling av en løsningsstrategi ved bruk av ikke-lineær elementanalyse for armerte betongbjelker med utsparinger

BY:

Line Nilsson
Kristine Reutz Nøttveit
Erlend Nygårdsvoll



SUMMARY:

Non-linear finite element analyses (NLFEA) can be used to predict the physical behaviour of reinforced concrete (RC) structures. However, in order to obtain numerical results in compliance with the real physical behaviour of RC structures, an accurate solution strategy, with a low modelling uncertainty, is desired. The numerical solution strategy contains choices regarding kinematic compatibility, material models and force equilibrium.

In this Master's Thesis, a solution strategy has been developed for a general set of reinforced concrete beams with web openings. The selected solution strategy has been established based on careful investigations of the outcome from several NLFEAs, run in a FEA software called DIANA, version 10.2. The obtained numerical results were compared to experimental results from different benchmark analyses. Several concrete constitutive sub-models were investigated in detail in a sensitivity study. Furthermore, a range of varying mesh densities were tested with the aim of finding an optimal FE discretization for a general set of beams with openings.

The modelling uncertainty, quantified by a mean ratio of the experimental to predicted capacity, $\theta_m=1.06$, and a coefficient of variation, $V_\theta=16.4\%$, was obtained in this study. The obtained values were based on eight different beams modelled with the selected solution strategy. Compared to the experimental results, this reflects a general underestimation of the capacity in the NLFEAs.

Significant sensitivities related to the material models are observed and discussed in this thesis. Consequently the selected solution strategy may not be able to obtain the realistic failure mode and failure load for all concrete beams with web openings. The solution strategy can be considered as an elementary procedure to evaluate the capacity for such beams, and may be improved by use of more detailed sub-models for the dominant material behaviours of the failure modes. However, as the failure modes may be difficult to predict for beams with complex geometries, the NLFEAs should be accompanied by thorough post-analysis checks. These checks aim to detect possible spurious strengths, resulting in false capacity, as detected in some NLFEAs reported in this thesis.

RESPONSIBLE TEACHER: Max A. N. Hendriks

SUPERVISOR(S): Max A. N. Hendriks, Morten Engen

CARRIED OUT AT: Department of Structural Engineering, NTNU, Trondheim



MASTEROPPGAVE 2018

FAGOMRÅDE: Prosjektering av Betongkonstruksjoner	DATO: 09.06.2018	ANTALL SIDER: 198
-----------------------------------------------------	---------------------	----------------------

TITTEL:

Utvikling av en løsningsstrategi ved bruk av ikke-lineær elementanalyse for armerte betongbjelker med utsparinger

Development of a Solution Strategy for Non-Linear Finite Element Modelling of Reinforced Concrete Beams with Web Openings

UTFØRT AV:

Line Nilsson
Kristine Reutz Nøttveit
Erlend Nygårdsvoll



SAMMENDRAG:

Ikke-lineære elementanalyser (NLFEA) kan brukes til å forutsi den fysiske oppførselen til armerte betongkonstruksjoner. For å oppnå numeriske resultater i samsvar med den reelle fysiske oppførselen, er det ønskelig med en nøyaktig løsningsstrategi med lav modelleringsusikkerhet. Den numeriske løsningsstrategien inneholder valg relatert til kinematisk kompatibilitet, materialmodeller og likevektsbetraktninger.

I denne masteroppgaven er det etablert en løsningsstrategi for numerisk modellering av et generelt sett av armerte betongbjelker med utsparinger. Den valgte løsningsstrategien er etablert basert på nøye undersøkelser av utfallet fra flere NLFEAs, kjørt i en FEA-programvare kalt DIANA, versjon 10.2. De oppnådde numeriske resultatene ble sammenlignet med eksperimentelle resultater fra ulike referanseanalyser. Flere delmodeller for materialoppførselen til betongen ble undersøkt i detalj i en sensitivitetsstudie. Videre ble en rekke forskjellige elementstørrelser testet med sikte på å finne en optimal FE-diskretisering.

Modelleringsusikkerheten, kvantifisert av en middelerverdi mellom eksperimentell og numerisk kapasitet, $\theta_m=1.06$ og en variasjonskoeffisient, $V_\theta=16.4\%$, ble oppnådd i dette studiet. De oppnådde verdiene er basert på analyser av åtte forskjellige bjelker modellert med den valgte løsningsstrategien, og gjenspeiler en generell undervurdering av den reelle kapasiteten i NLFEA.

Vesentlige sensitiviteter knyttet til materialmodellene ble observert i dette studiet. Den valgte løsningsstrategien kan betraktes som en grunnleggende prosedyre for å evaluere kapasiteten til slike bjelker, men bør likevel ledsages av grundige kontroller i etterkant. Disse kontrollene tar sikte på å oppdage mulige falske styrker, noe som resulterer i falsk kapasitet. Dette ble oppdaget i noen elementanalyser rapportert i denne oppgaven.

FAGLÆRER: Max A. N. Hendriks

VEILEDER(E): Max A. N. Hendriks, Morten Engen

UTFØRT VED: Institutt for konstruksjonsteknikk, NTNU, Trondheim

ABSTRACT

Non-linear finite element analyses (NLFEA) can be used to predict the physical behaviour of reinforced concrete (RC) structures. However, in order to obtain numerical results in compliance with the real physical behaviour of RC structures, an accurate solution strategy, with a low modelling uncertainty, is desired. The numerical solution strategy contains choices regarding kinematic compatibility, material models and force equilibrium.

In this Master's Thesis, a solution strategy has been developed for a general set of reinforced concrete beams with web openings. The selected solution strategy has been established based on careful investigations of the outcome from several NLFEAs, run in a FEA software called DIANA, version 10.2. The obtained numerical results were compared to experimental results from different benchmark analyses. Three beams with different geometries have been used to develop the solution strategy presented in this thesis. Additional results obtained by the selected solution strategy for five supplementary beams are presented, with the intention to validate its scope of application with respect to geometry. Several concrete constitutive sub-models were investigated in detail in a sensitivity study. Furthermore, a range of varying mesh densities were tested with the aim of finding an optimal FE discretization for a general set of beams with openings. Other modelling choices are based on recommendations from provided literature.

In this study, a modelling uncertainty of $\theta=1.06$, and a coefficient of variation of $V_\theta=16.4\%$, was achieved. The modelling uncertainty was quantified by a mean ratio of the experimental to predicted numerical capacity. These values were based on NLFEAs of eight different beams modelled according to the selected solution strategy. Compared to the experimental results, this modelling uncertainty reflects a general underestimation of the capacity in the NLFEAs.

Significant sensitivities related to the material models are observed and discussed in this thesis. Consequently the selected solution strategy may not be able to obtain the realistic failure mode and failure load for all concrete beams with web openings. The solution strategy can be considered as an elementary procedure to evaluate the capacity for such beams, and may be improved by use of more detailed sub-models for the dominant material behaviours of the failure modes. However, as the failure modes may be difficult to predict for beams with complex geometries, the NLFEAs should be accompanied by thorough post-analysis checks. These checks aim to detect possible spurious strengths, resulting in false capacity, as detected in some NLFEAs reported in this thesis.

Sammendrag

Ikke-lineære elementanalyser (NLFEA) kan brukes til å forutsi den fysiske oppførselen til armerte betongkonstruksjoner. For å oppnå numeriske resultater i samsvar med den reelle fysiske oppførselen, er det ønskelig med en nøyaktig løsningsstrategi med lav modelleringsusikkerhet. Den numeriske løsningsstrategien inneholder valg relatert til kinematisk kompatibilitet, materialmodeller og likevektsbetraktninger.

I denne masteroppgaven er det etablert en løsningsstrategi for numerisk modellering av et generelt sett av armerte betongbjelker med utsparinger. Den valgte løsningsstrategien er etablert basert på nøye undersøkelser av utfallet fra flere NLFEAs, kjørt i en FEA-programvare kalt DIANA, versjon 10.2. De oppnådde numeriske resultatene ble sammenlignet med eksperimentelle resultater fra ulike referanseanalyser. Tre bjelker med forskjellige geometrier ble brukt til å utvikle løsningsstrategien som presenteres i denne oppgaven. I tillegg presenteres resultater oppnådd med den valgte løsningsstrategien for fem andre bjelker, med det formål å validere anvendelsesområdet med hensyn til geometri. Flere konstitutive delmodeller for betong ble undersøkt i detalj i en sensitivitetsstudie. Videre ble en rekke forskjellige elementstørrelser testet med sikte på å finne en optimal FE-diskretisering for et generelt sett av bjelker med åpninger. Andre modelleringsvalg er basert på anbefalinger gitt i litteraturen.

Modelleringsusikkerheten, kvantifisert av en middelvei mellom eksperimentell og numerisk kapasitet, $\theta_m = 1.06$ og en variasjonskoeffisient, $V_\theta = 16.4\%$, ble oppnådd i dette studiet. De oppnådde verdiene er basert på analyser av åtte forskjellige bjelker modellert med den valgte løsningsstrategien. Sammenlignet med eksperimentelle resultater, gjenspeiler dette en generell undervurdering av kapasiteten i NLFEA.

Vesentlige sensitiviteter knyttet til materialmodellene ble observert i dette studiet. Følgelig vil den valgte løsningsstrategien ikke nødvendigvis være i stand til å oppnå den realistiske bruddmekanismen og lastkapasiteten for alle betongbjelker med utsparinger. Løsningsstrategien kan betraktes som en grunnleggende prosedyre for å evaluere kapasiteten til slike bjelker, og kan forbedres ved bruk av mer detaljerte delmodeller for å beskrive de dominerende materielle oppførselene som inngår i bruddmekanismene. Det kan imidlertid være vanskelig å forutsi bruddmekanismen for bjelker med komplekse geometrier. Derfor bør de numeriske analysene være ledsaget av grundige kontroller. Disse kontrollene tar sikte på å oppdage mulige falske styrker, noe som resulterer i falsk kapasitet. Dette ble oppdaget i noen elementanalyser rapportert i denne oppgaven.

PREFACE

This Master's Thesis is submitted at the Department of Structural Engineering (KT) at the Norwegian University of Science and Technology (NTNU) in Trondheim. All work related to the master's thesis has been carried out in the spring 2018, and corresponds to 20 weeks work and 30 credits.

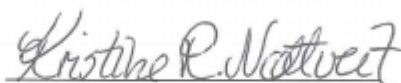
The main motivation for this thesis was to improve the understanding of concrete material behaviour and simplify the use of NLFEA in design of concrete structures with web openings.

We would like to thank our supervisors Professor Max. A. N. Hendriks from NTNU in Trondheim and Delft University of Technology in the Netherlands and PhD Morten Engen from Multiconsult ASA for helpful guidance and interesting discussions. Their advises and input have been extremely educational, and have contributed to an increased understanding of concrete material behaviour as well as increased knowledge related to implementation of NLFEAs in the software DIANA. We would also like to thank our fellow students for great motivation and positive work environment during the period.

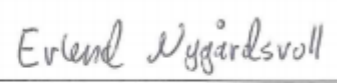
Trondheim, 09.06.2018



Line Nilsson



Kristine Reutz Nøttveit



Erlend Nygårdsvoll

Table of Contents

Abstract	V
Sammendrag	VII
Preface	IX
Notations	XIV
1 Introduction	1
2 Method	3
2.1 Non-Linear Finite Element Analysis	3
2.1.1 Material Properties	3
2.1.1.1 Concrete	3
2.1.1.2 Steel	4
2.1.2 Constitutive Models	5
2.1.2.1 Material Model for Concrete	5
2.1.2.2 Material Model for Reinforcement	6
2.1.2.3 Model for Concrete-Reinforcement Interaction	6
2.1.3 Finite Element Discretization	7
2.1.3.1 Mesh Order	7
2.1.3.2 Mesh Type	7
2.1.3.3 Mesh Density	8
2.1.3.4 Equivalent Length	8
2.1.3.5 Integration Scheme	8
2.1.4 Numerical Analysis	8
2.1.4.1 Load Application	8
2.1.4.2 Equilibrium Iteration	9
2.1.4.3 Convergence Criteria	9
2.2 Benchmark Analyses	10
2.2.1 Case Study 1	10
2.2.1.1 Experimental Setup	10
2.2.1.2 Material Parameters	13
2.2.1.3 Experimental Results	14
2.2.2 Case Study 2	15
2.2.2.1 Experimental Setup	15
2.2.2.2 Material Parameters	17
2.2.2.3 Experimental Results	19
2.2.3 Case Study 3	20
2.2.3.1 Experimental Setup	20
2.2.3.2 Material parameters	24
2.2.3.3 Experimental Results	25
2.3 Numerical Solution Strategy	26
2.3.1 FEA Software	26
2.3.2 Units	26
2.3.3 Selected Solution Strategy	26
2.3.3.1 FEA Discretization	27
2.3.3.2 Constitutive Model for Concrete	28
	XI

2.3.3.3	Constitutive Model for Reinforcement	31
2.3.3.4	Model for Concrete-Reinforcement Interaction	31
2.3.3.5	Specifications regarding the solution strategy for the numerical model in Case Study 3	32
2.3.4	Sensitivity Study of the Solution Strategy	35
2.3.4.1	FEA Discretization	35
2.3.4.2	Constitutive Model for Concrete	35
2.3.5	Post-Analysis Checks	37
2.4	Modelling Uncertainty	39
3	Numerical Results	42
3.0.1	NLFEA Results obtained by the selected Solution Strategy	42
3.0.1.1	Sensitivity Study from Case Study 1	45
3.0.1.2	Sensitivity Study from Case Study 2	46
3.0.1.3	Sensitivity Study from Case Study 3	47
3.1	Case study 1	48
3.1.1	NLFEA Results obtained by Selected Solution Strategy	48
3.1.1.1	Concrete Cracking	49
3.1.1.2	Concrete Crushing	51
3.1.1.3	Tension-Compression Interaction	51
3.1.1.4	Yielding of Reinforcement	53
3.1.1.5	Global Failure	53
3.1.2	Sensitivity Study of the Numerical Modelling in Case Study 1	54
3.1.2.1	Sensitivity regarding FE Discretization	54
3.1.2.2	Sensitivity to choice of Constitutive Model for Concrete	59
3.2	Case study 2	69
3.2.1	NLFEA Results obtained by the selected Solution Strategy	69
3.2.1.1	Concrete Cracking	70
3.2.1.2	Concrete Crushing	73
3.2.1.3	Tension-Compression Interaction	73
3.2.1.4	Yielding of Reinforcement	75
3.2.1.5	Global Failure	76
3.2.2	Sensitivity Study of the Numerical Modelling in Case Study 2	77
3.2.2.1	Sensitivity regarding FE Discretization	77
3.2.2.2	Sensitivity to choice of Constitutive Model for Concrete	83
3.3	Case Study 3	96
3.3.1	NLFEA Results obtained by the selected Solution Strategy	96
3.3.1.1	Concrete Cracking	99
3.3.1.2	Concrete Crushing	102
3.3.1.3	Tension-Compression Interaction	105
3.3.1.4	Yielding of Reinforcement	108
3.3.1.5	Global Failure	110
3.3.2	Sensitivity Study of the Numerical Modelling in Case Study 3	111
3.3.2.1	Sensitivity to Structural Interface Selection	111
3.3.2.2	Sensitivity regarding FE Discretization	113
3.3.2.3	Sensitivity to choice of Constitutive Model for Concrete	126
3.4	Quantification of Modelling Uncertainty	155
4	Discussion of Numerical Results	156

4.1	General Discussion	156
4.1.1	Sensitivity to Mesh Density	158
4.1.2	Sensitivity related to choice of Tension Softening Model	159
4.1.3	Sensitivity related to choice of Compressive Behaviour Function	159
4.1.4	Sensitivity related to choice of Shear Retention Model	160
4.1.5	Modelling Uncertainty	160
4.2	Case Study 1	162
4.2.1	Selected Solution Strategy	162
4.2.2	Sensitivity Study	163
4.2.2.1	Sensitivity regarding FE Discretization	163
4.2.2.2	Sensitivity to choice of Constitutive Model for Concrete	164
4.3	Case Study 2	167
4.3.1	Selected Solution Strategy	167
4.3.2	Sensitivity study	168
4.3.2.1	Sensitivity regarding FE Discretization	168
4.3.2.2	Sensitivity to choice of Constitutive Model for Concrete	169
4.4	Case Study 3	172
4.4.1	Selected Solution Strategy	172
4.4.2	Sensitivity Study	174
4.4.2.1	Sensitivity regarding FE Discretization	174
4.4.2.2	Sensitivity to choice of Constitutive Model for Concrete	175
5	Conclusions	178
6	Suggestions for Further Research	180

Notations

Acronyms

2D	Two-dimensional
3D	Three-dimensional
DG	Guidelines for Nonlinear Finite Element Analysis of Concrete Structures, RTD 1016-1:2017 [Hendriks et al., 2017]
EC	Eurocode
EC2	Eurocode NS-EN-1992-1-1
FE	Finite Element
FEA	Finite Element Analysis
FEM	Finite Element Method
fibMC2010	European CEB-FIP Model Code 2010
LD	Load Displacement
LDC	Load Displacement Curve
LFEA	Linear Finite Element Analysis
LS	Load Step
MC2010	Tension Softening approach according to Paragraph 5.1.8.2 in European CEB-FIP Model Code 2010
MNRM	Modified Newton Raphson Method
NLFEA	Nonlinear Finite Element Analysis
NRM	Newton Raphson Method
PDE	Partial Differential Equation
RC	Reinforced Concrete
RNRM	Regular Newton Raphson Method
TS	Tension Softening

Roman upper case letters

A	Area of finite element
B	Width of beam
D	Displacement
E^{adj}	Elastic modulus of adjacent mesh set
E_c	Young's modulus of concrete
E_s	Young's modulus of reinforcement steel
E_{har}	Hardening modulus
E_{steel}	Young's modulus of steel plates
G_F^{RC}	Modified fracture energy
G_C	Compressive fracture energy
G_F	Fracture energy
H	Height of beam
K	Stiffness
K_n	Normal stiffness
K_t	Tangential stiffness
L	Span length of beam

L_{tot}	Total length of beam
P	Total applied load
R_{exp}	Ultimate load capacity of the structure from the experiment
R_{NFLEA}	Ultimate predicted load capacity of the structure from the NLFEA
$S_{r,max}$	Maximum crack spacing
V	Volume of finite element
V_{θ}	Coefficient of variation of the variable to model the modelling uncertainty
S_2	Compressive stress in 2D model
S_3	Compressive stress in 3D model

Roman lower case letters

c	Cover of the reinforcement
f_{ck}	Characteristic compressive strength of concrete
f_{cm}	Mean cylinder compressive strength of concrete
f_{ctm}	Mean tensile strength of concrete
f_y	Yield strength of reinforcement
h	Finite element height
h_{eq}	Equivalent length of finite element
l^{el}	Length of finite element
l_{av}	Average crack spacing
n_{cr}	Number of cracks within a finite element, modification factor of the tensile fracture energy.

Greek lower case letters

α_c	Peak compressive strain of concrete, defining peak on the parabolic compression behaviour function
α_u	Ultimate compressive strain of concrete, defining completely softening on the parabolic compression behaviour function
ϵ_1	Principal tensile strain of concrete in both 2D and 3D model
ϵ_2	Principal compressive strain of concrete in 2D model
ϵ_3	Principal compressive strain of concrete in 3D model
ϵ_c	Compressive strain of concrete for constant behaviour function
ϵ_u	Ultimate tensile strain of concrete, defining completely softening on the tension softening curve
ϵ_{cu2}	Idealized ultimate compressive strain of concrete
ϵ_{nn}^{cr}	Normal crack strain
ϵ_{peak}	Peak tensile strain of concrete, defining peak on the tension softening curve
ϵ_{um}	Mean ultimate strain of reinforcement steel
ϵ_{ym}	Mean yield strain of reinforcement steel
ν	Poisson's ratio
$\rho_{p,ef}$	Effective reinforcement ratio
θ	Variable to model the modelling uncertainty
θ_m	Mean ratio of experimental to predicted load capacity
\emptyset	Reinforcement diameter

1. Introduction

Reinforced concrete (RC) beams used in concrete structures often include web openings. The purpose of these openings is to facilitate essential services such as ducts and pipes associated with mechanical, electrical and sewer systems or network system access. These structural beam elements provide an effective way to utilize the space in structures. However, openings disturb the load path from the applied load points to the supports. Consequently, this may result in a decreased strength and serviceability of the beam.

A relatively large number of experimental studies on beams with web openings have been conducted and published during the last decade. However, most of the existing code provisions do not provide sufficient guidance regarding non-linear modelling of these structural elements, which may be useful in order to understand and analyze its structural behaviour.

Due to web openings, these beams contain so called *discontinuity regions* (D-regions), which are characterized by nonlinear stress distributions. In those areas, the Bernoulli hypothesis about plane sections remaining plane after bending is not valid. D-regions are typically located in areas near concentrated loads, corners, openings etc.

The objective of this thesis is to come up with a general numerical *solution strategy* [Engen et al., 2017b] that may be valid for a various selection of such RC beams with openings. A non-linear finite element analysis (NLFEA) is used in order to determine the ultimate capacity and failure mode. NLFEAs have been receiving increasing attention these days. By use of fracture mechanics concepts used in conjunction with the finite element method, NLFEA provides a tool to assess information about the realistic structural behaviour of RC structures based on actual material properties. Compared to in a linear finite element analysis (LFEA), the non-linear extension makes the NLFEA more time consuming, and it demands many inputs regarding material non-linearities.

Challenges in NLFEAs are related to the many specifications regarding constitutive models, finite element (FE) discretizations, numerical solution methods, convergence criteria etc. Consequently, in order to generate accurate numerical models, careful considerations regarding these selections are required. However, well established numerical models may be advantageous in several situations, for example in strength analyses and establishment of the causes of a structural failure. Unless explicitly modelled, software simulations do not include material uncertainties and errors caused by devices, which may be crucial in physical experiments.

Previous experimental studies on RC beams with different geometries and various number of web openings enable comparison of numerical results with real physical results. Three experimentally tested beams will be used as benchmarks in order to come up with a general numerical solution strategy. *Guidelines for Nonlinear Finite Element Analysis of Concrete Structures, RTD 1016-1:2017* (DG) [Hendriks et al., 2017] and the *European CEB-FIP Model Code 2010* (fibMC2010) [Code, 2010a] provide guidance regarding specifications related to the abstraction from mechanical models to numerical models.

The test specimens from the experiments will be implemented in a finite element analysis (FEA) software called DIANA [DIANA FEA, 2018]. The results obtained in DIANA will be post-

processed, in order to detect the failure modes for the numerical models. Results obtained by the selected solution strategy and also results from a sensitivity study regarding some modelling choices will be elaborated. In the end, the numerical modelling uncertainty will be evaluated and discussed. Modelling uncertainty is an important aspect when it comes to the validity of the NLFEA. It indicates how realistic the obtained numerical results are by comparing the numerical response to the real capacity of the physical specimen.

2. Method

2.1 Non-Linear Finite Element Analysis

FE modelling of physical structures is a process that consists of two distinct abstraction steps: First the abstraction from physical structure to mechanical model and then from the mechanical model to a finite element model.

For the last abstraction step, the finite element method (FEM) is used. The physical behaviour for space- and time-dependent problems is usually expressed in terms of partial differential equations (PDE) [COMSOL Inc]. These PDEs are solved by use of numerical methods. FEM is used to compute these numerical approximations of the real solution. The main principle is to subdivide a structure into finite elements that may be described by simple linear equations. The relationship between the stiffness (K), displacement (D) and load (P) in each finite element, is given as: $[K]\{D\}=\{P\}$. The simple equations that model these finite elements are then assembled into a larger system of equations that models the entire structure.

NLFEAs allow for simulation of the expected real non-linear structural behaviour of RC structures. For the complex non-linear material response of concrete the system of differential equations is non-linear. The stiffness and load become functions of the displacement history: $[K(D)]\{D\}=\{P(D)\}$. FEM solves the system of non-linear differential equations by use of discretization techniques. Specifications regarding the solution strategy [Engen et al., 2017b], which constitute constitutive relations, kinematic compatibility and force equilibrium, have to be carefully considered in order to obtain accurate results. Options and specifications regarding the solution procedure in NLFEAs will be elaborated in this chapter.

2.1.1 Material Properties

The material properties should describe the physical state of materials in the structure. Material models are derived from these properties, and constitute the material behaviour in the FEA.

2.1.1.1 Concrete

According to DG, the concrete properties should be derived from provisions given in fibMC2010. The most important material properties of concrete can be related to the characteristic cylinder compressive strength, f_{ck} . Formulas for these material properties are provided in DG, and listed in Table 2.1.

Table 2.1: Material properties of concrete.

Parameter		Unit
Characteristic Cylinder Compressive Strength	f_{ck}	N/mm ²
Mean Compressive Strength	$f_{cm} = f_{ck} + \Delta f$	N/mm ²
Mean Tensile Strength (for \leq C50)	$f_{ctm} = 0.3 f_{ck}^{2/3}$	N/mm ²
Mean Tensile Strength (for $>$ C50)	$f_{ctm} = 2.12 \ln(1 + (f_{cm}/10))$	N/mm ²
Fracture Energy	$G_F = 73 f_{cm}^{0.18}$	Nmm/mm ²
Compressive Fracture Energy	$G_C = 250 G_F$	Nmm/mm ²
(Initial) Poisson's Ratio	$\nu = 0.15$	-

$$\Delta f = 8 \text{ N/mm}^2.$$

2.1.1.2 Steel

Reinforcement

Characteristics for the most important material responses of the reinforcement are listed in Table 2.2.

Table 2.2: Material properties of reinforcement.

Parameter		Unit
Yield Strength	f_y	N/mm ²
Characteristic Yield Strength	f_{yk}	N/mm ²
Tensile Strength	f_t	N/mm ²
Mean Yield Strength	$f_{ym} = f_{yk} + 10$	N/mm ²
Mean Tensile Strength	f_{tm}	N/mm ²
Mean Yield Strain	$\epsilon_{ym} = \frac{f_{ym}}{E_s}$	-
Mean Ultimate Strain	$\epsilon_{um} = \frac{(f_{tm} - f_{ym})}{E_{har}} + \epsilon_{ym}$	-
Young's Modulus of Elasticity	E_s	N/mm ²
Hardening Modulus	$E_{har} = 0.02 E_s$	N/mm ²
Poisson's Ratio	$\nu = 0.3$	-

The formula for the mean ultimate strain of the reinforcement, as shown in Eq. (2.1), is based on the curve in Figure 2.1 from fibMC2010.

$$\epsilon_{um} = \frac{(f_{tm} - f_{ym})}{E_{har}} + \epsilon_{ym} \quad (2.1)$$

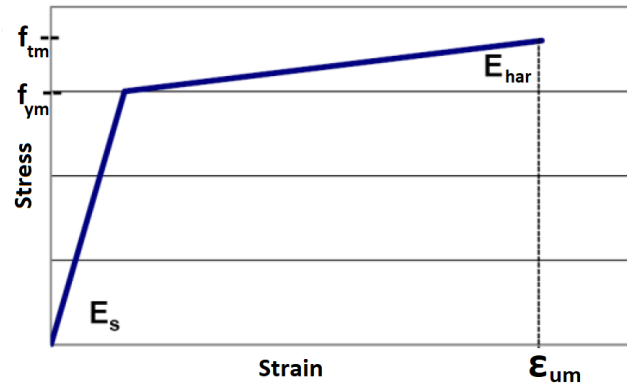


Figure 2.1: Stress-strain relationship for reinforcement steel bars [Code, 2010a].

2.1.2 Constitutive Models

In FEAs, material models, also called constitutive models, specify the constitutive behaviour of the materials in the structure by simplified abstractions of the true material behaviour.

2.1.2.1 Material Model for Concrete

According to DG, a total strain-based rotating crack or fixed crack model is preferred.

Total strain crack models describe the tensile and compressive behaviour of a material based on stress-strain relationships [Hendriks et al., 2017]. The stress is evaluated in the crack directions. Local strains are transformed to global strains by a transformation matrix. For a rotating crack model, this strain transformation matrix depends on the current strain vector, which means that the stress-strain relationship keeps updating with the strain vector. For a fixed crack model on the other hand, the strain transformation matrix is given by the incipient cracking, and is not updated for changed crack direction. Consequently, for a rotating crack model the planes of the cracks are rotating, while for fixed crack models, the planes are fixed in the a direction determined by the initial cracking direction [Du and CHEN, 2012]. Therefore, spurious stress-locking often occurs in fixed crack models, which results overestimation of the realistic failure load. Rotating crack models usually results in a lower failure load because it does not suffer as much from spurious stress locking.

Linear Elastic Properties

According to DG an isotropic linear-elastic material model based on the Young's modulus and Poisson's ratio should be used for concrete modelling. The Poisson's is assumed equal to 0.15, irrespective of the concrete strength [Hendriks et al., 2017].

Tensile Behaviour

Several tension softening (TS) functions could be used to describe the tensile behaviour of concrete. The softening curves are based on the fracture energy of the material and the crack-band width of the finite element.

An exponential TS curve is recommended [Hendriks et al., 2017]. This behaviour function shows an exponential softening behaviour after crack initiation. The area under the stress-strain curve constitutes the fracture energy, G_F , divided by the equivalent length, h_{eq} , also called *crack-band width*. After complete softening, when virtually no stresses are

transmitted, the crack is considered as *fully open*. The principal tensile strain at this point varies for the different TS approaches and for different crack-band widths.

Compressive Behaviour

According to DG, the compressive strength in a numerical concrete model should be limited. Hence the compressive behaviour should be modelled by a function that fulfills this recommendation. A parabolic compressive behaviour function, where the softening branch is based on the compressive fracture energy, G_C , is recommended [Hendriks et al., 2017]. By use of this function, the material gets fully softened in compression at a certain strain value.

Shear Behaviour

In concrete structures, the shear stiffness is usually reduced after cracking. FEA softwares usually provide different *Shear Retention Models*, where the shear retention indicates how much shear stiffness that is retained. The elastic shear modulus is reduced differently for the different shear retention models.

Tension-Compression Interaction

For concrete subjected to lateral tensile stresses, the strength and ductility is reduced. Lateral cracking also influence the material strength. Therefore the tension-compression interaction should be taken into account when the structure is subjected to a multi-axial stress state [Hendriks et al., 2017]. Several interaction models are available in the literature. Some of the models only provide reduction of the compressive strength, while others reduce both the compressive strength and the peak compressive strain.

Poisson's Ratio Reduction Model

The ratio between lateral strains and longitudinal strains decrease when the concrete cracks. Therefore the Poisson's ratio should be reduced as the damage caused by cracking increases.

Stress Confinement Model

Concrete subjected to compressive stress shows a pressure-dependent behaviour. Isotropic compressive stress results in an increased strength and ductility. Compression-compression interaction is an important feature in order to model confinement effects [Hendriks et al., 2017]. However, DG specifies that it is conservative to neglect this effect. Therefore, it is not specified any specifications regarding choice of model.

2.1.2.2 Material Model for Reinforcement

DG recommends an elasto-plastic material model for the reinforcement, where the elastic limit is equal to the yield strength of the steel. The post-yield behaviour is known as *hardening*, and improve the stability of the analysis [Hendriks et al., 2017].

2.1.2.3 Model for Concrete-Reinforcement Interaction

Bond-slip between Reinforcement and Concrete

DG recommends to use embedded reinforcement, which entails that slip between reinforcement and concrete is ignored.

Tension Stiffening

Tension stiffening describes the increase in tensile stiffness of reinforcement bars embedded in concrete compared to plain reinforcement bars alone. The TS model for the concrete material specifies the amount of added contribution of tensile stiffness to the reinforcement bars. DG suggests that if the average crack spacing, l_{av} , in the concrete is smaller than the equivalent length, h_{eq} , the amount of released energy, G_F , should be increased by a factor, n_{cr} , as given in Eq. (2.3). n_{cr} is equal to the number of cracks within a single element, given by Eq. (2.4). l_{av} could be calculated according to Eq. (2.2), where this length is referred to as $S_{r,max}$. If $S_{r,max} < h_{eq}$, the unmodified tensile fracture energy, G_F , can be used to determine the tension softening relation.

$$S_{r,max} = k_3 c + k_1 k_2 k_4 \frac{\phi}{\rho_{p,eff}} \quad (2.2)$$

Table 2.3: Factors included in the formula for the crack spacing.

k_1	0.8 for high-bond bars 1.6 for plain bars
k_2	0.5 for pure bending 1.0 for pure tension
k_3	3.4 (recommended value)
k_4	0.425 (recommended value)

$$G_F^{RC} = n_{cr} G_F \quad (2.3)$$

$$n_{cr} = \max\left(1, \frac{h_{eq}}{S_{r,max}}\right) \quad (2.4)$$

2.1.3 Finite Element Discretization

2.1.3.1 Mesh Order

According to DG, quadratic mesh order is recommended. Linear interpolation for the displacement field will show locking behaviour in certain cases. Quadratic elements can describe more deformation modes and complex failure modes such as shear failure [Hendriks et al., 2017].

2.1.3.2 Mesh Type

Regarding element type, either quadratic/hexagonal or triangular/tetrahedron can be used in 2D or 3D modelling respectively. 8-node quadrilateral elements are recommended for 2D structures and 20-node hexahedral elements for 3D structures [Hendriks et al., 2017].

2.1.3.3 Mesh Density

According to FEA theory, FE models with a fine mesh yield highly accurate results compared to FE models with a coarse mesh [COMSOL Inc]. In order to ensure that the constitutive model does not exhibit an undetected snap-back in the stress-strain relationship, and such that a considerably smooth stress field can be calculated, the maximum element size should be limited. According to DG, the maximum element size of a regular 2D beam should be limited to the smallest value of $L/50$ and $H/6$, where L is the span length and H is the height of the beam. It is not given any restrictions regarding the minimum element size, but this will be limited by the computational time. However, DG does not include recommendations for beams with web openings.

2.1.3.4 Equivalent Length

The equivalent length is an essential parameter in constitutive models [Hendriks et al., 2017]. h_{eq} is related to the dimension of the finite elements and the direction of the cracks. It describes a softening stress-strain relationship. For quadratic quadrilateral elements with a square shape and with a crack direction along one of the diagonals, the estimated crack-band width would be $h_{eq} = \sqrt{2}h$. For the same square elements with a crack along one of the element edges, $h_{eq} = h$ [Hendriks et al., 2017].

2.1.3.5 Integration Scheme

Both reduced (2x2) and full (3x3) integration scheme can be used in FEAs. Reduced integration scheme may introduce spurious non-zero energy modes when the stiffness of the element becomes small due to extensive cracking [Hendriks et al., 2017].

2.1.4 Numerical Analysis

2.1.4.1 Load Application

FEM solves the system of non-linear PDEs by use of discretization strategies. Time discretization strategies usually have the form of an incremental-iterative solution scheme, where the load or displacement is applied in several incremental steps and the structural response for each step is computed from the equilibrium conditions. Load Control Method (LCM) works well as long as the load increases monotonically. However, after the peak on the Load Displacement Curve (LDC), the solution may diverge. Further increase in the load cannot be resisted by the structure. With Displacement Control Method (DCM) on the other hand, the initial descending part of the LDC can be traced as long as the displacement increase monotonically. Many researchers conclude that DCM is the most efficient algorithm if there is no *snap-back* behaviour, meaning if the displacement is non-monotonic during tracing of the equilibrium path.

2.1.4.2 Equilibrium Iteration

Equilibrium between internal and external forces could be achieved by use of several different iterative procedures. According to DG, The Newton Raphson Method (NRM) is sufficiently accurate and efficient, hence it is the most commonly used procedure to perform equilibrium iterations. Several types of NRMs are available, where the stiffness matrix is updated differently. Two of these methods were considered for these NLFEMs, Regular Newton Raphson Method (RNRM) and Modified Newton Raphson Method (MNRM).

In RNRM, the stiffness relation is updated once per iteration within each incremental step. Hence, the stiffness matrix needs to be established in every iteration, which may be very time consuming [TNO DIANA, 2010a].

In MNRM, the stiffness relation is only updated once per incremental step. The tangential stiffness from the first iteration is used throughout the entire increment. Consequently the convergence rate could be poor for this method, especially when the load is close to the failure load [H.Zheng and L.G.Tham, 2005].

2.1.4.3 Convergence Criteria

To determine equilibrium it is necessary with suitable convergence criteria. According to DG, energy-norm combined with force-norm is preferred. In order to achieve convergence in an incremental step, the iteration method needs to at least fulfill one of the specified convergence criteria within the specified allowable number of iterations.

2.2 Benchmark Analyses

The aim of the work reported in this thesis was to come up with a general numerical solution strategy for finite element modelling of reinforced concrete beams with web openings. In order to come up with an accurate numerical solution strategy, three benchmark tests enabled comparison of the numerical response with a real physical response. This section presents specifications regarding test setup, material parameters and experimental results from the selected benchmark analyses. The numerical approaches of the selected test specimens are presented later.

2.2.1 Case Study 1

The paper *Structural behaviour of reinforced-concrete continuous deep beams with web openings* [Yang and Ashour] contains test results of ten RC continuous deep beams with web openings. Case Study 1 presents a numerical approach to the experimental results for one of the tested beam specimen, 6IT1, which was used as a benchmark analysis in order to come up with- and verify a numerical solution strategy. This section presents the experimental test setup, material parameters and test results for 6IT1. Results from the numerical modelling of 6IT1 will be presented in Sec. 3.1.1.

2.2.1.1 Experimental Setup

The geometry of 6IT1 is shown in Figure 2.2 and details of geometrical dimensions are listed in Table 2.4. Figures 2.3 and 2.4 illustrate the reinforcement arrangement in the beam.

This section explains how the experimental setup was arranged. A more detailed explanation, which includes information about the instruments used in the test, is found in the experimental report. Figure 2.5 was provided in the report, and illustrates the experimental test setup.

Table 2.4: 6IT1. Dimensions of geometry.

Concrete Beam		
Height	H	600 mm
Total length	L_{tot}	1790 mm
Span length	L	720 mm
Width	B	160 mm
Opening height		60 mm
Opening width		90 mm
Support and load plates		
Thickness		40 mm
Length		150 mm

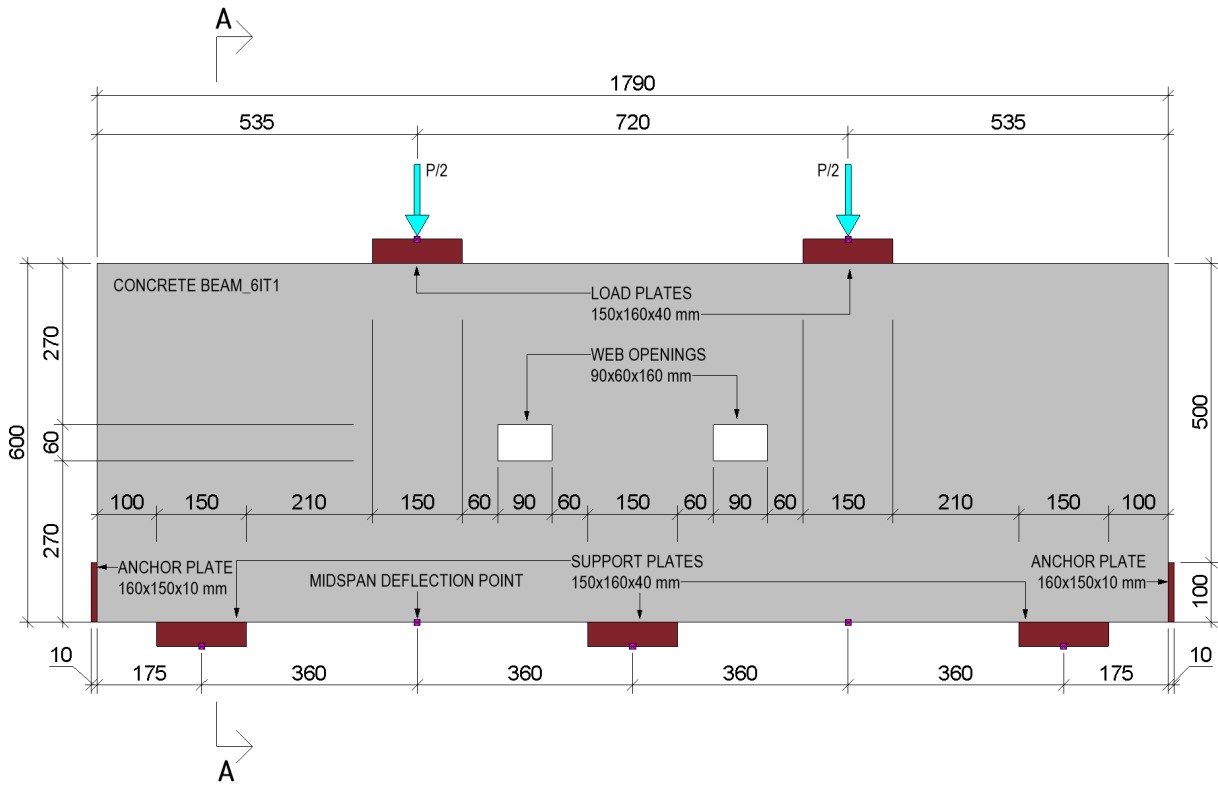


Figure 2.2: 6IT1. Geometrical dimensions given in mm. Modelling tool [Autodesk Inc., 2018].

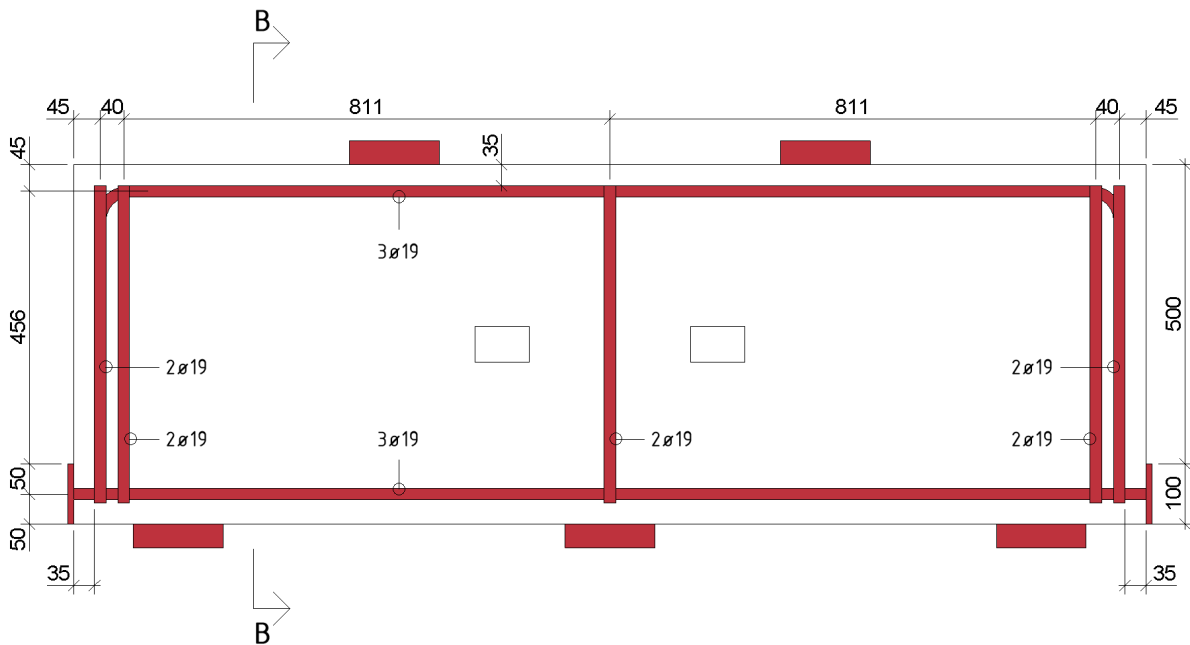


Figure 2.3: 6IT1. Rebar configurations. Nominal cover of 35 mm. Modelling tool [Autodesk Inc., 2018].

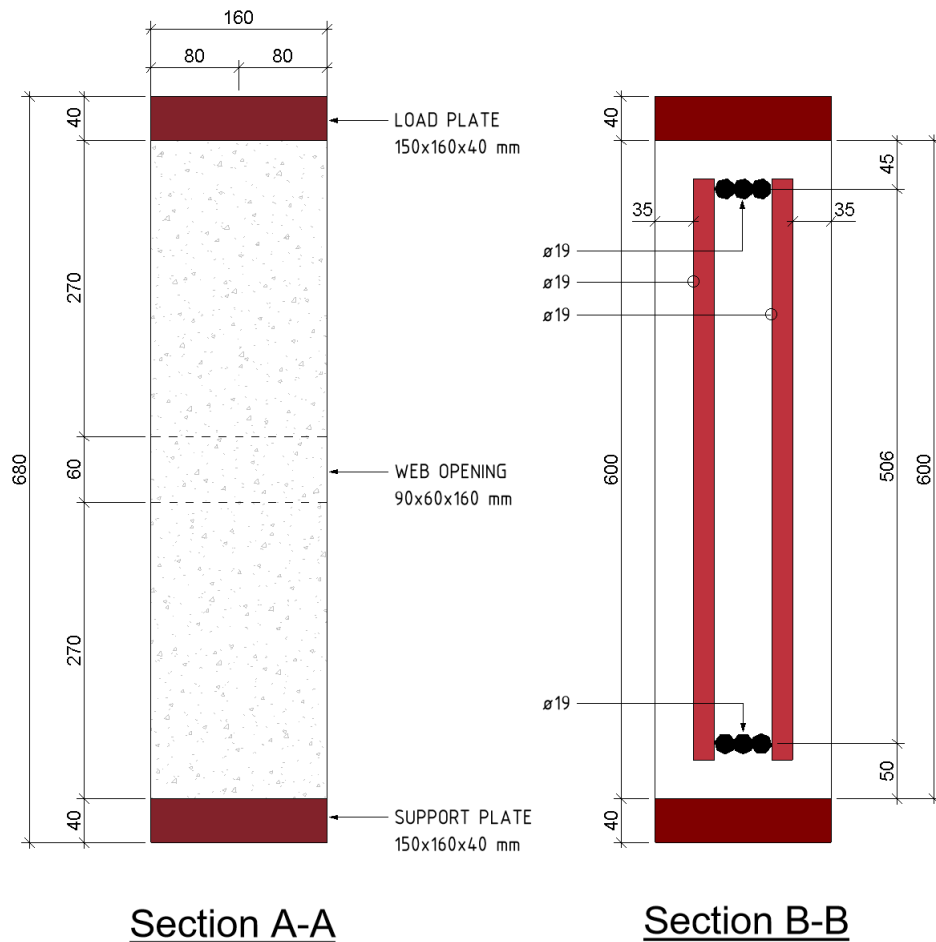


Figure 2.4: 6IT1. Rebar- and concrete cross section. Dimensions in mm. Modelling tool [Autodesk Inc., 2018].

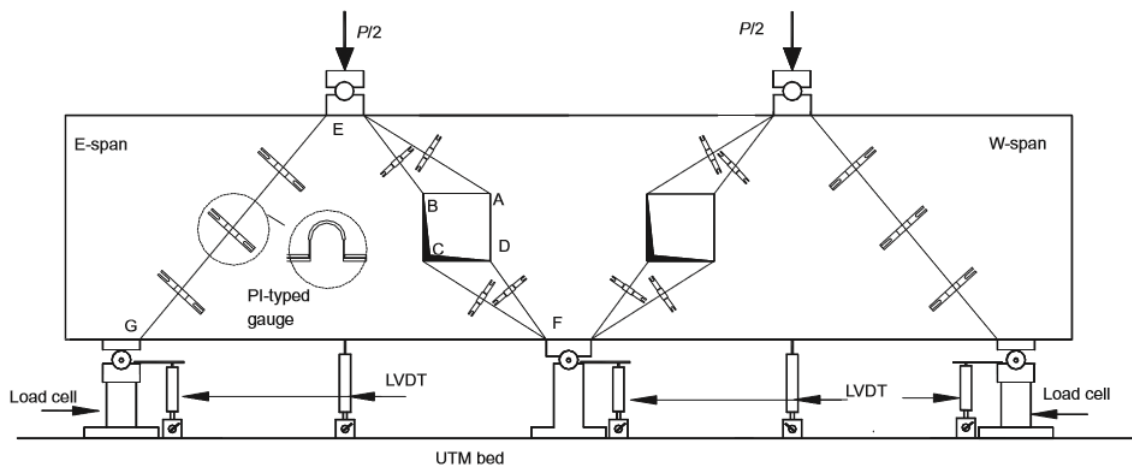


Figure 2.5: 6IT1. Loading and instrumentation arrangements for test setup. Figure from report [Yang and Ashour].

The beam was tested to failure under a symmetrical two-point top loading system with a loading rate of 30 kN/min. The two exterior end supports were designed to allow horizontal and rotational movements, whereas the intermediate support prevented horizontal move-

ment but allowed rotation. 150 mm wide steel plates were provided at the points of loading and support, in order to prevent premature crushing or bearing failure. The beam was preloaded up to a total load of 150 kN before testing, in order to assure a similar loading distribution to supports. This loading did not produce any cracks.

Some uncertainties regarding the numerical modelling of 6IT1 may have affected the numerical results. The numerical model of 6IT1 was not preloaded. Another discrepancy between the experimental and numerical models may have been the concrete cover. The report does not state the concrete cover in the tested specimen. For the NLFEAs of 6IT1 the cover was modelled according to Figures 2.3 and 2.4. The reinforcement configurations are modelled according to an assumed nominal cover of 35 mm, and hence not necessarily identical as in the experimental setup.

2.2.1.2 Material Parameters

The mean compressive strength of the concrete was given in the paper [Yang and Ashour]. This value was based on tests of cylinders with concrete from the same batch, that were cast simultaneously with the beams. However, it is not stated how many cylinders that were tested. The rest of the concrete parameters are calculated based on this value.

Regarding the steel, only the yield strength for the rebars were provided in the report. Values for the Young's modulus of the rebars and the steel plates were assumed. So was the yield strength of the steel plates.

All material parameters used in the NLFEAs of 6IT1 are listed in Table 2.5.

Table 2.5: 6IT1. Material parameters.

Concrete parameters		
Mean Compressive Strength	f_{cm}	68.2 N/mm ²
Mean Tensile Strength	$f_{ctm}=2.12\ln(1+(f_{cm}/10))$	4.35 N/mm ²
Fracture Energy	$G_F=0.073 f_{cm}^{0.18}$	0.15 N/mm
Compressive Fracture Energy	$G_C=250G_F$	39.03 N/mm
Young's Modulus of Elasticity	E_c	39000 N/mm ²
Poisson's Ratio	ν	0.15
Reinforcement parameters		
Diameter: 19 mm		
Yield Strength	f_y	560 N/mm ²
Young's Modulus of Elasticity	E_s	210000 N/mm ²
Steel plate parameters		
Yield Strength	f_y	355 N/mm ²
Young's Modulus of Elasticity	E_{steel}	210000 N/mm ²

2.2.1.3 Experimental Results

The experimental LDC is given in Figure 2.6.

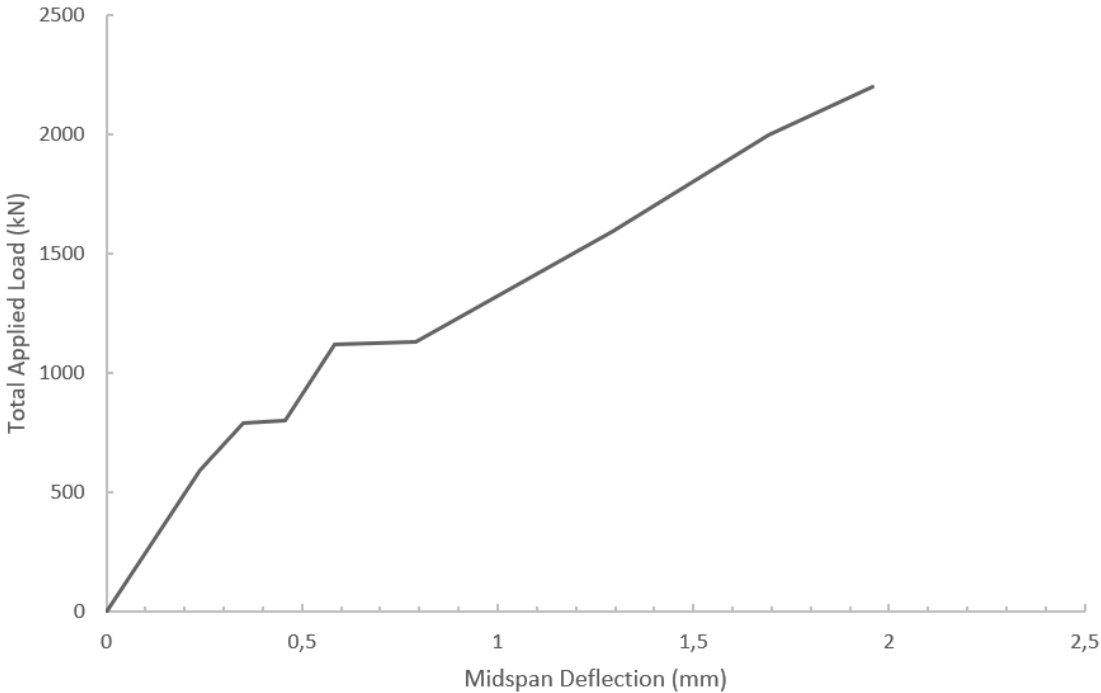


Figure 2.6: 6IT1. Experimental LDC.

The failure mode was characterized by a failure plane that formed along diagonal concrete struts joining the edges of the load plates and opening corners opposite to the load points, AE and CF in Figure 2.5. Figure 2.7 shows the crack pattern and at what load the different cracks occurred. Based on this, the first visible crack appeared after 610 kN was applied. Most cracks were concentrated at corners of openings. After the first diagonal crack appeared at web opening corners, the deflection of the beam sharply increased. This constituted the first horizontal plateau in the LDC which is shown in Figure 2.6. The reported failure load is 2199 kN.

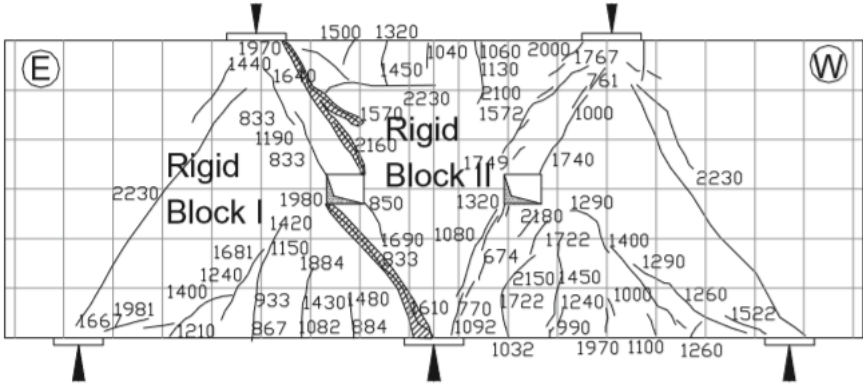


Figure 2.7: 6IT1. Experimental crack pattern. The numbers indicate the total applied load in kN for when the specific cracks occurred. Figure from the report [Yang and Ashour].

2.2.2 Case Study 2

The experimental result in this case study is collected from the paper *Influence of Inclined Web Reinforcement on Reinforced Concrete Deep Beams with Openings* [Yang et al., 2007]. The paper contains test results of 15 RC deep beams with various sized web openings and various amount of reinforcement. Case Study 2 presents a numerical approach to the experimental result for one of the tested beam specimen, *T1-0*, which was used as a benchmark analysis in order to come up with- and verify a numerical solution strategy. This section presents the test setup, material parameters and experimental results for T1-0. Numerical results will be presented in Sec. 3.2.1.

2.2.2.1 Experimental Setup

This section explains how the experimental setup was arranged. A more detailed explanation, which includes information about the instruments used in the test, is found in the experimental report.

T1-0 contains two small web openings and no inclined reinforcement. The beam is exposed to two point loads in the top of the beam, shown in Figure 2.8. It is a statically determined system with two supports in the bottom of the beam, one hinge and one roller. The geometry of the beam was given in the paper and is summarized in Table 2.6. It contains both vertical and horizontal shear reinforcement, in addition to rebars in the tensile and compressive zones, shown in Figures 2.9 and 2.10. The main longitudinal reinforcement in the bottom of the beam is cast into a steel plate at each beam end.

The main longitudinal bars were cast into a steel plate in each end of the beam. The beam was tested to failure under a symmetrical two-point top loading system with a loading rate of 20 kN/minute using a 3000 kN capacity universal testing machine. Both supports were designed to allow rotational movement. The vertical deflections were measured by 50 mm capacity linear variable differential transducers mounted at the bottom face at midspan. To observe the crack development the beam sides were whitewashed.

Table 2.6: T1-0. Dimensions of geometry.

Concrete Beam		
Height	H	600 mm
Total length	L_{tot}	1200 mm
Span length	L	900 mm
Width	B	160 mm
Opening height		60 mm
Opening length		75 mm
Support and load plates		
Thickness		50 mm
Length		100 mm

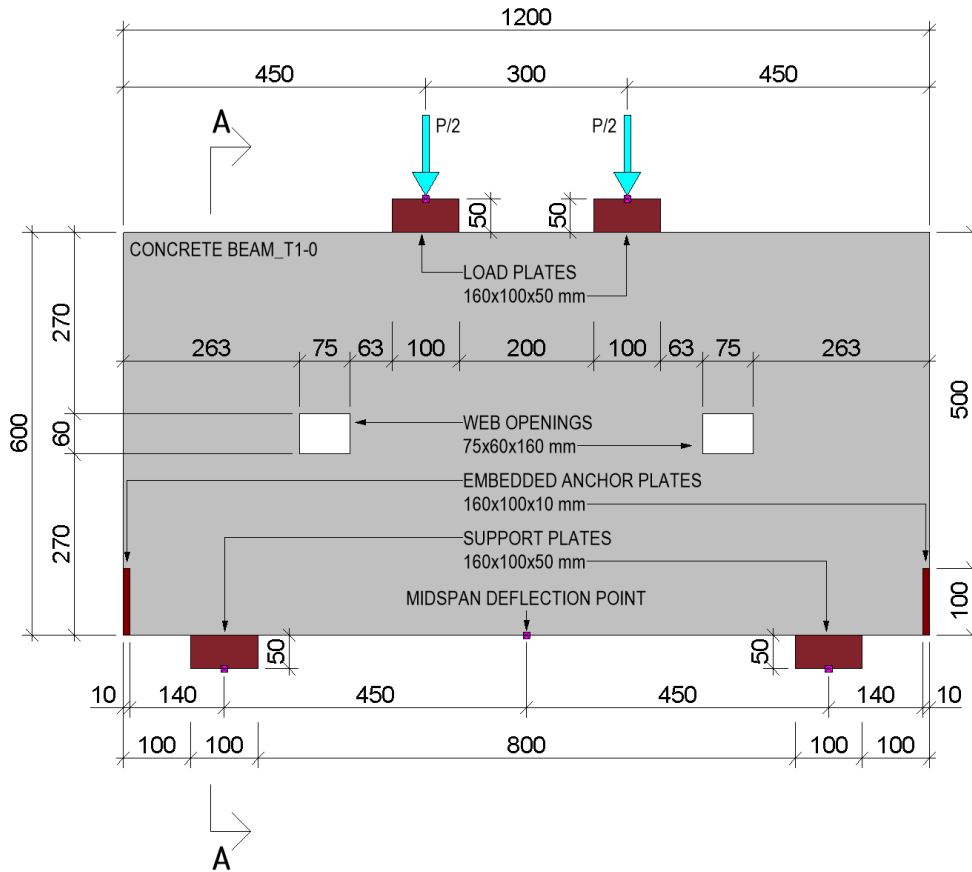


Figure 2.8: T1-0. Geometrical dimensions given in mm. Modelling tool [Autodesk Inc., 2018].

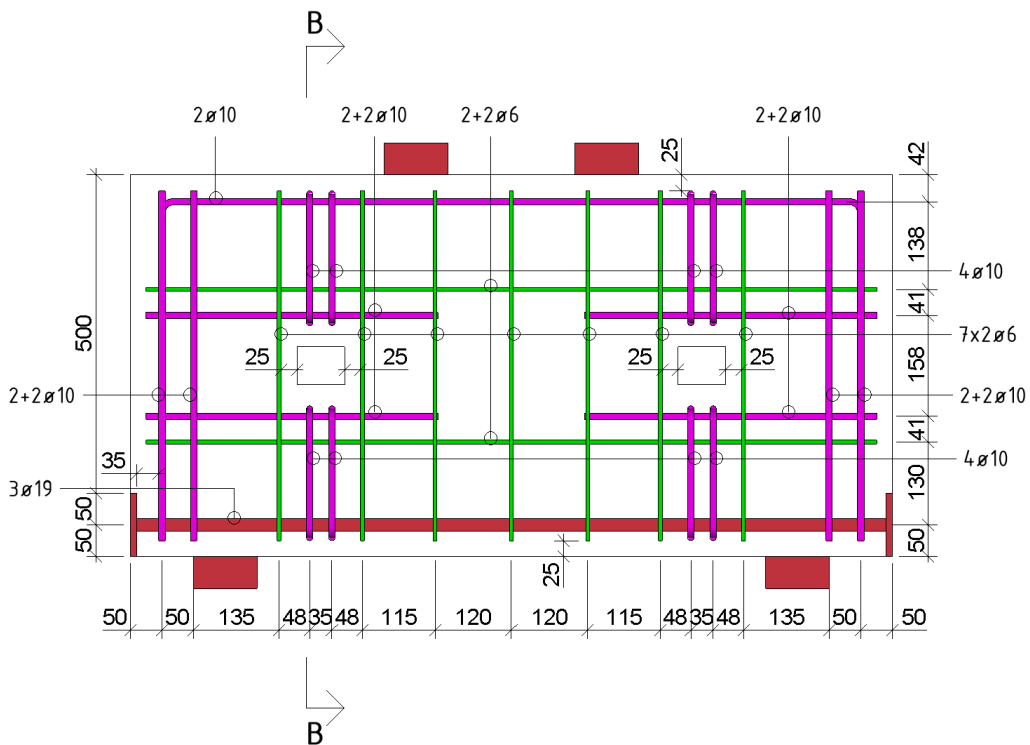


Figure 2.9: T1-0. Rebar configurations. Nominal cover of 25 mm. Modelling tool [Autodesk Inc., 2018].

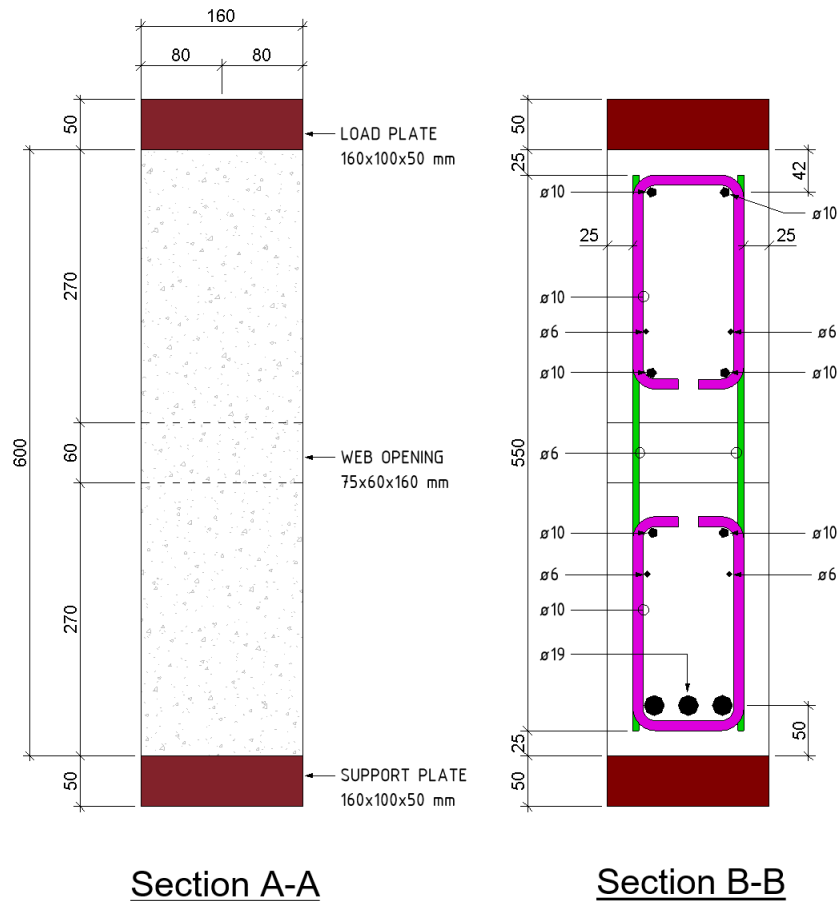


Figure 2.10: T1-0. Rebar- and concrete cross section. Dimensions in mm. Modelling tool [Autodesk Inc., 2018].

Some uncertainties regarding the numerical modelling of T1-0 may have affected the numerical results. The covers of the reinforcement were not given in the paper for T1-0. The reinforcement configurations are modelled according to an assumed nominal cover of 25 mm and 50 mm, and hence not necessarily identical as in the experiment. The rebar shapes are drawn according to [CEN, 2003]. Many assumptions had to be done regarding spacing of vertical and horizontal bars as well, where the arrangement is given in Figure 2.9.

2.2.2.2 Material Parameters

The mean compressive strength of the concrete was given in the paper. However, the Young's modulus was not stated, hence this value was requested by email, and received personally by the main researcher of the experimental study. All reinforcement properties and steel plate properties were given except the mean ultimate strain for the rebars. The yield strain for $\phi 6$ -bars was obtained by a 0.2% offset method, and the value was given in the report [Yang et al., 2007]. The material parameters are summarized in Table 2.7.

Table 2.7: T1-0. Material parameters.

Concrete parameters		
Mean Compressive Strength	f_{cm}	55.8 N/mm ²
Mean Tensile Strength	$f_{ctm}=2.12\ln(1+(f_{cm}/10))$	3.99 N/mm ²
Fracture Energy	$G_F=0.073f_{cm}^{0.18}$	0.15 N/mm
Compressive Fracture Energy	$G_C=250G_F$	37.64 N/mm
Young's Modulus of Elasticity	E_c	32400 N/mm ²
Poisson's Ratio	ν	0.15
Reinforcement parameters		
Diameter: 6 mm		
Mean Yield Strength*	f_{ym}	483 N/mm ²
Mean Yield Strain	$\epsilon_{ym,\phi6}$	$4.40 \cdot 10^{-3}$
Mean Tensile Strength	f_{tm}	549 N/mm ²
Mean Ultimate Strain	$\epsilon_{um,\phi6} = \frac{(f_{tm} - f_{ym})}{E_{har}} + \epsilon_{ym,\phi6}$	$2.10 \cdot 10^{-2}$
Young's Modulus of Elasticity	E_s	199000 N/mm ²
Nominal Hardening Modulus	$E_{har}=0.02E_s$	3980 N/mm ²
Diameter: 10 mm		
Mean Yield Strength	f_{ym}	408 N/mm ²
Mean Yield Strain	$\epsilon_{ym,\phi10}$	$2.10 \cdot 10^{-3}$
Mean Tensile Strength	f_{tm}	548 N/mm ²
Mean Ultimate Strain	$\epsilon_{um,\phi10} = \frac{(f_{tm} - f_{ym})}{E_{har}} + \epsilon_{ym,\phi10}$	$3.80 \cdot 10^{-2}$
Young's Modulus of Elasticity	E_s	195000 N/mm ²
Nominal Hardening Modulus	$E_{har}=0.02E_s$	3900 N/mm ²
Diameter: 19 mm		
Mean Yield Strength	f_{ym}	803 N/mm ²
Mean Yield Strain	$\epsilon_{ym,\phi19}$	$4.10 \cdot 10^{-3}$
Mean Tensile Strength	f_{tm}	898 N/mm ²
Mean Ultimate Strain	$\epsilon_{um,\phi19} = \frac{(f_{tm} - f_{ym})}{E_{har}} + \epsilon_{ym,\phi19}$	$2.86 \cdot 10^{-2}$
Young's Modulus of Elasticity	E_s	194000 N/mm ²
Nominal Hardening Modulus	$E_{har}=0.02E_s$	3880 N/mm ²
Steel plate parameters		
Young's Modulus of Elasticity	E_{steel}	210000 N/mm ²
Yield Strength	f_y	500 N/mm ²

2.2.2.3 Experimental Results

Figure 2.11 shows the experimental LDC. The peak load is 1452 kN, where 726 kN is equally applied to each load plate.

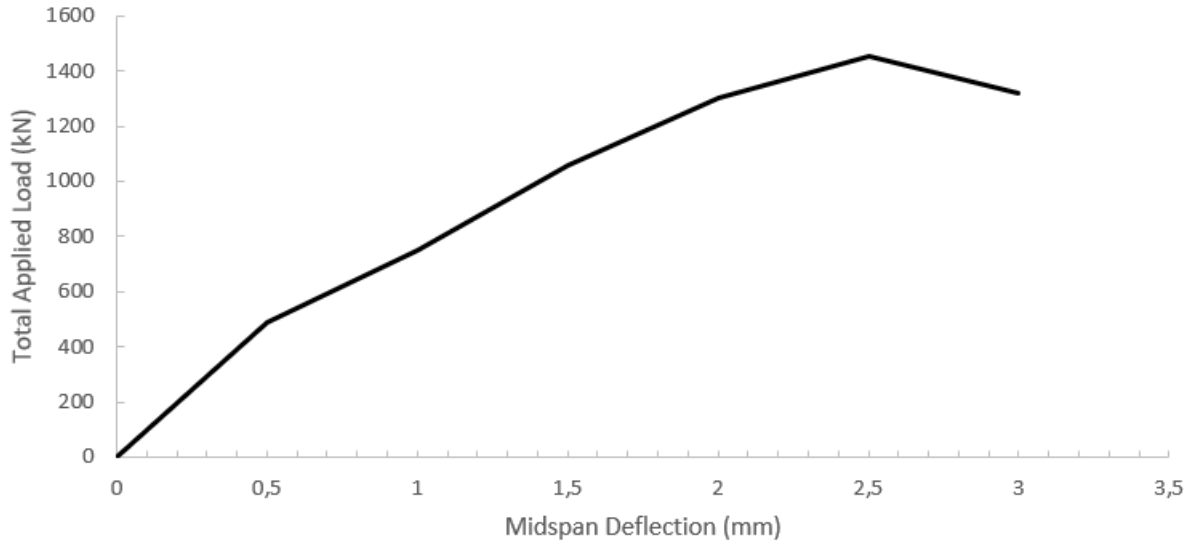


Figure 2.11: T1-0. Experimental LDC.

The experimental crack observations in T1-0 are collected from the experimental report. The first cracks were observed in the corners of the web openings, as shown in Figure 2.12. The first crack appeared on the left side when the total applied load was 326.6 kN. At a load of 350 kN the first cracks appeared at the right opening. The first flexural cracks at midspan were observed at a load of 359 kN. Diagonal cracks were formed through the beam height, from the opening corners to the edges of the load- and support plates. The failure mode was characterized by shear failure. The crack pattern was not completely symmetrical. The researchers argued that the beam could have been disturbed by an imperfection in the geometry, loading or the material.

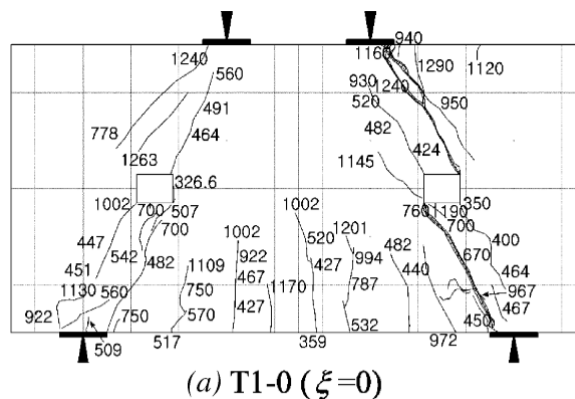


Figure 2.12: T1-0. Experimental crack pattern. The numbers indicate the total load in kN for when the specific cracks occurred. [Yang et al., 2007].

2.2.3 Case Study 3

The paper *Flexural Behaviour and Strength of Reinforced Concrete Beams with Multiple Transverse Openings* [Aykac et al., 2014] contains experimental test results of 10 rectangular reinforced concrete beams with and without multiple web openings. The difference in the RC beam configurations were mainly based on effects of opening geometry (circular vs. rectangular), stirrups in posts between openings, diagonal reinforcement around openings, and the effect of longitudinal reinforcement with respect to the flexible behaviour of the beams. Case Study 3 presents a numerical approach to the experimental results for one of the tested beam specimen, *RCxcb*, which was used as a benchmark analysis in order to come up with- and verify a numerical solution strategy. Out of the 10 test specimens presented in the paper, this specimen was the one that resisted the highest ultimate load, and exhibited greater ductility than the reference beam without openings. This section presents the experimental test setup, material parameters and test results for *RCxcb*. Results from the numerical modelling of this beam specimen will be presented in Sec. 3.3.1.

2.2.3.1 Experimental Setup

Details of geometrical dimensions of *RCxcb* are listed in Table 2.8. Aspects of geometry, reinforcement configuration and loading conditions are illustrated in Figures 2.13, 2.14, 2.15, 2.16 and 2.17. Numerical specifications regarding the boundary conditions are based on assumptions, and further described in Sec. 2.3.3.5 and Sec. 3.3.2.1. The reinforcement configurations are modelled according to a guessed nominal cover of 25 mm, and hence not necessarily identical to the real cover in the physical model. The bar shapes are drawn according to the Norwegian Standard [CEN, 2003].

The physical test specimen was exposed to a loading scheme characterized by evenly distributed loading. In order to approach a similar loading condition for the numerical model, a six-point bending regime was adapted. To receive a more realistic bending regime, the secondary spreader beam was modelled in DIANA. The presence of multiple openings was assumed to help distribute stress concentrations around openings to the entire beam length [Aykac et al., 2014]. Due to this, the authors pursued a more ductile flexural failure mode.

Table 2.8: *RCxcb*. Dimensions of geometry.

Beam		
Height	H	400 mm
Length	L_{tot}	4000 mm
Span length	L	3800 mm
Width	B	150mm
Number of web openings		12
Diameter of web openings		200 mm
Support and load plates		
Thickness		40 mm
Length of support plates		200 mm
Width		150 mm
Length of load plates		100 mm

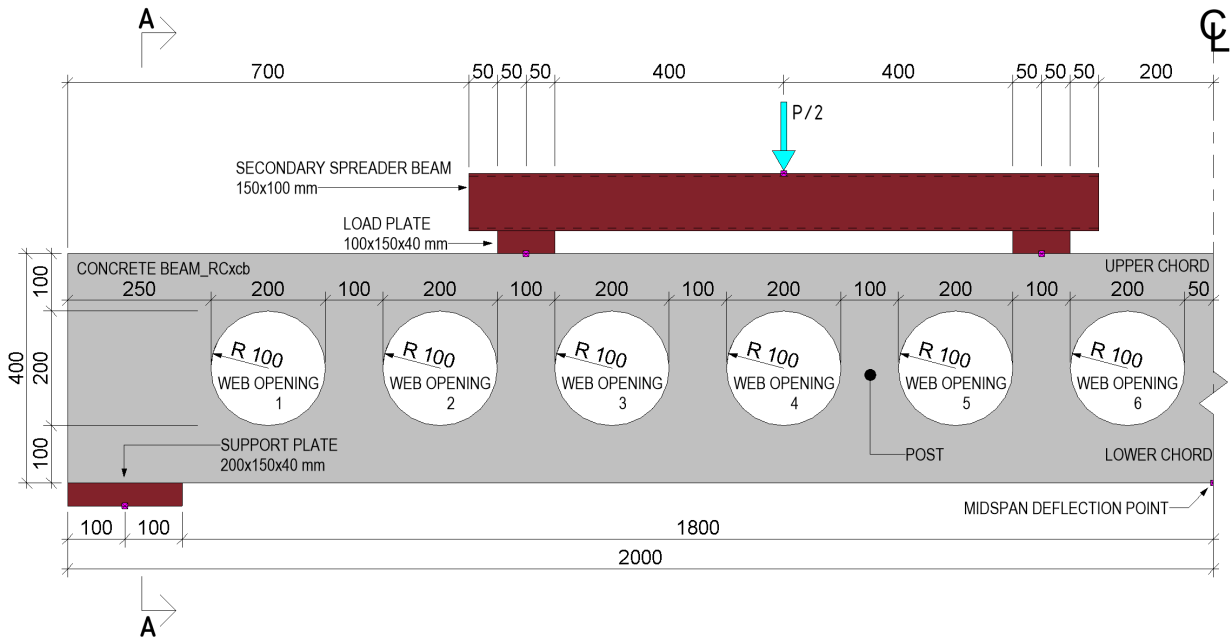


Figure 2.13: RCxcb. Geometrical dimensions given in mm. Modelling tool [Autodesk Inc., 2018].

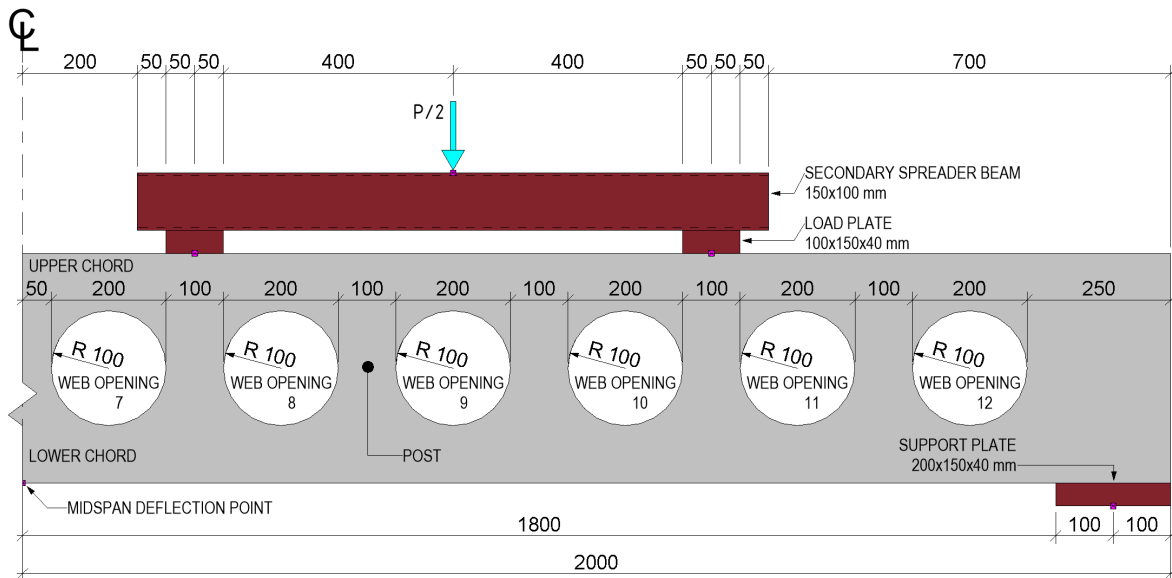


Figure 2.14: RCxcb. Geometrical dimensions given in mm. Modelling tool [Autodesk Inc., 2018].

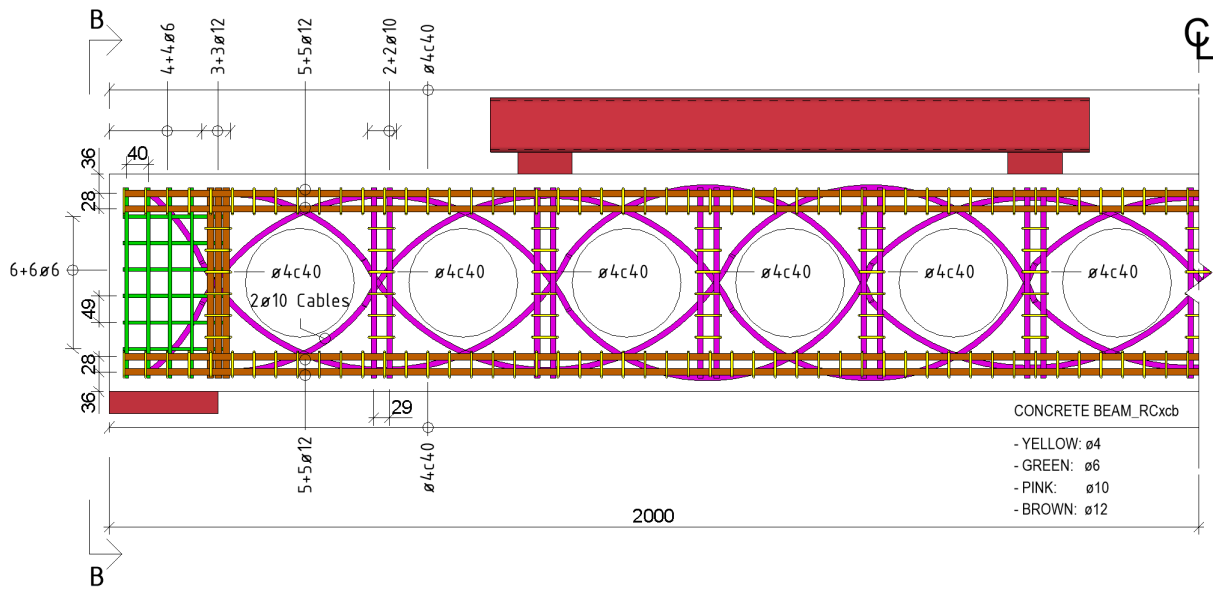


Figure 2.15: RCxcb. Rebar configurations. Nominal cover of 25 mm. Modelling tool [Autodesk Inc., 2018].

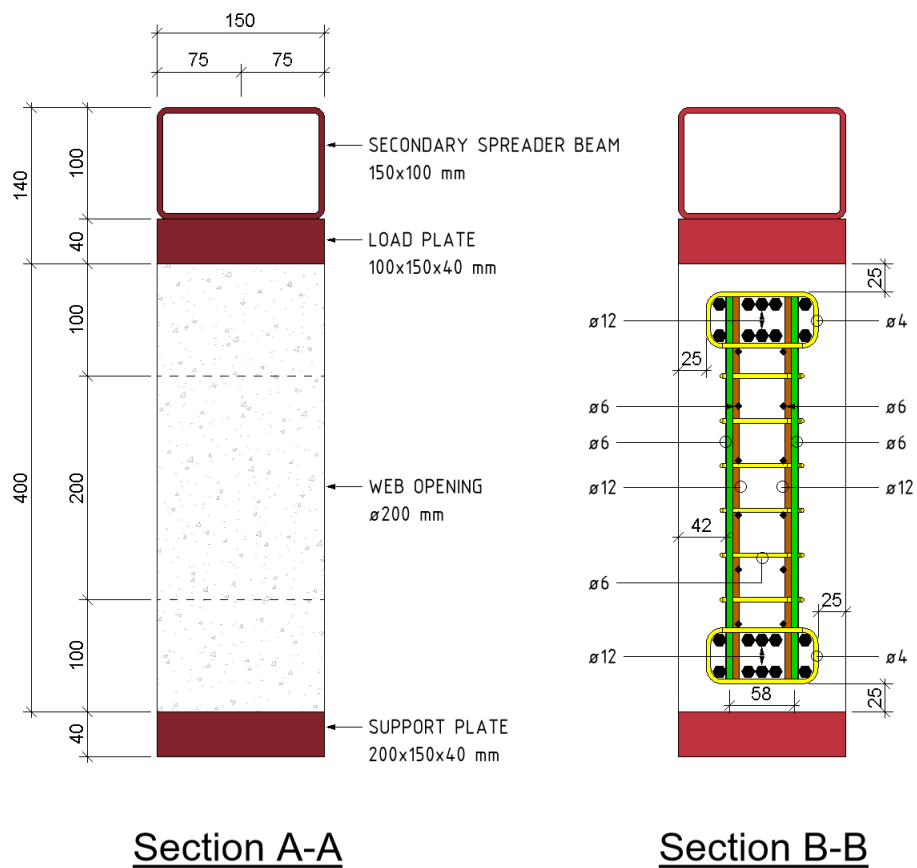
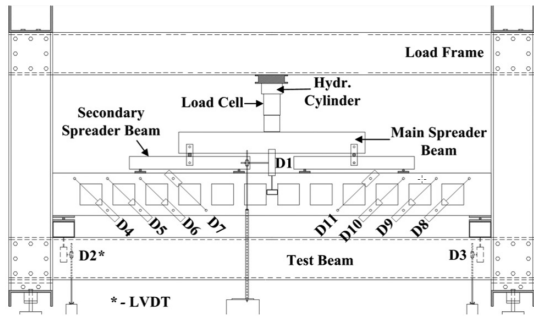
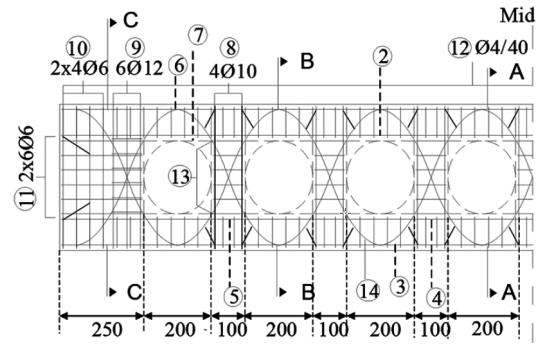


Figure 2.16: RCxcb. Rebar- and concrete cross section. Dimensions in mm. Modelling tool [Autodesk Inc., 2018].



(a) Test setup of experimental program.



(b) Experimental reinforcement details.

Figure 2.17: RCxcb. Loading and instrumentation arrangements for test setup, and reinforcement details. Figure from report [Aykaç et al., 2014].

2.2.3.2 Material parameters

The concrete and reinforcement properties are listed in Table 2.9. The parameters for $\phi 4$ stirrups and $\phi 6$ bars are based on assumptions, with data collected from a report by Mancini [Mancini, 2017]. The non-prestressed $\phi 10$ cables are based on same properties as $\phi 10$ bars.

Table 2.9: RCxcb. Material parameters.

Concrete parameters		
Mean Compressive Strength	f_{cm}	26.1 N/mm ²
Mean Tensile Strength	$f_{ctm} = 0.30 \cdot f_{ck}^{\frac{2}{3}}$	2.07 N/mm ²
Fracture Energy	$G_F = 0.073 f_{cm}^{0.18}$	0.13 N/mm
Compressive Fracture Energy	$G_C = 250 G_F$	32.83 N/mm
Young's Modulus of Elasticity	E_c	30290 N/mm ²
Poisson's Ratio	ν	0.15
Reinforcement parameters		
Diameter: 4 mm		
Mean Yield Strength	f_{ym}	520 N/mm ²
Mean Tensile Strength	f_{tm}	710 N/mm ²
Mean Yield Strain	$\epsilon_{ym,\phi 4}$	$2.60 \cdot 10^{-3}$
Mean Ultimate Strain	$\epsilon_{um,\phi 4} = \frac{(f_{tm} - f_{ym})}{E_{har}} + \epsilon_{ym,\phi 4}$	$5 \cdot 10^{-2}$
Young's Modulus of Elasticity	E_s	200000 N/mm ²
Diameter: 6 mm		
Mean Yield Strength	f_{ym}	520 N/mm ²
Mean Tensile Strength	f_{tm}	710 N/mm ²
Mean Yield Strain	$\epsilon_{ym,\phi 6}$	$2.60 \cdot 10^{-3}$
Mean Ultimate Strain	$\epsilon_{um,\phi 6} = \frac{(f_{tm} - f_{ym})}{E_{har}} + \epsilon_{ym,\phi 6}$	$5 \cdot 10^{-2}$
Young's Modulus of Elasticity	E_s	200000 N/mm ²
Diameter: 10 mm		
Mean Yield Strength	f_{ym}	476 N/mm ²
Mean Tensile Strength	f_{tm}	695.7 N/mm ²
Mean Yield Strain	$\epsilon_{ym,\phi 10} = \frac{f_{ym}}{E_s}$	$2.38 \cdot 10^{-3}$
Mean Ultimate Strain	$\epsilon_{um,\phi 10} = \frac{(f_{tm} - f_{ym})}{E_{har}} + \epsilon_{ym,\phi 10}$	$5.73 \cdot 10^{-2}$
Young's Modulus of Elasticity	E_s	200000 N/mm ²
Diameter: 12mm		
Mean Yield Strength	f_{ym}	550.5 N/mm ²
Mean Tensile Strength	f_{tm}	646 N/mm ²
Mean Yield Strain	$\epsilon_{ym,\phi 12}$	$2.75 \cdot 10^{-3}$
Mean Ultimate Strain	$\epsilon_{um,\phi 12} = \frac{(f_{tm} - f_{ym})}{E_{har}} + \epsilon_{ym,\phi 12}$	$2.66 \cdot 10^{-2}$
Young's Modulus of Elasticity	E_s	200000 N/mm ²
Steel plate/beam parameters		
Young's Modulus of Elasticity	E_{steel}	210000 N/mm ²
Yield Strength	f_y	355 N/mm ²

2.2.3.3 Experimental Results

The failure of RCxcb was caused by concrete crushing in upper centered core and buckling of longitudinal main compression reinforcement, after yielding of tension reinforcement. It was stated by the authors that the shear cracks initiated in the chords* and posts** at the beginning of loading did not widen nor propagate in further stages of loading. The flexural cracks at the central part of the beam controlled the behaviour. The LDC from the experiment, as shown in Figure 2.18, indicates a ductile failure mode. The long flattened plateau before ultimate failure, indicates that the concrete material capacity was fully utilized early in certain critical regions, and that reinforcement contributed to the resistance in the remaining deflection branch. The reported failure load is 284 kN.

* chords = area over/under openings in the beam.

** posts = area between openings in the beam.

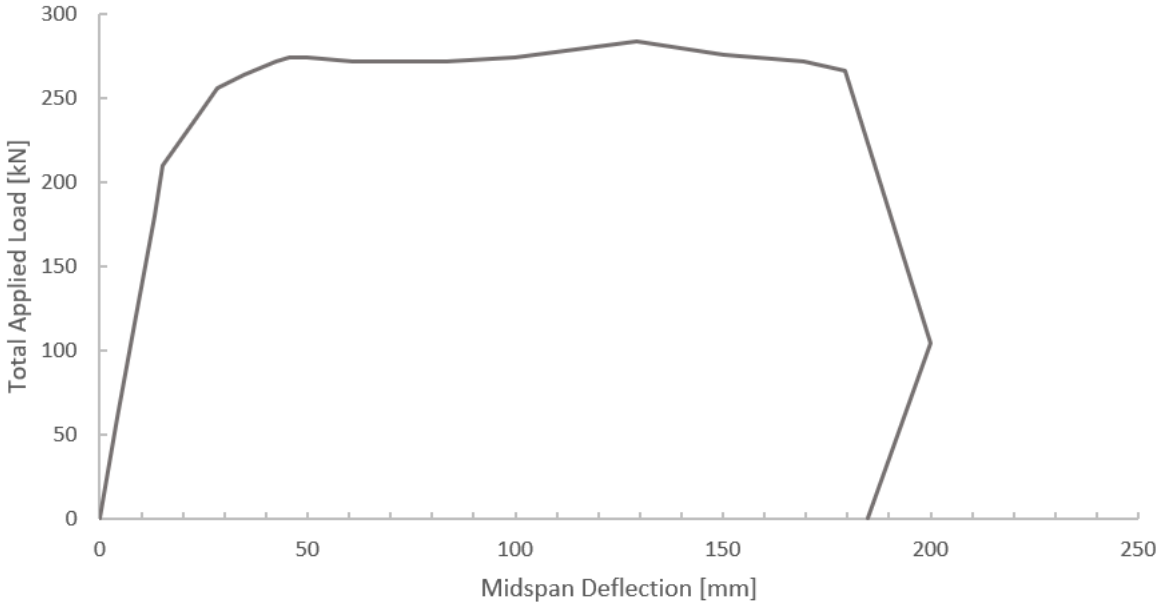


Figure 2.18: RCxcb. Experimental LDC.

2.3 Numerical Solution Strategy

The main objective of the numerical case studies was to come up with a general solution strategy for numerical modelling of deep beams with web openings, to be used for assessment of their failure modes and ultimate load capacities. The main differences between the beams from the case studies were shear span-to-overall depth, number of web openings and degree of static indeterminacy. This section will provide information regarding the constitutive relations, kinematic compatibility and force equilibrium that constituted our selected solution procedure.

2.3.1 FEA Software

The FEAs are conducted by use of the FEA software, *DIANA 10.2*. The software provides complex material models that can be implemented into non-linear finite element models by specification of solution strategy and material parameters. Mean values were used to model the material strengths in DIANA.

2.3.2 Units

In DIANA, the consistent set of units was defined by millimeters (mm) and Newton (N).

2.3.3 Selected Solution Strategy

Recommendations from DG were used to define a solution strategy for numerical modelling of the test specimens listed in Table 3.1. The parameters that constituted the selected solution strategy are listed in Table 2.10.

Table 2.10: Adapted Solution Strategy.

Concrete	
Finite Element	
Element Type	Plane Stress Element CQ16M
Mesh Density	$H/12$
Interpolation Scheme	Quadratic
Integration Scheme	Full (3x3 point Gauss)
Constitutive Modelling	
Material Model	Total strain based fixed crack model
Crack Bandwidth (2D elem.)	\sqrt{A}
Shear Retention Model	Damage based
Tension Softening Model	MC2010
Compressive Behavior Function	Parabolic
Reduction of Compressive Strength due to lateral cracking	Yes
Reduction Model	Vecchio & Collins 1993
Stress Confinement Model	Selby & Vecchio
Poisson's ratio Reduction Model	Damage based

Material Parameters	
Mean Compressive Strength	f_{cm}
Mean Tensile Strength ($\leq C50$)	$f_{ctm}=0.3 f_{ck}^{2/3}$
Mean Tensile Strength ($\geq C50$)	$f_{ctm}=2.12 \ln(1+(f_{cm}/10))$
Fracture Energy	$G_F = 0.073 f_{cm}^{0.18}$
Compressive Fracture Energy	$G_C = 250 G_F$
Linear Material Parameters	
Young's Modulus of Elasticity	E_c
Reinforcement Steel	
Finite Element	
Embedded Reinforcement	Yes
Interpolation Scheme	Quadratic
Integration Scheme	Reduced (2 points)
Constitutive Model	
Material Model	Von Mises Elastic Plastic Model $E_{har}=0.02E_s$
Linear Material Parameters	
Young's Modulus of Elasticity	E_s
Steel plates	
Finite Element	
Interpolation Scheme	Quadratic
Integration Scheme	Full
Constitutive Model	
Material Model	Tresca Plasticity Model
Loading, Iteration and Convergence Criterion	
Loading	Displacement Controlled
Load Steps	0.01
Equilibrium Iteration	RNRM
Maximum Number of Iterations	40
Line Searches per Iteration	10
Force Norm	0.01
Energy Norm	0.001

2.3.3.1 FEA Discretization

Discretization Strategy and Incremental Technique

Time discretization strategy, with the form of incremental-iterative solution scheme, was used to solve the non-linear PDEs in the case studies. Direct DCM was the selected incremental technique. With this method, deformation was prescribed incrementally and the structural response for each step was computed from the equilibrium conditions by use of the selected iterative procedure, which in this case was RNRM.

Finite Elements

In FEAs, the accuracy of the results are affected by the mesh density. As shown in Table 2.10, the adapted solution strategy operated with plane stress quadratic elements, referred to as CQ16M in DIANA. The selected mesh density was the height of the beam, H , divided by 12.

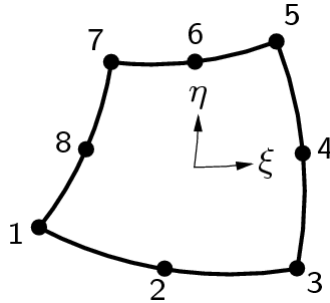


Figure 2.19: Topology of eight-node quadrilateral isoparametric plane stress element CQ16M [DIANA FEA, 2018].

Equivalent Length

A default crack-band width is generated in DIANA. For quadratic quadrilateral 2D elements, the crack-band width is considered \sqrt{A} , where A is the total area of the element.

For the strain values that constituted upper and lower bounds in contour plots used to present results from the post-process investigations, it was assumed that the elements were squares ($h \cdot h$). Consequently $\sqrt{A} = h$, and the crack-band width was considered to be equal to the element height, h .

2.3.3.2 Constitutive Model for Concrete

Total strain based fixed crack model was the selected concrete material model for the numerical solution procedure. In reality, the principal stress direction in concrete exposed to loading, rotates significantly after crack initiation. Consequently a disadvantage with the fixed crack model is that it may result in a FE model that suffers from spurious stress-locking, due to the fact that this rotation of the principal stress direction is neglected [Hendriks et al., 2017]. This may result in a considerable overestimation of the failure load for this specific constitutive model.

Linear-elastic Properties

The Young's modulus was based on the characteristic cylinder compressive strength of the material, and defined according to *Eurocode NS-EN-1992-1-1* (EC2) CEN [2004]. Initial cracking due to creep, shrinkage and such were neglected.

Tensile Behaviour

How the concrete material in numerical models behaves in tension is usually specified by a base function. For a total strain based crack model, DIANA provides predefined TS functions. For the selected solution strategy a TS approach according to Paragraph 5.1.8.2 in fibMC2010 [Code, 2010b] was chosen. This approach is referred to as *MC2010* throughout this thesis.

The stress-strain curve of MC2010, as shown in Figure 2.20, is characterized by specific strain values. For the evaluation of the fracture zone, the peak strain, ϵ_{peak} , indicating that the tensile strength is reached, can be estimated to $1.50 \cdot 10^{-4}$ [Code, 2010b]. At this strain level cracks arise. Complete softening, at the point when the tensile strength is reduced to zero, is characterized by a strain value that depends on the fracture energy, G_F , the tensile strength, f_{ctm} , and the equivalent length, h_{eq} . This strain value is referred to as ϵ_u , and characterize fully open cracks.

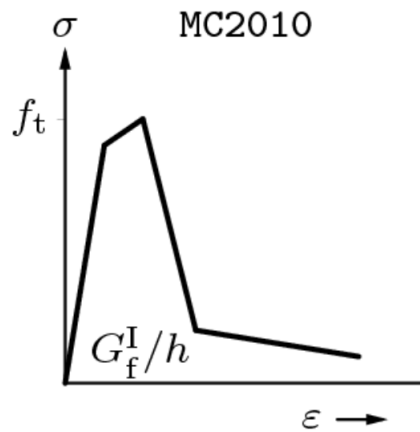


Figure 2.20: MC2010 stress-strain curve [DIANA FEA, 2018].

For evaluation of the tensile behaviour, an output file from DIANA regarding crack status was considered. Following information was provided in this output file [TNO DIANA, 2010b], and is discussed in Sec. 4:

- *No crack:* If no cracks were initiated yet.
- *Open:* For cracks on the fully open loading branch.
- *Closed:* For fully closed cracks. The material was now elastic in compression.
- *Active:* For cracks on the partially open loading branch.
- *Inactive:* For cracks on the fully open unloading branch.

Compressive Behaviour

The compressive behaviour of concrete may be specified by a number of different predefined and user-defined curves in DIANA. According to DG, the compressive behavior should be modelled such that the maximum compressive stress is limited. Parabolic stress strain diagram with softening branch is recommended. Therefore, this was the selected compressive behaviour function for the numerical solution strategy. The compressive softening is a function of the compressive fracture energy, G_C , which is based on the tensile fracture energy value, G_F . The parabolic diagram, as shown in Figure 2.21, can be used to model this. α_c is the principal compressive strain value at the stage when the concrete starts to soften in compression, i.e when it starts to crush, while α_u is the strain value at when it is completely softened. At this stage, the compressive capacity is fully utilized.

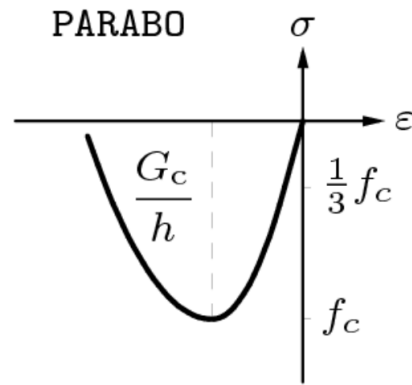


Figure 2.21: Parabolic stress-strain curve [DIANA FEA, 2018].

Shear Retention Model

After crack initiation, the shear stiffness is reduced. DIANA explicitly evaluates the shear retention behaviour for total strain based fixed crack models. According to DG, it is recommended to use a variable shear retention model, in which the shear stiffness is gradually reduced to zero. The selected solution strategy included a *Damage based shear retention model*, in which the shear retention was based on the material damage due to cracking. For this model, the shear capacity is reduced to zero when the concrete gets sufficiently damaged.

Tension-Compression Interaction

DIANA provides several interaction models for reduction of the compressive strength due to lateral cracking. For the selected solution strategy, this reduction was modelled according to *Vecchio & Collins 1993* [?]. The reduction factor for this model develops as shown in Figure 2.22.

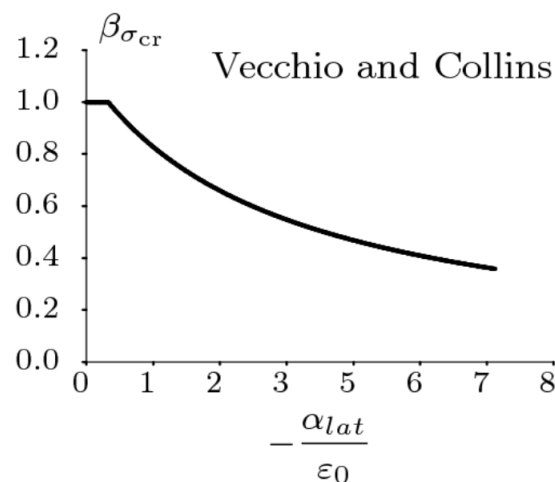


Figure 2.22: Vecchio & Collins reduction factor [DIANA FEA, 2018].

Poisson's Ratio Reduction Model

The Poisson's ratio reduction model for the selected solution strategy was damage based. Consequently, the ratio decreased as the damage caused by cracking increased.

Stress Confinement Model

The increase in compressive strength due to lateral confinement was modified according to the model proposed by *Selby & Vecchio*.

2.3.3.3 Constitutive Model for Reinforcement

Von Mises elasto-plastic material model was used for the reinforcement. This material model only requires tensile data. For the selected solution strategy a nominal hardening modulus, E_{har} , of 2% of the Young's modulus for the reinforcement, E_s , was used.

2.3.3.4 Model for Concrete-Reinforcement Interaction

Tension Stiffening

The crack spacing had to be considered relative to the crack-band width in order to decide if tension stiffening had to be accounted for in the numerical model. With a mesh density of $H/12$, the element height became 33.3 mm or 50 mm for the beams from the benchmark analyses. If the average crack spacing is smaller than the crack bandwidth, $h_{eq} = h$, G_F should be increased [Hendriks et al., 2017]. The first term in Eq. (2.2) includes the concrete cover multiplied by a factor of 3.4. The minimum cover for the benchmark specimens was 25 mm. Hence, the value of this first term become 85 or larger, which is greater than the maximum element size. Consequently, a tension softening model based on the unmodified tensile fracture energy, G_F , was used.

Bond-slip between reinforcement and concrete

The reinforcement was embedded in the concrete, which adds stiffness to the finite element model.

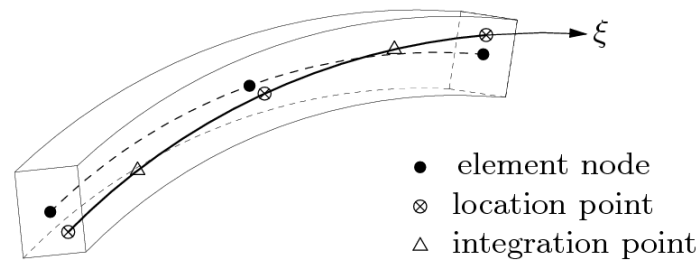


Figure 2.23: Topology of embedded reinforcement bar elements [DIANA FEA, 2018].

2.3.3.5 Specifications regarding the solution strategy for the numerical model in Case Study 3

The selected solution strategy was assigned to 2D numerical approaches of the beams in the case studies. As described, plane stress elements were used in these numerical models. However, due to the complex geometry of RCxcb, DIANA struggled with generation of a realistic stress distribution when the out-of plane stresses were neglected. Therefore, a 3D numerical approach of RCxcb was created in order to model the fully triaxial behaviour. The 3D model utilized the fully depth of the beam in order to create a three-dimensional stress situation. An internal comparison between the structural behaviour of a 2D and a 3D numerical model of RCxcb, as shown in Figures 2.24 and 2.25, will be presented in Sec. 3.3.

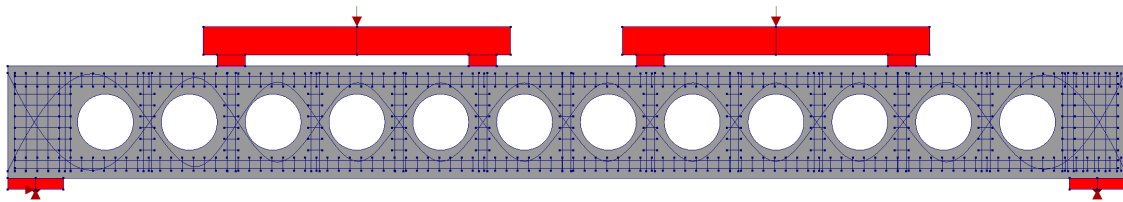


Figure 2.24: RCxcb. Geometry of the 2D finite element model, modelled in DIANA.

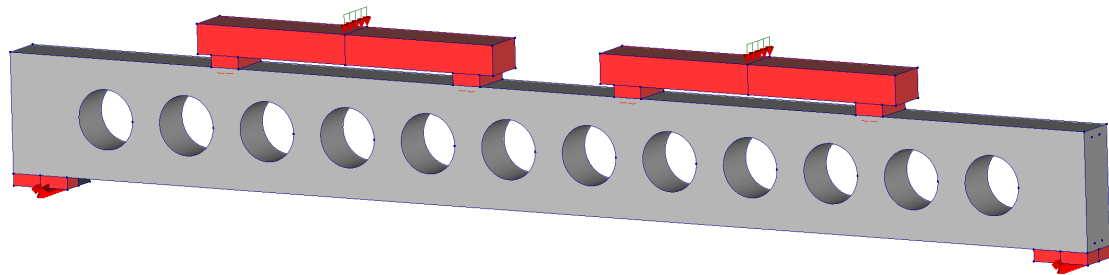


Figure 2.25: RCxcb. Geometry of the 3D finite element model, modelled in DIANA.

Boundary Conditions and Loading Scheme

Both 2D and 3D models were modelled as simply supported, restrained in all axial directions in the left support and free in the longitudinal x-axis in the right support. All connection nodes were set to rotate freely around the global axis. While the 2D model was loaded in single points, and had point supports, the 3D model was loaded by line loads, and had line supports connected to the nodes in the depth direction.

Connection Property Assignment

Due to large deformations and complex geometry of RCxcb, the comprehensive numerical model required specification of a structural interface between the concrete and the steel plates. All numerical analyses of RCxcb were performed with *soft* interface, which is further presented in Sec. 3.3.2.1.

In Case Study 1 and 2, the deflections were relatively small. Consequently, so were the friction/constrained friction forces. The numerical results were not affected by lack of structural interface elements in these case studies, and they were excluded in these models.

When two different materials interact with each other in a numerical program, the differences in transverse contraction between those materials can cause an effect in the state of stress that differs from the intended stress conditions. It is stated in Kotsovos' and Pavlovic's book about finite element analysis for limit state design of concrete structures [Kotsovos and Pavlovic, 1995] that the degree of lateral boundary constraint, in which develops at interface between load plates and concrete, has an effect on concrete strength properties. Kotsovos points out that this constraint develops as a result of the incompatible lateral deformation of specimen and plates, and rise frictional stresses at the specimen boundaries. This will also be a source of uncertainty with respect to the axial testing regime where properties for tested specimens are determined. DIANA has an initial set of normal- and tangential stiffness parameters, K_n and K_t , respectively, that take this effect into account.

The following formulas for the numerical interface are only used as an initial guess, and should be calibrated [DIANA FEA, 2018]:

$$K_n \cong 100 \sim 1000 \cdot \frac{E^{adj}}{l^{el}} \quad (2.5)$$

$$K_t \cong \frac{K_n}{10 \sim 100} \quad (2.6)$$

The visual effect of principal stresses beneath load plates with and without interface is presented in Figure 3.62 for the 2D finite element model. The chosen interface for all 2D and 3D numerical models in Case Study 3 was soft interface, which is presented in Sec. 3.3.2.1.

Finite Elements

The adapted solution strategy operated with plane stress quadratic elements, referred to as CQ16M in DIANA. The standard mesh density was the height of the beam, H , divided by 12. The circular web openings in Case Study 3, and the implemented connection property assignment with structural interface, resulted in additional element types. The 2D RCxcb model in DIANA generated three different finite element types: CQ16M, CT12M and CL12I.

- CQ16M was the specified element type, and was generated in all structural elements.
- CT12M is a six-node triangular isoparametric plane stress element, and was generated locally around all web openings in concrete.
- CL12I is a 3+3 node interface element between two lines in a two-dimensional configuration, and was generated in the interface between concrete and steel.

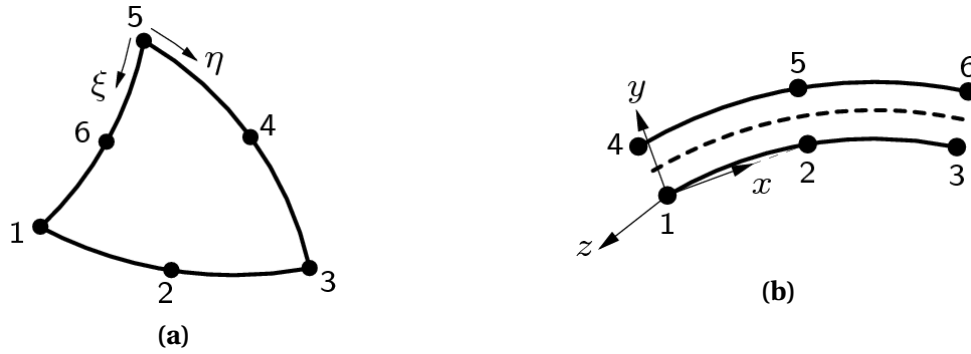


Figure 2.26: Topology of (a) Six-node triangular isoparametric plane stress element CT12M and (b) 3+3 node 2D interface element CL12I [DIANA FEA, 2018].

The 3D model generated five different element types: CHX60, CPY39, CTE30, CTP45 and CQ48I. The crack-band width is considered as $h = \sqrt[3]{V}$, where V is the volume of the element.

- CHX60 is a twenty-node isoparametric solid brick element, and was generated in all structural elements.
- CPY39 is a thirteen-node isoparametric solid pyramid element, and was generated locally in the edges of web opening 1, 4, 11 and 12.
- CTE30 is a ten-node, three-side isoparametric solid tetrahedron element, and was generated locally in the edges of web openings 1, 4, 11 and 12.
- CTP45 is a fifteen-node isoparametric solid wedge element, and was generated locally around all web openings in concrete.
- CQ48I is a 8+8 nodes interface element between two planes in a three-dimensional configuration, and was generated in the interface.

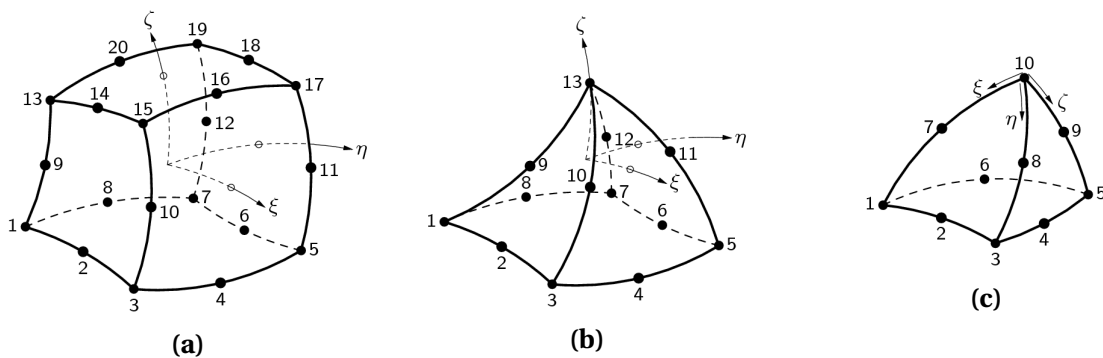


Figure 2.27: Topology of (a) twenty-node isoparametric solid brick element CHX60 and (b) thirteen-node isoparametric solid pyramid element CPY39 and (c) ten-node, three-side isoparametric solid tetrahedron element CTE30 [DIANA FEA, 2018].

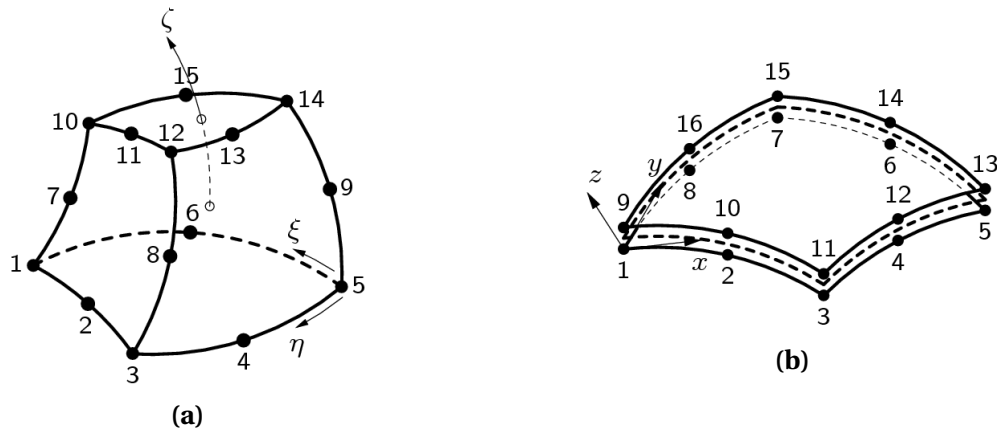


Figure 2.28: Topology of (a) fifteen-node isoparametric solid wedge element CTP45 and (b) 8+8 node 3D interface element CQ48I [DIANA FEA, 2018].

2.3.4 Sensitivity Study of the Solution Strategy

All selections regarding constitutive relations, kinematic compatibility and force equilibrium in NLFEMs influence the accuracy of the results. In order to identify possible sensitivities and limitations within the chosen solution strategy, the FEA discretization and certain constitutive relations were varied. The structural response obtained by the different models were evaluated and compared with each other.

In this numerical parameter study, sensitivity regarding the following topics were investigated:

- Mesh density
- Concrete TS model
- Concrete compressive behaviour function
- Concrete shear retention model

2.3.4.1 FEA Discretization

Mesh Density

As mentioned, DG includes recommendations regarding maximum element size for regular 2D beams, without openings. However, the beams investigated in this thesis had two or more web openings. Consequently, the optimal solution strategy may differ from the DG-recommendations. As shown in Table 2.10, the beam height, H , divided by 12 was chosen as standard mesh density. Additionally, one coarser and one finer mesh density were tested; the span length, L , divided by 50, and the beam height, H , divided by six.

2.3.4.2 Constitutive Model for Concrete

In order to investigate the sensitivity regarding constitutive relations, several material models were varied.

Tensile Behaviour

For the selected solution strategy, MC2010, was chosen as the standard TS model. In the sensitivity study, exponential TS model was tested as well. The stress strain diagrams for these two approaches are shown in Figure 2.29. The softening branches deviate remarkably. Complete softening of the concrete is achieved at a principal tensile strain value of $5 \cdot \frac{G_F}{f_{ctm} \cdot h}$ for MC2010 TS, and $2 \cdot \frac{G_F}{f_{ctm} \cdot h}$ for exponential TS. Consequently, exponential TS results in a less ductile FE model as the strain value for completely softened concrete in tension is 2.5 times lower than for MC2010. In DIANA, the Poisson's ratio is not an input parameter for MC2010 TS. For exponential TS on the other hand, this parameter needs to be specified, and was set to 0.15, as recommended in DG.

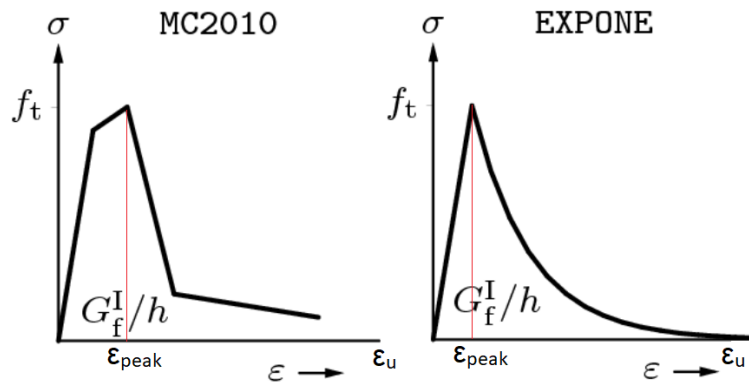


Figure 2.29: Stress-strain curves for MC2010- and exponential TS models [DIANA, 2017].

Compressive Behaviour

A *constant* compressive behaviour function was tested in addition to the parabolic softening-hardening function. The definition of these curves is shown in Figure 2.30. With a constant compressive behaviour the compressive capacity remains constant after the compressive strength is reached, while a parabolic compressive behaviour results in a material that gets completely softened in compression. According to DG, models that only limit the compressive strength, like the constant function does, are not advisable. The analyses was accompanied with post-analysis checks of the compressive strains [Hendriks et al., 2017].

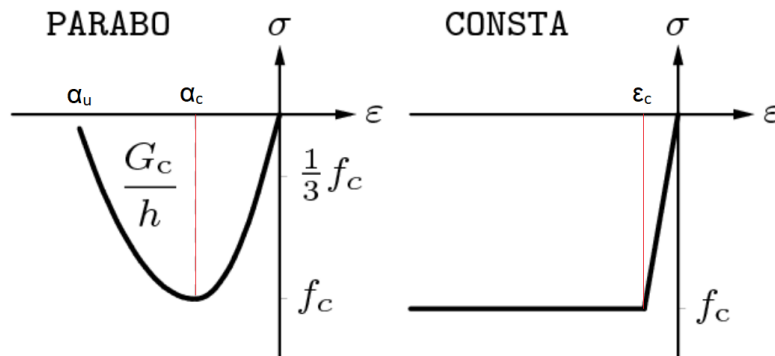


Figure 2.30: Stress-strain curves for parabolic- and constant compressive behaviour approaches [DIANA, 2017].

Shear Retention Model

Regarding shear retention model, *constant* models were tested in addition to the *damage based* model. Constant shear retention includes a reduction factor, β , that is equal to- or lower than one, but greater than zero. It indicates the percentage of remaining shear strength after cracking. According to DG, this approach is not advisable. Therefore the NLFEMs were followed by thorough post-analysis checks of spurious tensile stresses.

2.3.5 Post-Analysis Checks

In order to validate the accuracy of the numerical results, thorough post-analysis checks should be conducted. The post-analysis checks conducted in this thesis are based on concepts presented in DG. LDCs enabled comparison of the response of the numerical models from the NLFEMs and the response of the physical models from the experiments. This curve is a graphical representation of the response that characterizes the overall behaviour of the structure. Post-analysis checks were typically conducted at points on the curve where the applied load dropped drastically. Those points reflect changes in the global behaviour of the beam, and may be caused by:

- Crack generation due to local exceedance of the tensile strength in the concrete. ϵ_{peak} , described in Table 2.11, characterize the strain value at this point for the different numerical models.
- Complete tension softening of the concrete. ϵ_u , described in Table 2.11, characterize the strain value at this point for the different numerical models.
- Crushing of the concrete due to local exceedance of the compressive strength of the material. α_c , described in Table 2.11, characterize the strain value at this point for the different numerical models.
- Complete compression softening of the concrete. α_u , described in Table 2.11, characterize the strain value at this point for the different numerical models.
- Yielding in the reinforcement.
- Shear failure due to exceedance of the shear capacity.

Table 2.11: Description of strain parameters that were used in post-analysis checks.

ϵ_1	Principal tensile strain.
ϵ_2	Principal compressive strain. (ϵ_3 for 3D models).
ϵ_{peak}	Strain value for for when principal tensile stress reaches the tensile strength, f_{ctm} . Cracking starts when ϵ_1 exceeds ϵ_{peak} .
ϵ_u	Strain value for when the concrete is fully softened in tension.
α_c	Strain value for when principal compressive stress reaches the compressive strength, f_{cm} , when a parabolic function is used to describe the concrete compressive behaviour. Crushing starts when ϵ_2 exceeds α_c .
α_u	Strain value for when the concrete is fully softened in compression
ϵ_c	Strain value for when principal compressive stress reaches the compressive strength, f_{cm} , when a constant function is used to describe the concrete compressive behaviour. Crushing starts when ϵ_2 exceeds ϵ_c .
ϵ_{cu2}	Idealized fracture strain value obtained from [CEN, 2004], used as a reference value in the constant compressive behaviour function for Case Study 3.
ϵ_{nn}^{cr}	Represents the normal crack strain in the integration points of the elements, to obtain the crack pattern defined as $Eknn$ in DIANA [DIANA FEA, 2014].

2.4 Modelling Uncertainty

Modelling uncertainty indicates how good the numerical results are compared to the physical behaviour, and is therefore important when it comes to decision-making regarding the NLFEA results. The FE-outcome is uncertain as it represents simplifications of the physical behaviour of the structures [Engen, 2017]. The chosen solution strategy includes choices regarding kinematic compatibility, material models and equilibrium, where the different models will be more suited in some specific situations than others. All those choices contribute to the modelling uncertainty, in addition to uncertainties regarding the experimental setup. A higher complexity of the solution strategy will reduce the modelling uncertainty, as the variables will influence the model implicitly if it is not defined explicitly in the selected solution strategy.

The uncertainty could be divided into two main groups; physical uncertainties and modelling uncertainties. The physical uncertainties will not influence the choice of mechanical models regarding the solution strategy and influence the outcome from the FE-modelling, but will have an impact on the experimental results. Hence, it will influence the modelling uncertainty.

Physical Uncertainties

The physical uncertainties include uncertainty regarding the material properties, geometry, load application and boundary conditions. Different types of physical uncertainties that could influence the experimental capacity, are listed below. The list is collected from the Ph.D of Morten Engen [Engen, 2017].

Material uncertainties:

- The compressive and tensile strengths of concrete.
- The Young's modulus of concrete.
- The yield strength of the reinforcement steel.
- The uncertain relation between stresses and strains of the materials.

Geometrical uncertainties:

- Cross-sectional thickness
- The cover to the reinforcement
- The cross-sectional area of the reinforcement bars.
- Imperfections of the geometry.

Uncertainties due to load and boundary conditions:

- Distribution and intensity of distributed load.
- Locations and intensities of point loads.
- Ground motion intensity.
- The mass densities of the materials.

- The stiffness and strength of surrounding structures and foundations.
- Geometrical idealization of supports.

The material properties depend on the measuring technique, as well as the numbers of tests taken. An increased amount of tests will reduce the uncertainty of the material strength. Concrete properties are considered as the largest sources of error, as it is a heterogeneous material. Thus a part of the uncertainties will always remain even though the number of tests is increased or the machinery is calibrated.

Imperfections due to geometry, load and boundary conditions could occur and contribute to the physical uncertainty which would influence the experimental capacity. Uncertainty regarding load is dependent on the nature of the load, dead load or live load. Dead loads are comparable with the material parameters, while live load are based on random processes.

It is used a cylinder test to decide the concrete compressive strength in all case studies. In Case Study 3 two cylinder tests were performed, while in Case Study 1 and 2 it was not specified. Mean values are used, implementing uncertainty regarding the material properties. No information is given regarding the fabrication of the reinforcement, but it will contribute to the physical uncertainty which is implicitly included in the modelling uncertainty.

Modelling Uncertainties

To implement the experiment in a software for FE-modelling, material models have to be selected. The material models are defined as mathematical models that tries to describe the mechanical behaviour of the material, and are only approximations of the real physical behaviour of the structure. The mathematical models contain different degree of complexity. A multiple amount of combinations are available, causing complexity of finding the ultimate combination. Additionally, the models used are uncertain as they often are empirically based. The numerical outcome will also be uncertain, but not random. NLFEA will provide the same solution in every analysis. The lack of knowledge or experience regarding the choice of models add uncertainty to the FE-modelling.

If not all material properties are given from the experiment, sub-models should be used to calculate the remaining variables. The sub-models express variables as functions of given variables and are often empirically based. This contributes to modelling uncertainty as the material parameters are included in the FE-modelling. The sub-models should be implemented consistently for the different benchmark analyses, to obtain an accurate modelling uncertainty.

In most experiments, compressive strength was the only defined parameter for concrete. Sub-models for the other material parameters had to be adopted. EC2 is used to calculate the Young's modulus of concrete, as a function of the concrete compressive strength. The other material parameters are based on equations from DG. Sub-models for a various number of reinforcement properties had to be adopted as well.

The FE-modelling is based on the geometries, loads and boundary conditions given in the literature for the different case studies. Not all covers and spacing between reinforcement stirrups were given in the benchmark reports. Consequently some parameter values were based on assumptions in all case studies, which contributed to the modelling uncertainty.

The iterative solution of the NLFEA contributes to modelling uncertainty as it could never be assumed as 100% accurate. Lack of knowledge and experience regarding the software could also contribute to modelling uncertainty. Refinement of the FE-model could impact the results. RCxcb is tested with both 2D and 3D modelling.

Quantification of the Modelling Uncertainty

Quantification of the modelling uncertainty is important in validation of each benchmark analyses and the selected solution strategy.

For use of NLFEA, the modelling uncertainty, θ , is usually given as

$$\theta = \frac{R_{exp}}{R_{NLFEA}} \quad (2.7)$$

R_{exp} is the measured outcome from the experiment and R_{NLFEA} is the predicted outcome of the same experiment using NLFEA. For $\theta > 1.0$ the model prediction is underestimating the experimental capacity. R_{exp} is the outcome of a random process, hence the estimated modelling uncertainty depends on the physical uncertainties that influence the measured R_{exp} . When θ is calculated individually for each analysis, it describes the *between-model* uncertainty.

When all results from the benchmark analyses are included in one model uncertainty, the equations become

$$\theta_i = \left(\frac{R_{exp}}{R_{NLFEA}} \right)_i \quad (2.8)$$

$$\theta_m = \frac{1}{n} \sum_{i=1}^n \theta_i \quad (2.9)$$

where θ_i describes the uncertainty obtained in each analysis and θ_m describes the uncertainty obtained for n analyses with the selected solution strategy. θ_m describes the *within-model* uncertainty.

θ_m could be represented by a normally distributed random variable, where the probability distribution is given through a mean value, μ_θ , and a coefficient of variation, V_θ . Those values are estimated by comparing NLFEA outcomes with the experimental capacities. μ_θ is the bias and indicates the average fit to experimental results.

The following equations can be used if no information is given about the variable [Engen et al., 2017a]. The expected values for the mean and variance are given in Eq. (2.10) and (2.11), where the sample mean is given by θ_m and the sample variance is given by $s^2 = \frac{1}{n-1} \sum_{i=1}^n (\theta_i - \theta_m)^2$. The coefficient of variation is given by $V_\theta = \frac{\sigma}{\mu}$.

$$E[\mu|\theta] = \theta_m \quad (2.10)$$

$$E[\sigma^2|\theta] = \frac{n-1}{n-3} s^2 \quad (2.11)$$

3. Numerical Results

In this section results from several NLFEMs will be presented. Sec. 3.0.1 presents the main results from the NLFEMs obtained by the selected solution strategy. Sec. 3.1.1, 3.2.1 and 3.3.1 present post-process investigations of the numerical results of 6IT1, T1-0 and RCxcb, respectively.

3.0.1 NLFEM Results obtained by the selected Solution Strategy

The selected solution strategy was used to perform NLFEMs on all test specimens listed in Table 3.1. Table 3.2 shows a summary of the ultimate load capacities for the numerical models of these eight specimens. This table includes the achieved modelling uncertainties, which are based on their respective experimental failure loads. Table 3.3 lists the obtained experimental and numerical failure modes for these specimens. 6IT1, T1-0 and RCxcb are further studied in Case Study 1, 2 and 3, while the rest of the listed specimens were analyzed by the selected solution strategy, but the results will not be further elaborated in this paper.

Failure Modes

All numerical models listed in Table 3.1 experienced shear failure in the NLFEMs. The achieved numerical modes of failure, listed in Table 3.3 are defined below [Placas and Regan]:

- *Shear Compression Failure*: This mechanism occurs for shear cracking combined with crushing of the concrete, due to inadequate compressive capacity. It is typical for deep beams with shear reinforcement.
- *Diagonal Tension Failure*: This type of failure appears in beams where the amount of shear reinforcement is insufficient. Failure occurs immediately on the appearance of shear cracks. The diagonal tension failure is of a rapid and violent type of failure.
- *Web Crushing*: Shear cracks combined with crushing of the web in beams with thin webs.

Table 3.1: Summary of all test specimens.

6IT1	From Case Study 1 [Yang and Ashour]. Detailed post-process investigation presented in Sec. 3.1. Sensitivity study summed up in Table 3.4 and elaborated in Sec. 3.1.2
T1-0	From Case Study 2 [Yang et al., 2007]. Detailed post-process investigation presented in Sec. 3.2. Sensitivity study summed up in Table 3.5 and elaborated in Sec. 3.2.2.
RCxcb (2D & 3D)	From Case Study 3 [Aykac et al., 2014]. Detailed post-process investigation presented in Sec. 3.3. Sensitivity study summed up in Table 3.6 and elaborated in Sec. 3.3.2.
B-I-L	Beam from experimental study by A. F. Ashour and G. Rishi, 2000 [Ashour and Rishi, 2000]. Studied in detail by Line Nilsson in conjunction with a former project work on NTNU.
B-I-S	Beam from experimental study by A. F. Ashour and G. Rishi, 2000 [Ashour and Rishi, 2000]. Studied in detail by Kristine Nøttveit in conjunction with a former project work on NTNU.
B-E-L	Beam from experimental study by A. F. Ashour and G. Rishi, 2000 [Ashour and Rishi, 2000]. Studied in detail by Erlend Nygårdsvoll in conjunction with a former project work on NTNU.
T3-3	Beam from experimental study by K.-H Yang, H.-S Chung and A.F. Ashour [Yang et al., 2007]. Similar geometry as T1-0 from Case Study 2, but with larger web openings and inclined reinforcement.
T1-1	Beam from experimental study by K.-H Yang, H.-S Chung and A.F. Ashour [Yang et al., 2007]. Similar geometry as T1-0 from Case Study 2, but with inclined reinforcement.

Table 3.2: Failure loads obtained by the selected solution strategy in NLFEAs of the tested specimens.

Test Specimen	Numerical Failure Load	Modelling Uncertainty $(\frac{R_{exp}}{R_{NLFEA}})$
6IT1 (Case Study 1)	2565 kN	0.85
T1-0 (Case Study 2)	1670 kN	0.87
RCxcb (2D) (Case Study 3)	250 kN	1.14
RCxcb (3D) (Case Study 3)	242 kN	1.18
B-I-L*	348 kN	1.10
B-I-S *	601 kN	1.14
B-E-L*	557 kN	1.33
T3-3**	1889 kN	1.06
T1-1**	1751 kN	0.99

* Previously studied benchmark specimens. Details and source specified in Table 3.1.

** Benchmark test from the same experimental study as T1-0, referred to in Table 3.1.

Table 3.3: Experimental and numerical failure modes for the analyzed specimens.

Test Specimen	Numerical Failure Mode	Experimental Failure Mode
6IT1 Case Study 1	Diagonal Tension Failure combined with Shear Compression Failure	Unspecified Shear Failure
T1-0 Case Study 2	Shear Compression Failure	Unspecified Shear Failure
RCxcb (2D) Case Study 3	Diagonal Tension Failure combined with Web Crushing Failure	Beam-Type Flexural Failure
RCxcb (3D) Case Study 3	Diagonal Tension Failure combined with Web Crushing Failure	Beam-Type Flexural Failure
B-I-L*	Diagonal Tension Failure	Unspecified Shear Failure
B-I-S *	Diagonal Tension Failure	Unspecified Shear Failure
B-E-L*	Diagonal Tension Failure	
T3-3**	Shear Compression Failure	Unspecified Shear Failure
T1-1**	Shear Compression Failure	Unspecified Shear Failure

* Previously studied benchmark specimens. Details and source specified in Table 3.1.

** Benchmark test from the same experimental study as T1-0, referred to in Table 3.1.

3.0.1.1 Sensitivity Study from Case Study 1

Table 3.4: Numerical failure mode, failure load and modelling uncertainty obtained by different numerical solution strategies for 6IT1.

Parameter	Failure Mode	Failure Load	Modelling Uncertainty ($\frac{R_{exp}}{R_{NLFEA}}$)
Mesh Density			
$H/12 =$ element size 50 mm	Diagonal Tension Failure combined with Shear Compression Failure	2565 kN	0.85
$L/50 =$ element size 14.4 mm	No Failure*	No peak	—
$H/6 =$ element size 100 mm	Diagonal Tension Failure combined with Shear Compression Failure	2401 kN	0.92
Tension Softening Model			
MC2010 TS	Diagonal Tension Failure combined with Shear Compression Failure	2565 kN	0.85
Exponential TS	Diagonal Tension Failure	1590 kN	1.39
Compressive Behaviour Function			
Parabolic Compressive Behaviour Function	Diagonal Tension Failure combined with Shear Compression Failure	2565 kN	0.85
Constant Compressive Behaviour Function	No Failure**	2987 kN	0.74
Shear Retention Model			
Damage Based Behaviour Function	Diagonal Tension Failure combined with Shear Compression Failure	2565 kN	0.85
Constant ($\beta=0.1$)	No Failure***	No Peak	—
Constant ($\beta=0.01$)	No Failure***	No Peak	—

No Failure due to:

* Analysis ended before a failure mechanism was formed.

** Compressive capacity never fully utilized.

*** Shear capacity never fully utilized.

3.0.1.2 Sensitivity Study from Case Study 2

Table 3.5: Numerical failure mode, failure load and modelling uncertainty obtained by different numerical solution strategies for T1-0.

Parameter	Failure Mode	Failure Load	Modelling Uncertainty $(\frac{R_{exp}}{R_{NLFEA}})$
Mesh Density			
$H/12 =$ element size 50 mm	Shear Compression Failure	1670 kN	0.87
$L/50 =$ element size 18 mm	Shear Compression Failure	1528 kN	0.95
$H/6 =$ element size 100 mm	Shear Compression Failure	1708 kN	0.85
Tension Softening Model			
MC2010 TS	Shear Compression Failure	1670 kN	0.87
Exponential TS	Shear Compression Failure	1161 kN	1.25
Compressive Behaviour Function			
Parabolic Compressive Behaviour Function	Shear Compression Failure	1670 kN	0.87
Constant Compressive Behaviour Function	No Failure**	No peak	—
Shear Retention Model			
Damage Based	Shear Compression Failure	1670 kN	0.87
Constant ($\beta=0.1$)	No Failure***	No Peak	—
Constant ($\beta=0.01$)	No Failure***	No Peak	—

No Failure due to:

* Analysis ended before a failure mechanism was formed.

** Compressive capacity never fully utilized.

*** Shear capacity never fully utilized.

3.0.1.3 Sensitivity Study from Case Study 3

Table 3.6: Numerical failure mode, failure load and modelling uncertainty obtained by different numerical solution strategies for the 2D and 3D model of RCxcb.

Parameter	Failure Mode	Failure Load 2D / 3D	Modelling Uncertainty $(\frac{R_{exp}}{R_{NLFEA}})$ 2D / 3D
Mesh Density			
$H/12 =$ element size 33.33 mm	Diagonal Tension Failure combined with Web Crushing Failure	250.4 kN / 242 kN	1.14 / 1.18
$L/50 =$ element size 76 mm	Same as H/12	260 kN / 285.9 kN	1.09 / 0.99
$H/6 =$ element size 66.67 mm	Same as H/12	285.5 kN / 257.3 kN	0.99 / 1.10
$B/6 =$ element size 25 mm	Same as H/12	240.1 kN / 209.3 kN	1.18 / 1.35
Tension Softening Model			
MC2010 TS	Diagonal Tension Failure combined with Web Crushing Failure	250.4 kN / 242 kN	1.14 / 1.18
Exponential TS	Same as MC2010 TS	212.3 kN / 220.7 kN	1.33 / 1.28
Compressive Behaviour Function			
Parabolic Compressive Behaviour Function	Diagonal Tension Failure combined with Web Crushing Failure	250.4 kN / 242 kN	1.14 / 1.18
Constant Compressive Behaviour Function	Same as Parabolic Compressive Behaviour Function	255.3 kN / 243.7 kN	1.11 / 1.16
Shear Retention Model			
Damage Based	Diagonal Tension Failure combined with Web Crushing Failure	250.4 kN / 242 kN	1.14 / 1.18
Constant ($\beta=0.1$)	No Failure	No Peak	—
Constant ($\beta=0.01$)	As Damage Based Shear Retention Model	370.4 kN / 369 kN	0.77 / 0.77

3.1 Case study 1

The following case study is a numerical approach to the experimental test of 6IT1, collected from paper *Structural behaviour of reinforced-concrete continuous deep beams with web openings* [Yang and Ashour]. The FE model of 6IT1 will be referred to as 6IT1 throughout this section.

3.1.1 NLFEA Results obtained by Selected Solution Strategy

The NLFEA of 6IT1 conducted by the selected solution strategy specified in Table 2.10, was accompanied by thorough post-analysis checks. The aim was to detect the numerical failure mode and failure load. This was mainly conducted by investigation of the development and distribution of principal strains and stresses, crack initiation and crack distribution, and also detection of non-converged LSs.

Figure 3.1 compares the LDC obtained in the numerical analysis and the experiment. Dots represent essential observations that constituted specific responses in the FE model, while red crosses indicates non-converged LSs. As shown in the curve, non-converged LSs followed after peaks and flat plateaus. After the final peak, convergence was not achieved in any steps. The highest load taken up by the numerical model was 2565 kN in LS 74, at a deflection of 1.36 mm. After this LS a failure mechanism was formed.

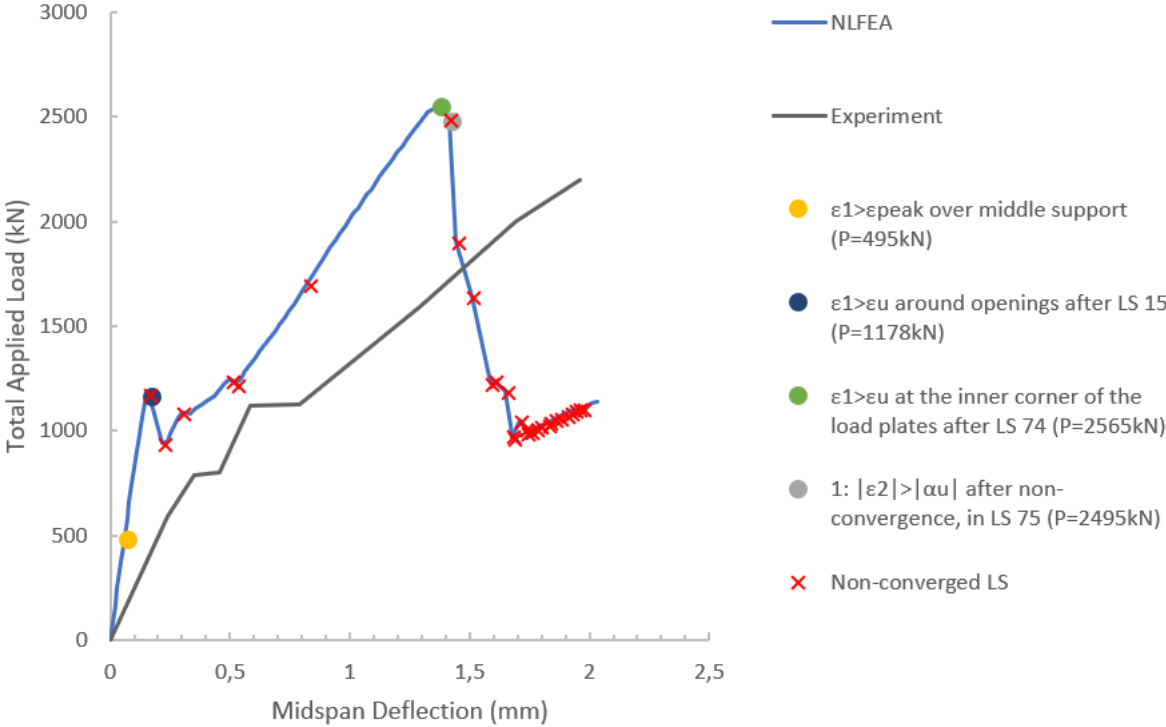


Figure 3.1: 6IT1. LDC from the numerical solution strategy and the experiment. The numerical LDC is marked with essential observations that affected the global behaviour.

The amount of transferred load to the different supports is shown in Figure 3.2. Due to symmetrical geometry and loading, it was assumed that the load transfer from the load plated to the two outer supports would be more or less identical. Therefore only the left

outer support reaction is plotted, in addition to the middle support. After application of 1178 kN in LS 15, which constituted the first peak in the LDC, the load transfer to the middle support was reduced. However, this load path was not entirely damaged, hence it still had load carrying capacity in the following 60 LSs. After LS 74 on the other hand, this path was fully damaged, and the applied load could no longer be transferred to the middle support. Hence, the global capacity was reached as the beam was split into separate blocks.

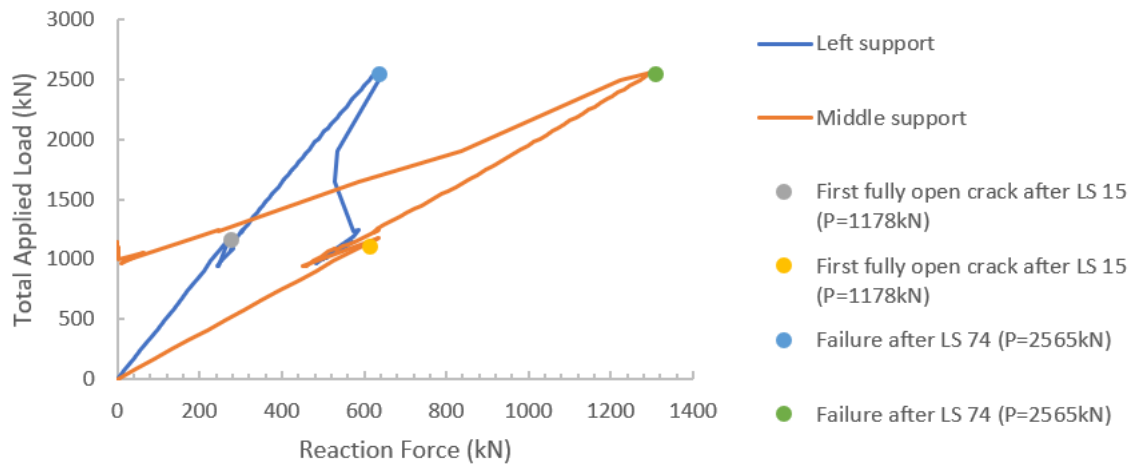


Figure 3.2: 6IT1. Support reactions against total applied load from the numerical solution strategy. The curves are marked with observations of fully open cracks and failure.

3.1.1.1 Concrete Cracking

The main crack observations are marked with dots in the LDC in Figure 3.1 and summarized in Table 3.7.

Table 3.7: T1-0. Crack observations from the numerical solution strategy.

LS	Observation	Location	Total applied load
6	First microcracks	Over middle support	495 kN
9	First microcracks	Web opening corners	742 kN
15	First fully open crack	Web opening corners	1178 kN
74	Fully open cracks	Entire beam height through openings	2565 kN

Figure 3.3 shows principal tensile strain plots for 6IT1 obtained by the selected solution strategy. Blue colour indicates strain values less than ϵ_{peak} , listed in Table 3.8, while red colour indicates strain values exceeding ϵ_u , listed in the same table.

Table 3.8: 6IT1. Specific tensile strain values for MC2010 TS curve.

Strain	Formula	Strain value	Tensile stress
ϵ_{peak}		$1.50 \cdot 10^{-4}$	$\sigma = f_{ctm}$
ϵ_u	$5 \cdot \frac{G_F}{f_{ctm} \cdot h}$	$3.59 \cdot 10^{-3}$	$\sigma = 0$

Microcracks formed at local weak points in the material when the tensile strain, ϵ_1 , exceeded ϵ_{peak} . Complete softening in tension was achieved when ϵ_1 exceeded ϵ_u . At this strain value cracks were considered to be fully open.

The initially most stressed point of the concrete in 6IT1 was located over the middle support. Here microcracks, with a principal crack width of $3.18 \cdot 10^{-4}$ mm, were initiated in LS 6 when 495 kN was applied. This situation is shown in Figure 3.3a, by hiding data outside of the limits in the contour plot. Consequently, the parts of the material where ϵ_1 exceeded ϵ_{peak} achieved colour.

With increased deflection, the deformations started to localize into a zone of microcracks at the most critical section of the specimen, which for 6IT1 was in the corners of the openings. The first fully open crack, with a principal crack width of 0.12 mm, was generated in these critical areas in LS 15, at a loading of 1178 kN, as shown in Figure 3.3b. After this stage the load capacity dropped drastically. Consequently, this response represents the first load drop in the LDC.

Further enforced deflection resulted in propagation of these diagonal cracks. Based on the principal tensile strain plot shown in Figure 3.3c, it looks like the shear cracks were fully open almost all the way through the beam in LS 74. However, the strain values in the nodes underneath the inner corners of the load plates, were still smaller than ϵ_u . By zooming in on this area, as illustrated in Figure 3.3e, it was observed that the crack was not fully open all the way through the top elements of the specimen yet. In LS 76 on the other hand, all nodes in the critical shear zone of 6IT1 had achieved strains larger than ϵ_u . The maximum crack width increased from 3.03 mm in LS 74 to 8.33 mm in LS 76. Figure 3.3d shows that the crack split the beam into separate blocks in LS 76.

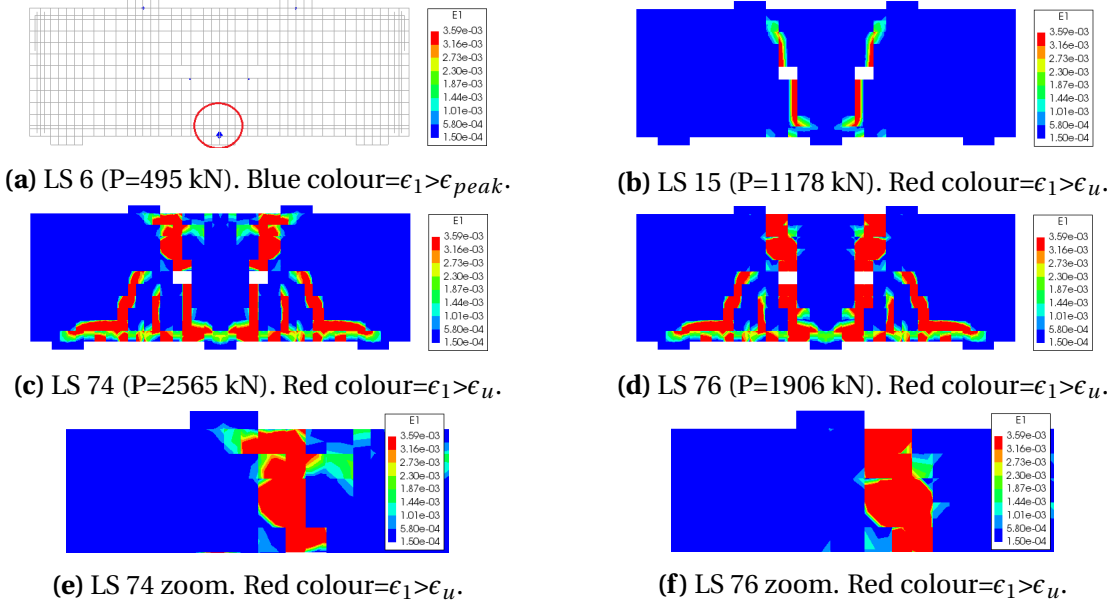


Figure 3.3: 6IT1. Principal tensile strain plots from essential load steps in NLFEA of the solution strategy.

3.1.1.2 Concrete Crushing

Figure 3.4 shows contour plots of the principal compressive strains in 6IT1 at the peak load level in the LDC, and immediately after, when a failure mechanism was formed. Red colour indicates concrete with $|\epsilon_2| > |\alpha_u|$, listed in Table 3.9. When $|\alpha_u|$ was exceeded, the concrete was completely softened in compression, hence the material had no remaining compressive capacity. As shown in the contour plot in Figure 3.4b, this strain value was obtained in LS 76. The concrete was softened in the upper part of the shear crack. Another observation that anticipated the large compressive stresses generated in this area was the slope of the cracks, which was remarkably reduced. As shown in Figure 3.5, the cracks in the top elements were almost horizontal.

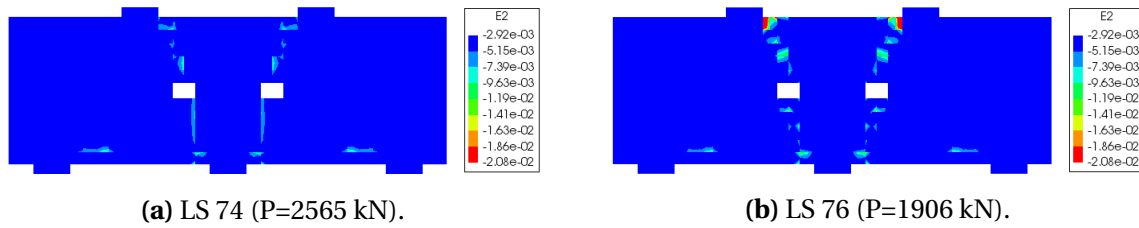


Figure 3.4: 6IT1. Principal compressive strain plots from the numerical solution strategy. Red colour= $|\epsilon_2| > |\alpha_u|$. Blue colour= $|\epsilon_2| < |\alpha_c|$.

Table 3.9: 6IT1. Specific compressive strain values for the parabolic stress-strain curve.

Strain	Formula	Strain value	Compressive stress
α_c	$-5 \cdot \frac{1}{3} \cdot \frac{f_c}{E_c}$	$-2.92 \cdot 10^{-3}$	$\sigma = f_c$
α_u	$\alpha_c - \frac{3}{2} \frac{G_c}{h f_c}$	$-2.08 \cdot 10^{-2}$	$\sigma = 0$

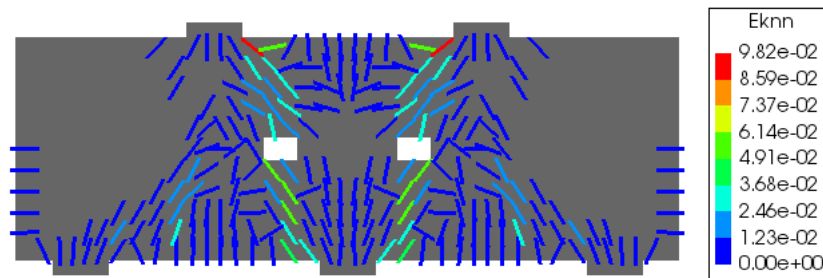


Figure 3.5: 6IT1. Crack strains in LS 76 (P=1906 kN) of the NLFEA by the selected solution strategy. Auto-scaled colour plot.

3.1.1.3 Tension-Compression Interaction

Three nodes in the concrete elements that had achieved complete tensile softening in LS 74 are highlighted in Figure 3.6. These nodes corresponded to node number 400, 397 and 390 in the FE model. They also comprised a part of the compressive strut that transferred the load from the load plates and down to the middle support. Hence this area achieved large compressive stresses as the applied load increased. Figure 3.7 visualizes the development

of principal compressive stresses, S_2 , in these nodes. The horizontal axis indicates at what load-factor the respective stress values were obtained. Load factor 0.7 indicates the point when 70% of the total prescribed deflection was applied. Consequently the decimals of the load-factor corresponds more or less to the LS number. As shown in this figure, the maximum compressive stress was therefore reached at some point between LS 70 and LS 80. The maximum absolute value was however lower than the absolute value of the specified compressive strength for 6IT1 which was 68.2 N/mm^2 .

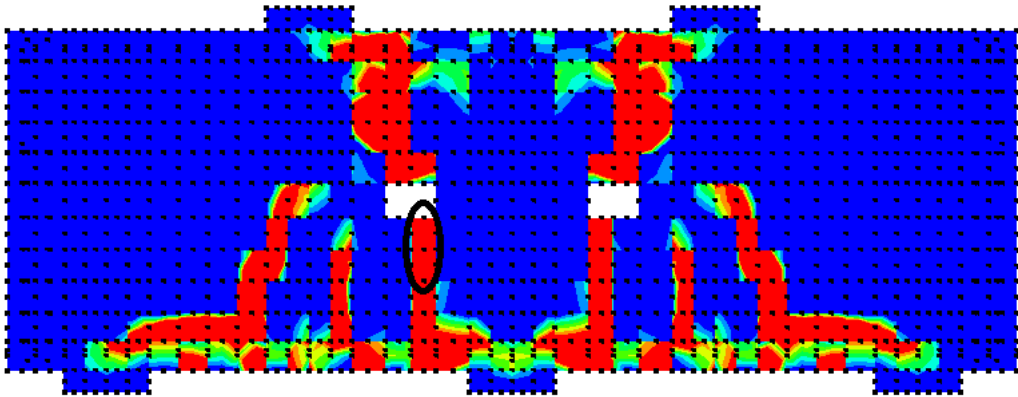


Figure 3.6: 6IT1. Principal tensile strain plot. Red colour= $\epsilon_1 > \epsilon_u$. Development of compressive stresses in highlighted nodes; 400, 397 and 390, are shown in Figure 3.7.

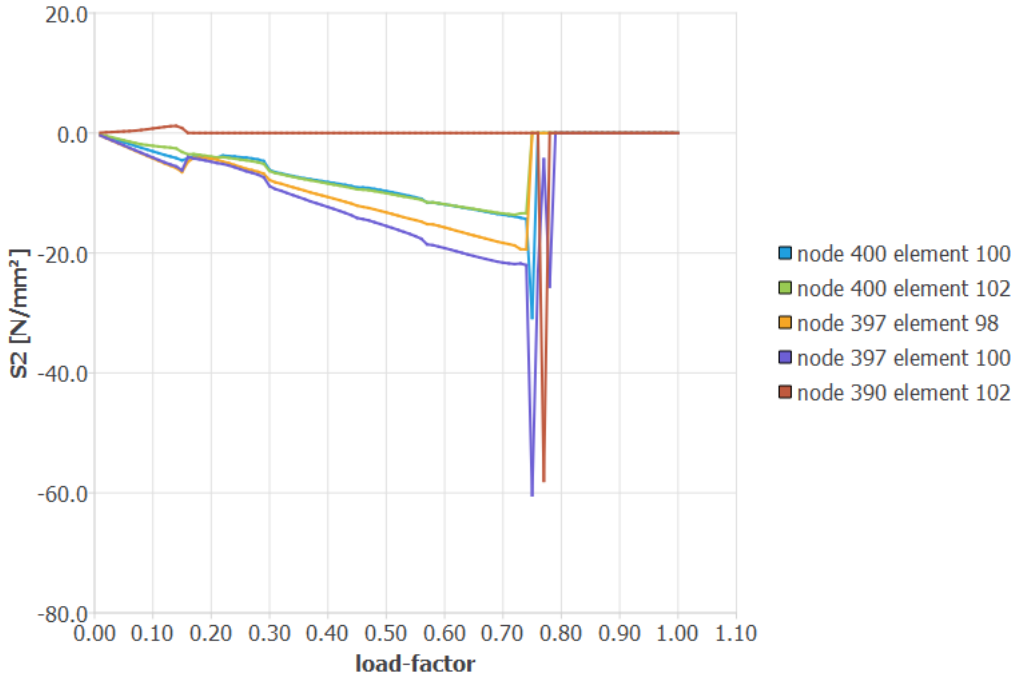


Figure 3.7: 6IT1. Table-output from DIANA, showing the development of principal compressive stresses, S_2 , in node 400, 397 and 390, highlighted in Figure 3.6.

3.1.1.4 Yielding of Reinforcement

With the selected solution strategy, the largest reinforcement stress achieved in the analysis before a failure mechanism was formed, was 450 N/mm². This was achieved in the longitudinal rebars, over the middle support. As the yielding limit for all reinforcement in 6IT1 was 560 N/mm², the selected solution strategy did not result in any yielding reinforcement bars.

3.1.1.5 Global Failure

The failure mode of 6IT1 was characterized by shear failure. After LS 74, the splitting shear crack was fully open almost all the way through the beam. However, the top of the shear spans were highly compressed. Hence, the beam was not split into separate blocks as long as these areas had remaining compressive capacity.

In LS 76 the concrete in these areas got completely softened in compression, and the material capacity was fully utilized in the entire critical section. Consequently, the global capacity dropped drastically. As shown in Table 3.10, the failure mode was therefore characterized by a combination of diagonal tension and shear compression failure. The failure load for 6IT1 obtained by the selected solution strategy was 2565 kN, which resulted in a modelling uncertainty of 0.85.

Table 3.10: 6IT1. Failure mode and failure load from NLFEA of solution strategy.

Failure Mode	Failure Load	Modelling Uncertainty ($\frac{R_{exp}}{R_{NLFEA}}$)
Diagonal Tension Failure combined with Shear Compression Failure	2565 kN	0.85

3.1.2 Sensitivity Study of the Numerical Modelling in Case Study 1

In this section results from a sensitivity study of the selected solution strategy for NLFEAs of 6IT1 from the experimental benchmark test [Yang and Ashour] are presented. The analysis conducted by the selected solution strategy, which is elaborated above, will be referred to as *Analysis 1* throughout this section. Analyses with complementary solution strategies, meaning other selections regarding FE discretization and sub-models for the concrete constitutive model, will be referred to as *Analysis 2* and *Analysis 3* within each separate sensitivity study. Only one aspect of the solution strategy was changed at a time, while the rest of the selections were in compliance with the solution strategy described in Table 2.10.

3.1.2.1 Sensitivity regarding FE Discretization

In this sensitivity study, three mesh densities were tested; $L/50$, $H/6$, and $H/12$ which was the mesh density for the selected solution strategy. For the geometry of 6IT1, these densities resulted in element heights of 14.4 mm, 100 mm and 50 mm respectively.

Throughout this sensitivity study, the following designations will be used as references for the three NLFEAs of 6IT1 with different FE discretizations:

Analysis 1: Mesh density $H/12$ (50 mm).

Analysis 2: Mesh density $L/50$ (14.4 mm).

Analysis 3: Mesh density $H/6$ (100 mm).

Figure 3.8 compares LDCs from the NLFEAs obtained in Analysis 1, 2 and 3, in addition to the experimental LDC. Appearance of non-converged LSs in Analysis 1, symbolized by red crosses in the LDC, are explained in the previous section. Green crosses represents non-converged steps in Analysis 2 and black in Analysis 3. As shown in the curves, Analysis 2 and 3 had less non-converged LSs than Analysis 1. Analysis 2 achieved convergence in almost all LSs, except in a few after the first peak. In Analysis 3, non-converged steps followed post all large peaks in the LDC.

In Analysis 3, with element discretization $H/6$, the first microcracks, with a principal crack width of $7.64 \cdot 10^{-4}$ mm, were generated in LS 9 ($P=773$ kN) as indicated in the LDC and mentioned in Table 3.11. With finer mesh densities, in Analysis 1 and 2, smaller microcracks were detected, and hence at lower loads. As mentioned the microcracks detected in Analysis 1 had a width of $3.18 \cdot 10^{-4}$ mm, while in Analysis 2 the detected microcracks had a width of $1.23 \cdot 10^{-5}$ mm. These cracks were initiated in LS 6 in Analysis 1, and LS 4 in Analysis 2. The corresponding load levels were 495 kN and 304 kN.

In all three analyses the first fully open cracks were generated in two diagonal corners of the web openings. These cracks constituted the first load drop in the LDCs, and one or two non-converged steps followed after this. The applied loads at this point in the respective models are listed in Table 3.11. Principal tensile strain plots illustrating this situation is visualized in Figure 3.9. Blue colour indicates principal tensile strain values less than the respective ϵ_{peak} -value, listed in Table 3.12. Red colour represents principal tensile strain values exceeding the respective ϵ_u -value, listed in the same table. The detected widths of these cracks were 0.12 mm, 0.03 mm and 0.11 mm for Analysis 1, 2 and 3, respectively. With increased loading, the tensile strains increased, and these cracks became wider. Regardless of the mesh density,

these cracks propagated towards the load plates and the middle support plate. However, the width of the cracks decreased with a refined mesh density.

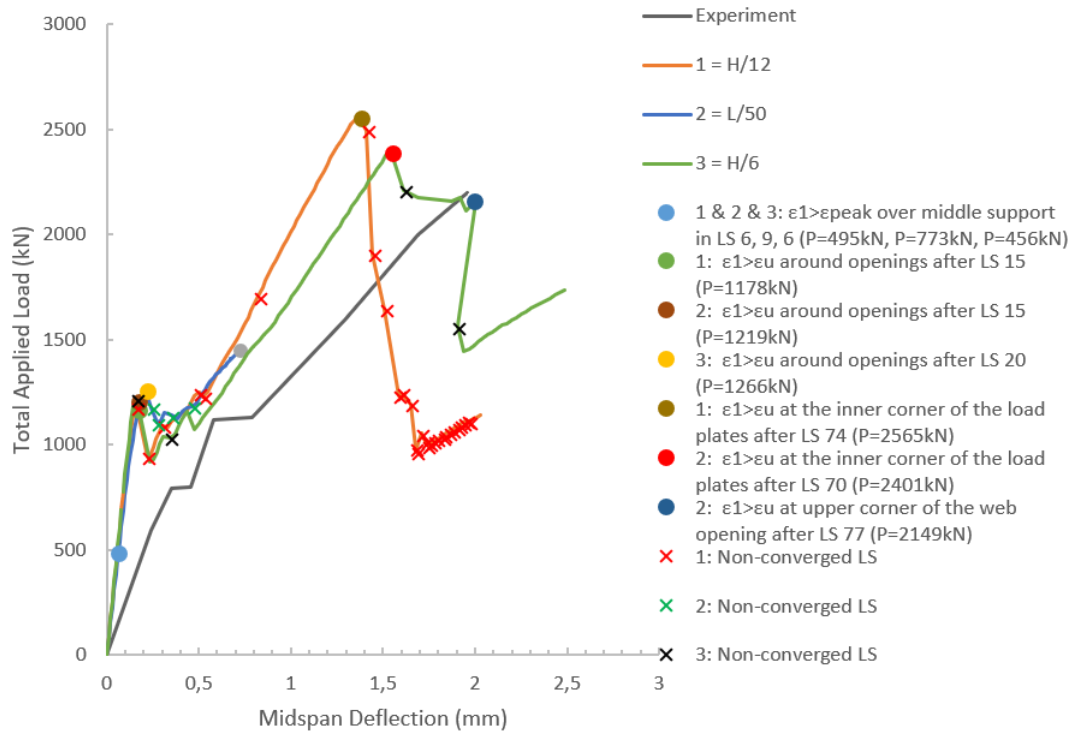


Figure 3.8: 6IT1. LDCs from the NLFEAs with different mesh densities, and the experimental LDC. The numerical LDCs are marked with essential observations that affected the global behaviour.

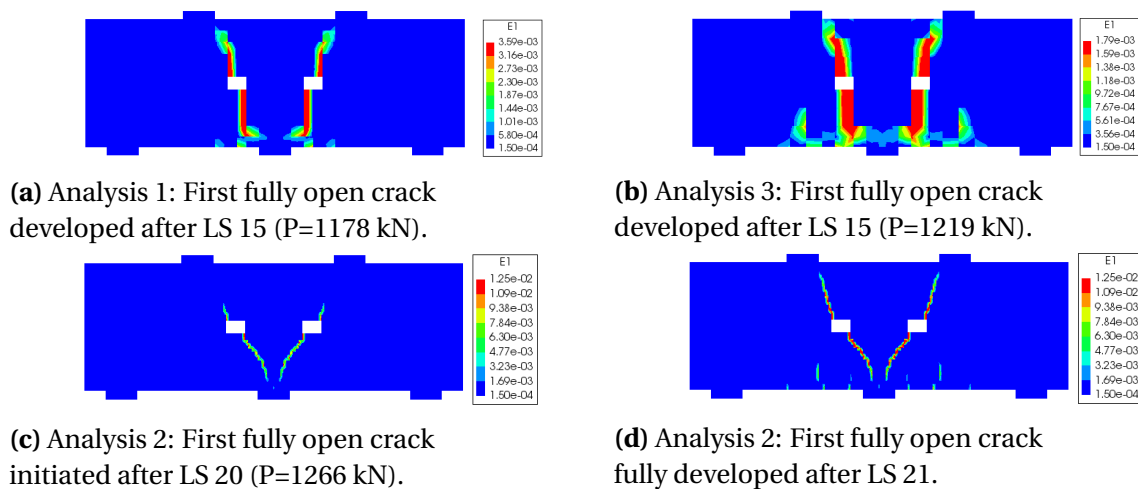


Figure 3.9: 6IT1. Principal tensile strain plots for different mesh densities. Red colour= $\epsilon_1 > \epsilon_u$. Blue colour= $\epsilon_1 < \epsilon_{peak}$.

Table 3.11: 6IT1. Crack observations from the NLFEMs with different mesh densities.

Observation, Location	Applied Load Analysis 1	Applied Load Analysis 2	Applied Load Analysis 3
First microcrack, over middle support	495 kN	304 kN	773 kN
First fully open crack, in critical shear zone	1178 kN	1219 kN	1266 kN

Table 3.12: 6IT1. Specific tensile strain values in the MC2010 TS curve for different mesh densities.

Strain	Formula	Strain value Analysis 1	Strain value Analysis 2	Strain value Analysis 3	Tensile stress
ϵ_{peak}		$1.50 \cdot 10^{-4}$	$1.50 \cdot 10^{-4}$	$1.50 \cdot 10^{-4}$	$\sigma = f_{ctm}$
ϵ_u	$5 \cdot \frac{G_F}{f_{ctm} \cdot h}$	$3.59 \cdot 10^{-3}$	$1.25 \cdot 10^{-2}$	$1.79 \cdot 10^{-3}$	$\sigma = 0$

In addition to different principal crack widths, a varying number of total initiated cracks were obtained in the three analyses. Table 3.13 summarizes output information regarding crack development in DIANA. It shows the total number of cracks, how many that were open and closed, number of active and inactive cracks and how many that raised, re-opened and closed in this specific LS. A larger number of cracks were generated in the FE model with refined mesh density. Figure 3.10 shows principal tensile strain plots from the ultimate steps before failure. From these plots it is observed that a refined mesh resulted in a greater quantity of cracks, while the width and length of the cracks seemed to be larger for coarser FE discretizations. For Analysis 3, both LS 70 and 77 are illustrated in the figure. The failure load, $P = 2401$ kN, was applied in LS 70, but the beam did not fail before after LS 77.

Neither of the analyses related to this sensitivity study resulted in yielding of reinforcement in the numerical model of 6IT1. The largest reinforcement stress, 522 N/mm², was obtained with the coarsest mesh, in LS 77. This stress value was obtained in the longitudinal reinforcement over the middle support. The location of the maximum rebar stress was identical in all three analyses, regardless of FE discretization.

Table 3.13: 6IT1. Summary of crack logging for different mesh densities at failure load, given by DIANA.

Analysis - LS number	Crack	Open	Closed	Active	Inactive	Arises	Re-	Closes
Analysis 1 - LS 74	1966	1934	32	1154	812	4	0	0
Analysis 2 - LS 100	18385	17753	632	4476	13909	0	0	0
Analysis 3 - LS 70	678	674	16	524	154	2	0	0
Analysis 3 - LS 77	794	778	16	464	330	6	0	0

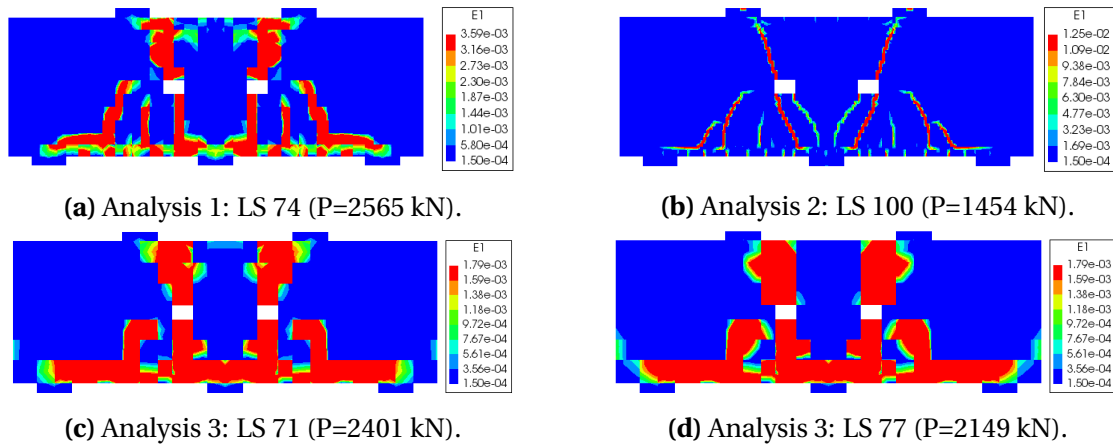


Figure 3.10: 6IT1. Principal tensile strain plots with different mesh densities, at maximum applied load levels. Red colour= $\epsilon_1 > \epsilon_u$.

Figure 3.11 shows contour plots of the principal compressive strains, at critical steps with respect to compressive capacity. Red colour indicates compressive strains exceeding the respective value of $|\alpha_u|$, listed in Table 3.14. As described Sec. 3.1.1, this occurred in LS 76 for Analysis 1. With the coarsest mesh, in Analysis 3, the $|\epsilon_2|$ exceeded the respective $|\alpha_u|$ -value in LS 71, after an applied load of 2401 kN. The area of completely compressed softened concrete increased when further deflection was enforced. After LS 77 a remarkable area underneath the inner corners of the load plates was completely softened in compression. In Analysis 2, with the finest mesh density, the concrete did not get completely softened in compression.

Table 3.14: 6IT1. Specific compressive strain values for parabolic stress-strain curve with different mesh densities.

Strain	Formula	Strain value Analysis 1	Strain value Analysis 2	Strain value Analysis 3	Compressive stress
α_c	$-5 \cdot \frac{1}{3} \cdot \frac{f_c}{E_c}$	$-2.92 \cdot 10^{-3}$	$-2.92 \cdot 10^{-3}$	$-2.92 \cdot 10^{-3}$	$\sigma = f_c$
α_u	$\alpha_c - \frac{3}{2} \cdot \frac{G_C}{h \cdot f_c}$	$-2.08 \cdot 10^{-2}$	$-6.27 \cdot 10^{-2}$	$-1.15 \cdot 10^{-2}$	$\sigma \approx 0$

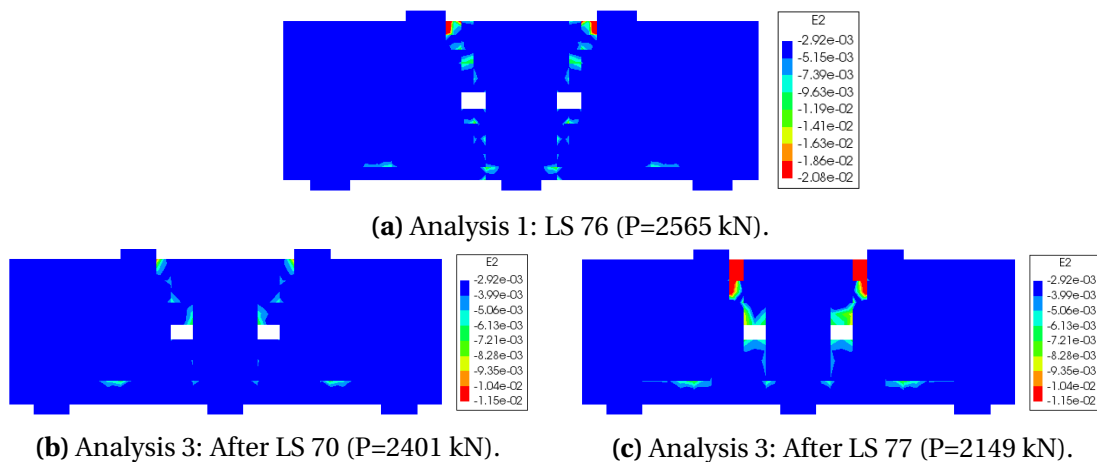


Figure 3.11: 6IT1. Principal compressive strain plots with different mesh densities. Red colour= $|\epsilon_2| > |\alpha_u|$.

Another prominent difference in the NLFEMs of 6IT1 with different mesh densities was the size of the LSs. According to the chosen solution strategy, the load step size should be 1% of the maximum prescribed displacement, which was 2 mm. Therefore the incremental displacement should be 0.02 mm, regardless of the mesh density. Due to default regulations within the software, the average load step size became 0.0203 mm, 0.0075 mm and 0.0249 mm in Analysis 1, 2 and 3, respectively.

As only 100 LSs were provided, a small LS-size resulted in limited total deflection and total applied load. Consequently, 6IT1 in Analysis 2 did not achieve failure during the specified 100 incremental displacement steps. The total deflection only reached 0.75 mm in the final LS, which corresponded to an applied load of 1454 kN. Besides the non-converged LSs after the first peak in the LDC, this analysis achieved convergence from LS 29 and out. The crack pattern maintained consistent, without any large changes. Figure 3.12 illustrates this consistency by showing that the principal tensile strain plots from LSs 29 and 100 were almost identical. The bounding colours are the same as in Figure 3.11.

Analysis 3 required the largest number of iterations within each load step before convergence was achieved. The ultimate failure was reached after LS 77 at a deflection of 2 mm. At this point the shear crack was fully open all the way through the beam. The final 0.4 mm deflection constituted a descending branch in the LDC in Figure 3.8. The largest applied load taken up by the numerical model before this branch was 2401 kN in LS 70, which corresponded to 1.54 mm deflection.

The achieved failure modes and the respective failure loads from this sensitivity study regarding mesh density are summed up in Table 3.15.

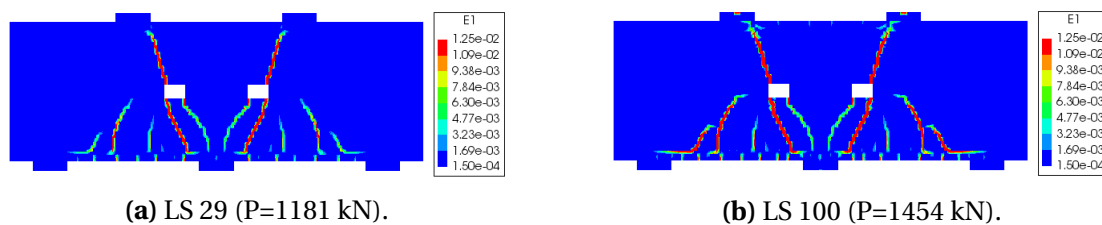


Figure 3.12: 6IT1. Principal tensile strain plot from Analysis 2. Red colour= $\epsilon_1 > \epsilon_u$.

Table 3.15: 6IT1. Failure mode and failure load from the NLFEMs with different mesh densities.

Analysis	Failure Mode	Failure Load	Modelling Uncertainty($\frac{R_{exp}}{R_{NLFEM}}$)
1	Diagonal Tension Failure combined with Shear Compression Failure	2565 kN	0.85
2	No Failure*	No peak	—
3	Diagonal Tension Failure combined with Shear Compression Failure	2401 kN	0.92

* The analysis ended before a failure mechanism was formed.

3.1.2.2 Sensitivity to choice of Constitutive Model for Concrete

Tension Softening Model For the selected solution strategy, MC2010 was chosen as the standard TS approach. According to DG, exponential TS is preferred. In order to investigate the sensitivity related to this sub-model, these two approaches were tested. Figure 3.13 shows the obtained LDCs from NLFEEAs of 6IT1 with the two respective TS sub-models. Based on these curves it is clear that the FE model was sensitive to choice of TS approach. Red crosses, which symbolize non-converged LSs from Analysis 1, are explained in the previous section. Green crosses symbolize non-converged steps for Analysis 2. As shown, Analysis 2 only had four such steps after the ultimate peak was reached.

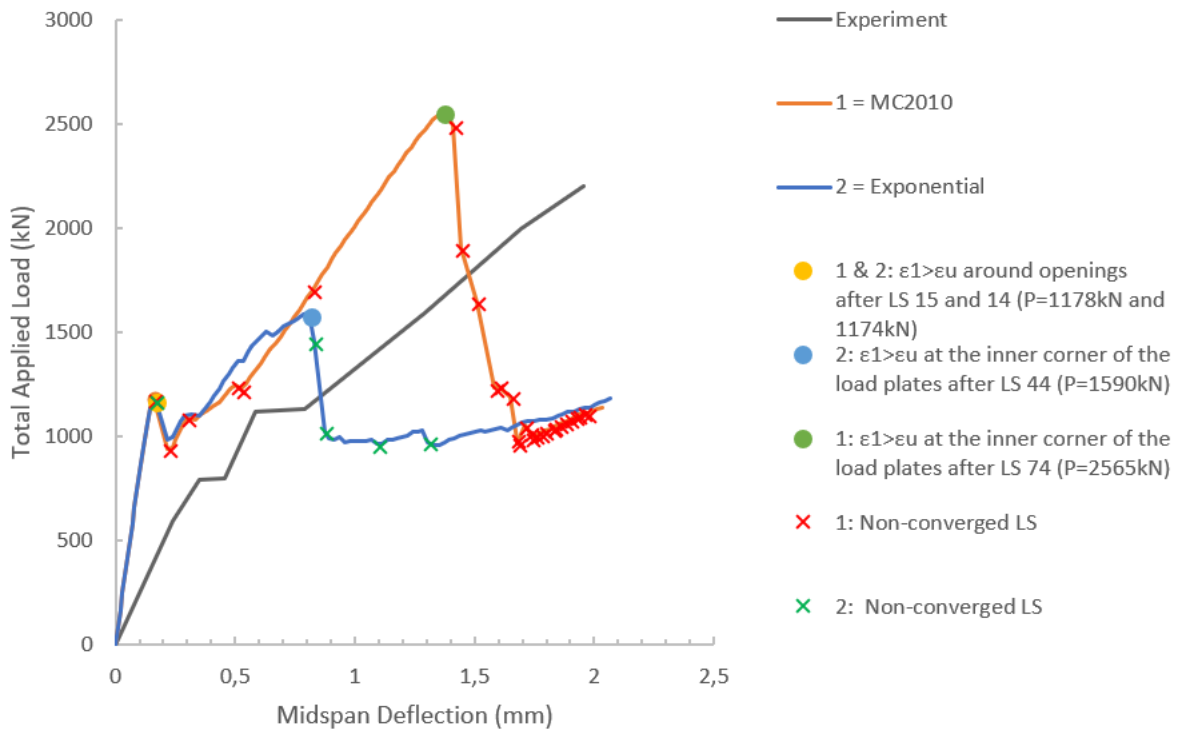


Figure 3.13: 6IT1. LDCs from the NLFEEAs with different TS models, and the experimental LDC. The numerical LDCs are marked with essential observations that affected the global behaviour.

Throughout this sensitivity study, the following designations will be used as references for the two NLFEEAs of 6IT1 with different TS approaches:

Analysis 1: MC2010 TS Model.

Analysis 2: Exponential TS Model.

Both analyses resulted in similar crack propagation before the stress level exceeded the strength, f_{ctm} , and the principal tensile strain reached the value of ϵ_{peak} listed in Table 3.8 and 3.16. When further deflection was enforced and the corresponding applied load increased, specific cracks appeared at different loads.

Figure 3.14 shows principal tensile strain plots of 6IT1 obtained in Analysis 2. Blue colour indicates strains below ϵ_{peak} , listed in Table 3.16, while red colour indicates strains larger than ϵ_u from the same table.

Table 3.16: 6IT1. Specific tensile strain values for exponential TS.

Strain	Formula	Strain value Analysis 2	Tensile stress
ϵ_{peak}	$\frac{f_{ctm}}{E_{cm}}$	$1.10 \cdot 10^{-4}$	$\sigma = f_{ctm}$
ϵ_u	$2 \cdot \frac{G_F}{f_{ctm} \cdot h}$	$1.44 \cdot 10^{-3}$	$\sigma \approx 0$

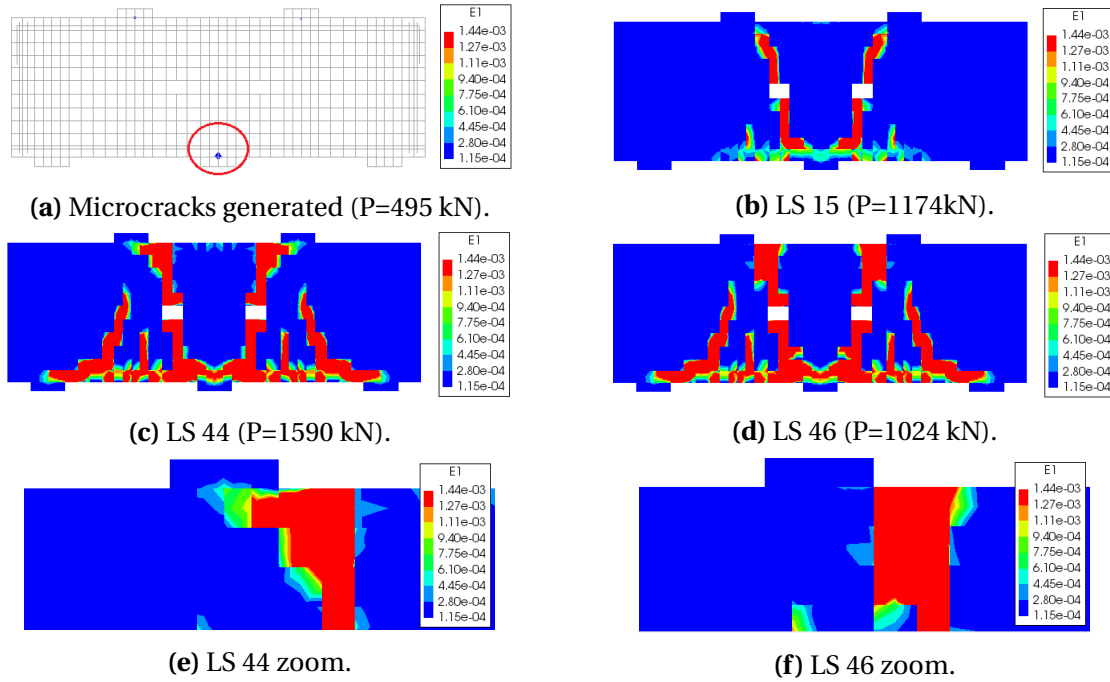


Figure 3.14: 6IT1. Principal tensile strain plots from essential LSs in Analysis 2. Red colour= $\epsilon_1 > \epsilon_u$. Blue colour= $\epsilon_1 < \epsilon_{peak}$.

Table 3.17 lists specific crack observations and their respective formation loads. 6IT1 generated microcracks at 495 kN applied load in both analyses. Figures 3.3a and 3.14a show that they were also generated in the same area of the specimen. The obtained crack widths were quite similar; $3.18 \cdot 10^{-4}$ mm and $4.08 \cdot 10^{-4}$ mm, for MC2010 and exponential TS, respectively.

Tensile strains larger than ϵ_u were achieved at similar load levels and at the same location in both analyses. Figures 3.3b and 3.14b show principal tensile strain plots from this stage for 6IT1 with MC2010 and exponential TS respectively. The bounding contour colours indicate strain values less than ϵ_{peak} and greater ϵ_u for 6IT1 with the respective tensile approaches. After this stage the load dropped drastically in both LDCs.

As further deflection was enforced, the strains continued to redistribute due to cracking. For both TS approaches, large cracks also started to form in the tension zones in the lower part of the midspans. Based on the principal tensile strain plot from Analysis 2, shown in Figure 3.14c, it looked like the shear cracks were fully open almost all the way through the beam in LS 44. In the following LS converge was not achieved. By looking into the strain values in the individual nodes underneath the inner corners of the load plates, ϵ_1 were still smaller than ϵ_u . In the zoomed figure from this LS, shown in Figure 3.14e, this is visualized. However, in

LS 46 on the other hand, the nodes in this area achieved strains larger than ϵ_u . Figure 3.14d visualizes that a sharp strain-division occurred between concrete that was fully softened in tension, and concrete that was less strained. This situation constituted the peak in the LDC in Analysis 2, at a loading of 1590 kN.

Table 3.17: 6IT1. Crack observations from the NLFEAs with different TS models.

Observation	Location	Total applied load, Analysis 1	Total applied load, Analysis 2
First microcrack	Over middle support	495 kN	495 kN
First fully open crack	Critical shear zone	1178 kN	1174 kN

Regarding compressive behaviour, 6IT1 responded differently in Analysis 1 and 2. All parameters that constitutes the formula for the specific compressive strain values in the parabolic compressive behaviour function were identical for the concrete in both analyses. Consequently the specific compressive strain values, α_c and α_u , were identical, and are listed in Table 3.9. In Analysis 1, with the MC2010 TS model, 6IT1 failed when the concrete was completely softened in compression in the top part of the beam. In Analysis 2, when an exponential TS model was used, 6IT1 failed before the compressive capacity was fully utilized in the concrete. Hence no parts of the concrete in 6IT1 experienced complete softening in compression when the TS model was characterized by an exponential function.

Consequently, as stated in Table 3.18, different failure modes were achieved for the different TS sub-models. With the selected solution strategy, including the MC2010 TS approach, the failure mode was characterized by diagonal tensile failure combined with shear compression failure, as described earlier. 6IT1 in Analysis 2 of this sensitivity study, which included an exponential TS approach, resulted in only diagonal tension failure. Compared to Analysis 1, Analysis 2 resulted in a remarkably lower global capacity. Therefore the stresses in the rebars were even lower than in Analysis 1, which knowingly did not achieve yielding. Consequently no rebars yielded in Analysis 2 either.

Table 3.18: 6IT1. Failure mode and failure load from the NLFEAs with different TS models.

Analysis	Failure Mode	Failure Load	Modelling Uncertainty($\frac{R_{exp}}{R_{NLFEA}}$)
1	Diagonal Tension Failure combined with Shear Compression Failure	2565 kN	0.85
2	Diagonal Tension Failure	1590 kN	1.61

Compressive Behaviour Function

In order to investigate the sensitivity related to choice of compressive behaviour function, constant function was tested in addition to parabolic function, which was the chosen sub-model for the common solution strategy.

Throughout this sensitivity study, the following designations will be used as references for the two NLFEAs of 6IT1 with different compressive behaviour functions:

Analysis 1: Parabolic compressive behaviour function.

Analysis 2: Constant compressive behaviour function.

Figure 3.15 shows the LDCs obtained in NLFEAs of 6IT1 with the two different compressive behaviour functions. Based on these curves it is obvious that the FE model responded differently based on selection of sub-model regarding the compressive behaviour. Red crosses symbolize non-converged LSs from Analysis 1 and green crosses symbolize non-converged steps for Analysis 2. As shown, after the non-converged step at a deflection of 0.79 mm, Analysis 2 converged in all remaining LSs.

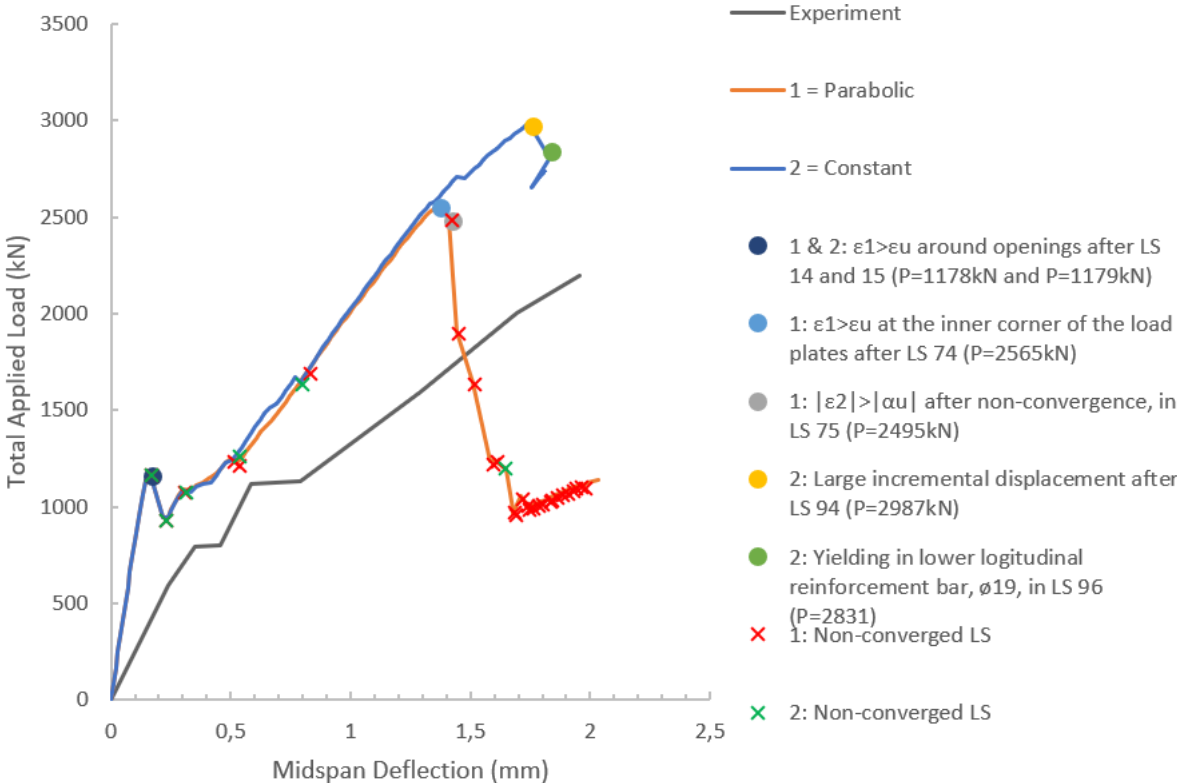


Figure 3.15: 6IT1. LDCs from the NLFEAs with different compressive behaviour functions, and the experimental LDC. The numerical LDCs are marked with essential observations that affected the global behaviour.

A post-process investigation was conducted in order to investigate the response of 6IT1 in the NLFEAs with different specifications regarding the compressive behaviour.

6IT1 achieved similar response in Analysis 1 and 2 all the way until a failure mechanism formed in Analysis 1. As Analysis 1 is identical to the selected solution strategy, the formation of this failure mode is elaborated in the previous sections. In Analysis 2, with the constant compressive behaviour function, 6IT1 still had load carrying capacity after this stage.

Figure 3.16 illustrates the situation in LS 94 and 95, which constituted a peak in the LDC for Analysis 2. In Figures 3.16a and 3.16b red colour indicated that the absolute value of the compressive strains exceeded the absolute value of ϵ_c , given in Table 3.40. Consequently, red areas in these plots indicated crushed concrete. By use of a constant approach for

the compressive behaviour, the compressive strength does not get reduced by increased compressive strains. Consequently, no ultimate compressive strain limits were provided for this compressive behaviour specification. Therefore, the concrete in 6IT1 never got completely softened when the compressive behaviour was characterized by a simplified constant function. However, Figure 3.16d indicates that large incremental displacements followed after LS 94. The fully softened areas in tension increased remarkably in the lower chord from LS 94 to LS 95, as shown in Figures 3.16e and 3.16f. However, as the compressed areas in the top part of the shear spans was not fully softened in compression, the beam did not fail globally at this stage. Consequently, with the compressive behaviour characterized by a constant function, 6IT1 was not split into separated blocks even though the crack had propagated through the beam. As mentioned in Table 3.20, this means that no failure mechanism was formed by this specific solution strategy. The failure mechanism generated in Analysis 1 is described earlier, as parabolic compressive behaviour constituted the selected solution strategy described in Table 2.10. However, it is also repeated in Table 3.20.

Table 3.19: 6IT1. Specific compressive strain values in the stress-strain curve of constant compressive behaviour function of concrete.

Strain	Formula	Strain value	Compressive stress
ϵ_c	$-\frac{f_c}{E_c}$	$-1.74 \cdot 10^{-3}$	$\sigma = f_c$

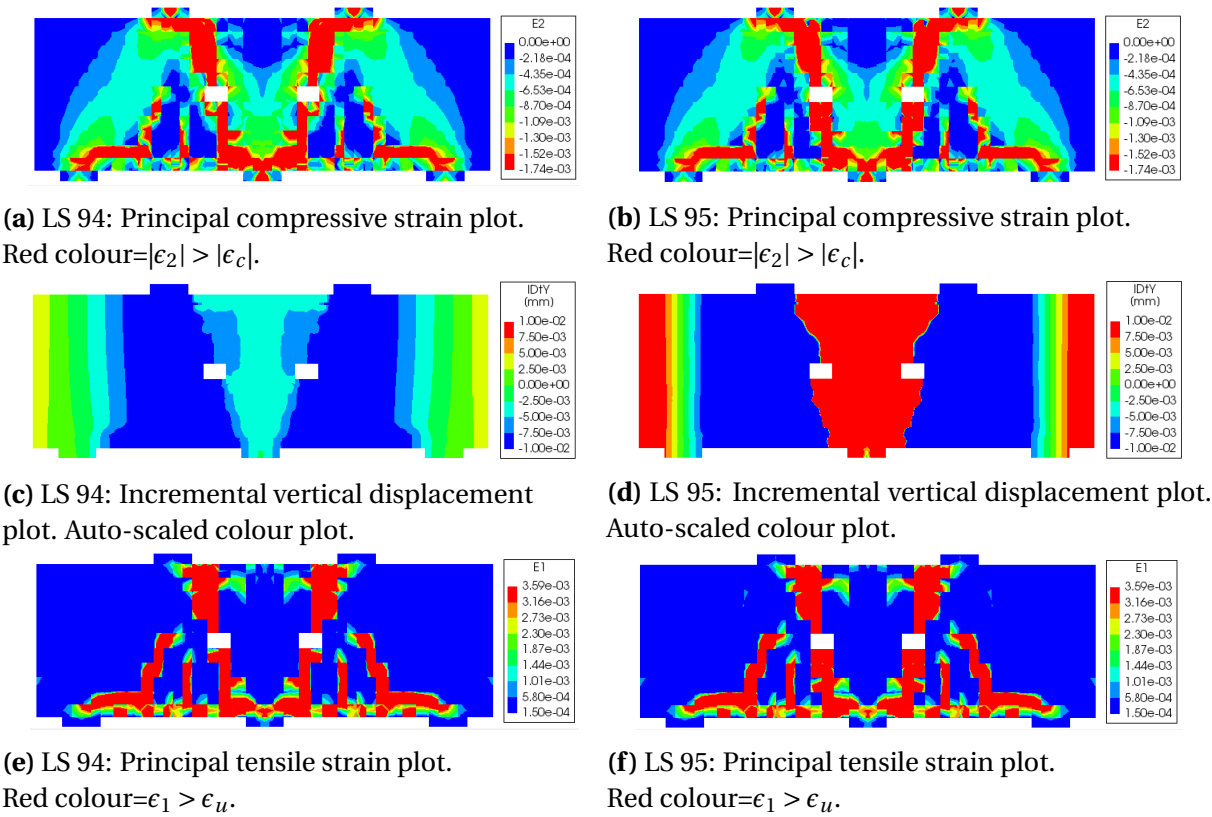


Figure 3.16: 6IT1. Principal compressive strain plots, incremental displacement plots and principal tensile strain plots from LS 94 and 95 in Analysis 2.

Table 3.20: 6IT1. Failure mode and failure load from the NLFEAs with different compressive behaviour functions.

Analysis	Failure Mode	Failure Load	Modelling Uncertainty($\frac{R_{exp}}{R_{NLFEA}}$)
1	Diagonal Tension Failure combined with Shear Compression Failure	2565 kN	0.85
2	No Failure*	—	—

* Diagonal Tension Cracking but no failure due to the fact that the compressive capacity remained constant.

As described earlier, the reinforcement in 6IT1 did not yield when the NLFEA was run by the selected solution strategy, i.e with parabolic compressive behaviour. However, the lack of failure in Analysis 2, with a constant compressive behaviour function, corresponded to larger deflections and strain values. This caused yielding in the lower longitudinal reinforcement bars in LS 98, in a small area over the middle support.

Shear Retention Model

Constant and damage based shear retention models were tested on the numerical models in order to investigate the sensitivity related to this aspect of the concrete material behaviour. Two shear retention factors, $\beta=0.1$ and $\beta=0.01$ were used for the constant model. Post-analysis checks for spurious tensile strength, crack pattern and load distribution were conducted.

Throughout this sensitivity study, the following designations will be used as references for the three NLFEAs of 6IT1 with different shear retention models:

Analysis 1: Damage based shear retention model.

Analysis 2: Constant shear retention model with $\beta=0.1$.

Analysis 2: Constant shear retention model with $\beta=0.01$.

The LDCs obtained for 6IT1 with the different shear retention models are shown in Figure 3.17. Based on these curves it is clear that 6IT1 was sensitive to choice of shear retention model. Red crosses symbolize non-converged LSs from Analysis 1, green from Analysis 2 and black from Analysis 3. As shown, all analyses resulted in non-converged steps after peaks.

As shown in Table 3.21, microcracks were detected at identical load levels in all three analyses. The width of these microcracks were $3.18 \cdot 10^{-4}$ mm. The first fully open crack in 6IT1 was detected after an applied load of 1048 kN in Analysis 3, and 1127 kN in Analysis 2. In Analysis 1 the first fully open crack was generated when the applied load exceeded 1178 kN. These situations represent the first peak in the LDCs in Figure 3.17. All approaches resulted in one or two non-converged LSs after this.

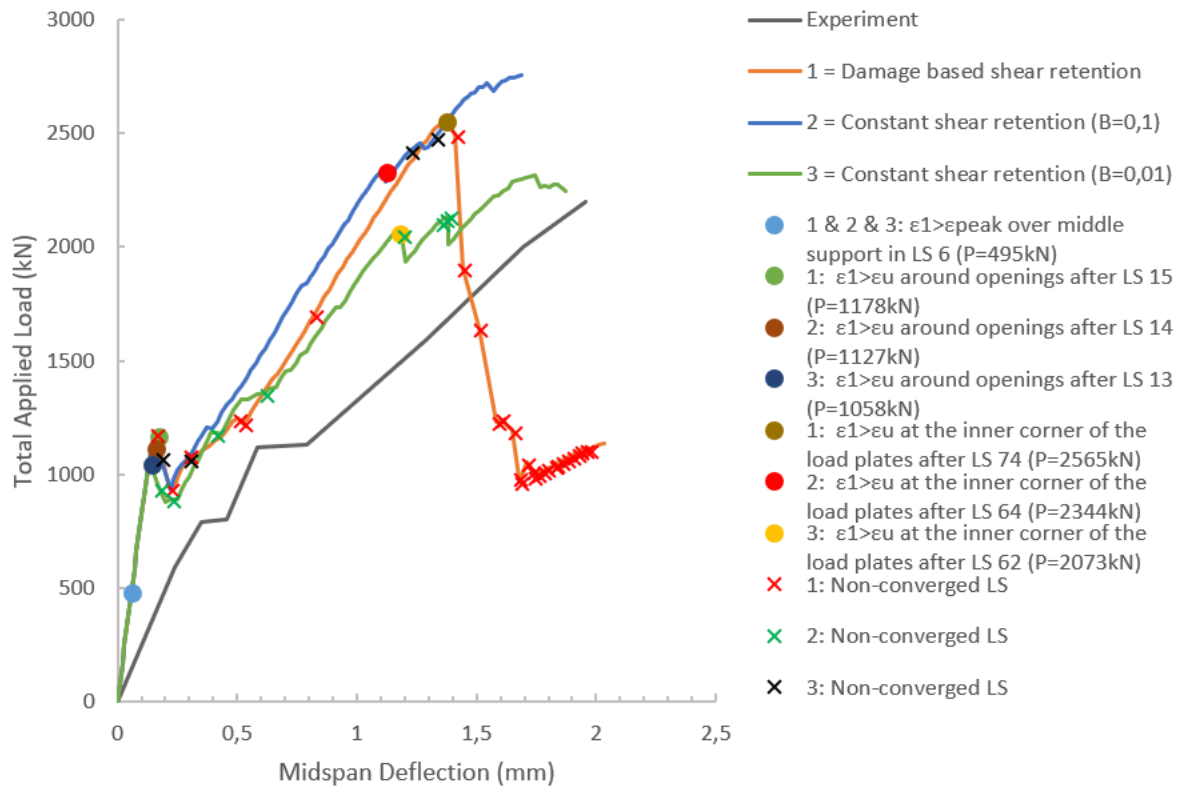


Figure 3.17: 6IT1. LDCs from the NLFEAs with different shear retention models, and the experimental LDC. The numerical LDCs are marked with essential observations that affected the global behaviour.

Table 3.21: 6IT1. Crack observations from the NLFEAs with different shear retention models.

Observation	Location	Total applied load, Analysis 1	Total applied load, Analysis 2	Total applied load, Analysis 3
First micro-crack	Over middle support	495 kN	495 kN	495 kN
First fully open crack	In corners of openings	1178 kN	1127 kN	1048 kN

Figure 3.2 confirms that 6IT1 in Analysis 1, which included the damage based shear retention model, failed after LS 76 as described previously. At this point the beam was cracked all the way through, and the concrete got completely softened in compression in the upper part. The load path from the load plates and down to the middle support could no longer transfer load. The beam was divided into separate blocks, and a failure mechanism was formed. From the principal tensile strain plots from this NLFEA shown in Figures 3.18a and 3.18b it is clear that the width of the maximum tensile strain path in 6IT1 increased remarkably from LS 74 and 76. The maximum principal crack width also increased remarkably; from 3.03 mm to 8.33 mm. The large changes and sharp distinction between the left and right side of the shear crack in the incremental displacement contour plots from these LSs, shown in Figures 3.18c and 3.18d, amplifies that the beam was split into separate blocks in LS 76.

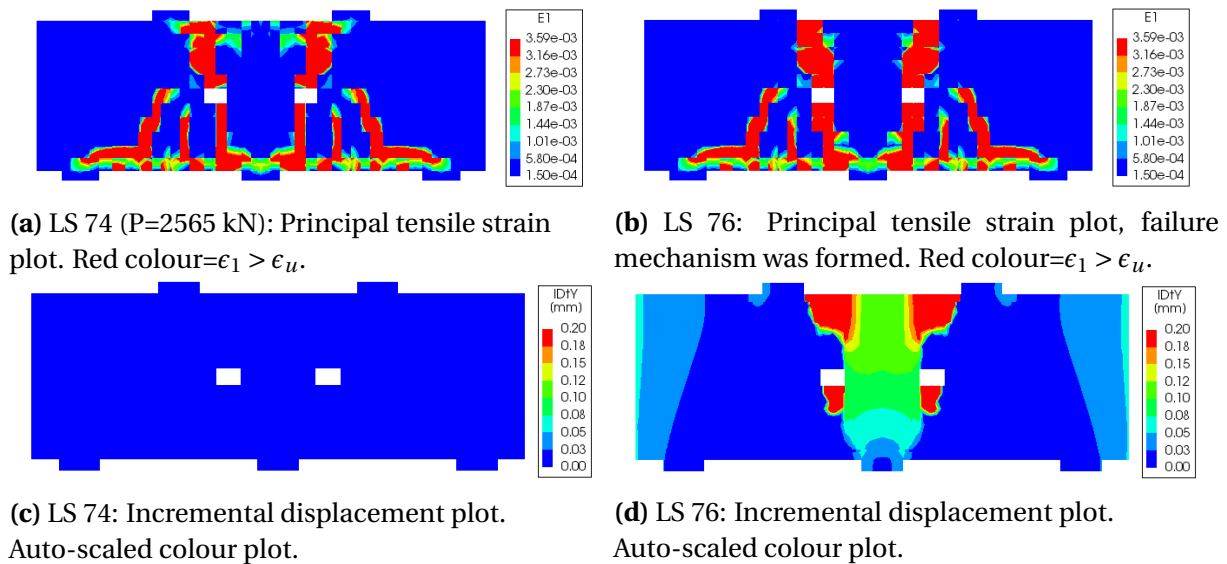


Figure 3.18: 6IT1. Shear crack development in Analysis 1.

Figures 3.19a and 3.19b illustrate the principal tensile strain plots from the last converged LS before failure, and the LS after the crack was fully open all the way through 6IT1 in Analysis 2. This corresponded to LS 64 and LS 65 respectively. However, the maximum principal crack width only increased 0.02 mm from LS 64 to LS 65. As mentioned, in Analysis 1 this width increased by 5.3 mm when 6IT1 were split into separate blocks. The largest crack width obtained in the final LS of Analysis 2 was 3.07 mm.

For Analysis 3, the specimen was fully softened in tension all the way through the beam height in LS 64. LS 62 was the last LS to achieve convergence before this. Principal tensile strain plots from these LSs are shown in Figures 3.20a and 3.20b. In this analysis the maximum principal crack width increased by 0.19 mm. Consequently, Analysis 3 resulted in a larger increase of maximum principal crack width than Analysis 2, but this increase was still significantly small compared to in Analysis 1. The largest principal crack width obtained in Analysis 3; 3.27 mm, was achieved in the final LS.

As shown in these tensile strain plots, 6IT1 with a shear retention model characterized by a simplified constant function, was cracked all the way through in LS 65 and 64 for $\beta=0.1$ and $\beta=0.01$ respectively. Compared to the corresponding LS in Analysis 1, LS 76, the incremental displacement plots from these LSs in Analysis 2 and 3 showed a more local displacement effect. This is shown in Figures 3.19c, 3.19d for $\beta=0.1$ and Figures 3.20c and 3.20d for $\beta=0.01$. Consequently Analysis 1 showed a more rapid development of the shear crack, with great incremental displacement in the critical LS. This difference is also reflected in the varied increases of the maximum crack widths. As stated, the constant shear retention models resulted in increases of 0.02 mm and 0.19 mm in the critical LSs with respect to cracking, while the crack width increased by 5.3 mm at this stage when the shear behaviour was characterized by a damage based retention model.

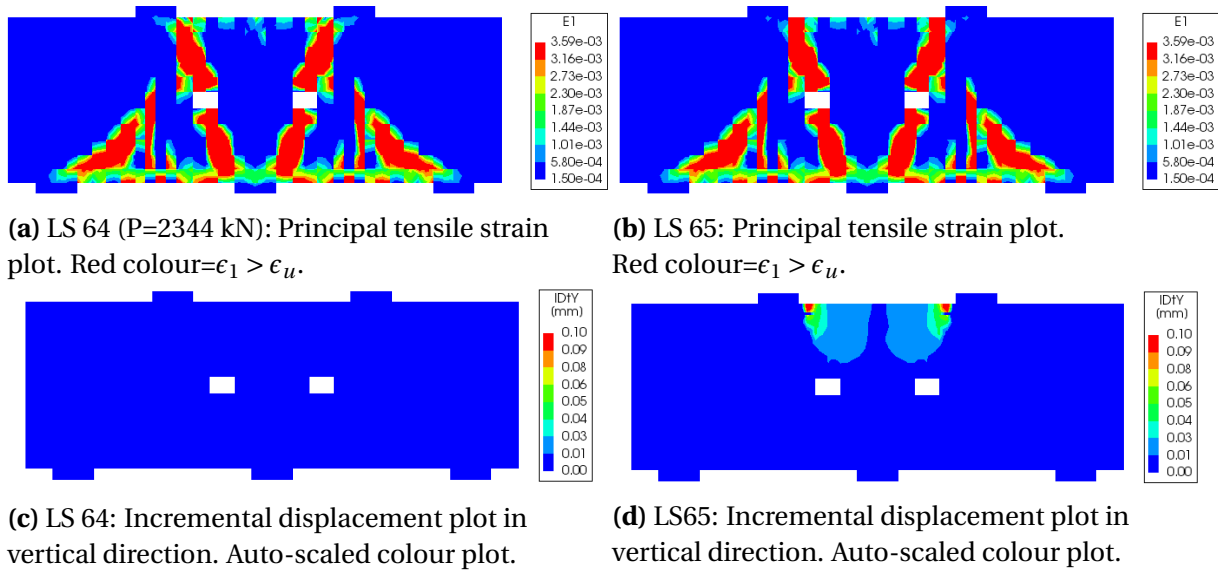


Figure 3.19: 6IT1. Shear crack development in Analysis 2.

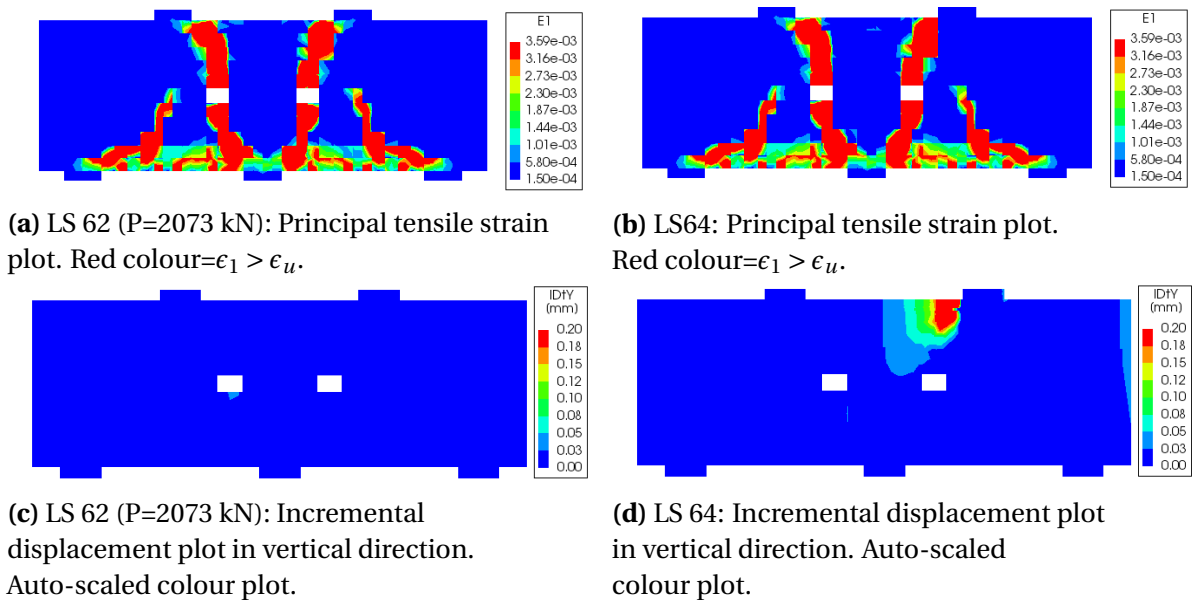
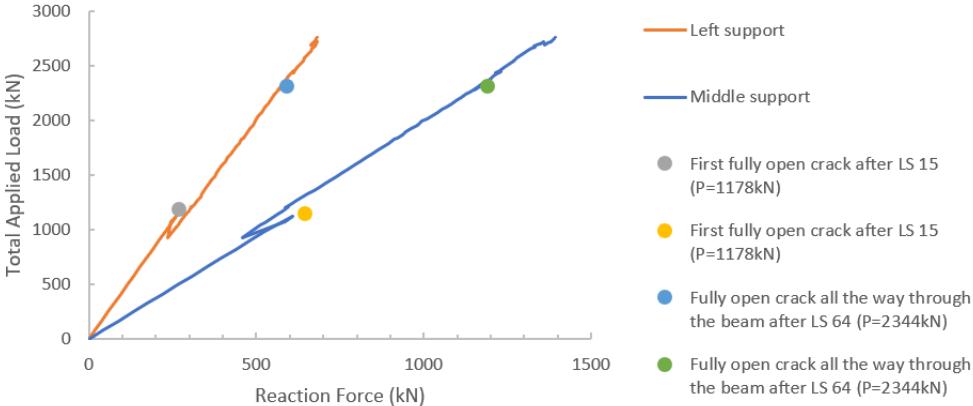


Figure 3.20: 6IT1. Shear crack development in Analysis 3.

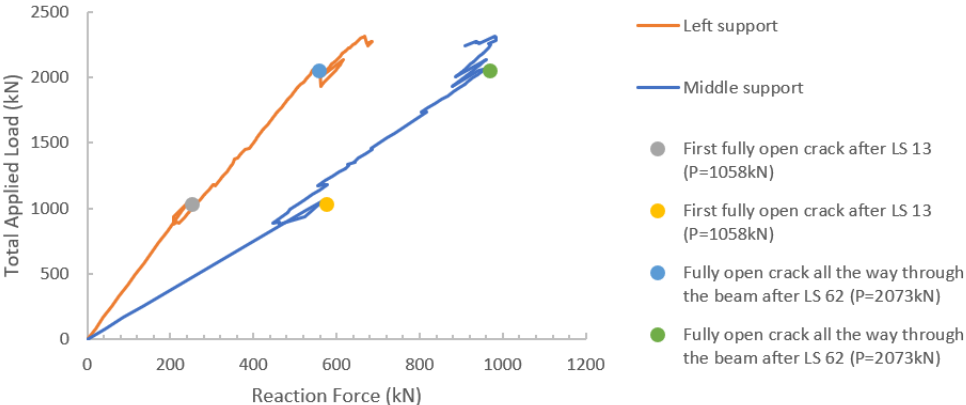
As described earlier, the selected solution strategy, which constituted Analysis 1 in this sensitivity study, resulted in an impaired load transfer to the middle support at the point when the shear crack was fully open all the way through the beam. In Analysis 2 and 3 on the other hand, the concrete along the shear crack still had load carrying capacity at this point. Consequently, with a constant shear retention model, 6IT1 did not lose its entire shear capacity in cracked regions. Figures 3.21a and 3.21b show that the applied load was transferred to the middle support, even though the beam was fully softened in tension all the way though the height of the beam from the middle support to the load plates.

Analysis 1 resulted in a significant load drop after LS 76, when ϵ_1 exceeded ϵ_u through the entire beam height, and $|\epsilon_2|$ exceeded $|\alpha_u|$ in the finite elements along the inner edge of the load plates. Hence, a failure mechanism formed and the LDC dropped. Contrary, as Table

3.22 states, no failure mechanism formed in 6IT1 at this point in neither Analysis 2 nor 3. The shear capacity was retained in the numerical model throughout the analyses when a constant shear retention model was used. Therefore, 6IT1 could still take up more load after the cracks were fully open all the way through the beam. Consequently, the LDCs for these analyses had no clear drop.



(a) Analysis 2.



(b) Analysis 3.

Figure 3.21: 6IT1. Support reactions against total applied load obtained in the NLFEA with constant shear retention models. The curves are marked with observations of fully open cracks and failure.

Table 3.22: 6IT1. Failure mode and failure load from the NLFEAs with different shear retention models.

Analysis	Failure Mode	Failure Load	Modelling Uncertainty($\frac{R_{exp}}{R_{NLFEA}}$)
1	Diagonal Tension Failure combined with Shear Compression Failure	2565 kN	0.85
2	No Failure*	—	—
3	No Failure*	—	—

* Diagonal Tension Cracking combined with Shear Compression Softening but no failure due to the fact that the shear capacity remained constant.

3.2 Case study 2

The following case study is a numerical approach to the experimental test of T1-0, collected from paper *Influence of Inclined Web Reinforcement on Reinforced Concrete Deep Beams with Openings* [Yang et al., 2007]. The FE model of T1-0 will be referred to as *T1-0* throughout this section.

3.2.1 NLFEA Results obtained by the selected Solution Strategy

Post-analysis checks of the NLFEA of T1-0 were conducted in order to determine its response and failure mode. Results obtained by the selected numerical solution strategy, specified in Table 2.10 is presented in this section.

Figure 3.22 compares the LDC obtained in the numerical analysis and the experiment, where red crosses indicate non-converged LSs. The NLFEA had four non-converged LSs; 9, 79, 93, 95. Non-convergence occurred when large redistribution of stresses was observed. The highest load taken up by T1-0 was 1670 kN in LS 92, with a corresponding midspan deflection of 2.74 mm. Consequently, after this LS the load dropped and a failure mechanism was formed. The load distribution to the supports was equal throughout the analysis.

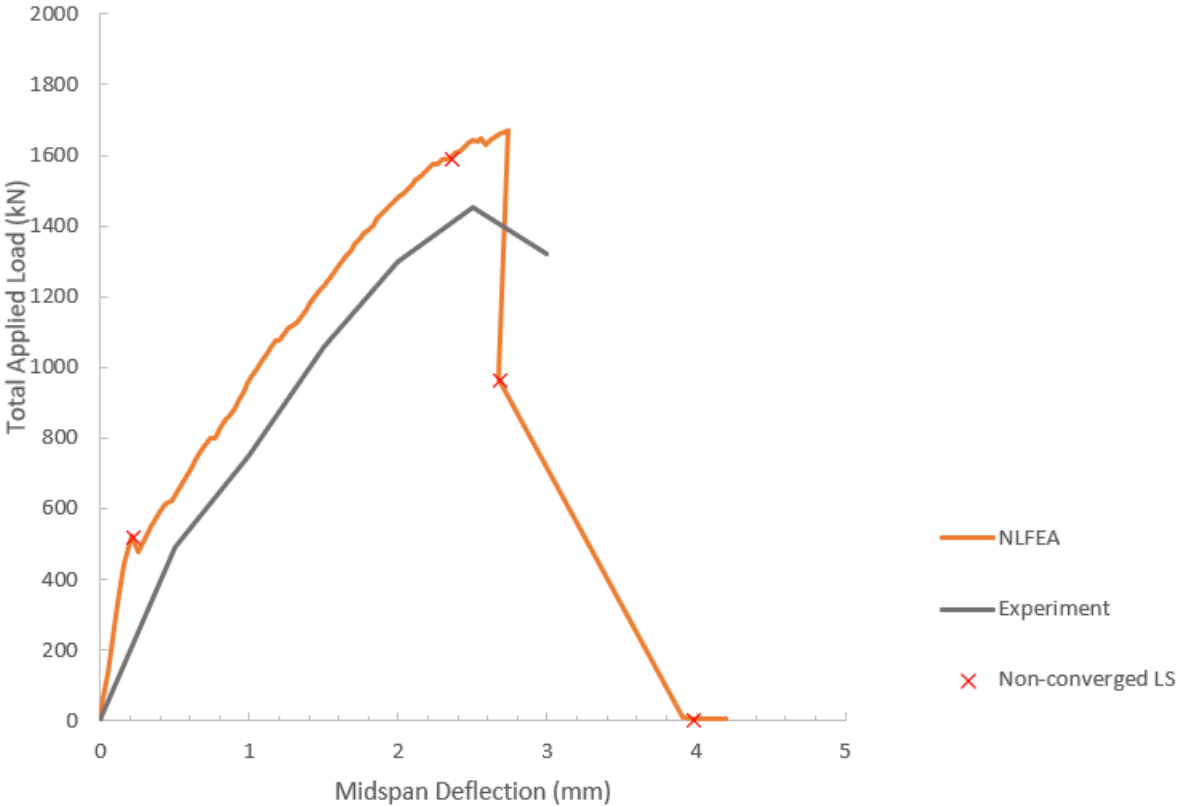


Figure 3.22: T1-0. LDC from the numerical solution strategy and the experiment. The numerical LDC is marked with non-converged LSs.

3.2.1.1 Concrete Cracking

Microcracks were formed in the concrete when the principal tensile strain, ϵ_1 , exceeded the peak tensile strain, ϵ_{peak} , as listed in Table 3.23. Fully open cracks occurred when ϵ_1 exceeded the ultimate tensile strain, ϵ_u , given in the same table. At this point the concrete was completely softened in tension, and the respective area did not have any remaining tensile capacity.

The main crack observations are marked with dots in the numerical LDC in Figure 3.23 and summarized in Table 3.24.

Table 3.23: T1-0. Specific tensile strains for the solution strategy.

Strain	Formula	Strain value	Tensile stress
ϵ_{peak}		$1.50 \cdot 10^{-4}$	$\sigma = f_{ctm}$
ϵ_u	$5 \cdot \frac{G_F}{f_{ctm} \cdot h}$	$3.77 \cdot 10^{-3}$	$\sigma = 0$

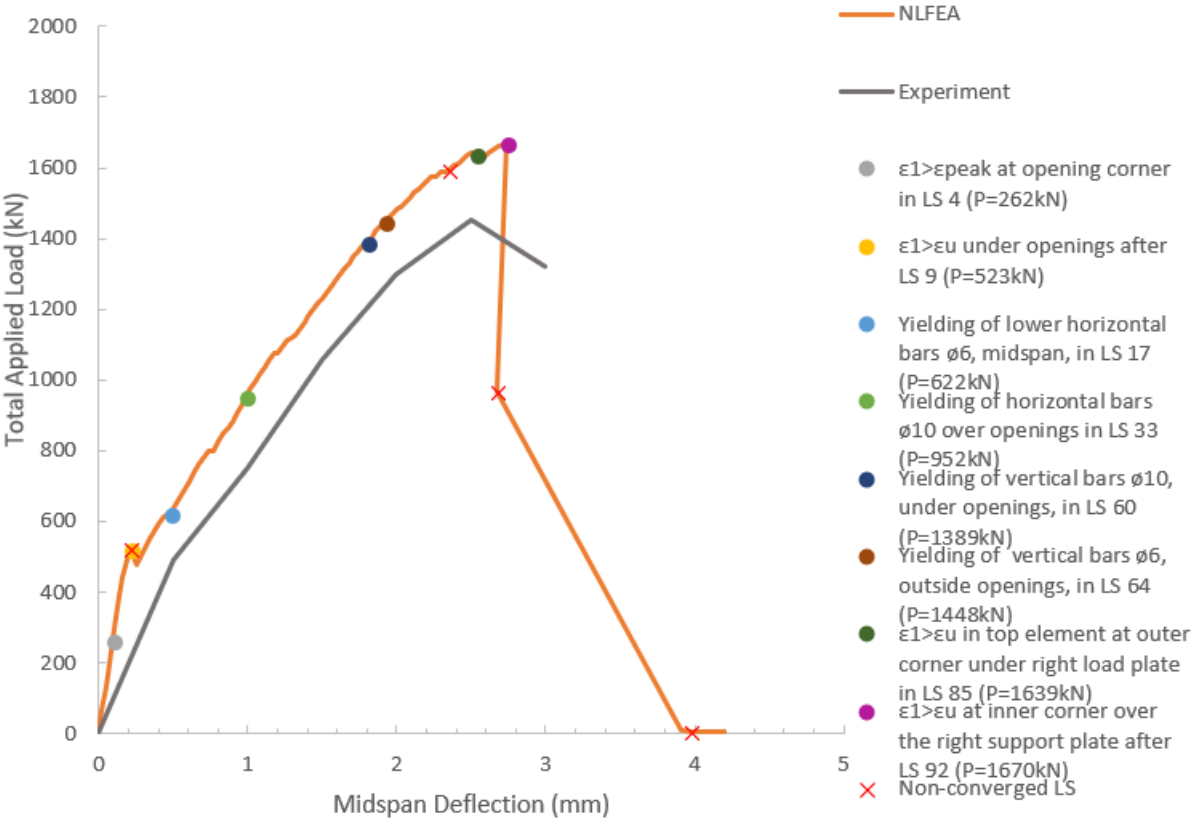


Figure 3.23: T1-0. LDC for the numerical solution strategy and the experiment. The numerical LDC is marked with essential observations that affected the global behaviour.

Table 3.24: T1-0. Crack observations from numerical solution strategy.

LS	Observation	Location	Total applied load
4	First microcracks	Around openings	262 kN
9-10	First fully open crack	in critical shear zone	523-479 kN
17	Crack propagation	midspan	622 kN
85	Fully open cracks	Below the right load plate	1639 kN
92	Fully open cracks	Inner corner of right support plate	1670 kN

The first microcracks appeared in LS 4 with a total applied load, P , of 262 kN. The cracks were observed around the web openings, in the corners close to the load points, as shown in Figure 3.24a. The maximum principal crack width was $1.45 \cdot 10^{-3}$ mm, located in the opening corners. The LDC did not show a decreased capacity at this point. Bottom flexural cracks were observed in the next step ($P=326$ kN), along with an increased crack area around the openings. This is illustrated in Figure 3.24b.

The first fully open cracks appeared in LS 10 with a principal crack width of 0.26 mm. Principal tensile strain plot from this LS is shown in Figure 3.24c. At this point the total applied load decreased from 523 kN in the non-converged LS 9 to 479 kN in LS 10. The cracks were located in a critical shear zone below the openings and propagated towards the supports. In LS 17 the flexural cracks propagated towards the middle of the beam height, as shown in the contour plot in Figure 3.24d.

The LDC showed a small drop in the applied load in LS 85, and the concrete was completely softened in tension in all the top nodes in an element below the right load plate, as shown in Figure 3.24e. In LS 92, ϵ_1 exceeded ϵ_u in several nodes above the right support. Figure 3.24f shows the principal tensile strain plot at this stage, but it is not possible to see the increased tensile strains in the respective nodes. Convergence was not achieved in the following LS. The LDC decreased drastically, and the amount of total cracks increased along with increased open, closed, inactive and closing cracks, as given in Table 3.25. This data was collected from an output file in DIANA. As shown in Eq. (3.1) and (3.2), the percentage of cracks that were inactive increased from 44.4% in LS 92 to 51.6% in LS 93. As shown in Figures 3.25a and 3.25b, the principal crack width increased from LS 92 to 93, from 3.72 mm to 14.56 mm above the right support.

Table 3.25: T1-0: Summary of crack logging at peak- and post peak load level for solution strategy, given by DIANA. The numbers indicate the amount of cracks.

Step number	Crack	Open	Closed	Active	Inactive	Arises	Re-opens	Closes
LS 92	1936	1915	21	1076	860	4	0	2
LS 93	2205	2145	60	1066	1139	269	7	46

$$\% \text{ of inactive cracks in LS 92} = \frac{\# \text{ of inactive cracks}}{\# \text{ of cracks in total}} \cdot 100\% = \frac{860}{1936} \cdot 100\% = 44.4\% \quad (3.1)$$

$$\% \text{ of inactive cracks in LS 93} = \frac{\# \text{ of inactive cracks}}{\# \text{ of cracks in total}} \cdot 100\% = \frac{1139}{2205} \cdot 100\% = 51.6\% \quad (3.2)$$

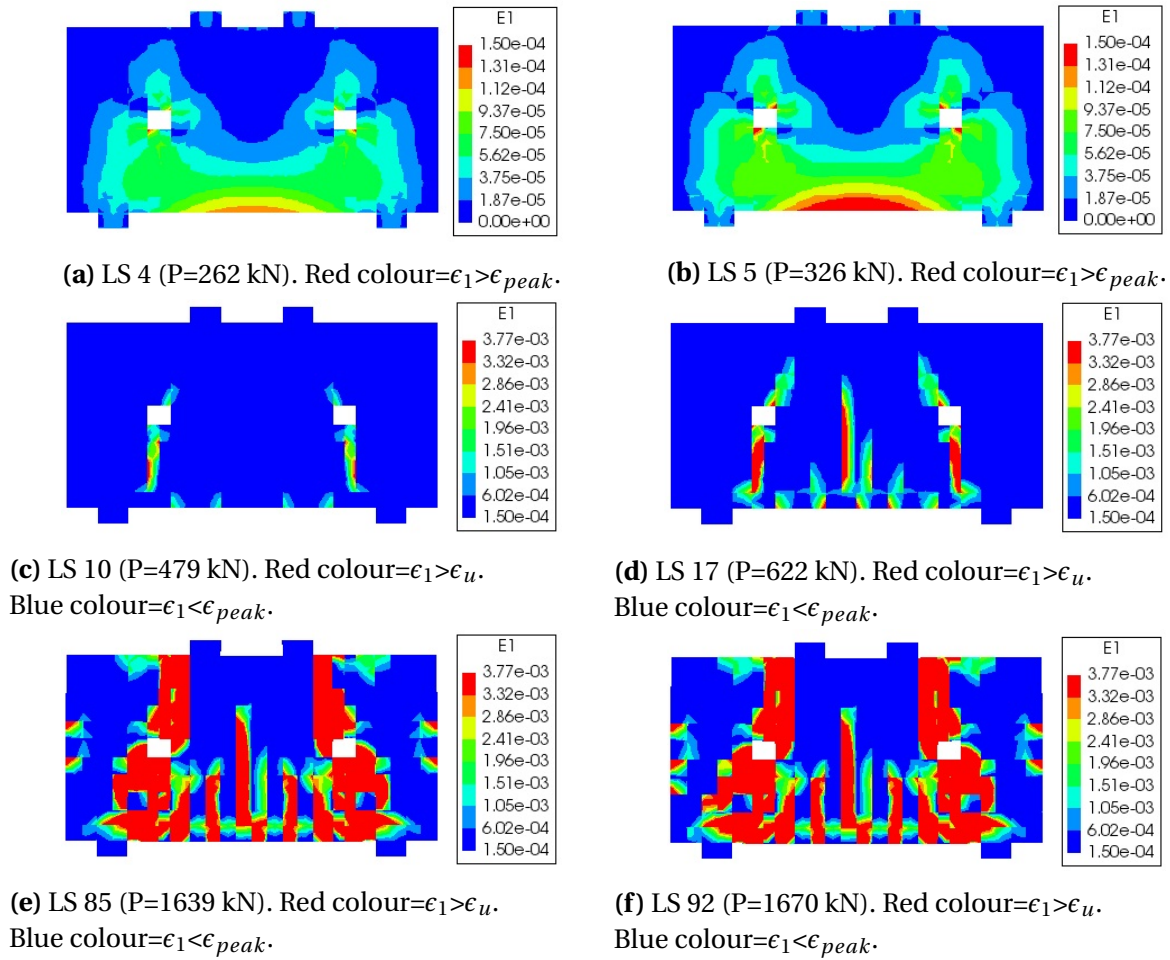


Figure 3.24: T1-0. Principal tensile strain plots from essential LSs in the NLFEA with the selected solution strategy.

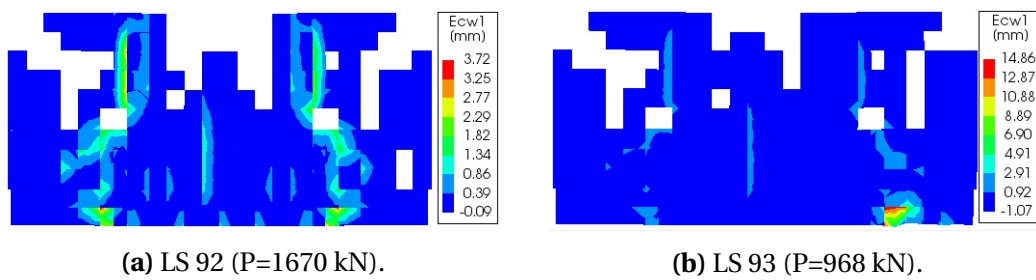


Figure 3.25: T1-0. Principal crack width from the last LSs in the NLFEA with the selected solution strategy. Auto-scaled colour plot.

3.2.1.2 Concrete Crushing

The compressive strain, $|\epsilon_2|$, exceeded the peak compressive strain, $|\alpha_c|$, listed in Table 3.26, in LS 38 (P=1057 kN). At this point the concrete in T1-0 started to crush in a small area below the inner corners of the load plates, without influencing the load carrying capacity, due to the LDC.

Table 3.26: T1-0. Specific compressive strain values for the parabolic stress-strain curve.

Strain	Formula	Strain value	Compressive stress
α_c	$-5 \cdot \frac{1}{3} \cdot \frac{f_c}{E_c}$	$-2.87 \cdot 10^{-3}$	$\sigma = f_c$
α_u	$\alpha_c - \frac{3}{2} \frac{G_c}{h f_c}$	$-2.31 \cdot 10^{-2}$	$\sigma = 0$

In LS 92, $|\epsilon_2|$ exceeded $|\alpha_u|$. The value of $|\alpha_u|$ is given in Table 3.26. The concrete was completely softened in compression above the right support plate. Principal compressive strain plots from LS 92 and 93 are shown in Figures 3.26a and 3.26b.

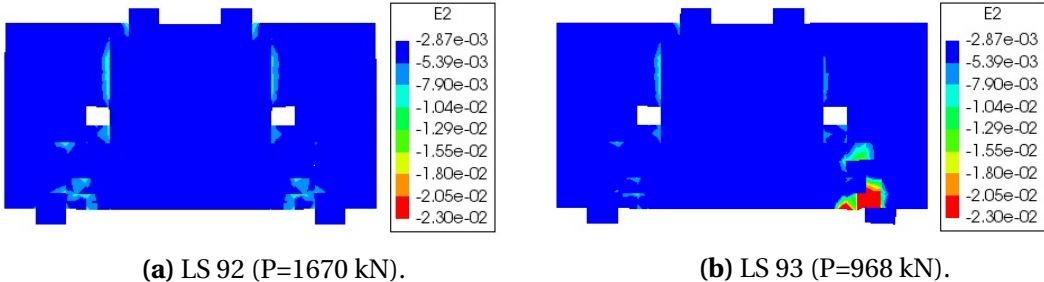


Figure 3.26: T1-0. Principal compressive strain plots from essential LSs in the NLFEA with the selected solution strategy. Red colour= $|\epsilon_2| > |\alpha_u|$. Blue colour= $|\epsilon_2| < |\alpha_c|$.

3.2.1.3 Tension-Compression Interaction

Two nodes in the concrete elements that had achieved complete tensile softening in LS 92 are highlighted in Figure 3.27. These nodes corresponded to node number 751 and 787 in the FE model. These nodes comprised a part of the strut that transferred the load from the load plate and down to the support. Hence, this area also achieved large compressive stresses during the analysis. Figure 3.28 visualizes the development of principal compressive stresses, S2, in these nodes. The horizontal axis indicates at what load-factor the respective stress values are obtained. Load factor 0.9 indicates the point when 90% of the total prescribed deflection is applied. Consequently the decimals of the load-factor corresponds more or less to the LS number. As shown in this figure, the maximum compressive stress was therefore reached at approximately LS 92-93. The maximum absolute value was however lower than the absolute value of the specified compressive strength for T1-0, which was 55.8 N/mm².

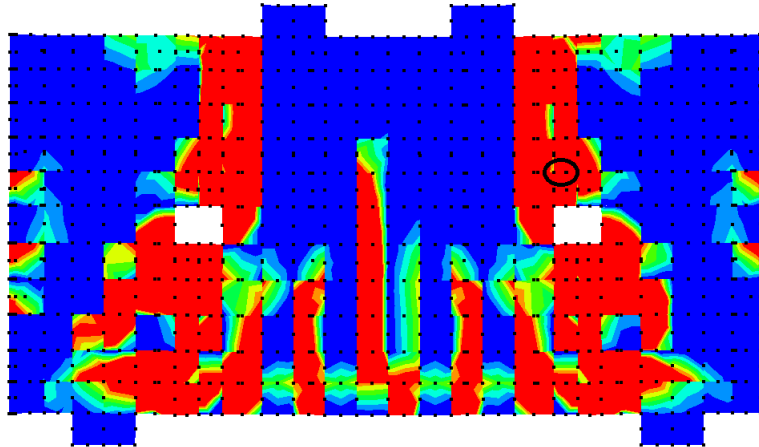


Figure 3.27: T1-0. Principal tensile strain plot. Red colour= $\epsilon_1 > \epsilon_u$. Development of compressive stresses in highlighted nodes; 751 and 787, are shown in Figure 3.28.

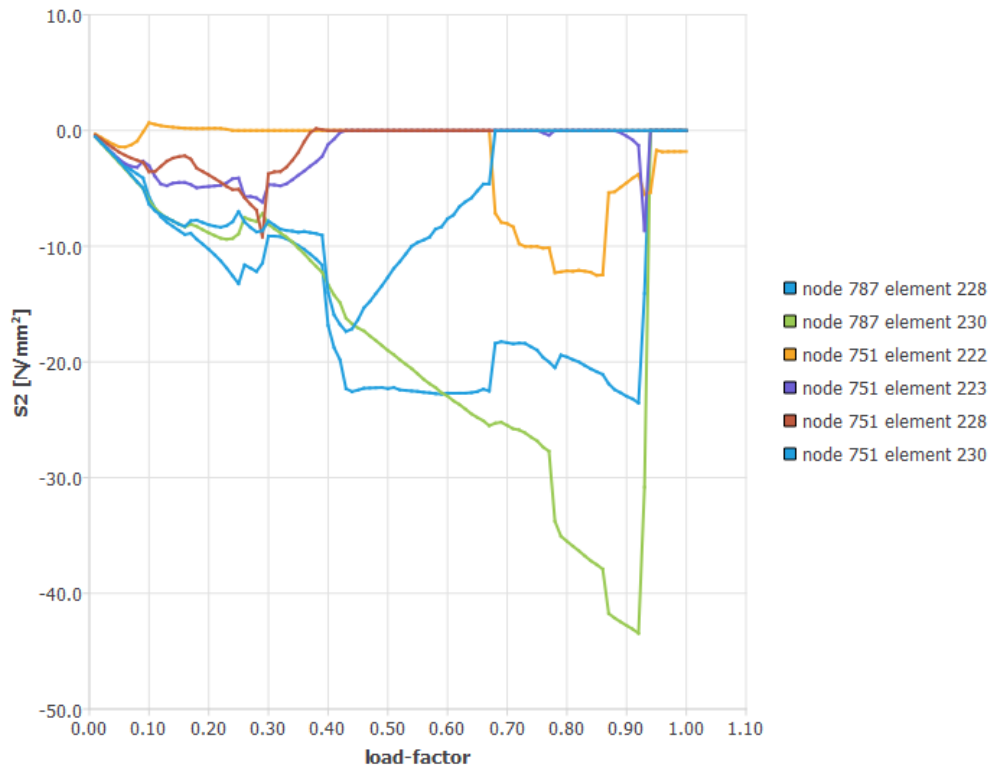


Figure 3.28: T1-0. Table-output from DIANA, showing the development of principal compressive stresses, S2, in node 751 and 787, highlighted in Figure 3.27.

3.2.1.4 Yielding of Reinforcement

Both vertical and horizontal bars of $\phi 6$ and $\phi 10$ started to yield during the numerical analysis. The yielding observations are marked in the numerical LDC, as shown in Figure 3.23. The yielding occurred in the same areas as the cracks developed, as illustrated in Figure 3.29, where the areas of yielding are marked with circles. Red colour indicates areas of yielding. The strain values that indicate yielding and ultimate capacity of the reinforcement bars are given in Table 2.7.

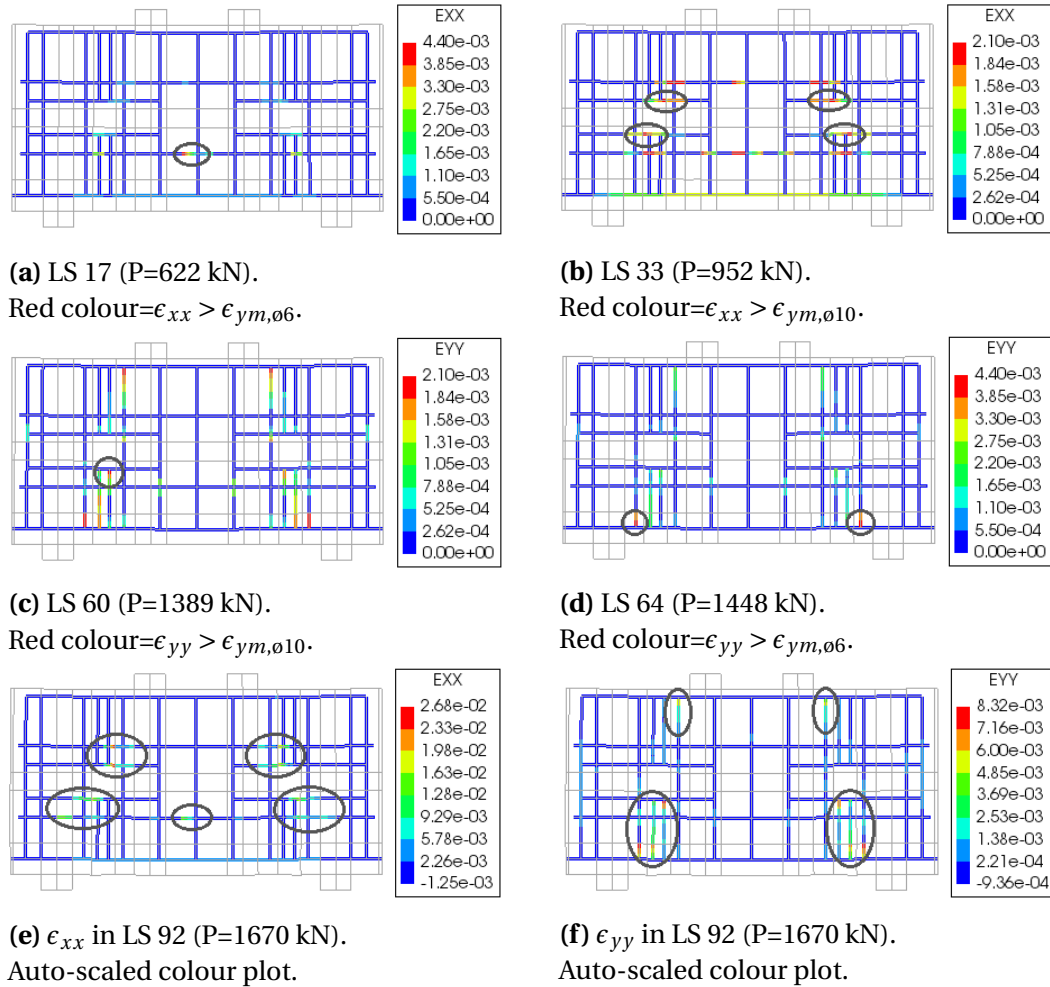


Figure 3.29: T1-0. Reinforcement strains in x- and y-direction in essential LSs from the NLFEA with the selected solution strategy. Areas of yielding are marked with circles.

In LS 17 (P=622 kN), the lower horizontal bars of $\phi 6$, started to yield in the midspan of the beam, as illustrated in Figure 3.29a. In the same step a vertical crack propagation was observed in the same area. The horizontal bars of $\phi 10$, below the openings, started to yield in LS 33 (P=952 kN), as shown in Figure 3.29b. The vertical stirrups of $\phi 10$, below the openings, started to yield in LS 60 (P=1389 kN), as shown in Figure 3.29c. The vertical stirrups of $\phi 6$, outside of the left opening, started to yield in LS 64 (P=1448 kN), as shown in Figure 3.29d. In LS 85 (P=1639 kN) the horizontal $\phi 6$ -bars above the openings, exceeded the ultimate strain value of $2.10 \cdot 10^{-2}$. The ultimate strain value for $\phi 10$ ($3.80 \cdot 10^{-2}$) was never exceeded. The main longitudinal reinforcement of $\phi 19$ never reached the yield strength of 803 N/mm^2 . The

maximum stress observed in these bars was 564 N/mm^2 at peak load level, in LS 92. Figures 3.29e and 3.29f show areas of yielding at peak load level.

3.2.1.5 Global Failure

Diagonal cracks were formed around both web openings, and propagated towards the four load points. The crack pattern ended near the load plates and the supports, as shown in Figure 3.24f. LS 93 was characterized by complete softened concrete in compression and fully open cracks above the right support, followed by large incremental displacements in the respective area. The crack width increased drastically in the same LS, along with the number of inactive cracks, as shown in Eq. (3.1) and (3.2). As mentioned, the obtained peak load before failure was 1670 kN, in LS 92, with a corresponding midspan deflection of 2.74 mm. Consequently, for T1-0 analyzed by the selected solution strategy, this resulted in a modelling uncertainty of 0.87, as given in Table 3.27.

Table 3.27: T1-0. Failure mode and failure load from the NLFEA with the selected solution strategy.

Failure Mode	Failure Load	Modelling Uncertainty ($\frac{R_{exp}}{R_{NLFEA}}$)
Shear Compression Failure	1670 kN	0.87

3.2.2 Sensitivity Study of the Numerical Modelling in Case Study 2

In this section results from a sensitivity study on the selected solution strategy for NLFEMs of T1-0 from the experimental benchmark test [Yang et al., 2007] are presented. The analysis conducted by the selected solution strategy, which is elaborated above, will be referred to as *Analysis 1* throughout this section. Just as for Case Study 1, analyses with complementary solution strategies, meaning other selections regarding the mesh density, tension softening model, compressive behaviour function or shear retention model, will be referred to as *Analysis 2* and *Analysis 3* within each separate sensitivity study.

3.2.2.1 Sensitivity regarding FE Discretization

In this sensitivity study the numerical response of T1-0 modelled by three different mesh densities were compared; $H/6$, $H/12$ and $L/50$. These mesh densities resulted in element heights of 100 mm, 50 mm and 18 mm, respectively.

Throughout this sensitivity study, the following designations will be used as references for the three NLFEMs of T1-0 with different FE discretizations:

Analysis 1: Mesh density $H/12$ (50 mm).

Analysis 2: Mesh density $L/50$ (18 mm).

Analysis 3: Mesh density $H/6$ (100 mm).

Figure 3.30 shows the LDC obtained with the different mesh densities. Non-converged steps are marked with crosses and crack observations are marked with dots in the numerical LDCs. Analysis 2 had 18 non-converged steps; LS 11, 18, 19, 27, 28, 40, 47, 81, 89-95 and 98-100, while Analysis 3 had five; LS 10, 27, 32, 58 and 92. The non-converged steps were mainly caused by significant changes in the stress distribution. The numerical LDCs behaved similarly. However, Analysis 2, with the finest mesh density, resulted in a lower failure load than Analysis 1 and 3.

Microcracks appeared in T1-0 when ϵ_1 exceeded ϵ_{peak} in the integration points. The cracks were defined as fully open when ϵ_1 exceeded the value of ϵ_u . The latter varied for different mesh densities. The respective strain values are given in Table 3.28. The crack observations for the three analyses are summarized in Table 3.29.

Table 3.28: T1-0. Specific tensile strain values in the MC2010 TS curve.

Strain	Formula	Strain value Analysis 1	Strain value Analysis 2	Strain value Analysis 3	Tensile stress
ϵ_{peak}		$1.50 \cdot 10^{-4}$	$1.50 \cdot 10^{-4}$	$1.50 \cdot 10^{-4}$	$\sigma = f_{ctm}$
ϵ_u	$5 \cdot \frac{G_F}{f_{ctm} \cdot h}$	$3.77 \cdot 10^{-3}$	$1.05 \cdot 10^{-2}$	$1.88 \cdot 10^{-3}$	$\sigma = 0$

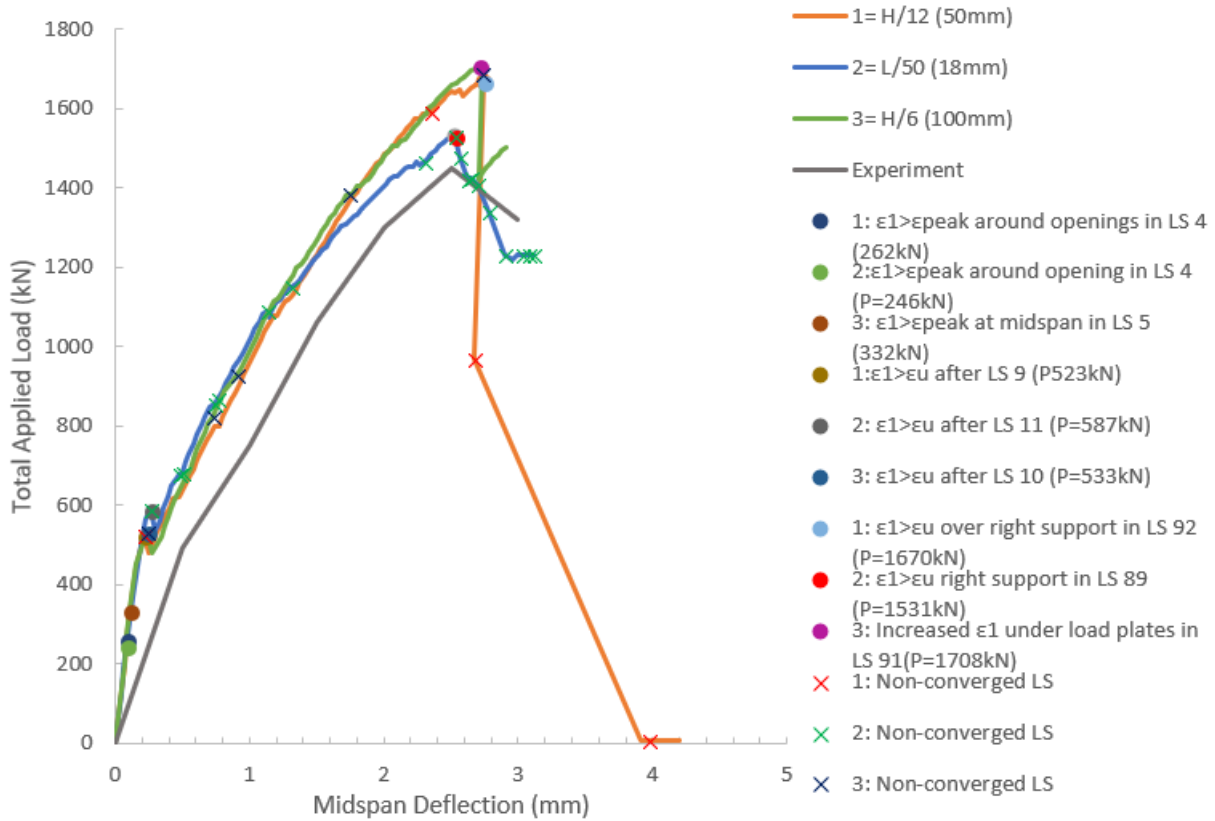


Figure 3.30: T1-0. LDCs from the NLFEMs with different mesh densities, and the experimental LDC. Numerical LDCs are marked with crack observations and non-converged LSs.

Table 3.29: T1-0. Crack observations from NLFEMs with different mesh densities.

Observation, Location	Applied Load Analysis 1	Applied Load Analysis 2	Applied Load Analysis 3
First microcrack, at opening corners	262 kN	246 kN	394 kN
First microcrack, at midspan	326 kN	307 kN	333 kN
First fully open crack, in critical shear zone	523 kN	586 kN	533 kN

Analysis 2, with the finest mesh, yielded earlier crack initiation than the other analyses. The first microcracks appeared around the openings in LS 4, at a loading of 246 kN. The principal crack width was $2.98 \cdot 10^{-3}$ mm. Flexural cracks at midspan arose in the next step. The total applied load dropped from 587 kN in LS 11 (non-converged LS) to 537 kN in LS 12, when the first fully open cracks developed below the openings with a principal crack width of 0.26 mm. At post peak level, in non-converged LS 89, ϵ_1 in the nodes above the right support plate exceeded ϵ_u . Consequently, the shear crack was fully open in this area. The maximum principal crack width, located at the inner edge of the right web opening, increased from 3.95 mm to 10.28 mm from LS 89 to LS 90.

In Analysis 3, with the coarsest mesh, the first microcracks appeared as flexural cracks in

the bottom of the beam, in LS 5 (P=332 kN). The principal crack width was $4.45 \cdot 10^{-3}$ mm. Similar as for Analysis 1 and 2, the total applied load decreased when the first fully open cracks developed. In Analysis 3 this occurred after LS 10 (non-converged LS), and the total applied load decreased from 533 kN to 478 kN. The principal crack width was 0.24 mm at this stage. After the peak load of 1708 kN was applied in LS 91, a larger area of nodes accomplished tensile strains larger than ϵ_u . Consequently, the area of concrete that was completely softened in tension increased. Especially, nodes in the areas below the load plates experienced increased tensile strains. A great incremental displacement followed in LS 91 and 92, outside the left load plate. In LS 91 the maximum principal crack width, observed at the outer lower corner of the right web opening, was 3.62 mm. The crack width did not increase in the next LSs.

As shown in Figures 3.31a, 3.31b and 3.31c, the crack pattern at peak load level was similar for the three analyses. A finer mesh density, used in Analysis 2, gave a more detailed crack pattern. Table 3.30 shows the amount of cracks and the crack status for Analysis 2 and 3 at the respective peak LSs. The data is given by an output file in DIANA. The analysis with the finest mesh had a total amount of 14362 cracks, while the analysis with the coarsest mesh had only 955 cracks in the last step before failure. 99% of the cracks were open at this stage, in all analyses. Analysis 2, with the finest mesh density, resulted in 59% inactive cracks in the peak LS, Analysis 1 resulted in 44%, while Analysis 3, with the coarsest mesh density, resulted in 34% inactive cracks in LS 91.

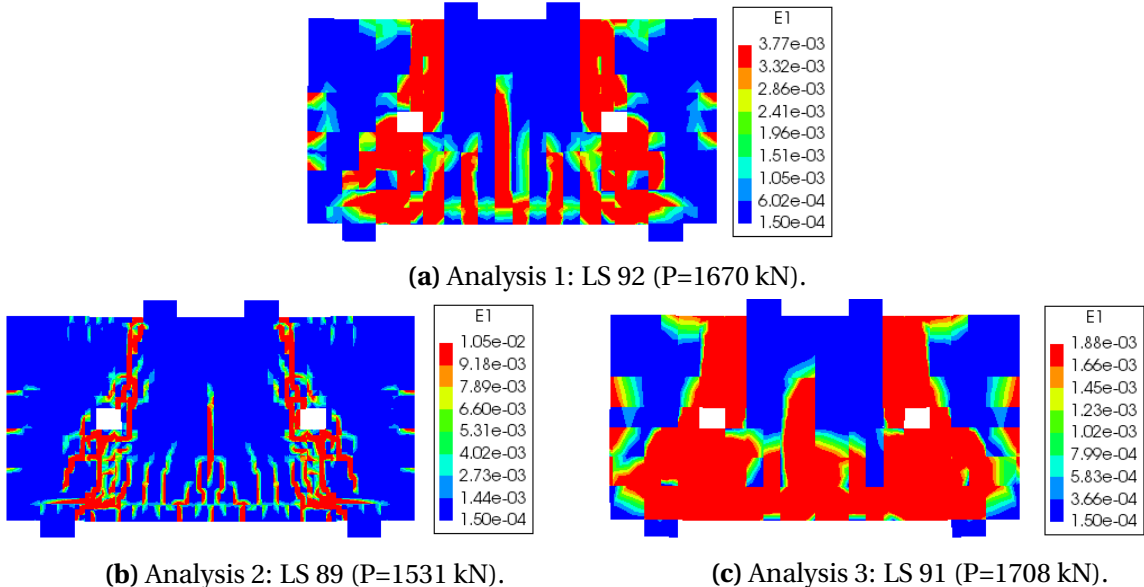


Figure 3.31: T1-0. Principal tensile strain plots at failure LS from the NLFEMs with different mesh densities. Red colour= $\epsilon_1 > \epsilon_u$. Blue colour= $\epsilon_1 < \epsilon_{peak}$.

Table 3.30: T1-0. Summary of crack logging for different mesh densities at failure load, given by DIANA. The numbers indicate the amount of cracks.

Analysis - step number	Crack	Open	Closed	Active	Inactive	Arises	Re-opens	Closes
2-LS 88	14362	14248	114	5917	8445	76	1	0
2-LS 89	14789	14639	150	4672	10117	427	6	42
3-LS 91	955	953	2	629	326	4	0	0
3-LS 92	959	957	2	594	365	4	0	0

The specific compressive strains for T1-0 with various mesh densities are given in Table 3.31. Figure 3.32 shows the contour plots of the principal compressive strain, ϵ_2 , at peak load level and post peak load level, for both Analysis 2 and 3. Red colour indicates areas where the concrete was completely softened in compression, as $|\epsilon_2| > |\alpha_u|$.

In Analysis 2, T1-0 started to crush ($|\epsilon_2| > |\alpha_c|$) at the inner and outer corners of the load plates in LS 17 (P=666 kN). The concrete in this area was never completely softened in compression in Analysis 2. However, as shown in Figure 3.32b, the concrete was completely softened in compression in a small area above the right support in LS 89 (P=1531 kN). This was in the same area as Analysis 1 achieved complete softening in compression.

In Analysis 3, T1-0 started to crush in the outer corners of the load plates in LS 41 (P=1122 kN). In the same areas, the concrete was completely softened in compression in LS 91 (P=1708 kN), as illustrated in Figures 3.32c and 3.32d. The concrete was partly crushed above the supports, but it was not completely softened in compression above the right support as it was in Analysis 1 and 2.

Table 3.31: T1-0. Specific compressive strain values for parabolic stress-strain curve with different mesh densities.

Strain	Formula	Strain value Analysis 1	Strain value Analysis 2	Strain value Analysis 3	Compressive stress
α_c	$5\alpha_c/3$	$-2.87 \cdot 10^{-3}$	$-2.87 \cdot 10^{-3}$	$-2.87 \cdot 10^{-3}$	$\sigma = f_c$
α_u	$\alpha_c - \frac{3}{2} \frac{G_c}{hf_c}$	$-2.30 \cdot 10^{-2}$	$-5.90 \cdot 10^{-2}$	$-1.30 \cdot 10^{-2}$	$\sigma = 0$

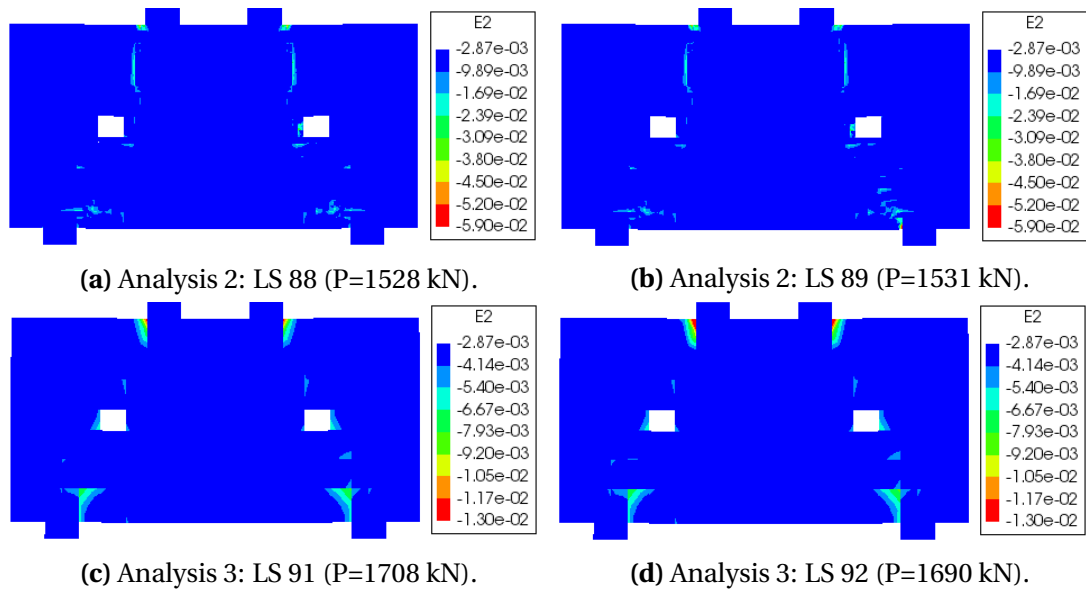


Figure 3.32: T1-0. Principal compressive strain plots for different mesh densities. Red colour= $|\epsilon_2| > |\alpha_u|$. Blue colour= $|\epsilon_2| < |\alpha_c|$.

Observations of reinforcement yielding in the analyses with various mesh densities, are marked with dots in the numerical LDCs in Figure 3.33, and summarized in Table 3.32. None of the yielding observations resulted in significant load drops in the LDCs. The yielding in Analysis 2 and 3 appeared in the same rebars as in Analysis 1, but at different load levels or locations in the respective bars.

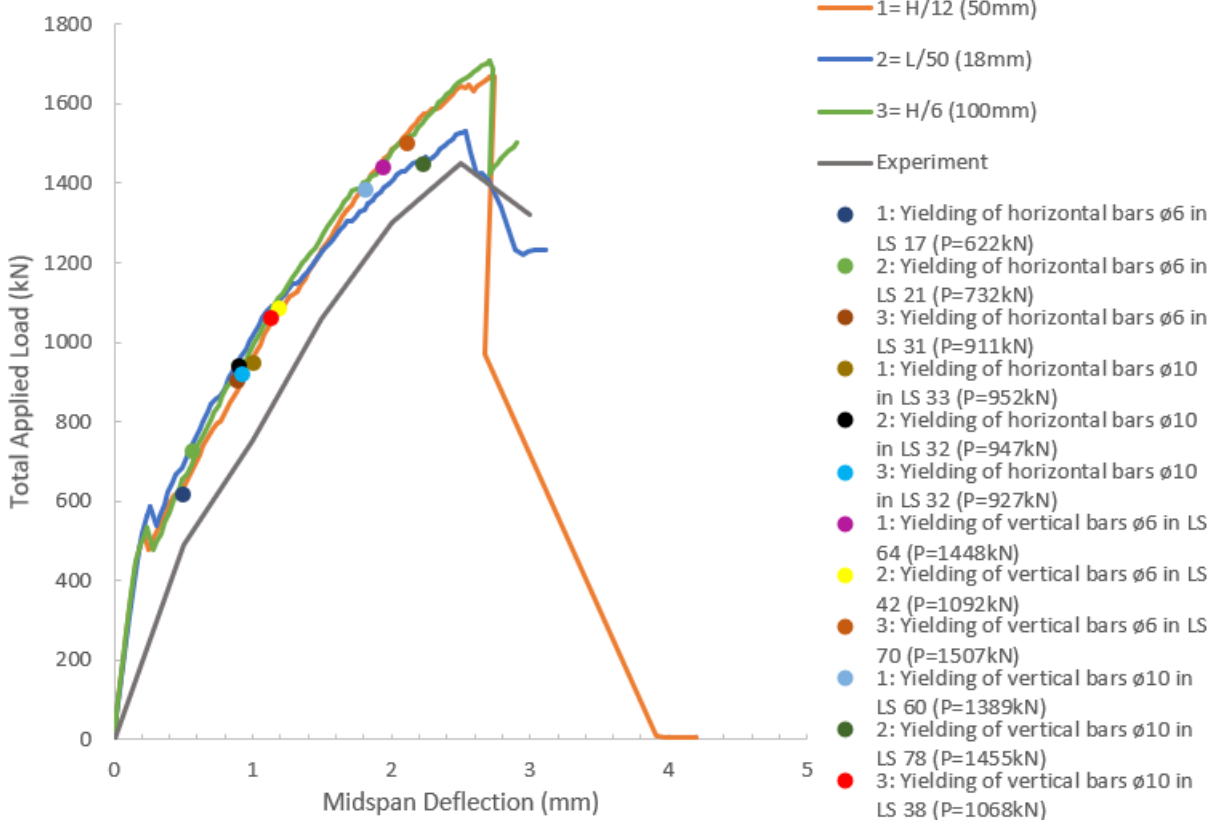


Figure 3.33: T1-0. LDCs from the NLFEAs with different mesh densities, and the experimental LDC. The numerical LDCs are marked with observations of reinforcement yielding.

Table 3.32: T1-0. Observations of yielding of reinforcement and its representative load levels with different mesh densities.

Observation, Location	Applied Load Analysis 1	Applied Load Analysis 2	Applied Load Analysis 3
Yielding of horizontal bars ø6, lower bars, variable location	622 kN	732 kN	911 kN
Yielding of vertical bars ø6, outside openings	1448 kN	1092 kN	1507 kN
Yielding of horizontal bars ø10, variable location	952 kN	947 kN	927 kN
Yielding of vertical bars ø10, below openings	1389 kN	1455 kN	1068 kN

In all analyses, bars in the cracked areas started to yield, except the main longitudinal reinforcement (3 ϕ 19). In the latter, the maximum stresses accomplished were 564, 526 and 573 N/mm² in Analysis 1, 2 and 3, respectively. None of the vertical stirrups of ϕ 6 and ϕ 10, reached the ultimate strain values for the respective bars.

In Analysis 2, with the finest mesh density, the horizontal bars of ϕ 6 above the openings, reached the ultimate strain in LS 77 (P=1455 kN), similarly as for Analysis 1 (LS 85, P= 1639 kN). The ultimate strain value was not exceeded in Analysis 3.

The yielding of ϕ 6-bars, horizontally and vertically, was located in the same areas for all analyses. Yielding of the horizontal bars of ϕ 10 was first observed below the openings in Analysis 1 and 2, and above the openings in Analysis 3. Yielding of the vertical stirrups of ϕ 10 was first observed below the openings for all analyses.

To sum up the main results from this sensitivity study regarding mesh density, the failure modes were evaluated, and are listed in Table 3.33. All analyses resulted in a diagonal crack pattern, as shown in Figure 3.31. The concrete above the right support was completely softened in compression in both Analysis 1 and 2, immediately after the peak load. Analysis 3 showed crushing above the support plates, but α_u was only exceeded in nodes below the load plates. Neither of the analyses where ϕ 6 bars reached the ultimate strain value, exhibited a reduced load carrying capacity due to this observation. The peak load obtained in Analysis 2, with the finest mesh, was 1528 kN in LS 88. This resulted in a modelling uncertainty of 0.95, as mentioned in Table 3.33. The peak load in Analysis 3 was 1708 kN in LS 91. Consequently, this resulted in a modelling uncertainty of of 0.85 for the NLFEA of T1-0 with the coarsest mesh density.

Table 3.33: T1-0. Failure mode and failure load from the NLFEAs with different mesh densities.

Analysis	Failure Mode	Failure Load	Modelling Uncertainty ($\frac{R_{exp}}{R_{NLFEA}}$)
1	Shear Compression Failure	1670 kN	0.87
2	Shear Compression Failure	1528 kN	0.95
3	Shear Compression Failure	1708 kN	0.85

3.2.2.2 Sensitivity to choice of Constitutive Model for Concrete

Tension Softening Model

For the selected solution strategy, MC2010 was chosen as the standard TS approach. According to DG, exponential TS is preferred. In order to investigate the sensitivity related to this constitutive approach, these two models were tested.

Throughout this sensitivity study, the following designations will be used as references for the two NLFEAs of T1-0 with different TS approaches:

Analysis 1: MC2010 TS model.

Analysis 2: Exponential TS model.

Figure 3.34 shows the LDCs for the two analyses and the experiment. The numerical LDCs are marked with crosses that indicate non-converged LSs and dots that indicate crack

observations. Analysis 2 had five non-converged steps; LS 9, 57, 60, 72 and 81, marked with green crosses in the curve.

Table 3.34 lists the specific tensile strain values for exponential TS, used in post-processing of T1-0 in Analysis 2. The crack observations for the two analyses are summarized in Table 3.35.

Table 3.34: T1-0. Specific tensile strain values for exponential TS.

Strain	Formula	Value	Tensile stress
ϵ_{peak}	$\frac{f_{ctm}}{E_{cm}}$	$1.23 \cdot 10^{-4}$	$\sigma = f_{ctm}$
ϵ_u	$2 \frac{G_F}{f_{ctm} \cdot h}$	$1.51 \cdot 10^{-3}$	$\sigma \approx 0$

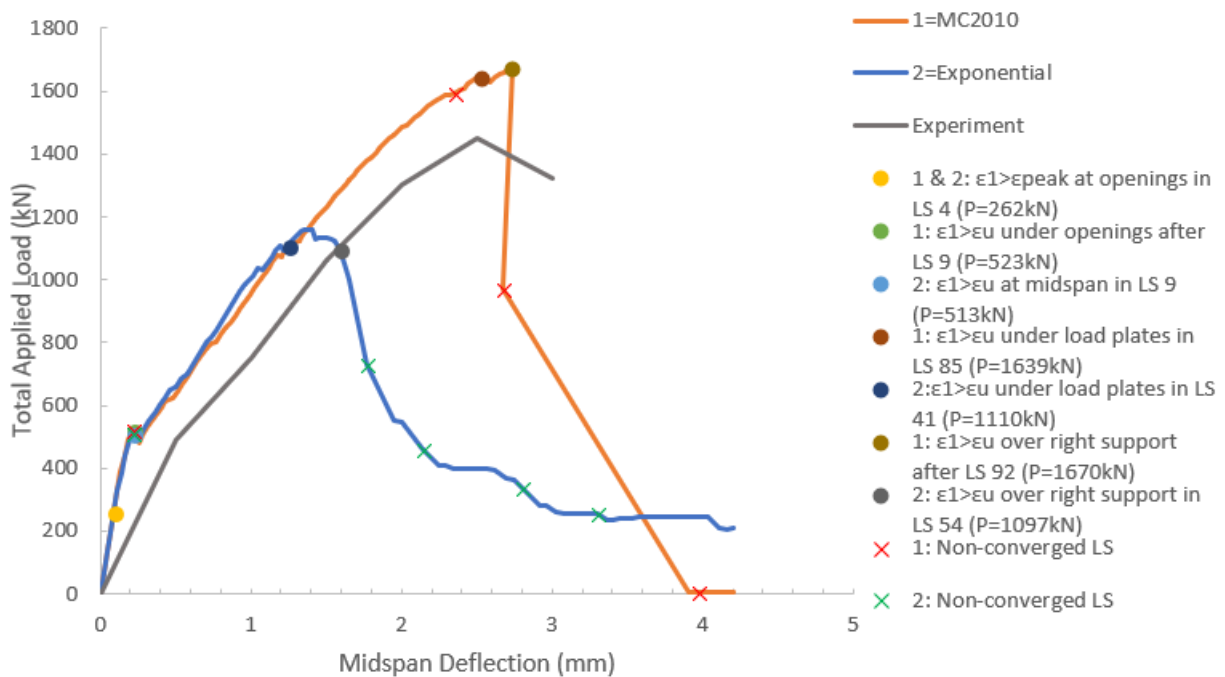


Figure 3.34: T1-0. LDCs from the NLFEMs with different TS models, and the experimental LDC. The numerical LDCs are marked with crack observations and non-converged LSs.

Table 3.35: T1-0. Summary of crack logging from the NLFEMs with different TS models, given by DIANA.

Observation, Location	Applied Load Analysis 1	Applied Load Analysis 2
First microcrack, at opening corners	262 kN	262 kN
First microcrack, at midspan	326 kN	326 kN
First fully open crack, in critical shear zone	523 kN	513 kN

In Analysis 2, the first microcracks appeared around the openings and in the midspan of the beam, as flexural cracks. It occurred in the same load levels as in Analysis 1, even though the ϵ_{peak} values were slightly different for the two TS models. A diagonal crack pattern propagated below the openings after LS 8, for a similar applied load as in Analysis 1. The crack propagation led to a drop in the total applied load, which resulted in lack of convergence in LS 9 in Analysis 2. It was observed open cracks below the load plates in LS 41, resulting in a small drop in the total applied load. Cracks opened above the right support plate and the load dropped drastically after LS 56. The next LS did not converge. At this stage the amount of inactive cracks increased in Analysis 2, from 78% to 83%, based on values given in Table 3.36. 99.5% of the cracks were open. With an exponential TS approach, the crack pattern on the right side of T1-0 gradually disappeared as the load decreased after the peak. In LS 73, all of the cracks had disappeared, as shown in Figure 3.35. In the crack pattern on the left side the strain values and crack width increased during these LSs.

Analysis 1 achieved more open longitudinal cracks at the beam ends than Analysis 2, as shown in Figure 3.36. However, this did not affect the response of the beam. Analysis 1 also resulted in larger areas of cracked concrete around the load plates, as illustrated in Figure 3.36.

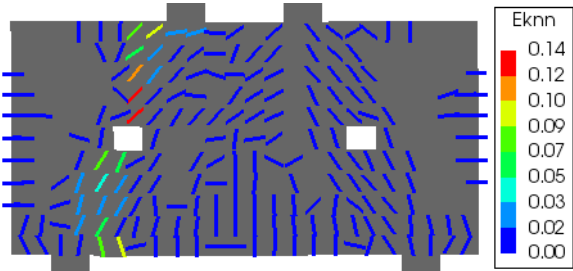


Figure 3.35: T1-0. Crack strain in LS 73 for Analysis 2. Auto-scaled colour plot.

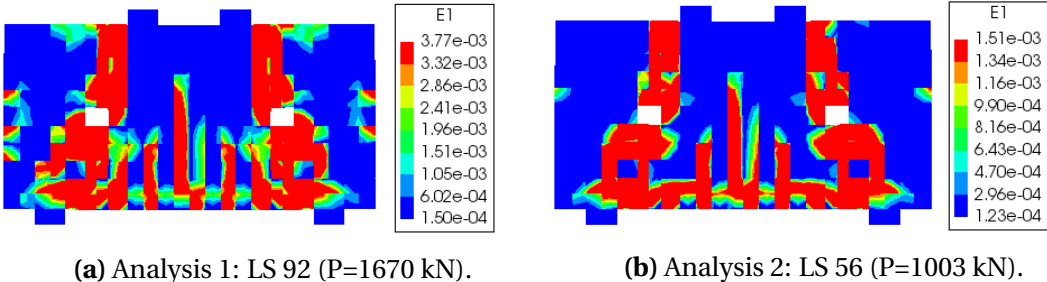


Figure 3.36: T1-0. Principal tensile strain plots before failure from the NLFEAs with different TS models. Red colour= $\epsilon_1 > \epsilon_u$. Blue colour= $\epsilon_1 < \epsilon_{peak}$.

Table 3.36: T1-0. Summary of crack logging from NLFEA with exponential TS, given by DIANA. The numbers indicate the amount of cracks.

Analysis - step number	Crack	Open	Closed	Active	Inactive	Arises	Re-opens	Closes
2-LS 56	1305	1299	6	287	1018	18	0	1
2-LS 57	1402	1390	12	236	1166	97	0	6

Both analyses were based on parabolic compression behaviour function of concrete. Consequently, the same strain values were used to analyze the compressive behaviour in Analysis 2 as in Analysis 1, listed in Table 3.26.

In Analysis 2, crushed concrete was first observed in the outer corner of the left load plate. This was not in the same area as for Analysis 1, where crushing first was observed below the inner corners of the load plates. In LS 52, the area beneath the left load plate was completely softened in compression in Analysis 2. A diagonal pattern of crushed concrete was formed along the left crack pattern after LS 56, as shown in Figure 3.37a. In LS 57 the concrete got completely softened in compression above the left support plate, as shown in Figure 3.37b. Due to large changes in the stress distribution, convergence was not achieved in this LS.

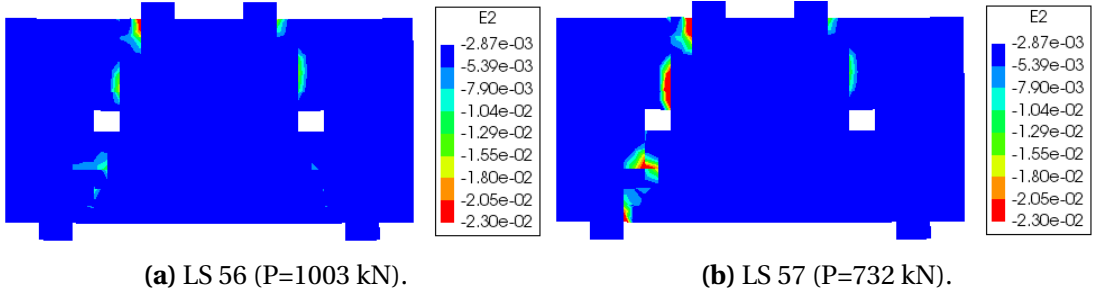


Figure 3.37: T1-0. Principal compressive strain plots for Analysis 2. Red colour= $|\epsilon_2| > |\alpha_u|$. Blue colour= $|\epsilon_2| < |\alpha_{peak}|$.

The behaviour of reinforcement yielding was quite similar for the two analyses. The first observations of yielding are listed in Table 3.37 for the two analyses. Essential LSs for observations of yielding are marked on the numerical LDC of Analysis 2, as shown in Figure 3.38. The horizontal bars, both $\phi 6$ and $\phi 10$, achieved yielding at almost identical load levels. For the vertical bars, the yielding occurred earlier in Analysis 2 than in Analysis 1. In Analysis 2, the strains in the bars located in the cracked areas decreased after LS 55. None of the bars were close to exceed the respective ultimate strain values in Analysis 2. The maximum stress observed in the main longitudinal reinforcement ($3\phi 19$) in Analysis 2 was (383 N/mm^2), lower than in Analysis 1 (564 N/mm^2).

Table 3.37: T1-0. Observations of reinforcement yielding and its representative load levels from the NLFEMs with different TS models.

Observation, Location	Applied Load Analysis 1	Applied Load Analysis 2
Yielding of horizontal bars $\phi 6$, lower bars, midspan	622 kN	658 kN
Yielding of vertical bars $\phi 6$, variable location	1448 kN	1158 kN
Yielding of horizontal bars $\phi 10$, variable location	952 kN	987 kN
Yielding of vertical bars $\phi 10$, variable location	1389 kN	1131 kN

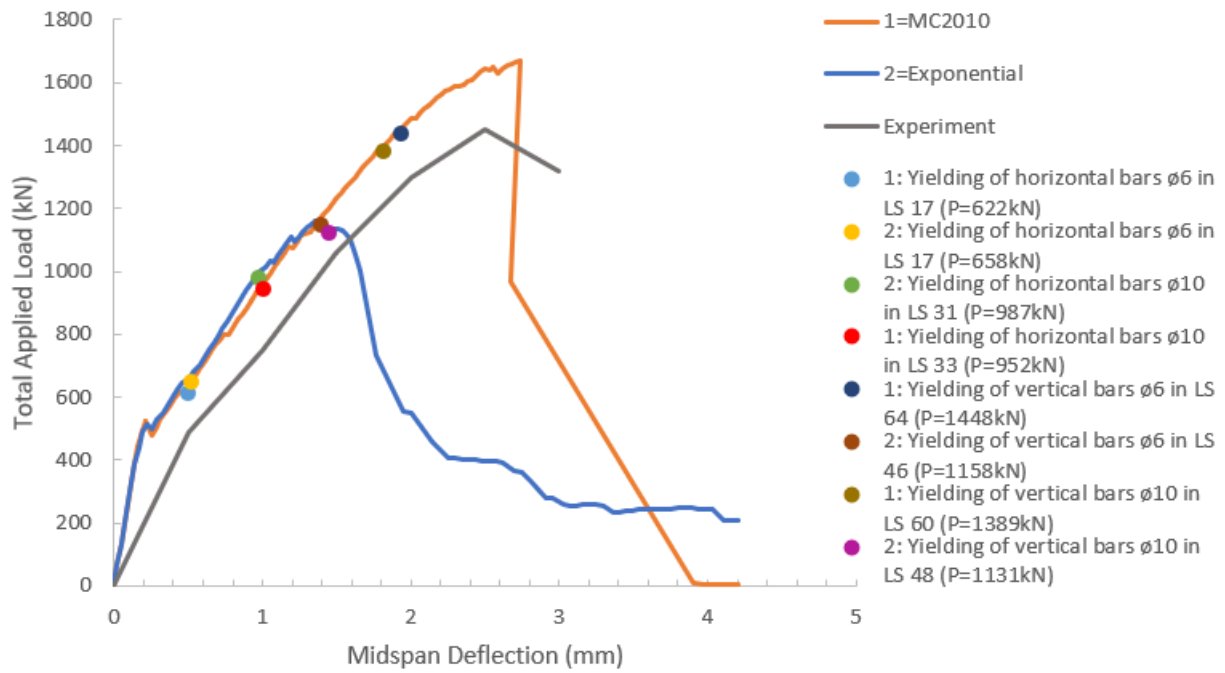


Figure 3.38: T1-0. LDCs from the NLFEAs with different TS models, and the experimental LDC. The numerical LDCs are marked with observations of reinforcement yielding.

Failure modes and failure loads for this sensitivity study, where T1-0 was analyzed with two different TS approaches, are given in Table 3.38. Both analyses formed a similar diagonal crack pattern in the load path from the load plates to the supports. The concrete got crushed below the left load plate in Analysis 2, while this happened above the right support in Analysis 1. T1-0 was able to take up larger loads in Analysis 1 than in Analysis 2. Analysis 2 resulted in a peak load of 1161 kN in LS 45, which gave a modelling uncertainty of 0.80. In the following descending branch, the force distribution became unsymmetrical. The left support gradually received more load than the right support.

Table 3.38: T1-0. Failure mode and failure load from the NLFEAs with different TS models.

Analysis	Failure Mode	Failure Load	Modelling Uncertainty ($\frac{R_{exp}}{R_{NLFEA}}$)
1	Shear Compression Failure	1670 kN	0.87
2	Shear Compression Failure	1161 kN	1.25

Compressive Behaviour Function

In this sensitivity study the influence of two different compressive behaviour functions of concrete were tested on T1-0. For the selected solution strategy, a parabolic softening-hardening function was used. In addition to this, an idealized constant function was tested.

Throughout this sensitivity study, the following designations will be used as references for the two NLFEAs of T1-0 with different compressive behaviour approaches:

Analysis 1: Parabolic compressive behaviour function.

Analysis 2: Constant compressive behaviour function.

The LDCs obtained in the two analyses are shown in Figure 3.39, in addition to the experimental LDC. The numerical LDCs are marked with dots that imply observations of concrete or yielding of the reinforcement. The crosses imply non-converged LSs. Analysis 2 only had two non-converged LSs; LS 9 and 89.

The crack observations were almost identical in the two analyses. Therefore, not all observations are plotted in the LDC for Analysis 2. They are however plotted in the LDC in Figure 3.23, which were obtained by the selected solution strategy, constituting Analysis 1 in the sensitivity studies.

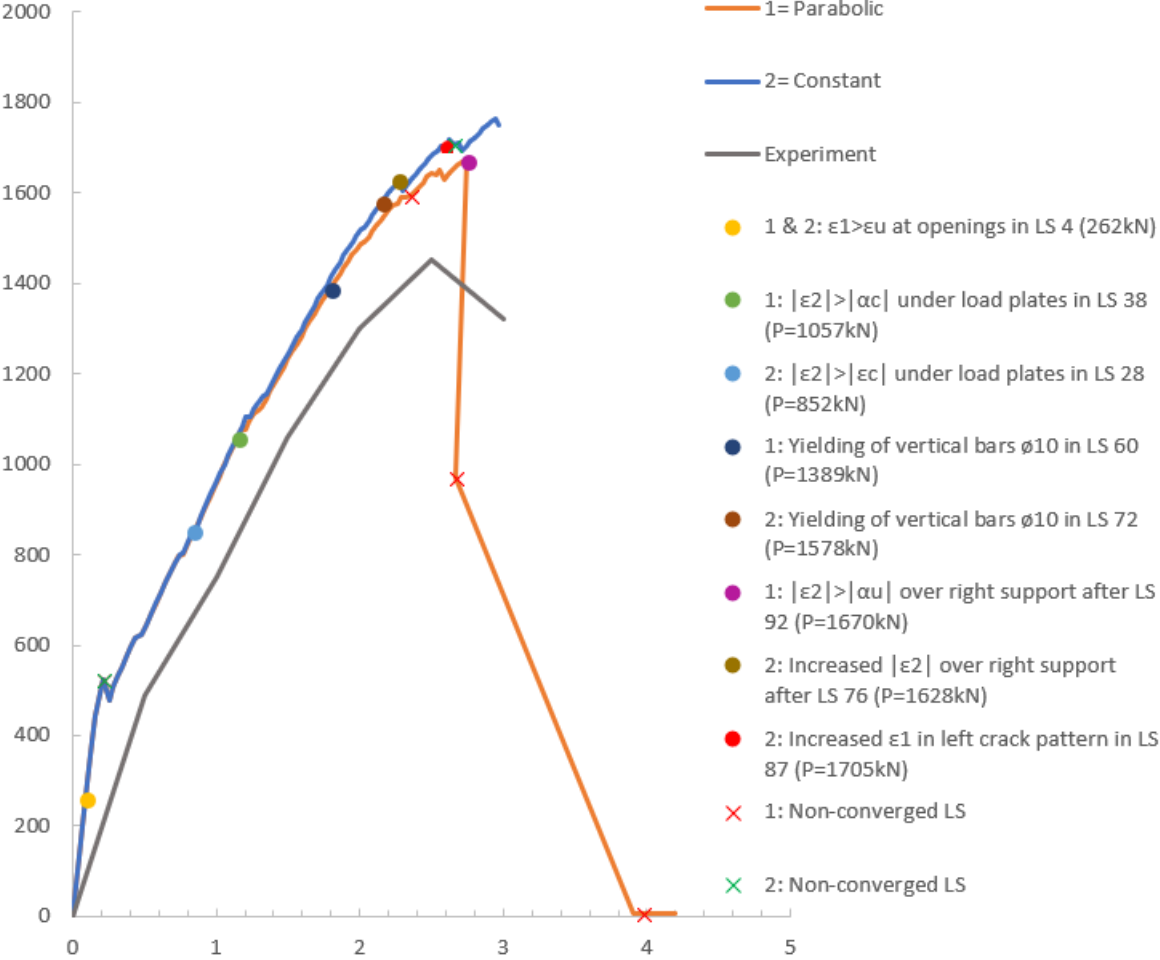


Figure 3.39: T1-0. LDCs from the NLFEAs with different compressive behaviour functions, and the experimental LDC. The numerical LDCs are marked with essential observations that affected the global behaviour.

In Analysis 2, the load dropped after the non-converging LS 89. Based on the values given in Table 3.39, the amount of inactive cracks increased from 40% to 46% from LS 88 to LS 89, similar as in Analysis 1 at peak load level. In these LSs, 99% of the cracks were open. The amount of cracks continued to grow until the last step, LS 100, where 47% of the cracks did not transfer load. The two compressive behaviour approaches resulted in a similar crack pattern in T1-0, as shown in Figure 3.40.

Table 3.39: T1-0. Summary of crack logging with constant compressive behaviour function of concrete, given by DIANA.

Analysis - step number	Crack	Open	Closed	Active	Inactive	Arises	Re-opens	Closes
2-LS 88	1909	1892	17	1145	764	7	0	0
2-LS 89	1918	1899	19	1027	891	9	0	2
2-LS 100	2047	2020	27	1075	972	23	1	6

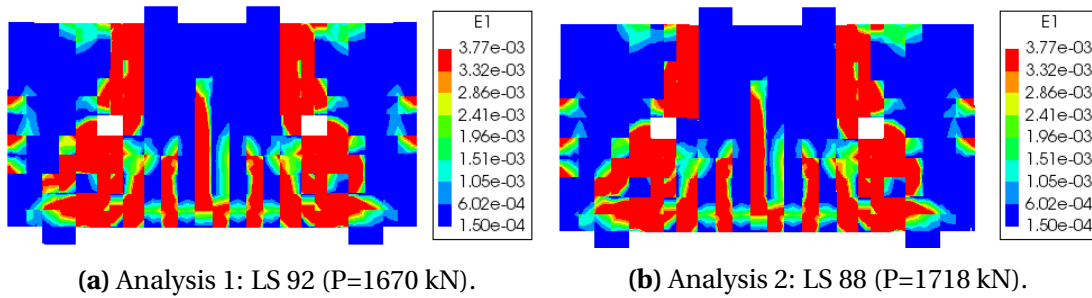


Figure 3.40: T1-0. Principal tensile strain plots from the NLFEAs with different compressive behaviour functions. Red colour= $\epsilon_1 > \epsilon_u$.

In Analysis 2, with constant compressive behaviour function of concrete, the compressive capacity remained constant after the elastic regime was exceeded. Consequently, only one strain value is used to describe the stress-strain curve of this approach. ϵ_c , given in Table 3.40, indicates the strain value at the point when the material started to crush in Analysis 2. The corresponding value in Analysis 1 was called α_c , and is given in Table 3.26. Crushing below the load plates occurred earlier in Analysis 2 than in Analysis 1. Crushing in Analysis 2 started at the inner and outer corners below the load plates in LS 27. This corresponded to an applied load of 828 kN. The concrete started to crush in LS 38 for Analysis 1, with an applied load of 1057 kN.

Table 3.40: T1-0. Specific compressive strain values for constant compressive behaviour function of concrete.

Strain	Formula	Strain value	Compressive stress
ϵ_c	$\frac{f_c}{E_c}$	$-1.72 \cdot 10^{-3}$	$\sigma = f_c$

The yielding behaviour was similar for the two analyses. The horizontal bars of $\phi 6$ above the openings exceeded the ultimate strain value of $2.10 \cdot 10^{-2}$ in LS 88, similar as in Analysis 1. The observations regarding the first yielding of the different bars are summarized in Table 3.41. In Figure 3.39, only observations that were significantly different in the two analyses are marked. The vertical stirrups of $\phi 10$ started to yield in the same location as in Analysis 1, with a different load level. The stresses in the reinforcement increased throughout Analysis 2, while they were drastically reduced after the peak in Analysis 1. In Analysis 2, the main longitudinal bars reached a maximum stress of 587 N/mm^2 in LS 99, which was higher than in Analysis 1 (564 N/mm^2).

Table 3.41: T1-0. Observations of yielding of reinforcement and its representative load levels from NLFEA with two different concrete compressive behaviour functions.

Observation, Location	Applied Load Analysis 1	Applied Load Analysis 2
Yielding of horizontal bars $\phi 6$, lower bars, midspan	622 kN	622 kN
Yielding of vertical bars $\phi 6$, outside openings	1448 kN	1489 kN
Yielding of horizontal bars $\phi 10$, Above openings	952 kN	956 kN
Yielding of vertical bars $\phi 10$, Below openings	1389 kN	1578 kN

The obtained failure modes and failure loads for T1-0 with the two different concrete compressive behaviour functions are given in Table 3.42. In Analysis 2, the LDC showed small load drops in LSs 77, 89 and 100. However, except in these LSs, the applied load increased monotonically throughout the analysis. The highest load taken up by T1-0 with Analysis 2 was 1764 kN in LS 99. Consequently, as given in Table 3.42, T1-0 in Analysis 2 did not achieve a clear failure mode, hence no failure load was detected. However, a diagonal crack pattern combined with crushing of the concrete was achieved, similarly as in Analysis 1.

Table 3.42: T1-0. Failure mode and failure load from the NLFEAs with different compressive behaviour functions.

Analysis	Failure Mode	Failure Load	Modelling Uncertainty ($\frac{R_{exp}}{R_{NLFEA}}$)
1	Shear Compression Failure	1670 kN	0.87
2	No Failure*	—	—

* Shear cracking but no failure due to the fact that the concrete did not soften in compression.

Shear Retention Model

In order to investigate the sensitivity related to the shear behaviour of the concrete, three shear retention models were tested on T1-0. A damage based shear retention model was selected for the standard solution strategy, elaborated in Table 2.10. Additionally, the response of T1-0 with two different constant shear retention models were investigated. The shear retention factors for the respective constant approaches were $\beta=0.1$ and $\beta=0.01$.

Throughout this sensitivity study, the following designations will be used as references for the three NLFEAs of T1-0 with different shear behaviour approaches:

Analysis 1: Damage based shear retention model.

Analysis 2: Constant shear retention model with $\beta=0.1$.

Analysis 3: Constant shear retention model with $\beta=0.01$.

Figure 3.41 shows the different LDCs from NLFEAs of T1-0 with the various shear retention models. The LDCs are marked with crosses that indicate non-converged LSs. Analysis 2 had only one such step; LS 24, while Analysis 3 had five non-converged steps; LS 8, 16, 35, 89 and 92.

The principal tensile and compressive strain values are equal for all analyses, and are given in Tables 3.23 and 3.26, respectively.

The numerical LDCs are also marked with dots that indicate observations of tensile and compressive behaviour of concrete for the respective analyses. The first microcracks were observed at identical load levels and in the same areas for the three analyses, when $\epsilon_1 > \epsilon_{peak}$. All LDCs showed a small load drop after the first fully open cracks were generated, when $\epsilon_1 > \epsilon_u$.

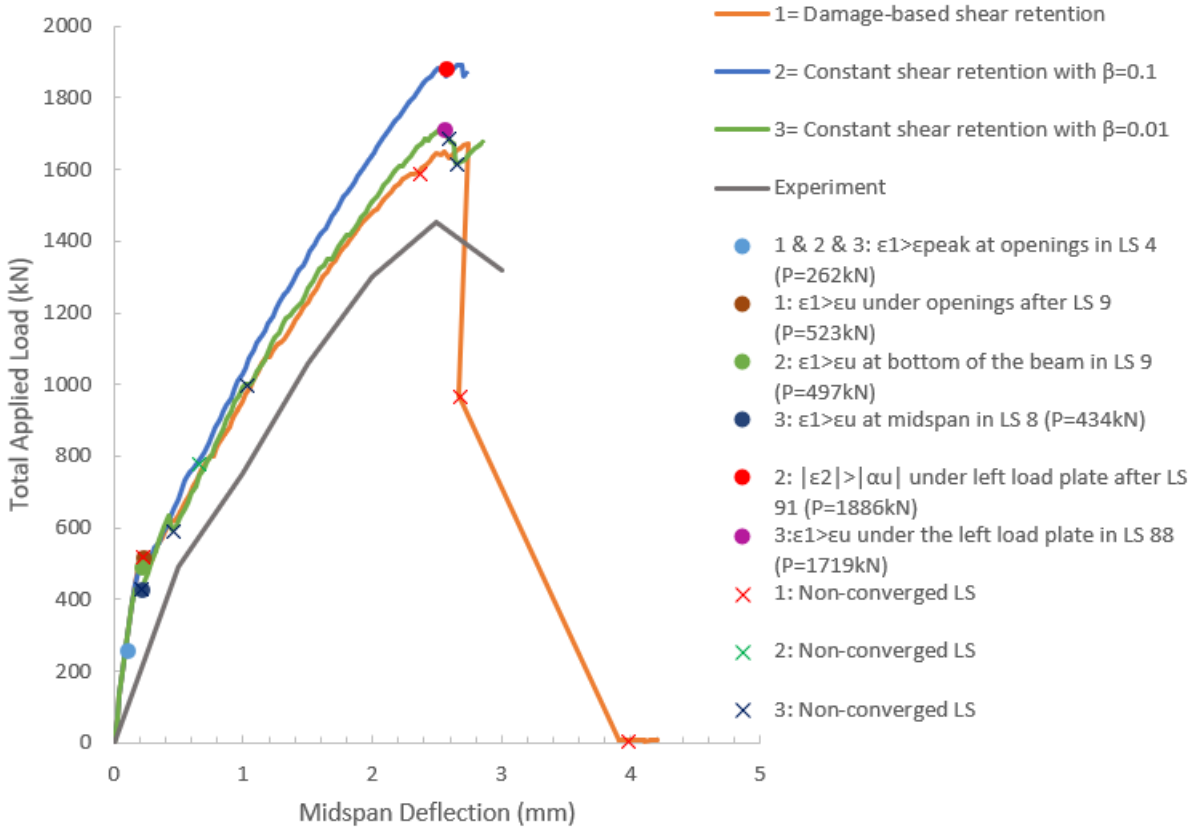


Figure 3.41: T1-0. LDCs from the NLFEMs with different shear retention models, and the experimental LDC. The numerical LDCs are marked with essential observations that affected the global behaviour.

Figure 3.42 shows principal tensile strain plots for some essential LSs in the three analyses. Red colour indicates areas with fully open cracks. The sub-figures represent the LSs when the first fully open cracks developed and when a final crack pattern was established.

In Analysis 2, the first fully open cracks appeared in the bottom of the beam as flexural cracks, as shown in Figure 3.42c. This caused a small load drop in the LDC for Analysis 2 and a non-converged LS followed. Further, fully open cracks developed in a diagonal path, as shown in Figure 3.42d.

In Analysis 3, the first fully open cracks were observed in the midspan of the beam, as shown in Figure 3.42e. Diagonal cracks developed in later LSs, and the final crack pattern was similar as for Analysis 1, as shown in Figure 3.42f. Analysis 3 resulted in less comprehensive flexural cracks in the final crack pattern than for Analysis 1 and 2. A peak in the LDC for Analysis 3 was observed after LS 88 (P=1719 kN). At this point the concrete at the outer corner

of the left load plate was completely softened in tension, meaning that this area had achieved principal tensile strains larger than ϵ_u . However, after a few descending LSs, T1-0 continued to take up more load throughout the analysis.

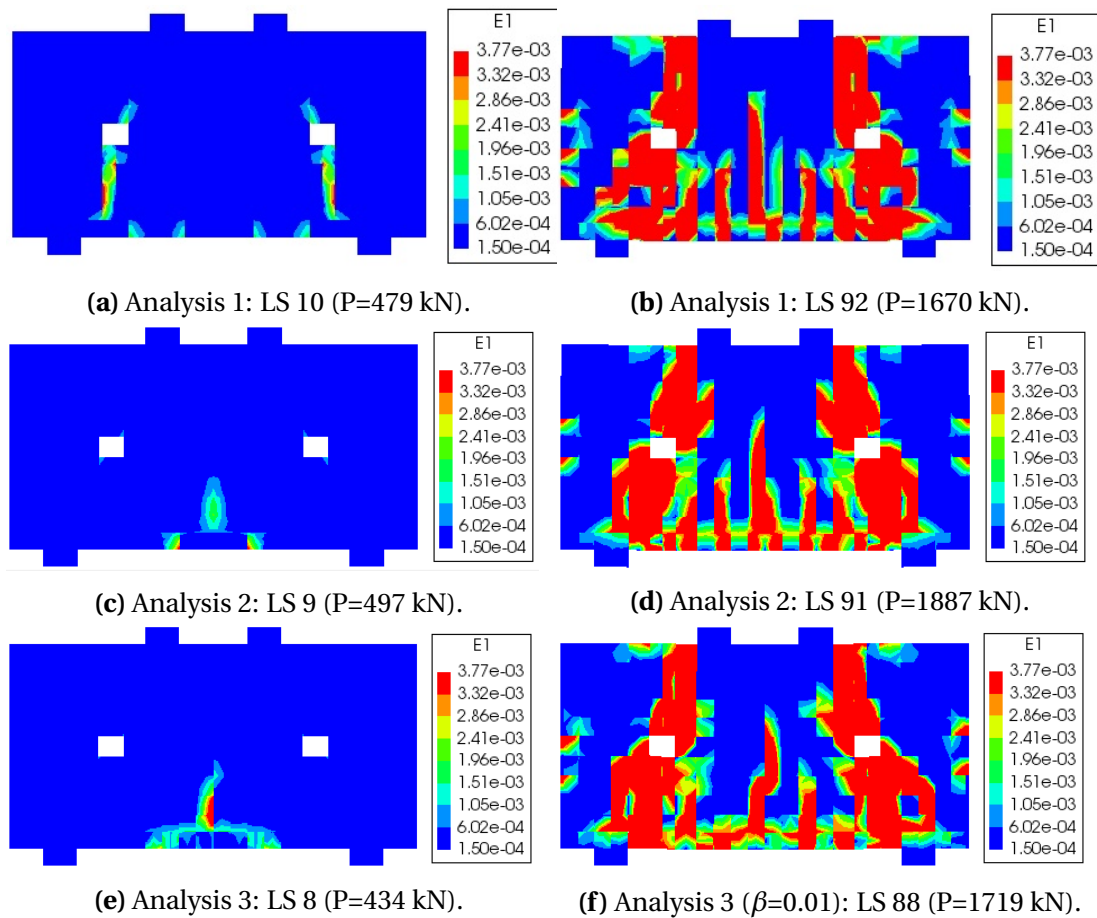


Figure 3.42: T1-0. Principal tensile strain plots from essential LSs in the NLFEAs with different shear retention models. Red colour= $\epsilon_1 > \epsilon_u$. Blue colour= $\epsilon_1 < \epsilon_{peak}$.

The compressive behaviour of T1-0 was also affected by the choice of shear retention model. However, the concrete started to crush below the load plates for all analyses, and at similar load levels. For Analysis 2 and 3, it started to crush at the outer corners beneath the load plates. As opposed to in Analysis 1, neither Analysis 2 nor Analysis 3 achieved compressive strains larger than $|\alpha_u|$ above the right support. Consequently, these areas of T1-0 did not get completely softened in compression when a constant shear retention model was used. However, the concrete got completely softened in compression underneath the outer corners of the load plates in Analysis 2 and 3, as shown in Figure 3.43. In Analysis 2, a small area of concrete was completely softened in compression in LS 92 (P=1861 kN), as shown in Figure 3.43a. The area of crushed concrete increased throughout the analysis.

In Analysis 3, the concrete got completely softened in compression in a small area in the outer corner of the left load plate in LS 89 (P=1693 kN). This is shown in Figure 3.43b. The crushed area increased throughout Analysis 3, similarly as in Analysis 2.

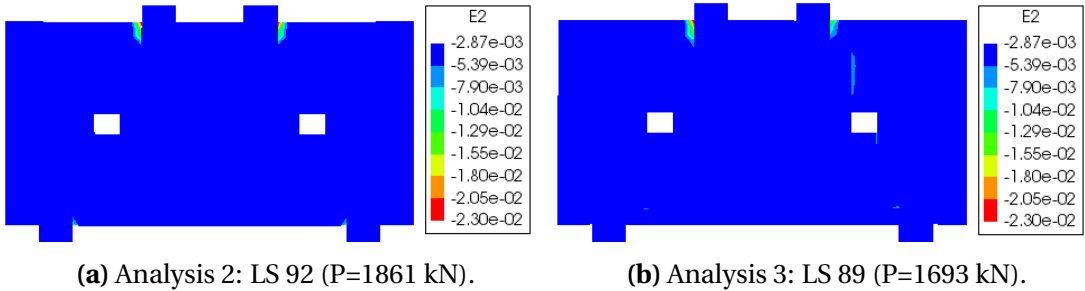


Figure 3.43: T1-0. Principal compressive strain plots from the NLFEMs with constant shear retention. Red colour= $|\epsilon_2| > |\alpha_u|$. Blue colour= $|\epsilon_2| < |\alpha_c|$

The main observations regarding reinforcement yielding in T1-0 are marked with dots in the numerical LDCs, as shown in Figure 3.44, and summarized in Table 3.43. In both Analysis 2 and 3, the reinforcement stresses increased throughout the analysis. In the final LSs, rebars were yielding in the same areas in all analyses, which mainly were exposed to cracking of concrete.

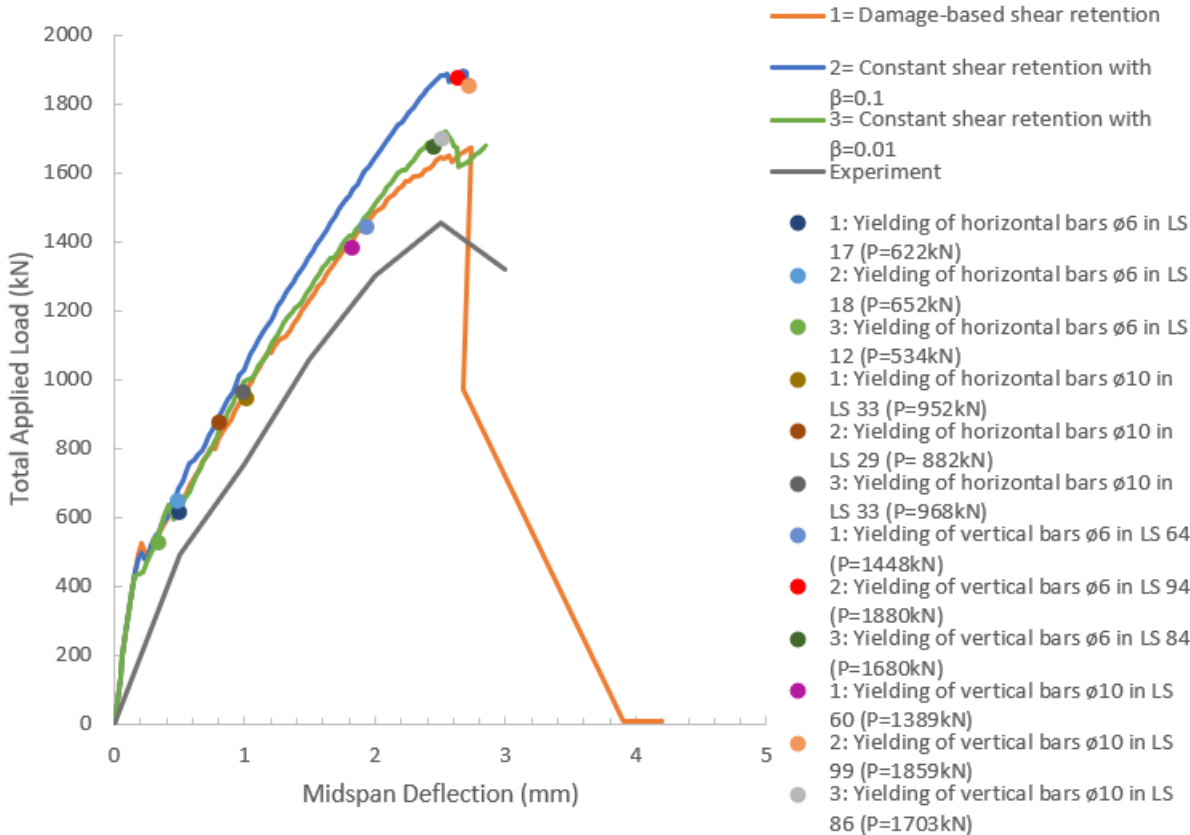


Figure 3.44: T1-0. LDCs from the NLFEMs with different shear retention models, and the experimental LDC. The numerical LDCs are marked with observations of reinforcement yielding.

Table 3.43: T1-0. Observations of reinforcement yielding and its representative load levels from the NLFEAs with different shear retention models.

Observation, Location	Applied Load Analysis 1	Applied Load Analysis 2	Applied Load Analysis 3
Yielding of horizontal bars $\phi 6$, lower bars, midspan	622 kN	652 kN	534 kN
Yielding of vertical bars $\phi 6$, variable location	1448 kN	1880 kN	1680 kN
Yielding of horizontal bars $\phi 10$, Above openings	952 kN	882 kN	968 kN
Yielding of vertical bars $\phi 10$, variable location	1389 kN	1859 kN	1703 kN

In all analyses, yielding was first observed in the lower horizontal bars of $\phi 6$, located in the midspan of the beam where flexural cracks developed. The yielding of the horizontal bars of $\phi 10$ was observed at similar load levels in all analyses. These bars yielded in the same areas as exposed to diagonal cracking around the openings. The yielding of vertical stirrups of $\phi 6$ was observed late in the analyses with constant shear retention. Yielding was observed in the stirrups close to the openings in LS 94 ($P=1880$ kN) and in LS 84 ($P=1680$ kN), in Analysis 2 and 3, respectively.

None of the bars of $\phi 6$ had strain values close to the ultimate strain ($2.10 \cdot 10^{-2}$) in neither Analysis 2 nor 3. In Analysis 2, the highest strain value was observed in the lower horizontal bars in the midspan of the beam in LS 97 with a maximum strain equal to $1.32 \cdot 10^{-2}$. In Analysis 3, the maximum strain was $1.45 \cdot 10^{-2}$ in LS 89. The latter was observed in the horizontal bars above the right opening, at the same location as where the respective bars exceeded the ultimate strain in Analysis 1. None of the strain values in the $\phi 10$ -bars were close to exceed the ultimate strain value of $3.80 \cdot 10^{-2}$. The main longitudinal reinforcement obtained maximum stresses of 564, 673, 610 N/mm² in Analysis 1, 2 and 3, respectively. All analyses were far from the yield strength of 803 N/mm².

In order to detect failure modes of T1-0 in these three analyses, all observations were taken into account. In Analysis 2, it was observed several load drops in the LDC in the end of the analysis. However, in the post-process investigation, it was not observed any clear failure mechanism. The concrete in T1-0 was completely softened in compression at the outer corners of both load plates, simultaneously as a small load drop was observed in the response curve. The reinforcement stresses increased throughout the analysis, but no areas achieved the respective ultimate strain value. Hence, the applied load continued to increase throughout the analysis and no clear failure was detected.

Analysis 3 did not achieve a clear failure mechanism of T1-0 either. The LDC in this analysis had several small load drops in the last LSs, similarly as in Analysis 2. These drops were constituted by completely softened concrete in compression, crack propagation and yielding in some reinforcement bars.

T1-0 was able to resist a larger load with a constant shear retention factor of $\beta=0.1$ than $\beta=0.01$. The maximum load taken up by T1-0 in Analysis 2, with $\beta=0.1$, was 1894 kN, while it was 1719 kN in Analysis 3, with $\beta=0.01$. Compared to Analysis 1, when a damage based shear retention model was used, both constant shear retention models resulted in larger capacity

of T1-0. These results are summarized in Table 3.44, but as no failure mechanisms were observed, the failure loads could not be stated.

Table 3.44: T1-0. Failure mode and failure load from the NLFEEAs with different shear retention models.

Analysis	Failure mode	Failure Load	Modelling Uncertainty ($\frac{R_{exp}}{R_{NLFEEA}}$)
1	Shear Compression Failure	1670 kN	0.87
2		No Failure*	—
3		No Failure*	—

* Shear cracking but no failure due to the fact that the shear capacity remained constant.

3.3 Case Study 3

The following case study is a numerical approach to the experimental test of RCxcb, collected from paper *Flexural Behaviour and Strength of Reinforced Concrete Beams with Multiple Transverse Openings* [Aykac et al., 2014]. The FE model of RCxcb will be referred to as *RCxcb* throughout this section. Both 2D and 3D numerical models of RCxcb were developed in DIANA.

3.3.1 NLFEA Results obtained by the selected Solution Strategy

Post-analysis checks of the 2D and 3D NLFEAs of RCxcb were conducted in order to determine the numerical responses and failure modes. This section will present results obtained by the selected solution strategy, specified in Table 2.10. However, additional selections was necessary for the 3D model. Consequently only the 2D model of RCxcb is used to verify the selected solution strategy. However, results for both models will be presented and compared in this section.

Figures 3.45 and 3.46 compare the LDCs obtained in the experiment and in the numerical analyses with 2D and 3D modelling, respectively. LDCs are marked with dots that represent essential observations that constituted specific responses in the FE model. Red crosses indicate non-converged LSs. As shown in the curves, non-converged LSs followed post peaks for both models. The highest load taken up by the 2D model was 250 kN in LS 8, at a corresponding deflection of 19.3 mm. The highest load taken up by the 3D model was 242 kN in LS 7, at a deflection of 17.2 mm. Consequently, after these LSs, a failure mechanism was formed.

Load transfer and distribution between the supports are shown in Figures 3.47 and 3.48, for 2D and 3D modelling, respectively. A more detailed representation of the load distribution are presented in Table 3.45. After the peak loads were reached, and failure mechanisms were formed, both models experienced a reduced load transfer to the supports. However, the load path to the left support in the 2D model still had some load transferring capacity. Yet, non of the supports were able to take up any additional forces.

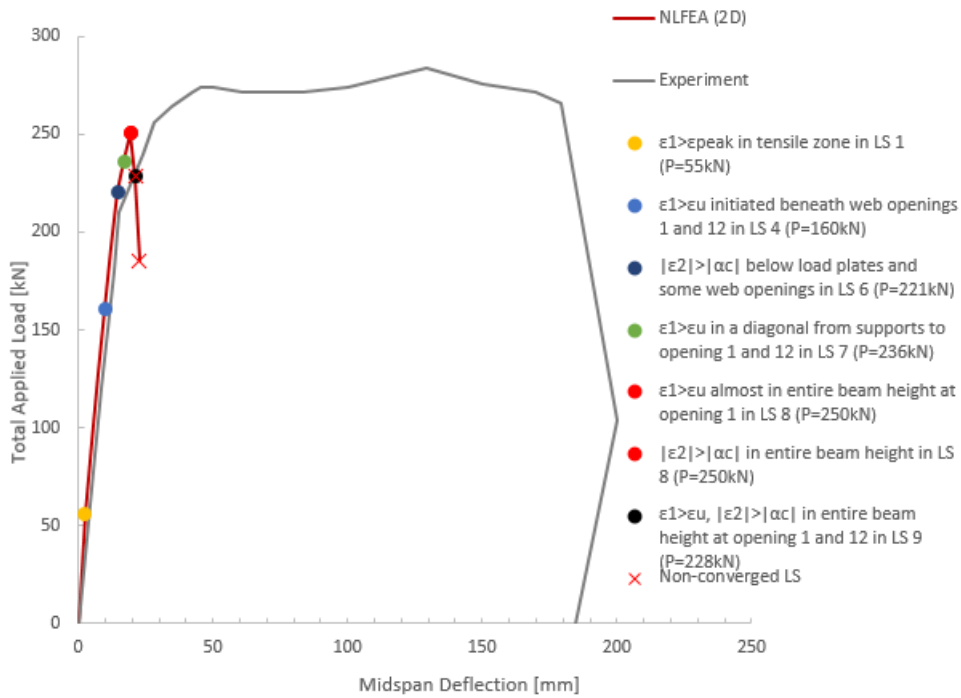


Figure 3.45: RCxcb (2D). LDC from the numerical solution strategy and the experiment. The numerical LDC is marked with essential observations that affected the global behaviour.

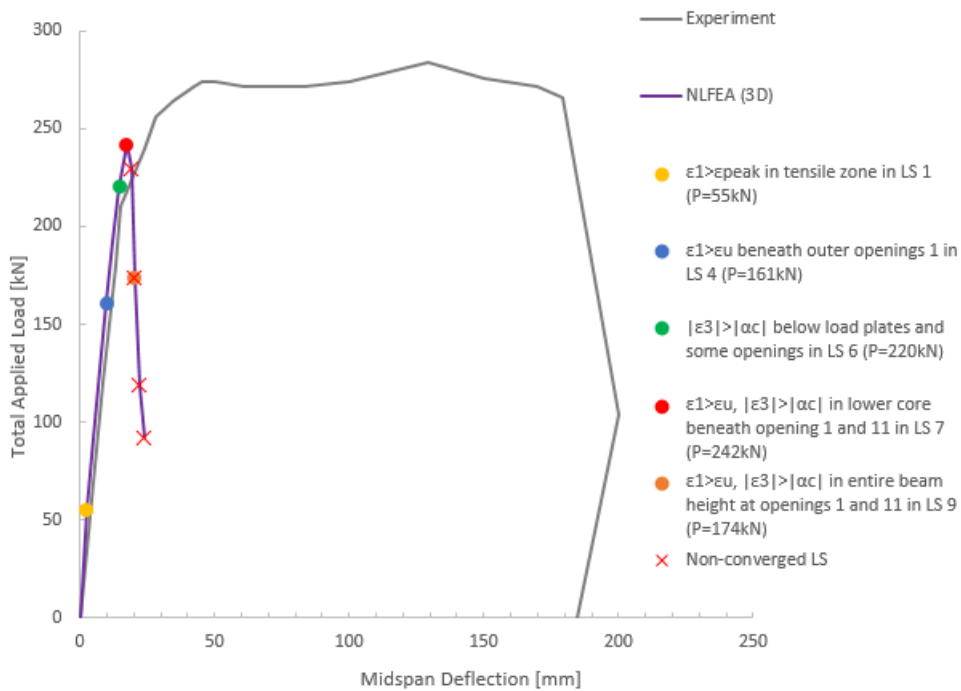


Figure 3.46: RCxcb (3D). LDC from the numerical solution strategy and the experiment. The numerical LDC is marked with essential observations that affected the global behaviour.

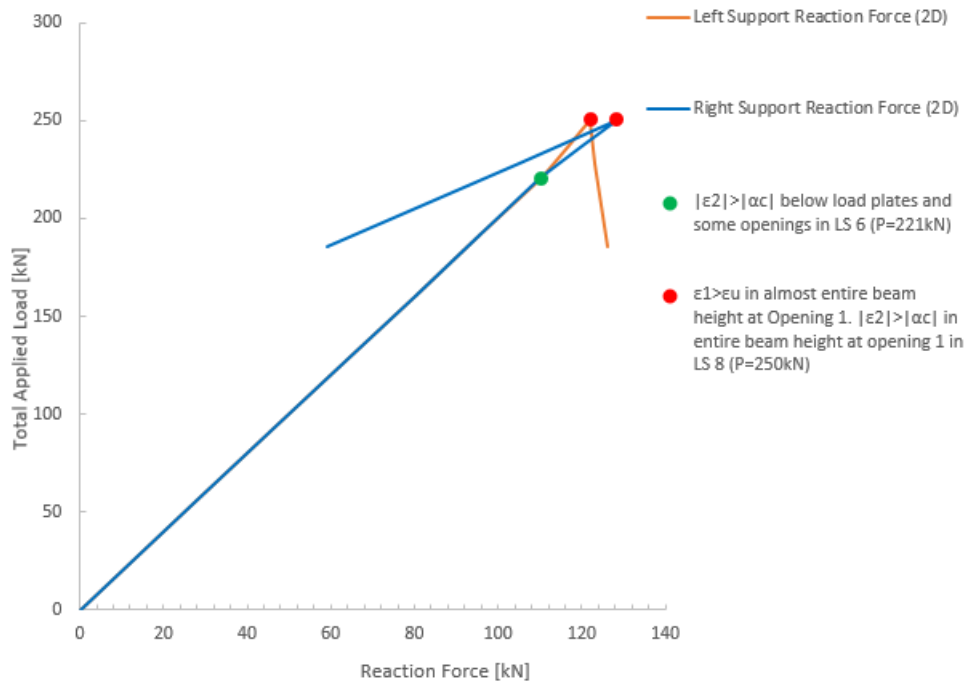


Figure 3.47: RCxcb (2D). Support reactions against total applied load from the numerical solution strategy. The curves are marked with essential observations that affected the global behaviour.

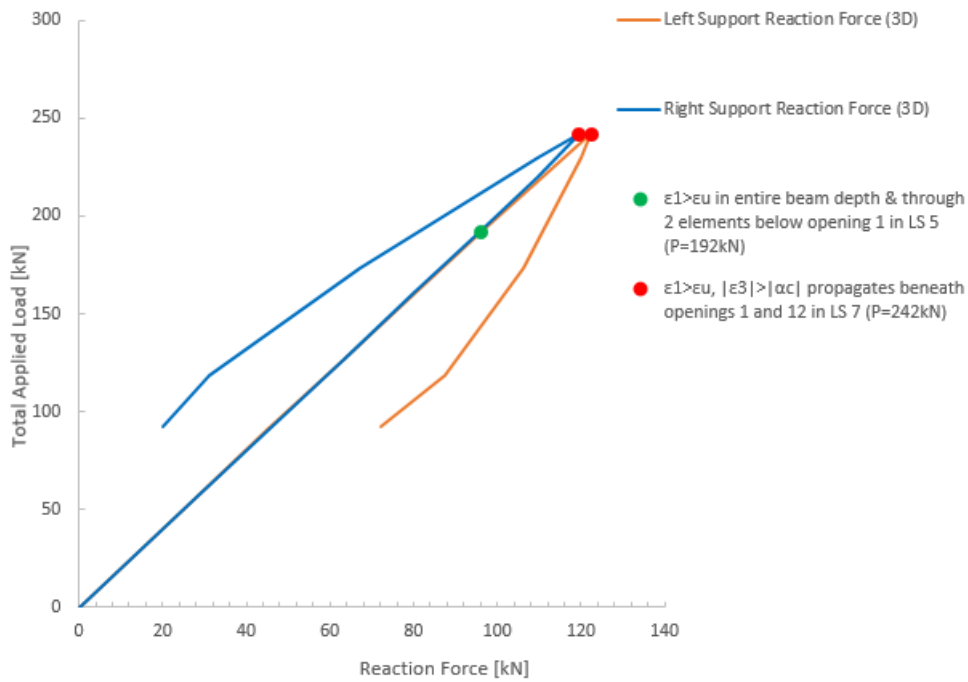


Figure 3.48: RCxcb (3D). Support reactions against total applied load from the numerical solution strategy. The curves are marked with essential observations that affected the global behaviour.

Table 3.45: RCxcb. Reaction forces and amount of force distribution between supports in numerical models.

Analysis	Peak Load Step	Peak Load Value	Left Reaction Force	Right Reaction Force
2D Model	8	250 kN	122 kN (48.8% of peak load)	128 kN (51.2% of peak load)
3D Model	7	242 kN	122kN (50.6% of peak load)	120 kN (49.4% of peak load)
Analysis	Last Load Step	Last Load Value	Left Reaction Force	Right Reaction Force
2D Model	10	186 kN	126 kN (68% of last load)	59 kN (32% of last load)
3D Model	11	92kN	72 kN (78.4% of last load)	20 kN (21.6% of last load)

3.3.1.1 Concrete Cracking

Microcracks were formed in the numerical models when the principal tensile strain, ϵ_1 , exceeded the peak tensile strain, ϵ_{peak} , given in Table 3.46. Further, cracks were considered as fully open when the ultimate tensile strain, ϵ_u , from the same table was exceeded. At this point the concrete was completely softened in tension, meaning that the material did not have any remaining tensile capacity.

Table 3.46: RCxcb. Specific tensile strain values for MC2010 TS curve.

Strain	Formula	Value	Tensile stress
ϵ_{peak}		$1.50 \cdot 10^{-4}$	$\sigma = f_{ctm}$
ϵ_u	$5 \cdot \frac{G_F}{f_{ctm} \cdot h}$	$9.52 \cdot 10^{-3}$	$\sigma = 0$

RCxcb 2D Model:

The main crack observations from the NLFEA of RCxcb (2D Model) are listed in Table 3.47.

Table 3.47: RCxcb (2D). Crack observations from the numerical solution strategy.

LS	Observation	Location	Total applied load
1	First microcracks appeared	Bottom of beam and around openings	55 kN
5	Horizontal discrete cracks	Beneath load plates	192 kN
7	Horizontal discrete cracks	Beam ends	236 kN
7-8	Fully open cracks	Beneath opening 1 and 12	236-250 kN
8-9	Fully open cracks	Entire beam height at opening 1 and 12	250-228 kN

Microcracks were observed in LS 1 at an applied load, P, of 55 kN. Principal tensile strain plot from this LS is shown in Figure 3.49a, where red colour indicates tensile strains larger than ϵ_{peak} . Here microcracks, with a principal crack width of $3.85 \cdot 10^{-2}$ mm, were initiated. Flexural vertical cracks occurred in the tensile zone of the beam, and cracks with an angle of 45° were initiated at the outer openings, going towards load- and support plates, as shown in Figure 3.50a. The first horizontal cracks occurred in LS 3, at an applied load of 127 kN, and were located beneath the two middle load plates. In LS 5 (P=195 kN), horizontal cracks appeared under all load plates.

In LS 4 (P=160 kN) fully open cracks were observed beneath opening 1 and 12. From LS 7 towards the peak load of 250 kN, in LS 8, fully open cracks propagated from the opening edge towards the bottom of the beam, at openings 1 and 12. This is shown in the principal tensile strain plots in Figures 3.49b and 3.49c, where red colour indicates tensile strains larger

than ϵ_u , while blue colour represents strains less than ϵ_{peak} . The maximum principal crack width was generated in LS 8, with a width of 4.74 mm. From LS 8 to LS 9 (P=228 kN), fully open cracks propagated through the entire beam height at openings 1 and 12, shown in Figure 3.49d. The crack strain patterns and crack directions obtained in LSs 1, 8 and 10 are shown in Figures 3.50a, 3.50b and 3.50c. Horizontal crack strains were established beneath the load plates, in some posts, and under some openings. The maximum principal crack width increased from 4.74 mm in LS 8 to 475.7 mm in LS 9.

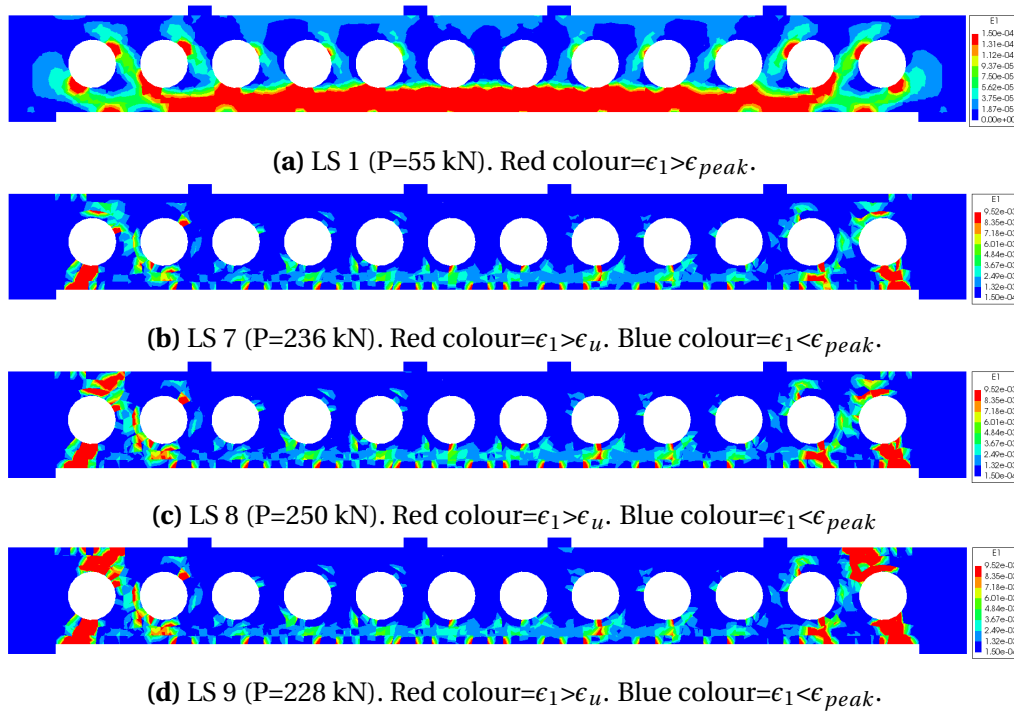


Figure 3.49: RCxcb (2D). Principal tensile strain plots from essential LSs in the NLFEA with the selected solution strategy.

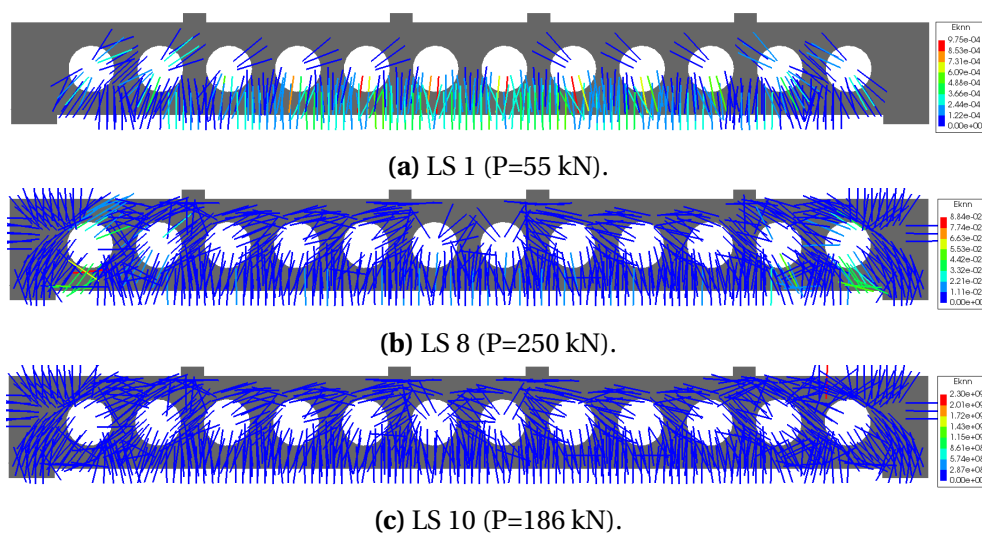


Figure 3.50: RCxcb (2D). Crack pattern development from essential LSs in the NLFEA with the selected solution strategy. Auto-scaled colour plot.

RCxcb 3D Model:

The main crack observations of RCxcb (3D Model) obtained by the selected solution strategy are listed in Table 3.48.

Table 3.48: RCxcb (3D). Crack observations from the numerical solution strategy.

LS	Observation	Location	Total applied load
1	First microcracks appeared	Bottom of beam and around openings	55 kN
4	Horizontal discrete cracks	Beneath load plates	161 kN
7	Horizontal discrete cracks	Beam ends	242 kN
7	Fully open cracks	Beneath opening 1 and 11	242 kN
7-9	Fully open cracks	Entire beam height at opening 1 and 11	242-174 kN

The appearance of cracks in LS 1 ($P=55$ kN) and LS 2 ($P=92$ kN) were identical as for the 2D model. The principal tensile strain plot from LS 1 is illustrated in Figure 3.52a. The first horizontal cracks occurred in LS 3 ($P=127$ kN) in the 3D model. It was observed beneath the two middle load plates and the left load plate. In LS 4 ($P=161$ kN) horizontal cracks appeared under all load plates.

In LS 4 fully open cracks were most prominent beneath opening 1. In the same LS fully open cracks were observed in a small area under opening 11 and 12. From LS 7 to 8 ($P=230$ kN) fully open cracks from the opening edge towards the lower beam edge under openings 1 and 11 were observed. The tensile strain plot from LS 7 is shown in Figure 3.51c. Additionally, fully open cracks propagated from opening 11 towards the upper edge of the beam. From LS 8 to LS 9, fully open cracks propagated in the entire beam height at opening 1 and 11, as shown in Figure 3.51c.

The crack strain patterns obtained in LS 1, 7 and 11 are shown in Figures 3.52a, 3.52b and 3.52c. As for the 2D model, horizontal cracks were established beneath load plates, in some posts, and beneath some openings, as visualized in the figures.

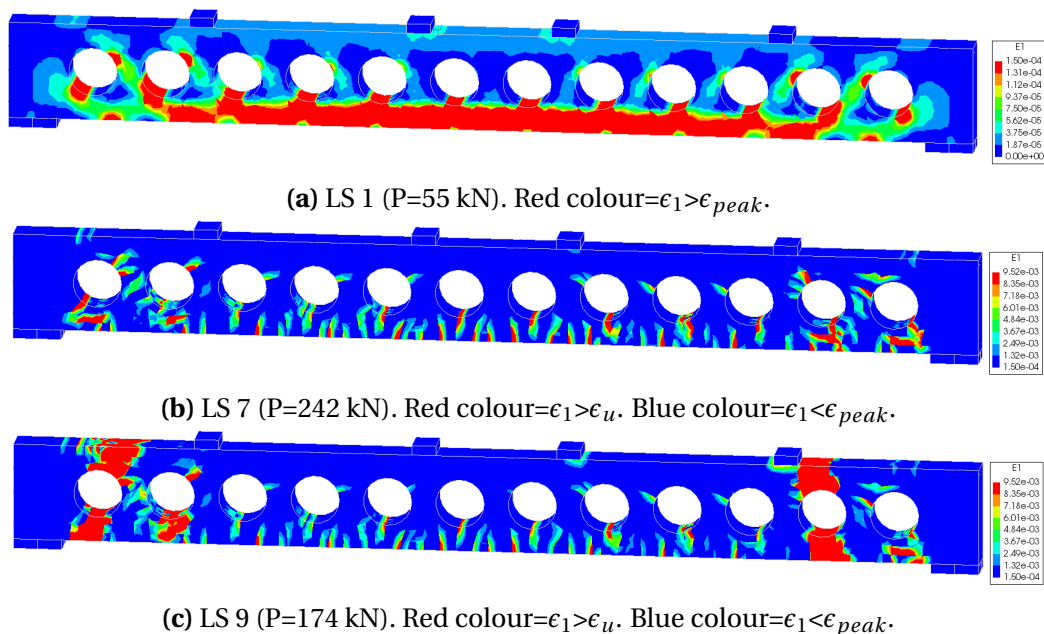


Figure 3.51: RCxcb (3D). Principal tensile strain plots for essential LSs in the NLFEA with the selected solution strategy.

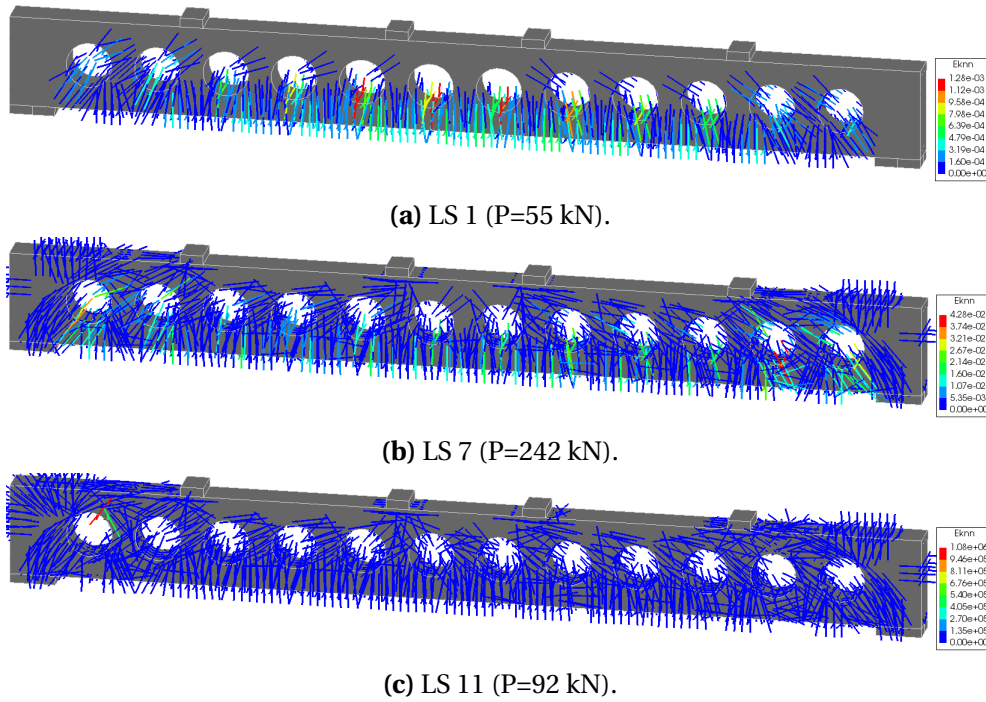


Figure 3.52: RCxcb (3D). Crack pattern development in essential LSs in the NLFEA with the selected solution strategy. Auto-scaled colour plot.

A summary of the crack situation from the peak LSs and the post peak LSs in the NLFEAs of both the 2D and 3D models are shown in Table 3.49. The data was collected from an output file in DIANA.

Table 3.49: RCxcb (2D and 3D). Summary of crack logging at peak- and post peak load, given by DIANA. The numbers indicate the amount of cracks.

Analysis - step number	Crack	Open	Closed	Active	Inactive	Arises	Re-opens	Closes
2D - LS 8	7390	7314	76	5346	2044	346	7	13
2D - LS 9	7681	7556	125	2354	5327	291	13	62
3D - LS 7	134817	134034	783	103805	31012	13892	81	276
3D - LS 8	148230	146523	1707	59662	88568	13413	219	1143

3.3.1.2 Concrete Crushing

Crushing of concrete was characterized by principal compressive strains, ϵ_2 , with an absolute value larger than the absolute value of α_c , given in Table 3.50. Further increased compressive strains led to compression softening of the concrete. At the point when $|\epsilon_2| > |\alpha_u|$, from Table 3.50, the concrete was completely softened in compression.

Table 3.50: RCxcb. Specific compressive strain values for parabolic stress-strain curve.

Strain	Formula	Value	Compressive stress
α_c	$-5 \cdot \frac{1}{3} \cdot \frac{f_{cm}}{E_c}$	$-1.44 \cdot 10^{-3}$	$\sigma = f_{cm}$
α_u	$\alpha_c - \frac{3}{2} \cdot \frac{G_C}{h \cdot f_{cm}}$	$-5.66 \cdot 10^{-2}$	$\sigma = 0$

RCxcb 2D Model:

The main observations of the concrete compressive behaviour for RCxcb (2D model) are listed in Table 3.51.

The first signs of crushing in the concrete were observed beneath opening 8, 11 and 12 in LS 4 (P=160 kN), as shown in Figure 3.53a. A clear compressive path in the beam was formed with an angle of 45° from the supports to the outer load plates. This is shown in the contour plot of principal compressive strains in Figure 3.53b. In LS 6 (P=221 kN), concrete crushed locally beneath all load plates and beneath all openings, except opening 7. At peak load level, in LS 8 (P=250 kN), areas of crushed concrete propagated through the entire beam height at opening 1, and in the lower core beneath opening 11 and 12. $|e_2|$ increased in the upper central core. Post peak, in LS 9 (P=228 kN), the concrete was crushed through the entire beam height at both opening 1 and 12, as shown in Figure 3.53c. The concrete was completely softened in compression above and below opening 12 at this stage, as $|e_2| > |\alpha_u|$ in these areas. The compression softening strain path in RCxcb formed a 45° path, as shown in Figure 3.54e. RCxcb was also completely softened in compression in an area over the right support.

Table 3.51: RCxcb (2D). Observations of crushing from the NLFEA with the selected solution strategy.

LS	Observation	Location	Total applied load
4	First signs of crushing	See Figure 3.53a)	160 kN
6	Localized crushing	Beneath load plates and web openings	221 kN
8	Critical crushing	See Figure 3.53b)	250 kN
9	Critical crushing	See Figure 3.53c)	228 kN
9	Concrete fully softened in compression	Above web opening 12	228 kN

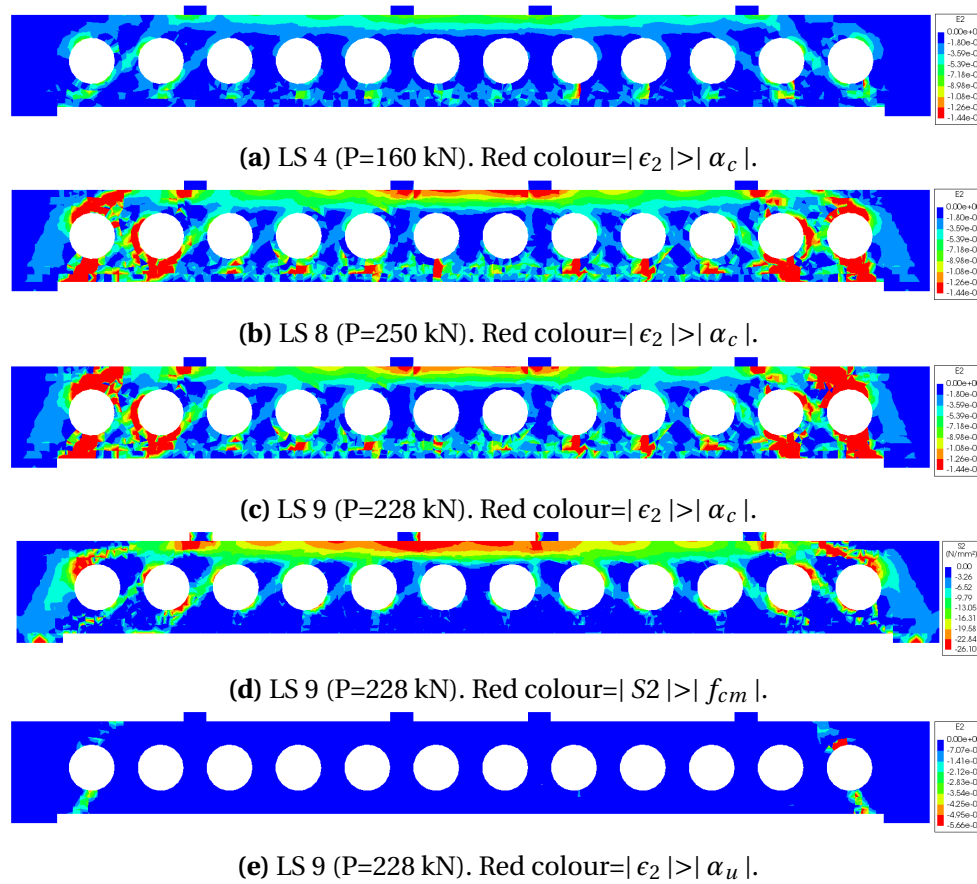


Figure 3.53: RCxcb (2D). Principal compressive strain and stress plots from essential LS in the NLFEA with the selected solution strategy.

RCxcb 3D Model:

The main observations of the concrete compressive behaviour for RCxcb (3D model) are listed in Table 3.52.

Table 3.52: RCxcb (3D). Observations of crushing from the NLFEA with the selected solution strategy.

LS	Observation	Location	Total applied load
5	First signs of crushing	See Figure 3.54a)	192 kN
7	Localized crushing	Upper central core and web openings	242 kN
7	Localized crushing	At outer openings	242kN
9	Critical crushing	See Figure 3.54c)	174 kN
10	Fully softened concrete in compression	At openings 1 and 11	119 kN

The first signs of crushing of concrete were observed beneath opening 1, 8, 9, 11 and 12 in LS 5 (P=192 kN), shown in Figure 3.54a. A compressive strut formed identically as in the 2D model. This is shown in Figure 3.54b. At the peak load level, in LS 7 (P=242 kN), the concrete was crushed beneath opening 1, 2, 11 and 12. At post peak level, in LS 9 (P=174 kN), the concrete was crushed in the entire beam height at opening 1 and 11, as illustrated in Figure 3.54c. In LS 10 (P=119 kN) the concrete was completely softened in compression in the entire beam height at opening 1 and 11, as shown in Figure 3.54e.

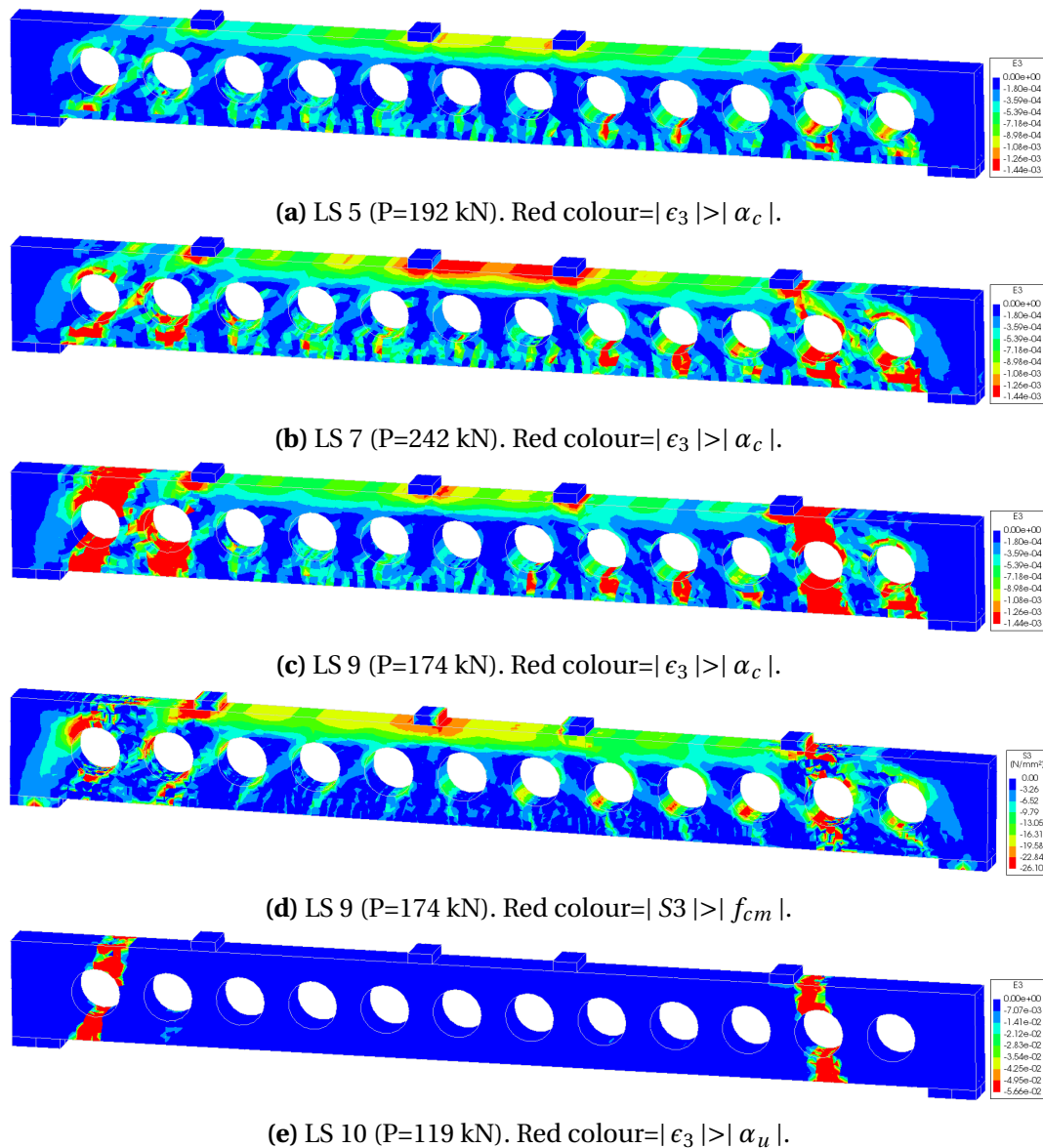


Figure 3.54: RCxcb (3D). Principal compressive strain and stress plots from essential LS in the NLFEA with the selected solution strategy.

3.3.1.3 Tension-Compression Interaction

RCxcb 2D Model

Two nodes in the concrete elements that had achieved strains that indicated fully tensile softening are highlighted in Figure 3.55. These nodes corresponded to node number 2448 and 2795 in the FE model. However, these nodes also comprised a part of the strut that transferred load from the load plate to the support. Hence this area also achieved large compressive stresses during the analysis. Figure 3.56 visualizes the development of principal compressive stresses, S2, in these nodes. The horizontal axis indicates at what load-factor the respective stress values were obtained. Load factor 0.06 indicates the point when 6% of the total prescribed deflection was applied. Consequently the decimals of the load-factor corresponds to the LS number. As shown in this figure, the maximum compressive stress was therefore reached in LS 6. The maximum absolute value was however lower than the

absolute value of the specified compressive strength for RCxcb which was 26.1 N/mm^2 .

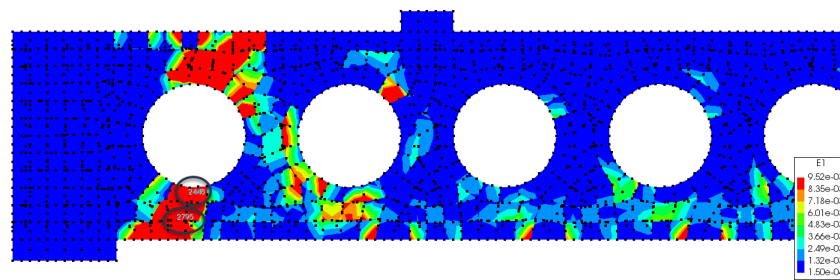


Figure 3.55: RCxcb. Principal tensile strain plot. Red colour= $\epsilon_1 > \epsilon_u$. Development of compressive stresses in highlighted nodes; 2448 and 2795, are shown in Figure 3.56.

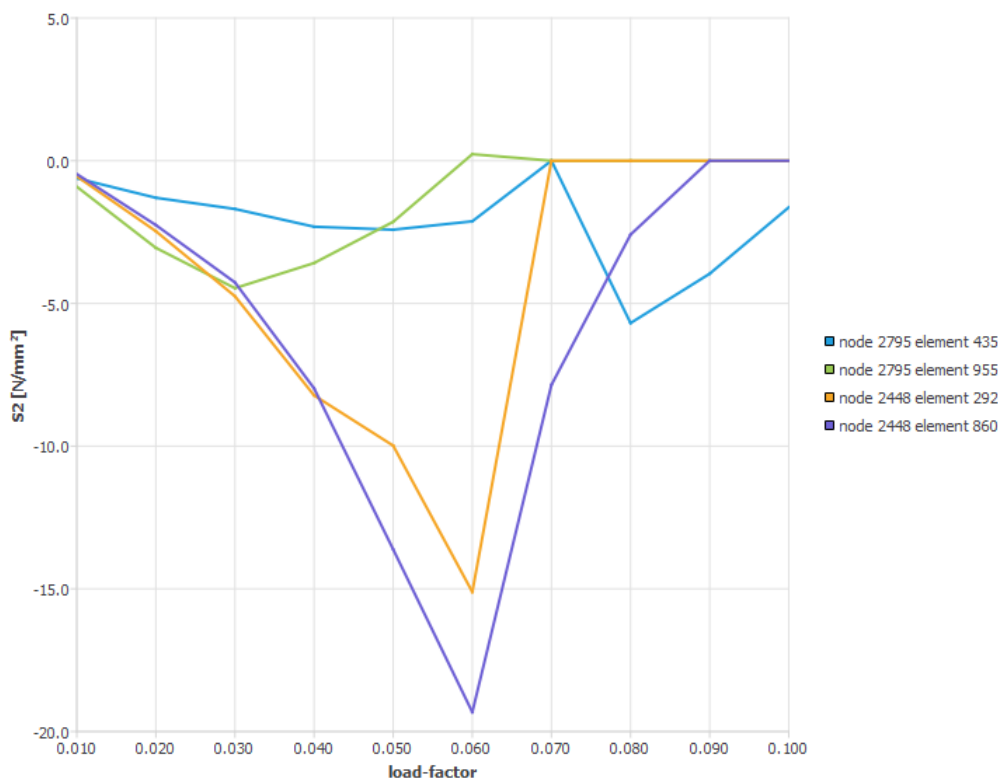


Figure 3.56: RCxcb. Table-output from DIANA, showing the development of principal compressive stresses, S2, in node 2448 and 2795, highlighted in Figure 3.55.

RCxcb 3D Model

Two nodes in the concrete elements that had achieved strains that indicated fully tensile softening are highlighted in Figure 3.57. These nodes corresponded to node number 12455 and 12456 in the FE model. However these nodes also comprised a part of the strut that transferred load from the load plate to the support. Hence this area also achieved large compressive stresses during the analysis. Figure 3.58 visualizes the development of principal compressive stresses, S2, in these nodes. As shown in this figure, the maximum compressive stress was therefore reached in LS 10. The maximum absolute value was however lower than the absolute value of the specified compressive strength.

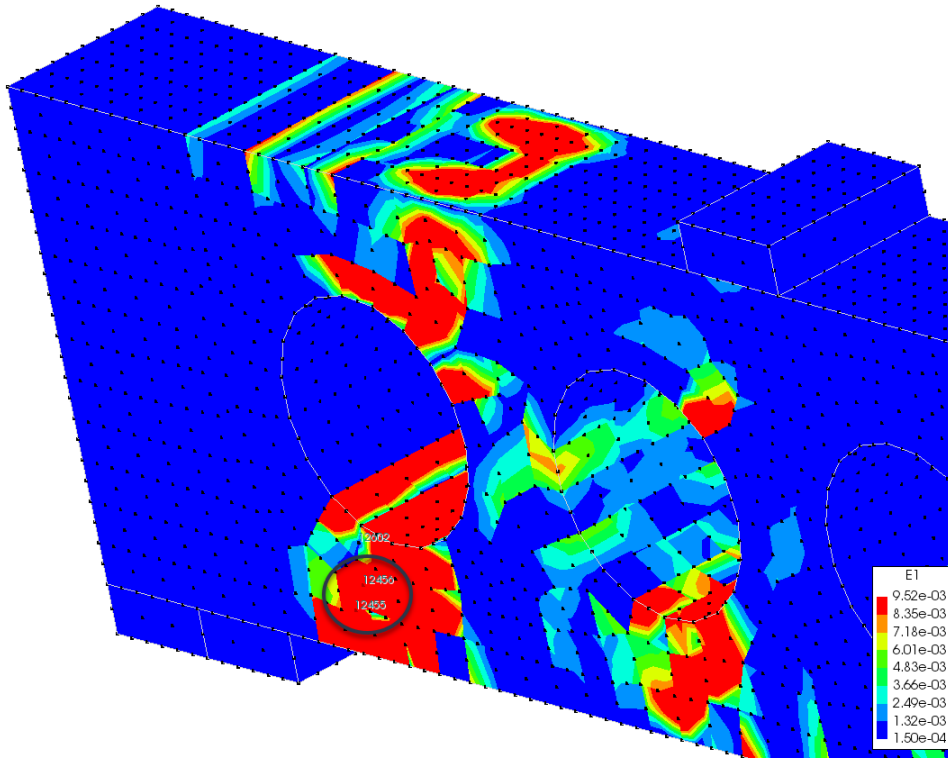


Figure 3.57: 6IT1. Principal tensile strain plot. Red colour= $\epsilon_1 > \epsilon_u$. Development of compressive stresses in highlighted nodes; 12455 and 12456, are shown in Figure 3.58.

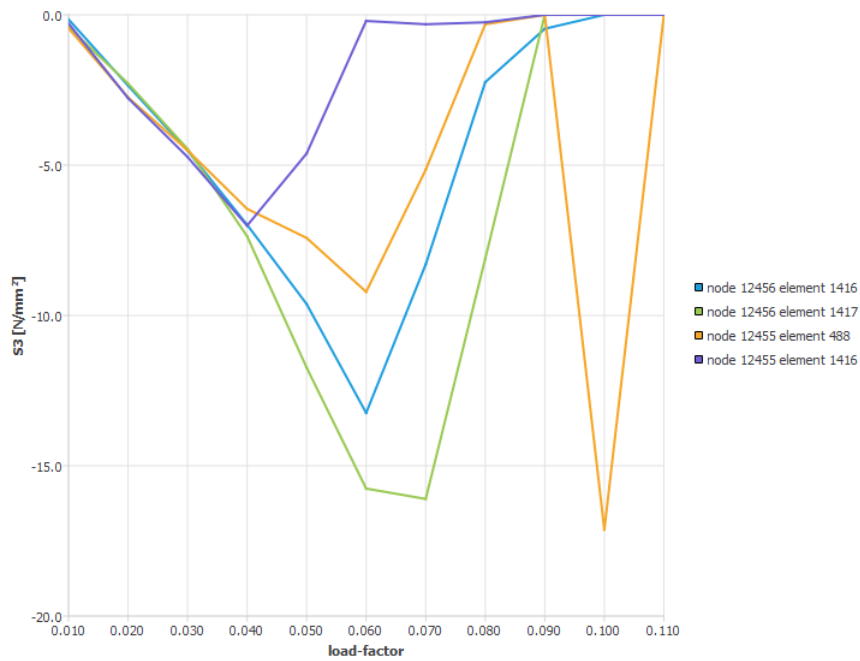


Figure 3.58: 6IT1. Table-output from DIANA, showing the development of principal compressive stresses, S2, in node 12455 and 12456, highlighted in Figure 3.57.

3.3.1.4 Yielding of Reinforcement

Yield strains and ultimate strain limits for the reinforcement in RCxcb are given in Table 2.9. The evaluated strain values in the reinforcement were extracted from the nodes of the embedded bar elements.

RCxcb 2D Model:

Figure 3.59 shows the reinforcement strains in x- and y-direction at different LSs for the RCxcb 2D model, where yielding and ultimate strain areas are marked with circles. In LS 6 yielding occurred in stirrups ($\phi 4$) beneath opening 1, 8, 11 and 12. At peak load level, in LS 8 ($P=250$ kN), yielding was detected in stirrups beneath and above opening 1, 2, 11 and 12. At post peak level, in LS 9, the mean ultimate strain was reached in stirrups beneath openings 1 and 12. The maximum registered strain value was 0.3 in a stirrup beneath openings 12 in LS 10. The maximum strain in the main longitudinal reinforcement ($\phi 12$) was observed in LS 8 with a value of $2.30 \cdot 10^{-3}$. Consequently it did not reach the yield strain value of $2.75 \cdot 10^{-3}$. In the cable reinforcement ($\phi 10$), the maximum obtained strain was $1.35 \cdot 10^{-2}$ in LS 9, and the bars yielded beneath opening 1. The main reinforcement in the central compressive zone achieved a maximum detected strain of $-9.30 \cdot 10^{-4}$ at peak load level, in LS 8. The respective bars did not yield.

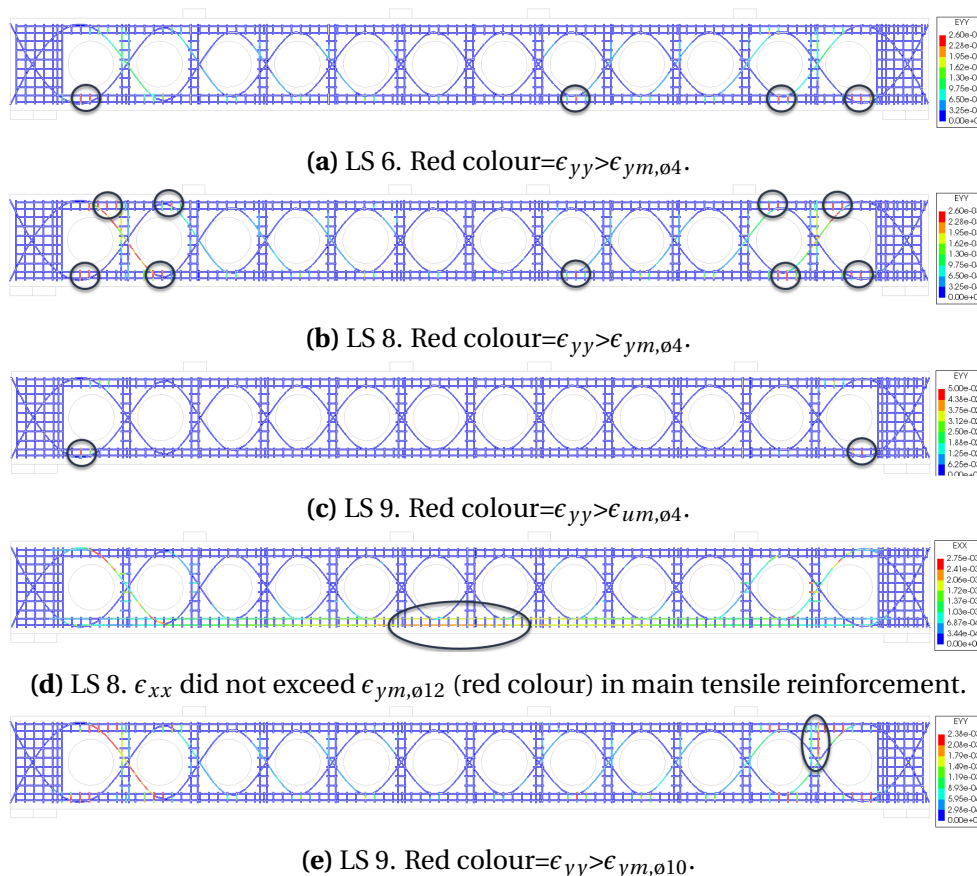


Figure 3.59: RCxcb (2D). Reinforcement strains in x- and y-direction in essential LSs from the NLFEA with the selected solution strategy. Areas of yielding and ultimate strains are marked with circles.

RCxcb 3D Model:

Figure 3.60 shows the reinforcement strains in x-, y- and z-direction at different LSs for the RCxcb 3D model, where yielding and ultimate strain areas are marked with circles. In LS 6, yielding occurred in vertical stirrups ($\phi 4$) beneath opening 1, 11 and 12. At peak load level, in LS 7 ($P=242$ kN), yielding was observed in stirrups beneath opening 1, 2, 8, 11 and 12. In LS 8, yielding was reached in stirrups beneath opening 11, in the out-of-plane direction. Mean ultimate strains were reached in stirrups above and beneath opening 1 and 11 in LS 10. The maximum observed strain value was $6 \cdot 10^{-2}$ beneath opening 1 in this LS. The maximum strain in the main longitudinal reinforcement ($\phi 12$) was observed in LS 7 with a value of $2.1 \cdot 10^{-3}$. Consequently it did not reach the yield strain value of $2.75 \cdot 10^{-3}$. In the cable reinforcement ($\phi 10$), the maximum observed strain was $3 \cdot 10^{-2}$ in LS 10, and the bars yielded in horizontal direction. The main reinforcement in the central compressive zone achieved a maximum strain of almost $-1 \cdot 10^{-3}$, in LS 7.



Figure 3.60: RCxcb (3D). Reinforcement strains in x-, y- and z-direction in essential LSs from the NLFEA with the selected solution strategy. Areas of yielding and ultimate strains are marked with circles.

3.3.1.5 Global Failure

The failure mode for RCxcb, in both the 2D and 3D models, was characterized by a reduction of compressive capacity due to large lateral tensile forces, which resulted in a combined failure mode of diagonal tension failure combined with web crushing failure. The failure modes for the numerical models were brittle, in contrast to the experimental failure modes, which yielded a ductile behaviour for RCxcb.

As observed during post-processing, the failure mechanism occurred at peak load level with a failure load as presented in Table 3.53. Consequently, this resulted in a modelling uncertainty of 1.14 and 1.18, for the 2D and 3D models, respectively.

Table 3.53: RCxcb. Failure mode and failure load from the NLFEA of the solution strategy.

Analysis	Failure Mode	Failure Load	Modelling Uncertainty $(\frac{R_{exp}}{R_{NLFEA}})$
2D Model	Diagonal Tension Failure combined with Web Crushing Failure	250 kN	1.14
3D Model	Diagonal Tension Failure combined with Web Crushing Failure	242 kN	1.18

3.3.2 Sensitivity Study of the Numerical Modelling in Case Study 3

3.3.2.1 Sensitivity to Structural Interface Selection

Three different interface schemes were tested numerically in the 2D numerical RCxcb model. Formulas used to calculate the interface stiffness are defined in Eq. (2.5) and (2.6). One of the tested schemes were defined with a normal stiffness, K_n , of 1000 times E_{steel} divided by the selected length of the elements, and a tangential stiffness, K_t , of zero. This scheme is referred to as a *soft* interface. The second tested scheme had the same normal stiffness as described above, and a tangential stiffness equal to K_n divided by 10. This scheme is referred to as *stiff* interface. The third test was without any interface material, and is therefore referred to as *no* interface.

Analysis 1: Soft interface ($K_n = 1000 \cdot \frac{E_{steel}}{h}$, $K_t=0$).

Analysis 2: Stiff interface ($K_n = 1000 \cdot \frac{E_{steel}}{h}$, $K_t=\frac{K_n}{10}$).

Analysis 3: No interface

LDCs from the NLFEMs of RCxcb with the different interfaces are shown in Figure 3.61 for the 2D numerical model.

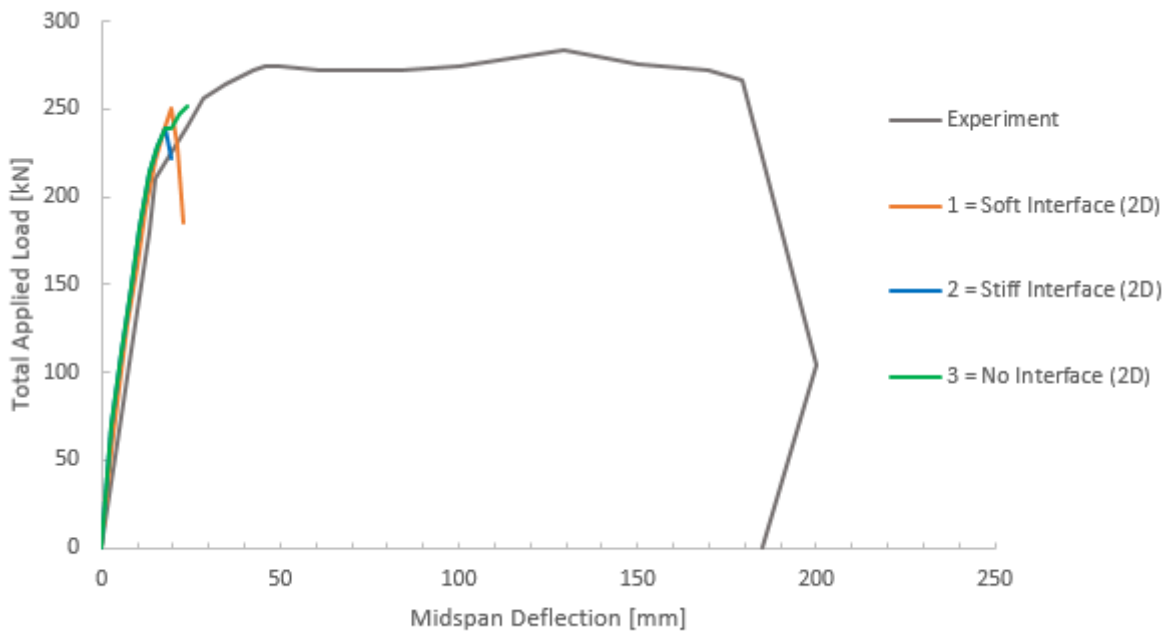


Figure 3.61: RCxcb (2D). LDCs with different interface schemes and the experimental LDC.

Figure 3.62 presents the principal compressive stress plots from the NLFEMs obtained for the 2D model with different interface schemes. The plots describe the stress pattern at peak load level. Analyses 1 and 2 achieved peaks in the LDCs, while Analysis 3 did not gain a peak load before the last LS diverged and the analysis terminated. Both Analyses 2 and 3 yielded stress concentrations, propagating from the right load plate towards opening 11. In order to reduce stress concentrations under the load plates, DG recommends to use a no-friction interface between steel load plates and the concrete core. However, as observed in the contour

plots, all analyses did to some extent generate stress concentrations beneath the load plates. Yet, in compliance with the DG recommendation, the analysis without tangential stiffness, hence no-friction interface, achieved less comprehensive principal compressive stresses propagating from the load plate towards the web opening beneath.

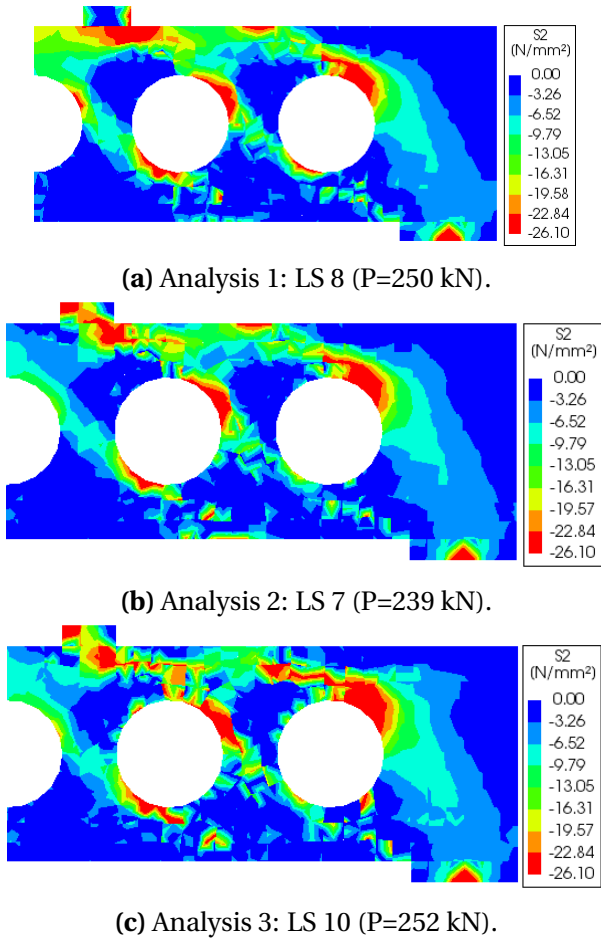


Figure 3.62: RCxcb (2D model). Principal compressive stress plots from the 2D solution strategy model with different interface schemes. Red colour= $| S_2 | > | f_{cm} |$.

Table 3.54: RCxcb. Midspan deflection, failure load and modelling uncertainty from NLFEAs with interfaces.

Analysis	Midspan Deflection	Failure Load	Modelling Uncertainty ($\frac{R_{exp}}{R_{NLFEA}}$)
1 (2D)	19.3 mm	250 kN	1.14
2 (2D)	17.7 mm	239 kN	1.19
3 (2D)	—	No Peak	—

3.3.2.2 Sensitivity regarding FE Discretization

In this sensitivity study, the numerical responses from NLFEAs of RCxcb with four different mesh densities were compared. As for Case Study 1 and 2, the tested densities were $H/6$, $H/12$ and $L/50$, which for RCxcb resulted in element sizes of 66.67 mm, 33.33 mm and 76 mm, respectively. These NLFEAs are defined as *Analysis 1*, *2* and *3*. According to DG, maximum element size for 3D modelling of beam structures should be limited to the beam width, B , divided by six. Therefore, as Case Study 3 included 3D modelling, an additional mesh density was implemented in *Analysis 4*.

Throughout this sensitivity study, the following designations will be used as references for the four NLFEAs of RCxcb with different FE discretizations:

Analysis 1: Mesh density $H/12$ (33.33 mm)

Analysis 2: Mesh density $L/50$ (76 mm)

Analysis 3: Mesh density $H/6$ (66.67 mm)

Analysis 4: Mesh density $B/6$ (25 mm)

Figures 3.63 and 3.64 show the LDCs obtained with the different mesh densities, for the 2D and 3D models, respectively. The different curves are marked with dots that represent observations regarding the tensile behaviour of the concrete. Non-converged LSs are marked with crosses. In Analysis 2 for the 2D model, eight LSs did not achieve convergence; LS 15, 17, 18, 19, 20, 21, 22 and 23. The 3D model in Analysis 2 had two non-converged steps; LS 10 and LS11. In Analysis 3 of the 2D model, six LSs did not achieve convergence; LS 12, 14, 16, 19, 20 and 21, while the 3D model resulted in seven such steps; LS 9, 10, 11, 12, 13, 14 and 15. Finally, in Analysis 4, the 2D model only had in two non-converged steps; LS 9 and 10, while the 3D model had four; LS 7, 8, 9 and 10. The last non-converged LS, marked on each curve, is defined as *diverged* LS in DIANA.

Microcracks were formed at local weak points in the material when the tensile strain, ϵ_1 , exceeded ϵ_{peak} , given in Table 3.55. Fully softening in tension was achieved when ϵ_1 exceeded ϵ_u , listed in the same table. At this strain value cracks were considered to be fully open.

The principal tensile strain plots for the 2D and 3D models with different mesh densities are presented in Figures 3.65 and 3.66, respectively. The plots represent essential LSs for the concrete tensile behaviour. Red colour indicates $\epsilon_1 > \epsilon_u$.

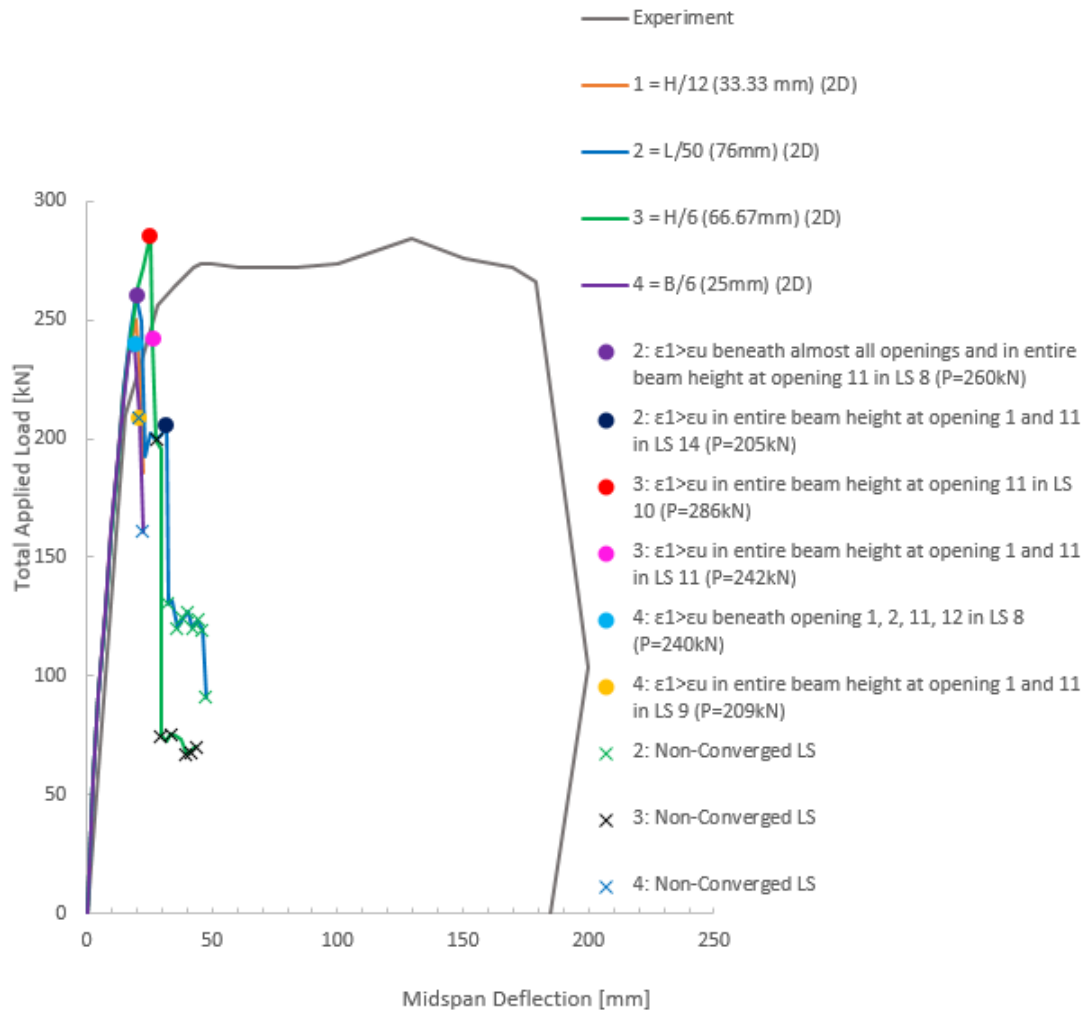


Figure 3.63: RCxcb (2D). LDCs from the NLFEAs with different mesh densities, and the experimental LDC. The numerical LDCs are marked with crack observations and non-converged LSs.

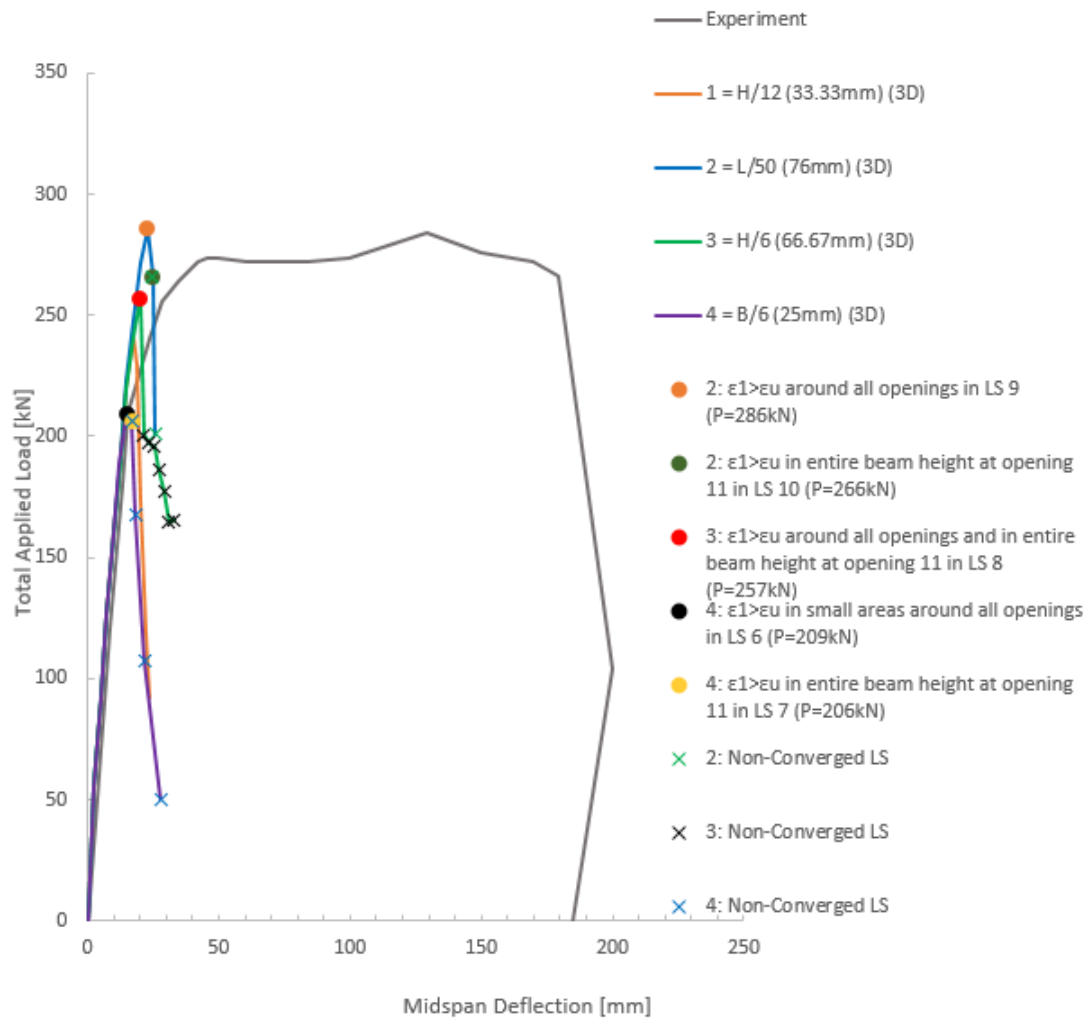


Figure 3.64: RCxcb (3D). LDCs from the NLFEAs with different mesh densities, and the experimental LDC. The numerical LDCs are marked with crack observations and non-converged LSs.

Table 3.55: RCxcb. Specific tensile strain values in the MC2010 TS curve with different mesh densities.

Strain	Formula	Strain value Analysis 1	Strain value Analysis 2	Strain value Analysis 3	Strain value Analysis 4	Tensile stress
ϵ_{peak}		$1.50 \cdot 10^{-4}$	$1.50 \cdot 10^{-4}$	$1.50 \cdot 10^{-4}$	$1.50 \cdot 10^{-4}$	$\sigma = f_{ctm}$
ϵ_u	$5 \cdot \frac{G_F}{f_{ctm} \cdot h}$	$9.52 \cdot 10^{-3}$	$4.18 \cdot 10^{-3}$	$4.76 \cdot 10^{-3}$	$1.27 \cdot 10^{-2}$	$\sigma = 0$

In all 2D and 3D analyses, the largest mesh density yielded a more comprehensive area of fully open cracks than with a finer mesh.

In Analysis 2-4 of the 2D model, the cracks going through the entire beam height were unsymmetrically located in the beam. The crack pattern was more symmetrical in Analysis 1. In Analysis 4, the fully open cracks were propagated through the entire beam height after peak load level.

Unlike for the 2D model, all 3D analyses yielded fully tensile softened concrete through the

entire beam height at post-peak level. The diagonal crack pattern was propagated in the same critical path connected to opening 11, in both the 2D and 3D models, except for the 2D model in Analysis 1, where this path was localized at opening 12 instead of 11. In all analyses the 2D model yielded fully open cracks in the entire beam height at an earlier stage than the 3D model. Larger areas of completely tensile softened concrete were observed in the 2D model than in the 3D model with indential mesh density.

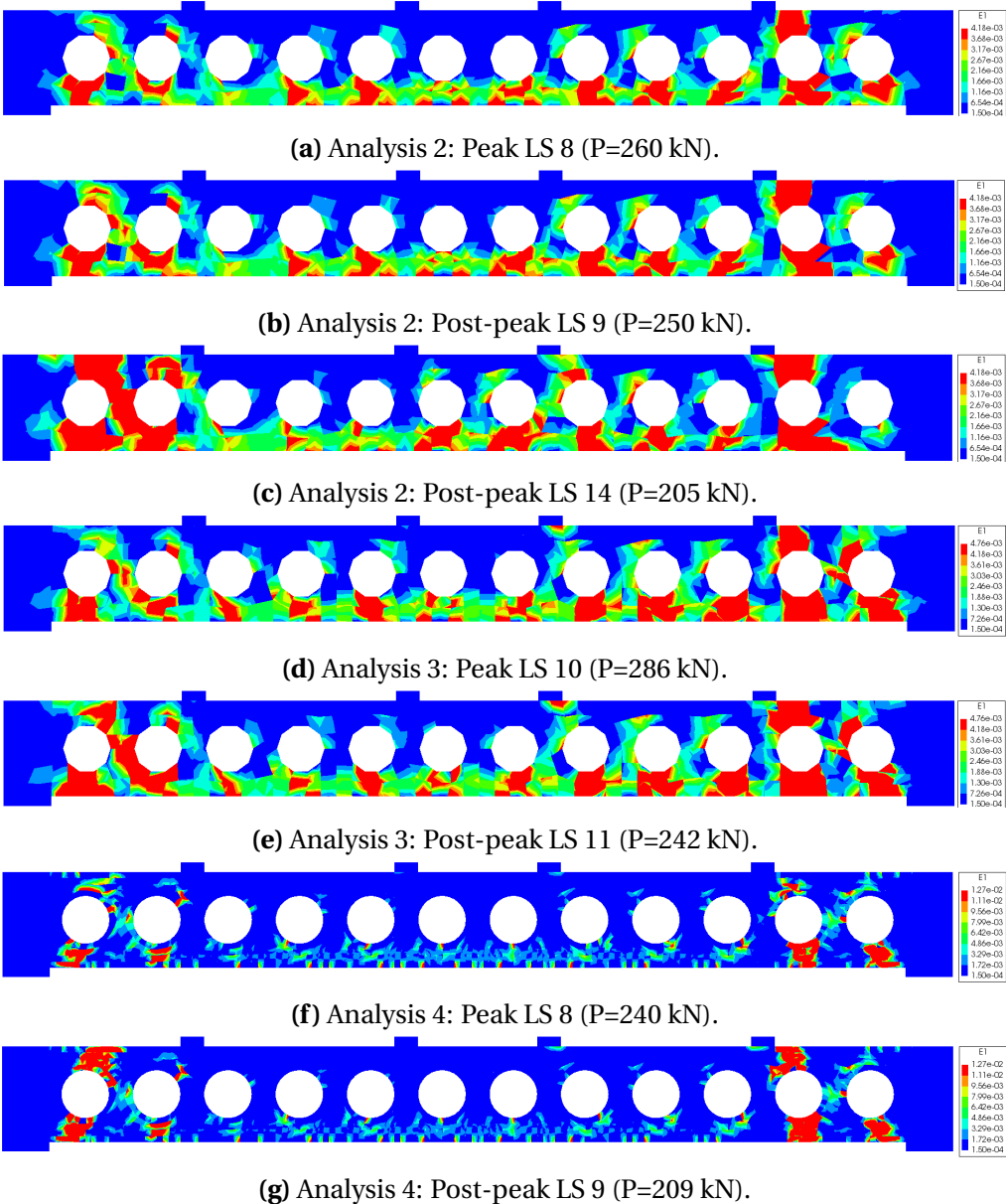
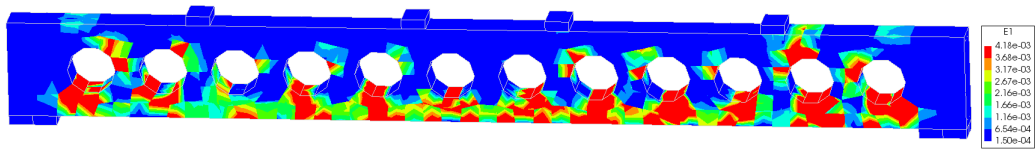
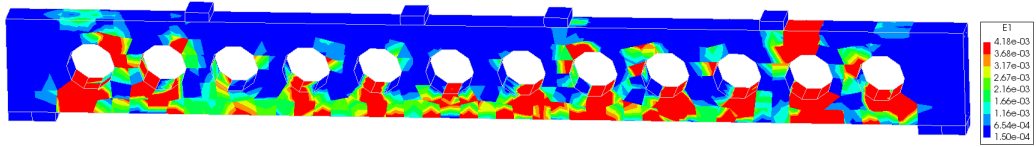


Figure 3.65: RCxcb (2D). Principal tensile strain plots from essential LSs in the NLFEMs with different mesh densities. Red colour= $\epsilon_1 > \epsilon_u$. Blue colour= $\epsilon_1 < \epsilon_{peak}$.

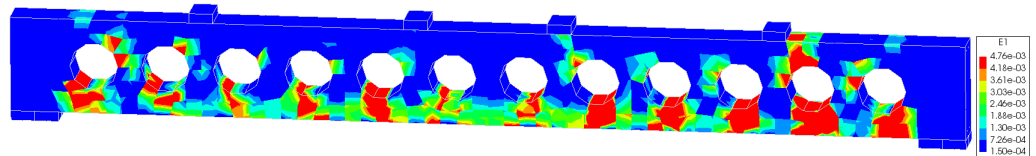
Table 3.56 presents a summary of crack logging from the NLFEMs with different mesh densities. The table shows the amount of cracks that were developed at the given LS and the respective crack status. Two values are highlighted from each analysis; the peak load level and the post-peak load level. A larger amount of cracks were developed in the models with the finest meshes. In the 3D model, the coarsest mesh yielded the lowest amount of cracks at peak load level. This was obtained with the next coarsest mesh in the 2D model.



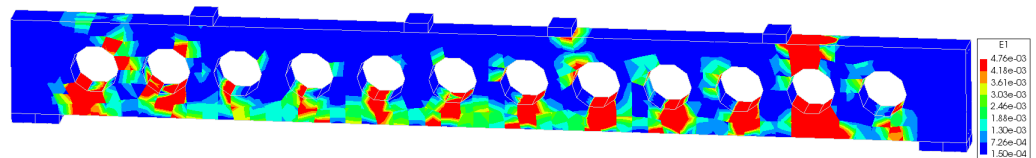
(a) Analysis 2: Peak LS 9 (P=286 kN).



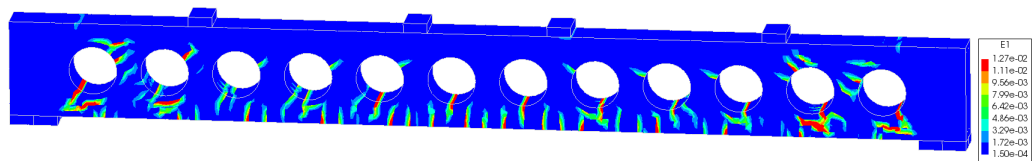
(b) Analysis 2: Post-peak LS 10 (P=266 kN).



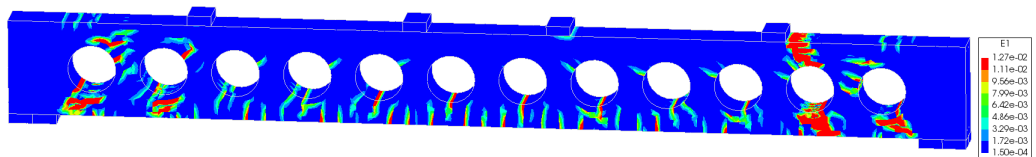
(c) Analysis 3: Peak LS 8 (P=257 kN).



(d) Analysis 3: Post-peak LS 9 (P=200 kN).



(e) Analysis 4: Peak LS 6 (P=209 kN).



(f) Analysis 4: Post-peak LS 7 (P=206 kN).

Figure 3.66: RCxcb (3D). Principal tensile strain plots from essential LSs in the NLFEAs with different mesh densities. Red colour= $\epsilon_1 > \epsilon_u$. Blue colour= $\epsilon_1 < \epsilon_{peak}$.

Figures 3.67 and 3.68 show the LDCs obtained with the different mesh densities, for the 2D and 3D models. The different curves are marked with dots which represents LSs with essential observations of compressive behaviour of concrete.

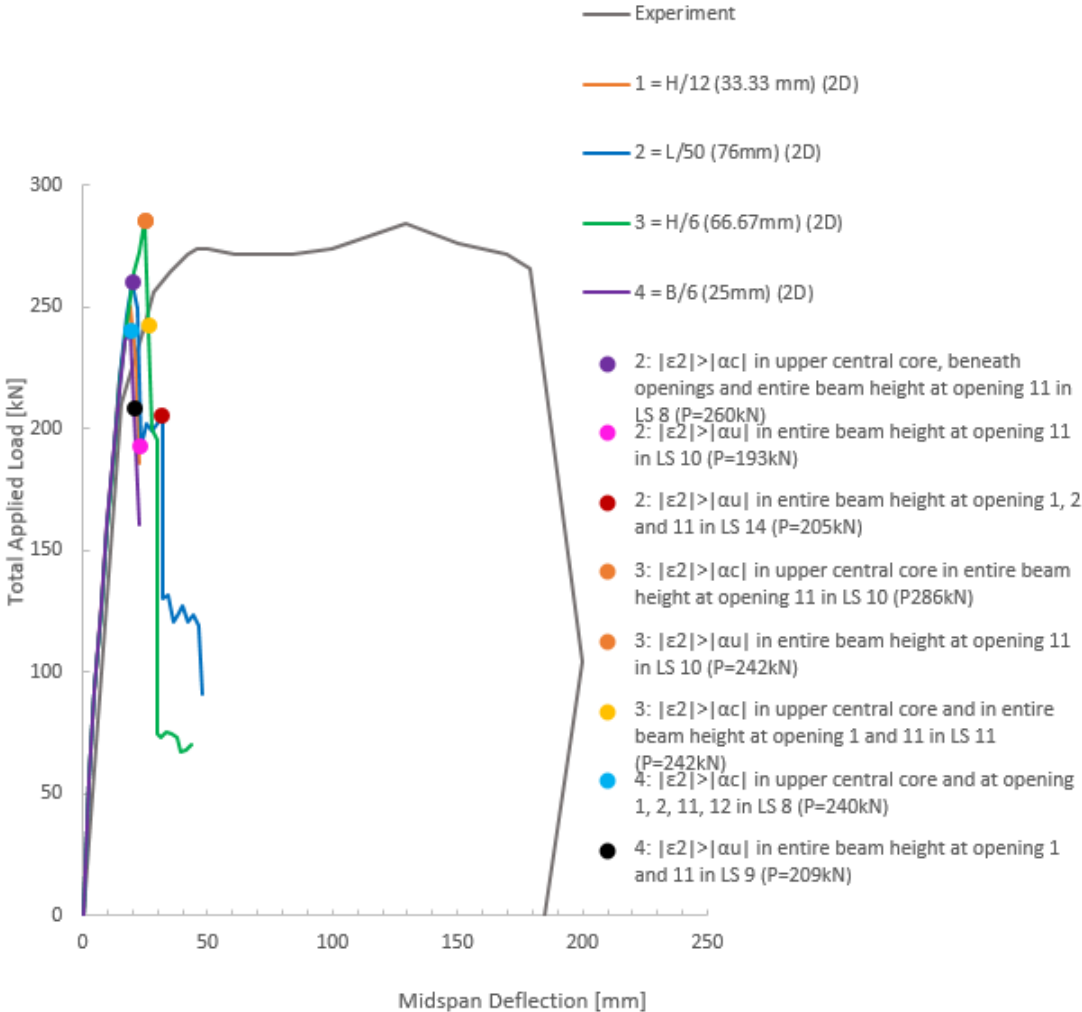


Figure 3.67: RCxcb (2D). LDCs from the NLFEMs with different mesh densities, and the experimental LDC. The numerical LDCs are marked with observations of crushing.

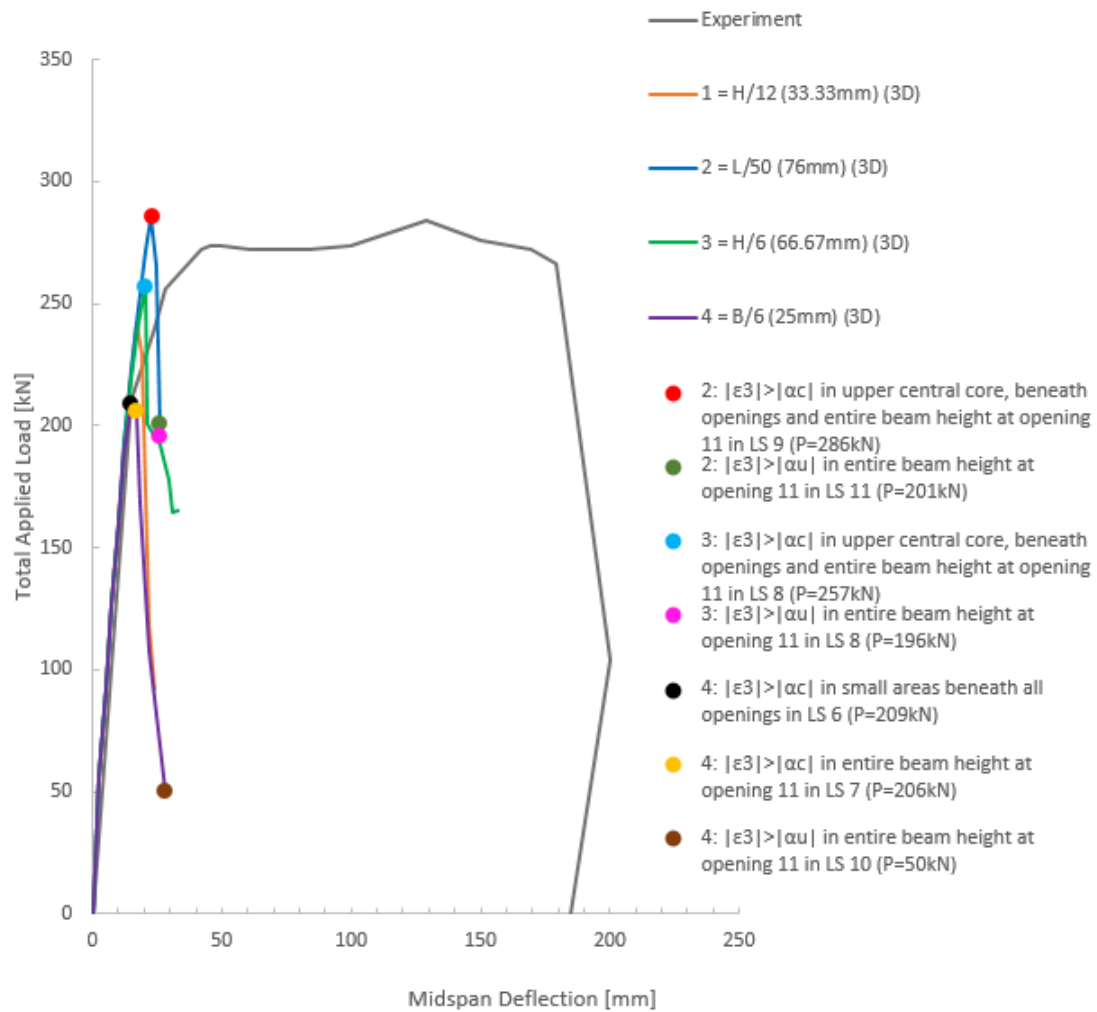


Figure 3.68: RCxcb (3D). LDCs from the NLFEAs with different mesh densities, and the experimental LDC. The numerical LDCs are marked with observations of crushing.

Table 3.56: RCxcb (2D and 3D). Summary of crack logging from the NLFEAs with different mesh densities, given by DIANA.

Analysis - step number	Crack	Open	Closed	Active	Inactive	Arises	Re-opens	Closes
2: LS 8 (2D)	2184	2167	17	1703	481	153	3	6
2: LS 9 (2D)	2313	2284	29	1176	1137	129	2	14
3: LS10 (2D)	2688	2663	25	2136	552	79	2	2
3: LS 11 (2D)	2874	2830	44	1214	1660	186	6	25
4: LS 8 (2D)	13472	13275	197	8046	5426	885	22	93
4: LS 9 (2D)	13901	13586	315	2384	11517	429	38	156
2: LS 9 (3D)	21156	21040	116	16789	4367	1768	15	50
2: LS 10 (3D)	22855	22557	298	11863	10992	1699	37	219
3: LS 8 (3D)	22992	22879	113	18587	4405	2007	21	39
3: LS 9 (3D)	25353	24833	520	11434	13919	2361	34	441
4: LS 6 (3D)	292884	290299	2585	206454	86430	38377	192	1166
4: LS 7 (3D)	324930	320509	4421	160921	164009	32046	634	2470

Table 3.57 shows the defined specific compressive strain values that are used to describe the compressive behaviour in the different analyses in this section. When the principal compressive strain (2D: $|\epsilon_2|$, 3D: $|\epsilon_3|$) exceeded $|\alpha_c|$, the concrete started to crush in the respective area. When α_u was reached, the concrete was defined as completely softened in compression in that area. The plots in Figures 3.69 and 3.70 show the principal compressive strains for the 2D and 3D model, respectively. The red areas show how the beam was disposed to crushing and complete softening in compression, as α_c and α_u were reached in the integration points of the elements.

Table 3.57: RCxcb. Specific compressive strain values for the parabolic stress-strain curve with different mesh densities.

Strain	Formula	Strain value (H/12)	Strain value (L/50)	Strain value (H/6)	Strain value (B/6)	Compressive stress
α_c	$-5 \cdot \frac{1}{3} \frac{f_c}{E}$	$-1.44 \cdot 10^{-3}$	$-1.44 \cdot 10^{-3}$	$-1.44 \cdot 10^{-3}$	$-1.44 \cdot 10^{-3}$	$\sigma = f_c$
α_u	$\alpha_c - \frac{3}{2} \frac{G_C}{h f_c}$	$-5.66 \cdot 10^{-2}$	$-2.63 \cdot 10^{-2}$	$-2.97 \cdot 10^{-2}$	$-7.69 \cdot 10^{-2}$	$\sigma = 0$

The principal compressive strain plots for the 2D and 3D models with different mesh densities are visualized in Figures 3.69 and 3.70. The larger mesh densities yielded more comprehensive crushing areas. Crushing occurred in the same LSs and at the same locations as where the concrete was defined as completely softened in tension. Crushed concrete was observed in the entire beam height at opening 11 in both the 2D and the 3D models. In addition, crushing was also prominent in the upper central chord.

As for tensile strains, areas of crushed concrete covered larger areas when coarser mesh densities were used. Complete softening was more prominent for coarse meshes at post peak level. As for the principal tensile strains, the concrete crushed in a non-symmetrical path in all analyses of the 2D model.

Unlike the 2D model, the 3D model was only crushed in entire beam height at opening 11, not at opening 1. The 3D model yielded complete softening in larger areas than the 2D model.

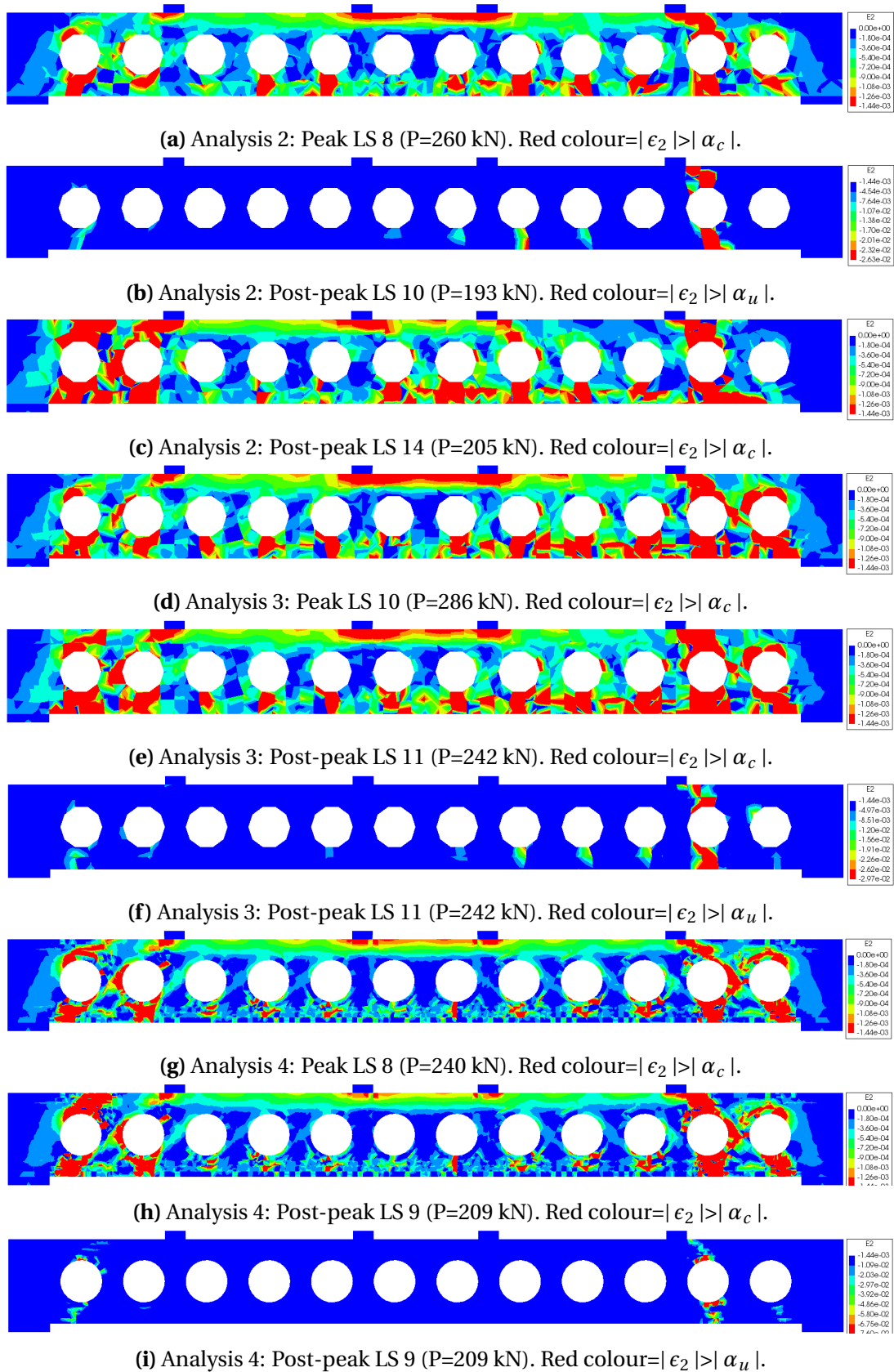
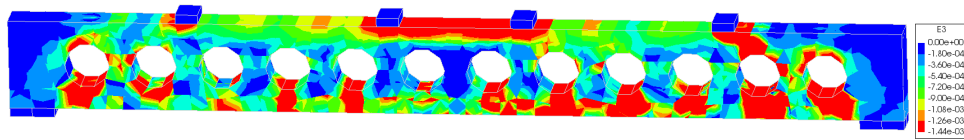
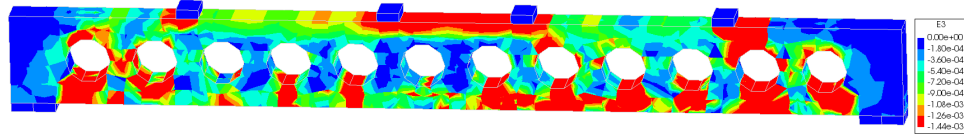


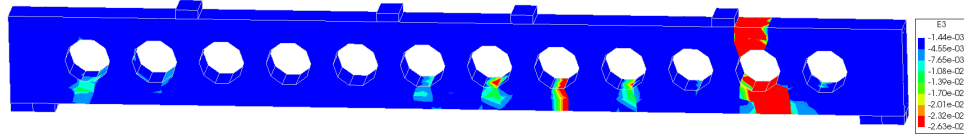
Figure 3.69: RCxcb (2D). Principal compressive strain plots from essential LSs in the NLFEMs with different mesh densities.



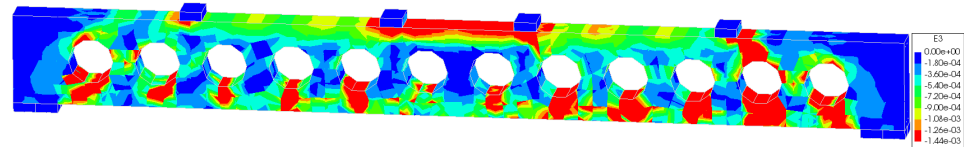
(a) Analysis 2: Peak LS 9 (P=286 kN). Red colour= $|\epsilon_3| > |\alpha_c|$.



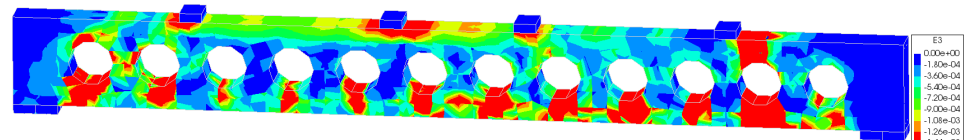
(b) Analysis 2: Post-peak LS 10 (P=266 kN). Red colour= $|\epsilon_3| > |\alpha_c|$.



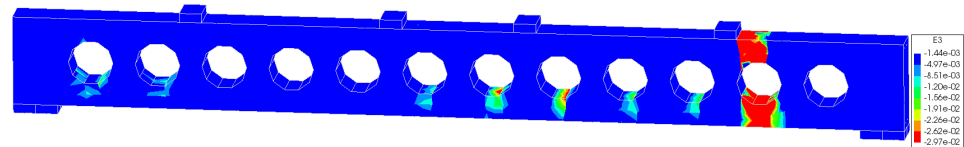
(c) Analysis 2: Post-peak LS 11 (P=201 kN). Red colour= $|\epsilon_3| > |\alpha_u|$.



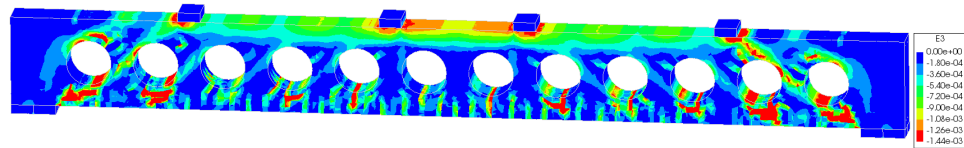
(d) Analysis 3: Peak LS 8 (P=257 kN). Red colour= $|\epsilon_3| > |\alpha_c|$.



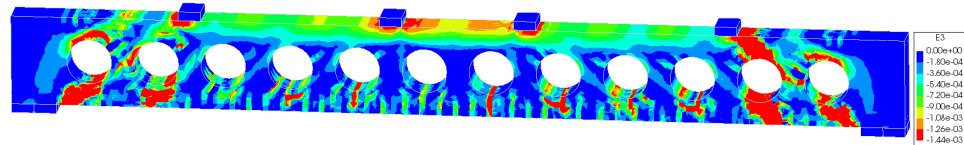
(e) Analysis 3: Post-peak LS 9 (P=200 kN). Red colour= $|\epsilon_3| > |\alpha_c|$.



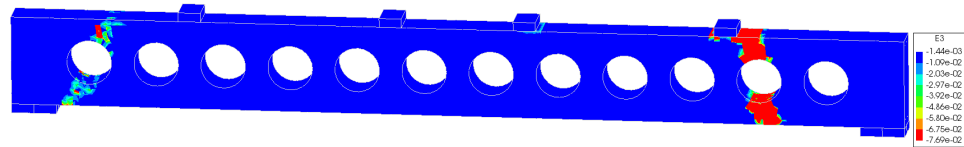
(f) Analysis 3: Post-peak LS 11 (P=196 kN). Red colour= $|\epsilon_3| > |\alpha_u|$.



(g) Analysis 4: Peak LS 6 (P=209 kN). Red colour= $|\epsilon_3| > |\alpha_c|$.



(h) Analysis 4: Post-peak LS 7 (P=206 kN). Red colour= $|\epsilon_3| > |\alpha_c|$.



(i) Analysis 4: Post-peak LS 10 (P=50 kN). Red colour= $|\epsilon_3| > |\alpha_u|$.

Figure 3.70: RCxcb (3D). Principal compressive strain plots from essential LSS in the NLFEAs with different mesh densities.

Figures 3.71 and 3.72 show the development of the reaction forces in the supports from the different analyses with various mesh densities. All peak values for the reaction forces were coherent with peaks in the LDCs visualized in Figures 3.67 and 3.68. The clear drop in all curves, for the both 2D and 3D models, indicated that non of these models were able to take up any additional forces after the failure mechanisms were established.

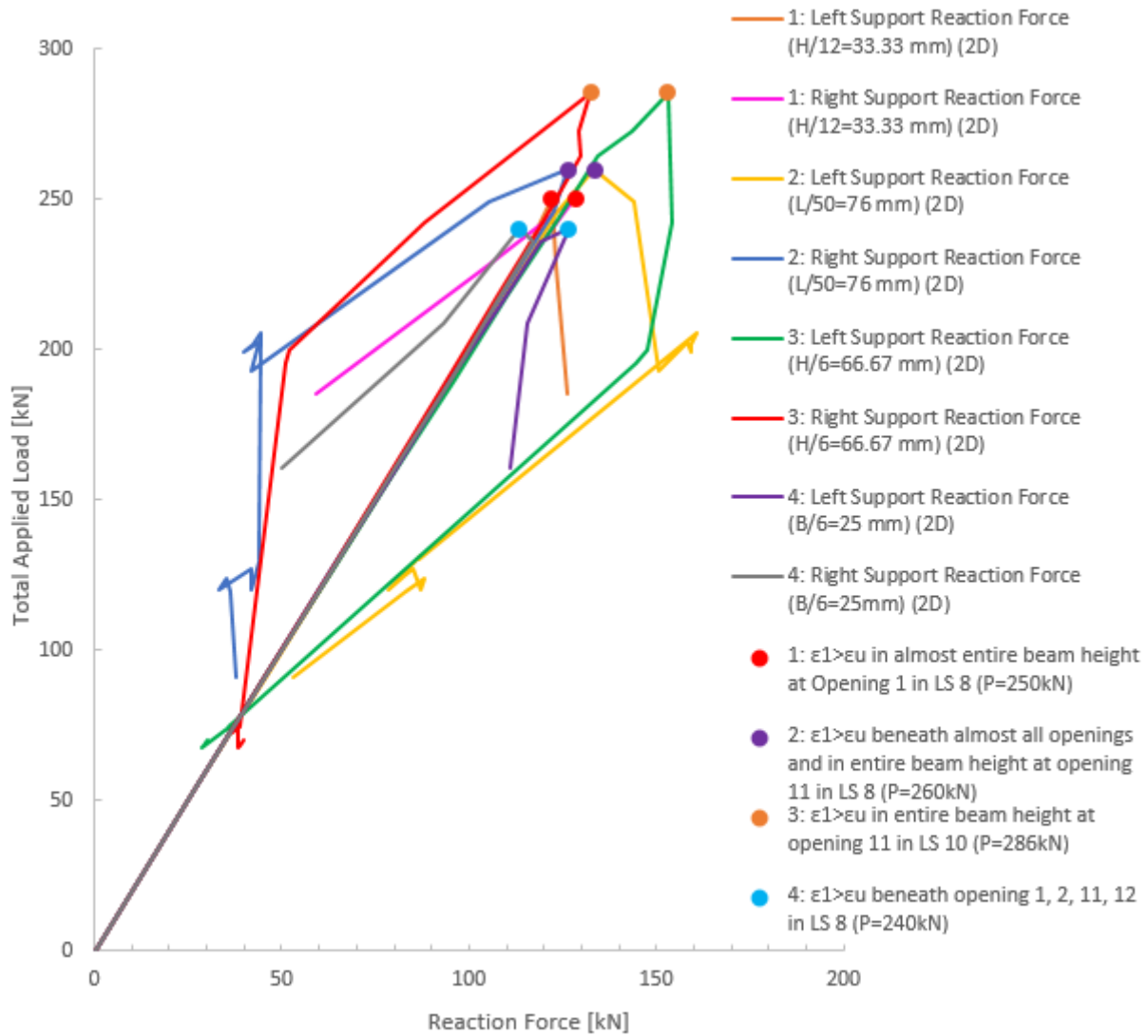


Figure 3.71: RCxcb (2D). Support reactions against total applied load from the NLFEAs with different mesh densities. The curves are marked with crack observations.

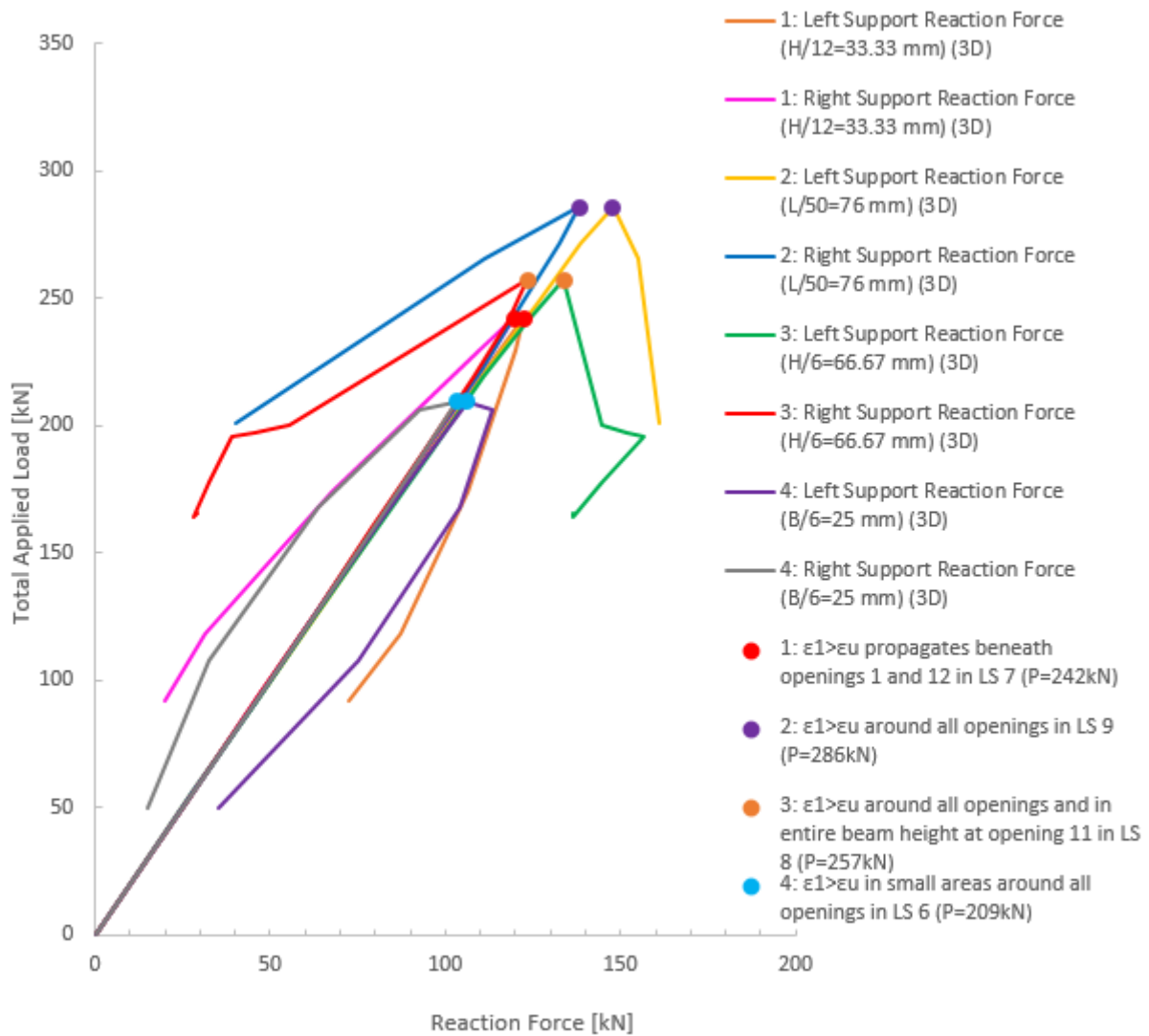


Figure 3.72: RCxcb (3D). Support reactions against total applied load from the NLFEAs with different mesh densities. The curves are marked with crack observations.

Table 3.58 shows the amount of force distribution in supports for the 2D and 3D models with different mesh densities. A greater amount of forces were transferred to the left support in all analyses, except for Analysis 1. From peak load level to the last LS, the left supports were able to take up more load than the right supports in all analyses, except for Analysis 3 (2D).

Table 3.58: RCxcb (2D and 3D). Reaction forces and amount of force distribution in supports from the NLFEAs with different mesh densities.

Mesh Density	Peak LS	Deformation (Peak)	Left Reaction Force (Peak)	Right Reaction Force (Peak)
1: 33.33mm (2D)	8	19.3mm	122.1 kN (48.8% of peak load)	128.3 kN (51.2% of peak load)
1: 33.33mm (3D)	7	17.2mm	122.4 kN (50.6% of peak load)	119.6 kN (49.4% of peak load)
2: 76mm (2D)	8	20.0mm	133.5 kN (51.3% of peak load)	126.5 kN (48.7% of peak load)
2: 76mm (3D)	9	22.7mm	147.7 kN (51.7% of peak load)	138.2 kN (48.3% of peak load)
3: 66.67mm (2D)	10	25.1mm	153 kN (53.6% of peak load)	132.5 kN (46.4% of peak load)
3: 66.67mm (3D)	8	20.2mm	133.9 kN (52% of peak load)	123.4 kN (48% of peak load)
4: 25mm (2D)	8	19.1mm	126.6 kN (52.7% of peak load)	113.5 kN (47.3% of peak load)
4: 25mm (3D)	6	14.7mm	106.1 kN (50.7% of peak load)	103.2 kN (49.3% of peak load)
Analysis	Last LS	Last Load Value	Left Reaction Force (Last LS)	Right Reaction Force (Last LS)
1 (2D)	10	185.5 kN	126.2 kN (68% of last load)	59.3 kN (32% of last load)
1 (3D)	11	92.1 kN	72.2 kN (78.4% of last load)	19.9 kN (21.6% of last load)
2 (2D)	23	91.1 kN	53.3 kN (58.5% of last load)	37.8 kN (41.5% of last load)
2 (3D)	11	201 kN	161 kN (80% of last load)	40 kN (20% of last load)
3 (2D)	21	70.3 kN	30.3 kN (43.1% of last load)	40 kN (56.9% of last load)
3 (3D)	15	165.6 kN	136.5 kN (82.4% of last load)	29.1 kN (17.6% of last load)
4 (2D)	10	160.7 kN	110.8 kN (68.9% of last load)	49.9 kN (31.1% of last load)
4 (3D)	10	50.1 kN	35.2 kN (70.3% of last load)	14.9 kN (29.7% of last load)

As for the solution strategy in Analysis 1, the reinforcement yielded in the same critical areas in the other analyses as well. The main reinforcement in the tensile zone did not yield before a failure mechanism was established.

Analysis 4, with the finest mesh density, achieved the lowest failure load in both 2D and 3D modelling. Analysis 2, with largest element sizes, withstood the greatest deformations in both the 2D and 3D model. The 2D model in Analysis 3 accomplished the highest 2D load capacity with a peak load of 286 kN at 25.1 mm deflection. The 3D model in Analysis 2 accomplished the highest 3D load capacity with a peak load of 286 kN at 22.7 mm deflection.

Table 3.59 presents the failure modes achieved in the different analyses in this sensitivity study. All four analyses yielded a brittle failure mechanism, characterized by a combination of cracking and crushing of concrete.

Table 3.59: RCxcb (2D and 3D). Failure mode and failure load from the NLFEAs with different mesh densities.

Analysis	Failure Mode	Failure Load	Modelling Uncertainty ($\frac{R_{exp}}{R_{NLFEA}}$)
1 (2D)	Same as 2D Model in Fig. 3.53	250 kN	1.14
1 (3D)	Same as 3D Model in Fig. 3.53	242 kN	1.17
2 (2D)	Same as 2D Model in Fig. 3.53	260 kN	1.09
2 (3D)	Same as 3D Model in Fig. 3.53	286 kN	0.99
3 (2D)	Same as 2D Model in Fig. 3.53	286 kN	0.99
3 (3D)	Same as 3D Model in Fig. 3.53	257 kN	1.10
4 (2D)	Same as 2D Model in Fig. 3.53	240 kN	1.18
4 (3D)	Same as 3D Model in Fig. 3.53	209 kN	1.36

3.3.2.3 Sensitivity to choice of Constitutive Model for Concrete

Tension Softening Model

For the selected solution strategy, MC2010 was chosen as the standard TS approach. According to DG, exponential TS is preferred. In order to investigate the sensitivity related to this constitutive approach, these two models were tested. Figures 3.73 and 3.74 show the obtained LDCs from NLFEAs with the two different TS models, in 2D and 3D modelling respectively. The curves are marked with observations of tensile softening of concrete and non-converged LSs.

Throughout this sensitivity study, the following designations will be used as references for the two NLFEAs of RCxcb with different TS models:

Analysis 1: MC2010 TS Model

Analysis 2: Exponential TS Model

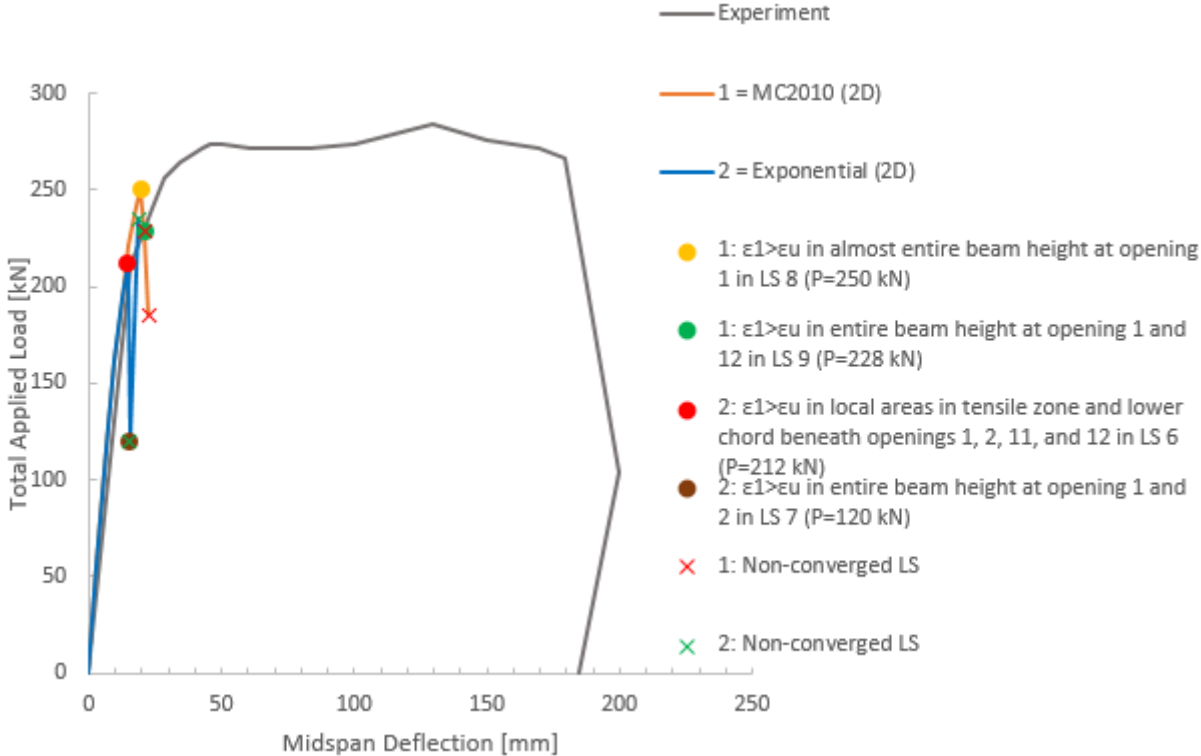


Figure 3.73: RCxcb (2D). LDCs from the NLFEAs with different TS models, and the experimental LDC. The numerical LDCs are marked with crack observations and non-converged LSs.

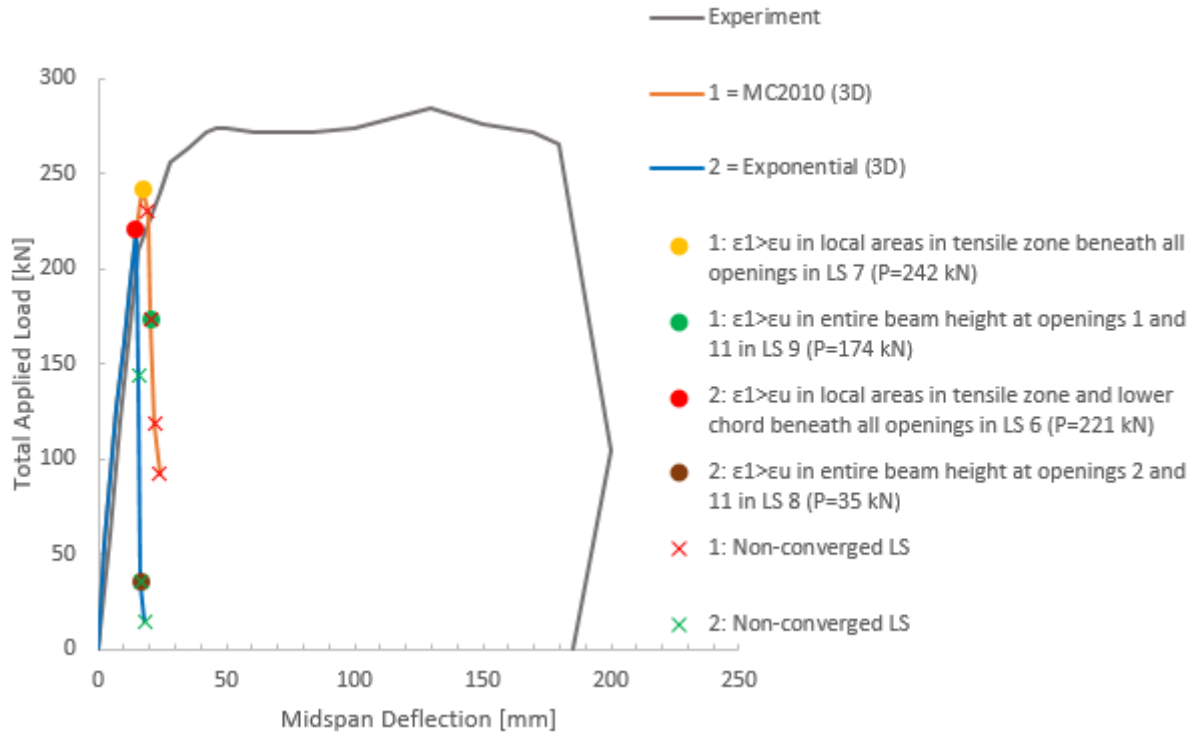


Figure 3.74: RCxcb (3D). LDCs from the NLFEAs with different TS models, and the experimental LDC. The numerical LDCs are marked with crack observations and non-converged LSs.

Table 3.60 shows the specific tensile strain values that are used to describe the exponential TS behaviour. Figures 3.75 and 3.76 show principal tensile strain plots of RCxcb obtained in Analysis 2 for 2D and 3D modelling respectively. Blue colour indicates strain values less than ϵ_{peak} , listed in Table 3.60, while red colour indicates strains larger than the value of ϵ_u from the same table. The red areas show where the beam generated fully open cracks as the limit strain value in tension softening was reached.

Table 3.60: RCxcb. Specific tensile strain values for the exponential TS.

Strain	Formula	Value	Tensile stress
ϵ_{peak}	$\frac{f_{ctm}}{E_{cm}}$	$6.83 \cdot 10^{-5}$	$\sigma = f_{ctm}$
ϵ_u	$2 \cdot \frac{G_F}{f_{ctm} \cdot h}$	$3.81 \cdot 10^{-3}$	$\sigma \approx 0$

In 2D Analysis 2, the cracks were fully open through the entire beam height at opening 1 and 12 in the LS after the peak load in the LDC. Similarly as in Analysis 1, the obtained crack pattern was symmetrical. However, the fully open crack pattern in the upper chord showed a different angle in Analysis 2 than in Analysis 1.

In 3D Analysis 2, the cracks were fully open through the entire beam height at opening 2 and 11 in the LS after the peak load in the LDC. Also similar as in Analysis 1, the 3D model obtained an unsymmetrical crack pattern.

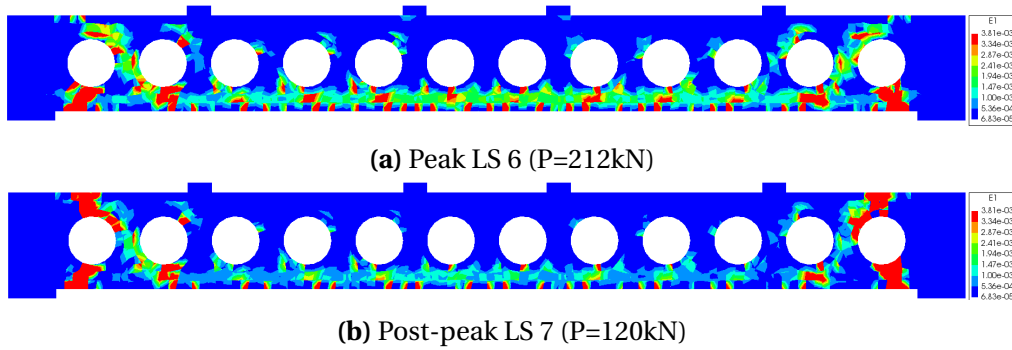


Figure 3.75: RCxcb (2D). Principal tensile strain plots from essential LSs in the NLFEA with exponential TS. Red colour= $\epsilon_1 > \epsilon_u$. Blue colour= $\epsilon_1 < \epsilon_{peak}$.

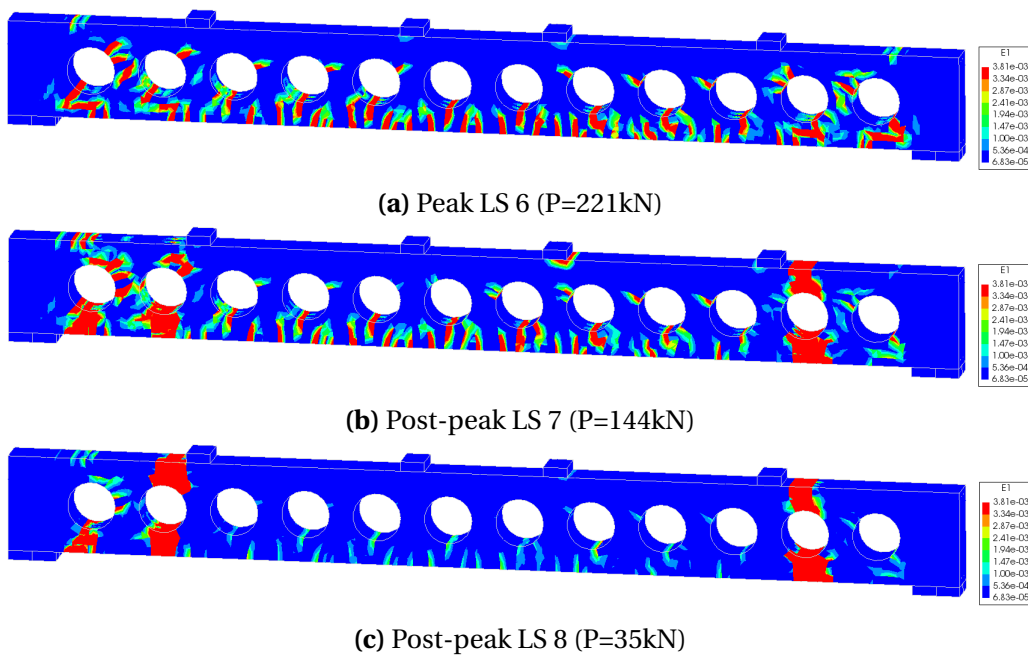


Figure 3.76: RCxcb (3D). Principal tensile strain plots from essential LSs in the NLFEA with exponential TS. Red colour= $\epsilon_1 > \epsilon_u$. Blue colour= $\epsilon_1 < \epsilon_{peak}$.

Figures 3.77 and 3.78 show the LDCs obtained with different TS models, for the 2D and 3D modelling, respectively. The different curves are marked with dots that indicate specific compressive behaviour observations. Compressive strain values that describe the parabolic behaviour function of concrete are defined in Table 3.50. The red areas in the principal compressive strain plots in Figures 3.79 and 3.80 indicate concrete that were completely softened in compression.

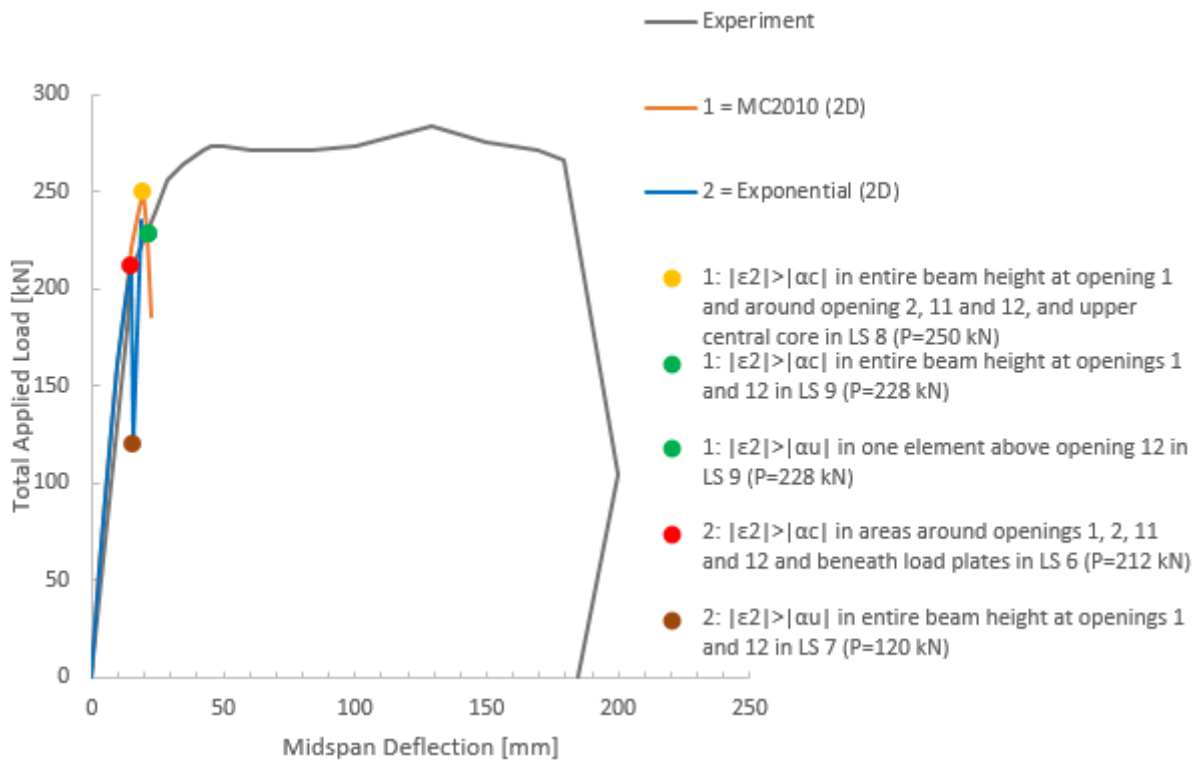


Figure 3.77: RCxcb (2D). LDCs from the NLFEMs with different TS models, and the experimental LDC. The numerical LDCs are marked with observations of concrete crushing.

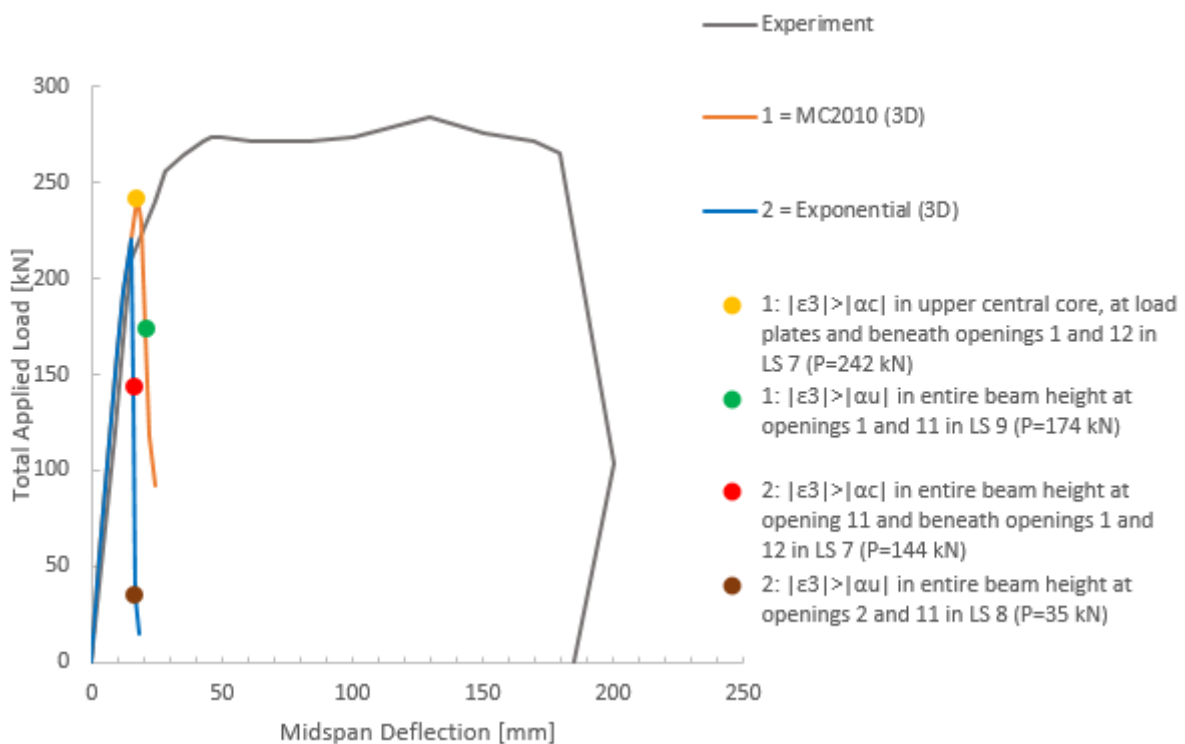


Figure 3.78: RCxcb (3D). LDCs from NLFEMs with two different TS models, and the experimental LDC. The numerical LDCs are marked with compressive strain observations of concrete.

In the 2D Analysis 2, crushed areas were observed through the entire beam height at opening 1 and 12, in the same area as the critical shear crack developed. In contrast to Analysis 1, crushing was not prominent in the upper central chord in Analysis 2. However, completely softening in compression at opening 1 and 12 was more prominent in Analysis 2 than in Analysis 1, as only a small area over and under opening 12 was completely softened in compression in 2D Analysis 1.

In the 3D Analysis 2, crushing of concrete was observed in the same path and LS as the fully open cracks were observed. In contrast to Analysis 1, where the concrete was completely softened in compression at openings 1 and 11, this corresponded to opening 2 and 11 in Analysis 2.

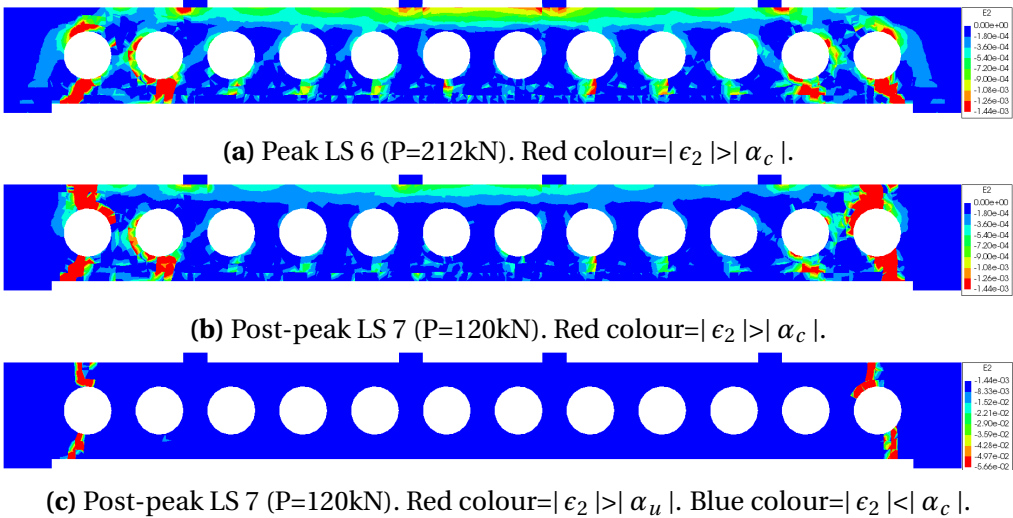


Figure 3.79: RCxcb (2D). Principal compressive strain plots from essential LSs in the NLFEA with exponential TS.

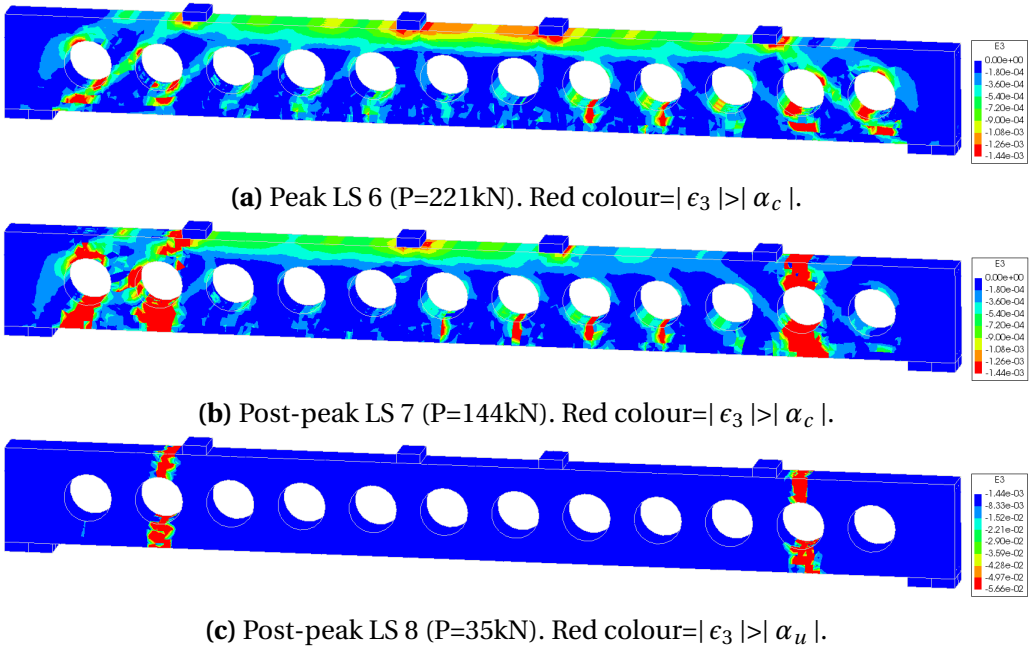


Figure 3.80: RCxcb (3D). Principal compressive strain plots from essential LSs in the NLFEA with exponential TS.

Figures 3.81 and 3.82 show the development of the reaction forces in the supports from the different analyses. The clear drop in all curves, for both the 2D and 3D models, indicates that non of the analyzed models were able to take up more load after failure mechanisms were established.

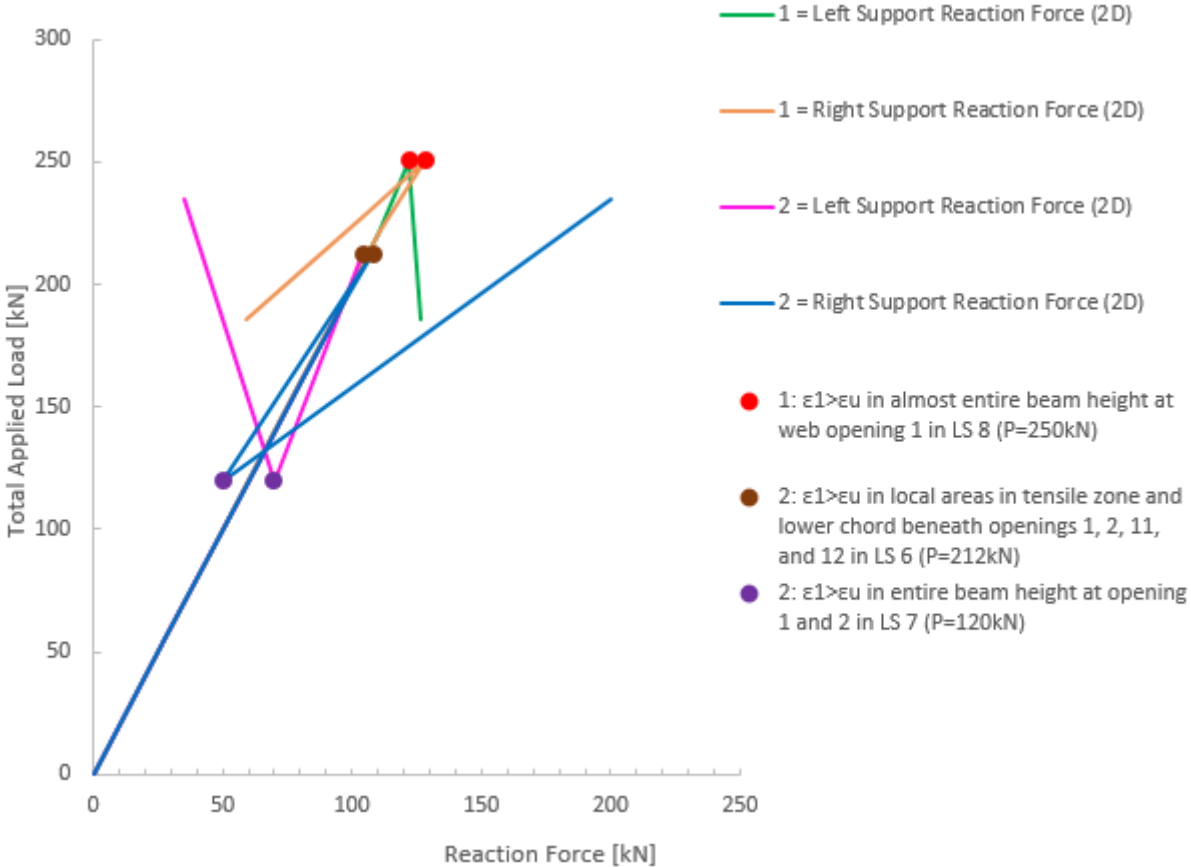


Figure 3.81: RCxcb (2D). Reaction forces from NLFEA with different tension softening models. The curves are marked with crack observations.

As for the solution strategy in Analysis 1, yielding of the reinforcement was localized at the same critical areas in Analysis 2. The main longitudinal reinforcement did not yield before the failure mechanism was established.

Table 3.61 presents the failure mode achieved for both the 2D and the 3D model in the different analyses related to this sensitivity study. Both TS approaches resulted in formation of the same brittle failure mechanism. Both models in Analysis 2, with exponential TS, failed at lower loads and achieved higher modelling uncertainties than in Analysis 1.

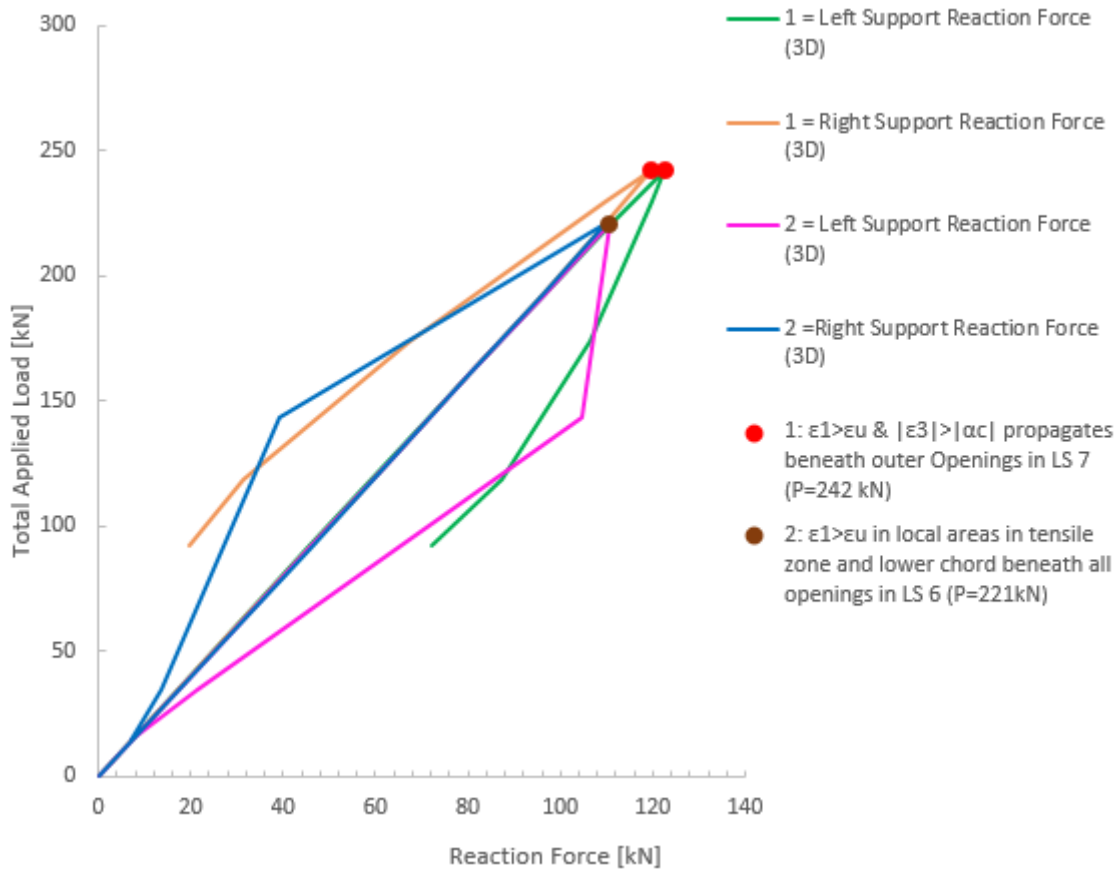


Figure 3.82: RCxcb (3D). Reaction forces from NLFEA with different tension softening models. The curves are marked with crack- and crushing observations.

Table 3.61: RCxcb. Failure mode and failure load from the NLFEAs with different TS models.

Analysis	Failure Mode	Failure Load	Modelling Uncertainty ($\frac{R_{exp}}{R_{NLFEA}}$)
1 (2D)	Diagonal Tension Failure combined with Web Crushing Failure	250 kN	1.14
2 (2D)	Diagonal Tension Failure combined with Web Crushing Failure	212 kN	1.33
1 (3D)	Diagonal Tension Failure combined with Web Crushing Failure	242 kN	1.18
2 (3D)	Diagonal Tension Failure combined with Web Crushing Failure	221 kN	1.28

Compressive Behaviour Function

In order to investigate the sensitivity related to choice of compressive behaviour function, constant function was tested in addition to parabolic function, which was the chosen behaviour in the selected solution strategy.

Throughout this sensitivity study, the following designations will be used as references for the two NLFEMs of RCxcb with different compressive behaviour functions: Analysis 1: Parabolic compressive behaviour function.

Analysis 2: Constant compressive behaviour function.

The constant compressive behaviour function provides a simplified approach to the concrete compressive behaviour, where the material do not soften in compression. The concrete is given a so-called idealized plastic behaviour. As opposed to for the parabolic curve, no compressive strain values indicates reduced concrete capacity in the constant curve. Therefore, a reference value, ϵ_{cu2} , described in Table 2.11, was used in the post-analysis investigation of RCxcb in order to be able to evaluate how the compressive behaviour developed in the FE model. Compressive strain value for RCxcb at the point when crushing was initiated, and also this reference value, yielding an indicative limit value, are further defined in Table 3.62. Corresponding strain values describing the parabolic curve is given in Table 3.50. However, α_u in this table is not an indicative limit value, but a strain value that indicates completely softened concrete in compression.

Figures 3.83 and 3.84 show the LDCs obtained with the different compressive behaviour functions, with 2D and 3D modelling. The different curves are marked with dots that indicates specific tensile strain observations, and crosses that indicate non-converged LSs.

The specific tensile strain values used to evaluate crack development in this sensitivity study are identical as for the selected solution strategy, and are listed in Table 3.46.

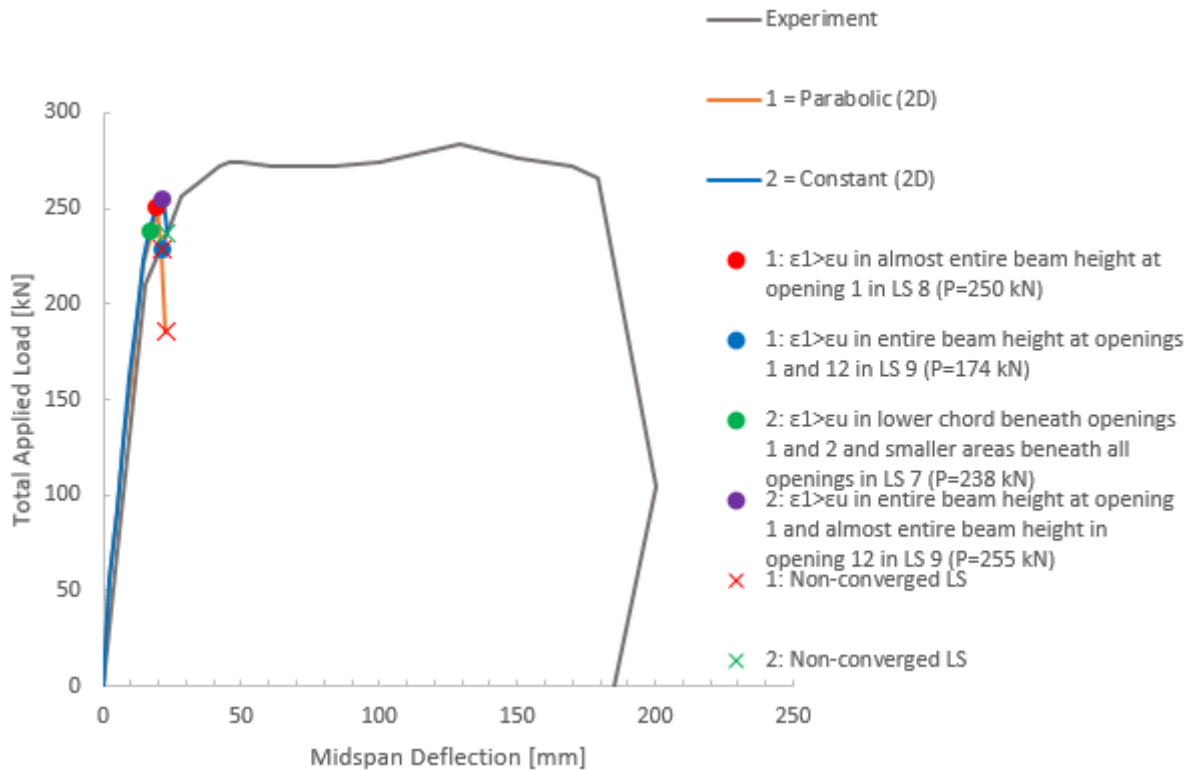


Figure 3.83: RCxcb (2D). LDCs from the NLFEAs with different compressive behaviour functions, and the experimental LDC. The numerical LDCs are marked crack observations and non-converged LSs.

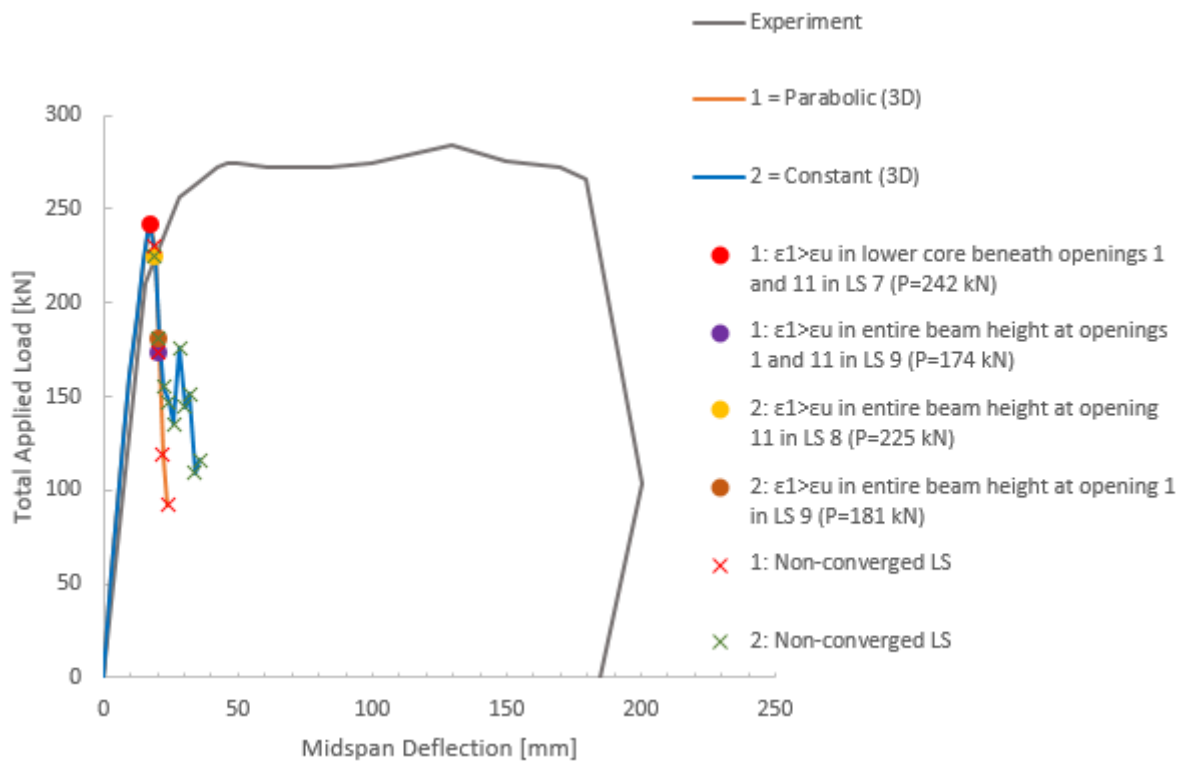


Figure 3.84: RCxcb (3D). LDCs from the NLFEAs with different compressive behaviour functions, and the experimental LDC. The numerical LDCs are marked with crack observations and non-converged LSs.

Figures 3.85 and 3.86 shows principal tensile strain plots from essential LSs in Analysis 2 of the 2D and the 3D model respectively. Red areas represent $\epsilon_1 > \epsilon_{u}$, indicating completely tensile softened concrete and hence fully open crack strains.

Figure 3.85 presents plots of the 2D model, obtained in Analysis 2. In LS 7 (P=238 kN), fully open shear cracks propagated in entire lower chord beneath opening 1 and 12, and in small areas beneath all web openings. At peak load level in LS 9 (P=255 kN), fully open cracks were prominent in entire beam height at web opening 1, and almost in the entire beam height at web opening 12. The final crack pattern was symmetrical, similarly as in Analysis 1.

Figure 3.86 presents plots of the 3D model, obtained in Analysis 2. At post peak level, in LS 8 (P=225 kN), fully open shear cracks propagated below web opening 11, and almost through the entire height of the beam at web opening 1. In LS 9 (P=181 kN), fully open cracks propagated through the entire height of the beam at web opening 1 and 11. Also, fully open cracks propagated in areas beneath all web openings. Similarly as in Analysis 1, the 3D model in Analysis 2 generated an unsymmetrical final crack pattern.

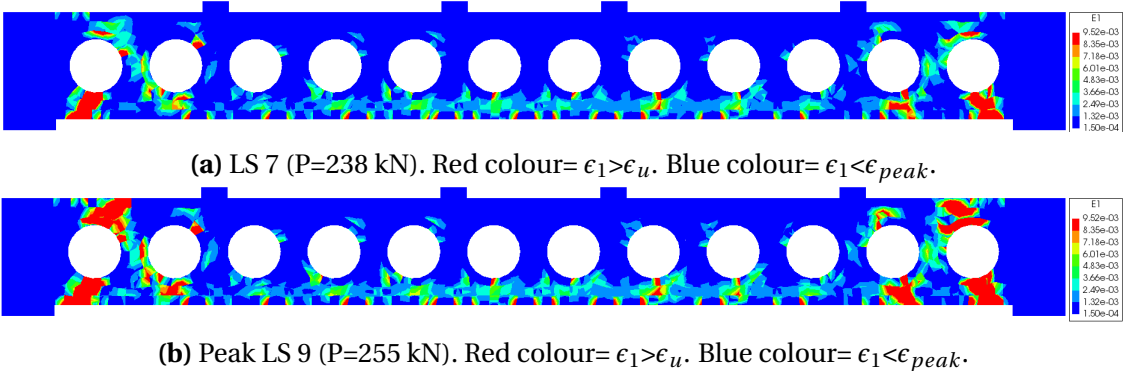


Figure 3.85: RCxcb (2D). Principal tensile strain plots from essential LSs in NLFEA with constant compressive behaviour function.

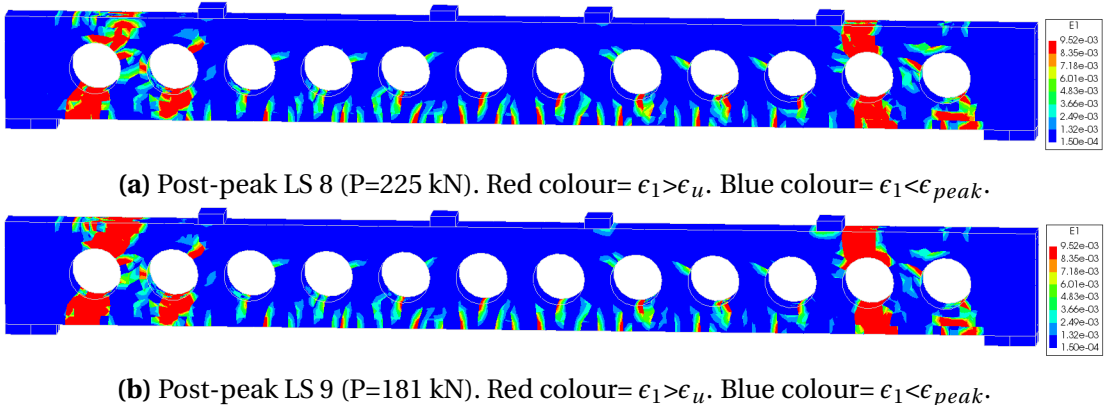


Figure 3.86: RCxcb (3D). Principal tensile strain plots from essential LSs in NLFEA with constant compressive behaviour function.

Figures 3.87 and 3.88 show the LDCs obtained with the different compressive behaviour functions, for the 2D and 3D models of RCxcb. The different curves are marked with dots that indicates specific observations related to the compressive behaviour of the concrete.

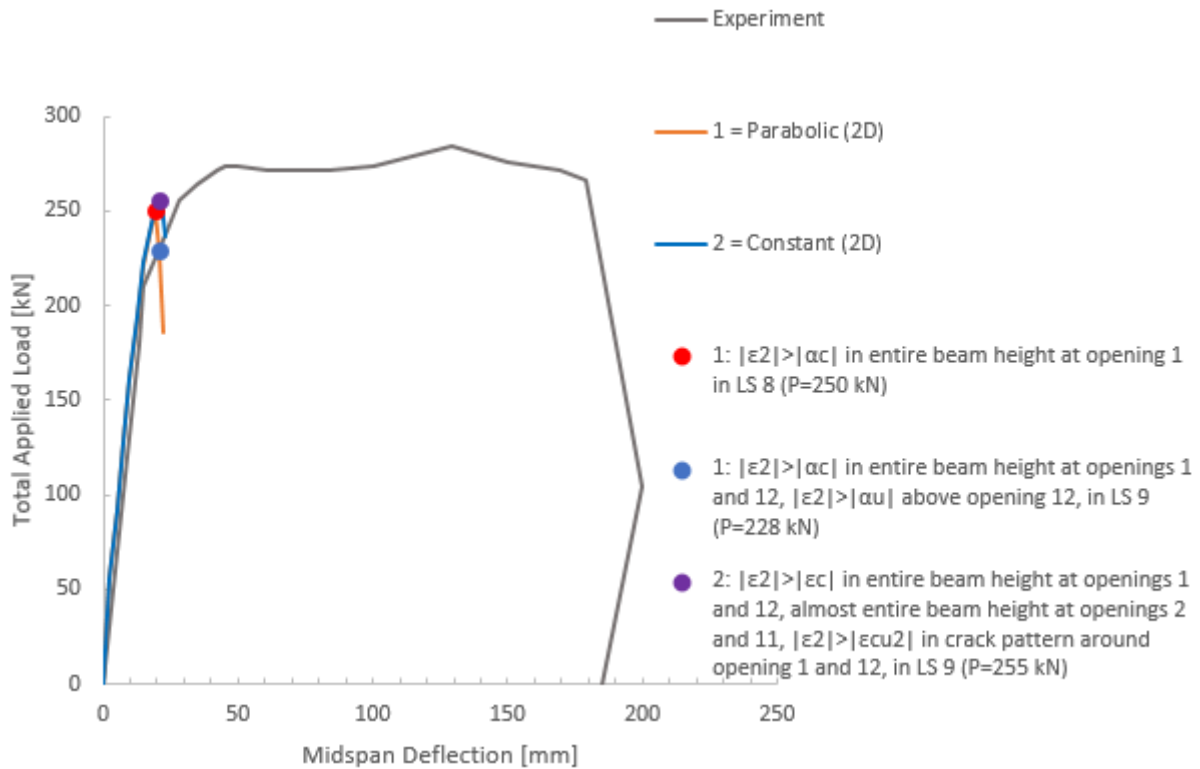


Figure 3.87: RCxcb (2D). LDCs from the NLFEAs with different compressive behaviour functions, and the experimental LDC. The numerical LDCs are marked with observations of concrete crushing.

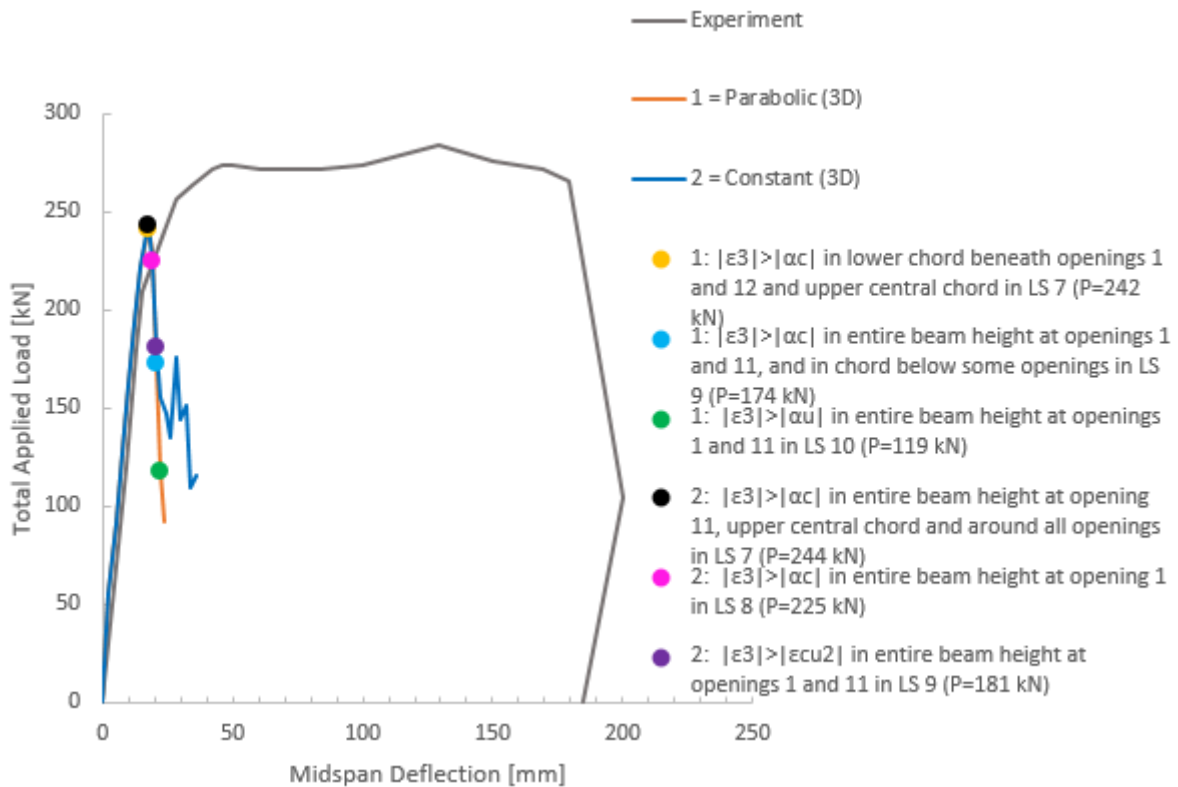


Figure 3.88: RCxcb (3D). LDCs from the NLFEAs with different compressive behaviour functions, and the experimental LDC. The numerical LDCs are marked with observations of concrete crushing.

The specific compressive strain values that are used to post-process Analysis 2, are listed in Table 3.62. When the absolute value of the principal compressive strain (2D: $|\epsilon_2|$, 3D: $|\epsilon_3|$) exceeded $|\epsilon_c|$ in the integration points of the finite elements, the concrete compressive capacity was reached. As mentioned, $|\epsilon_{cu2}|$ was used as a limit value in order to evaluate the development of compressive strains in this analysis. Figures 3.89 and 3.90 show principal compressive strain plots from essential LSs with respect to crushing in the 2D and the 3D model in Analysis 2.

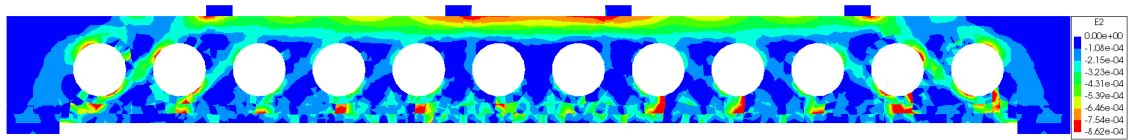
Table 3.62: RCxcb. Specific compressive strain values for constant stress-strain curve.

Strain (Constant)	Formula	Value	Compressive stress
ϵ_c	$-\frac{f_{cm}}{E_c}$	$-8.62 \cdot 10^{-4}$	$\sigma = f_{cm}$
ϵ_{cu2}		$-3.50 \cdot 10^{-3}$	$\sigma = f_{cm}$

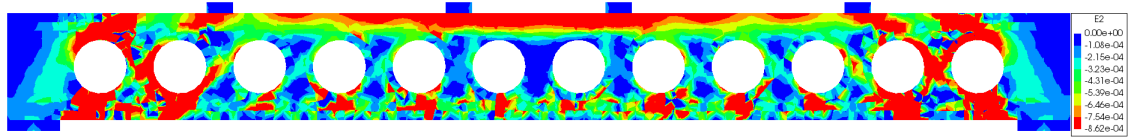
Figure 3.89 presents the strain plots for the 2D model in Analysis 2. The first signs of crushing was observed in LS 4 (P=162 kN), under the load plates and in smaller areas around the web openings. In LS 9 (P=255 kN), crushing was prominent in the entire beam height at web opening 1 and 12, and almost in the entire beam height at web opening 2 and 11. Additionally, crushing was observed in the upper central chord and beneath all web openings. In this LS, $|\epsilon_{cu2}|$ was also exceeded in the entire beam height at web opening 1, and almost in the entire height at web opening 12. The areas of crushed concrete were located in the same path as where the critical shear crack developed. Similarly as in Analysis 1, the 2D model got crushed concrete in a symmetrical pattern in Analysis 2.

Figure 3.90 presents the compressive strain plots for the 3D model in Analysis 3. The first signs of crushing occurred in the upper central chord, below load plates and in smaller areas around web openings in LS 4 (P=161 kN). At peak load level, in LS 7 (P=244 kN), areas of crushed concrete propagated through opening 11, along with in local areas around openings and in upper central chord. Post peak, in LS 8 (P=225 kN), it was observed areas of crushed concrete in the entire beam height at web openings 1 and 11. In LS 9 (P=181 kN), ϵ_{cu2} was reached in these areas, and additionally in the lower chord beneath web opening 2 and 12. A similar unsymmetrical path of crushed concrete was established for the 3D model in both Analysis 1 and 2.

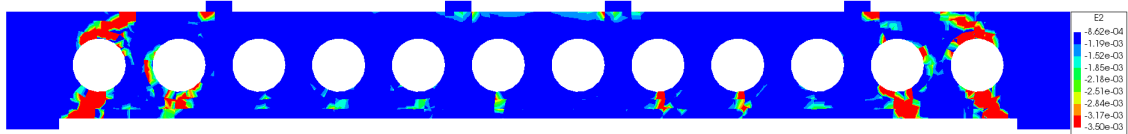
However, the area of crushed concrete was more comprehensive in Analysis 2 than in Analysis 1, in both the 2D and the 3D model. The 2D model reached a higher peak load than the 3D model in Analysis 2. A higher applied load was required in order to achieve crushed concrete through the entire beam height in the 2D model compared to in the 3D model.



(a) LS 4 (P=162 kN). Red colour= $|\epsilon_2| > |\epsilon_c|$.

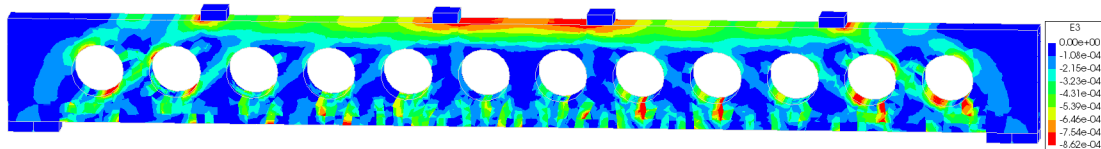


(b) Peak LS 9 (P=255 kN). Red colour= $|\epsilon_2| > |\epsilon_c|$.

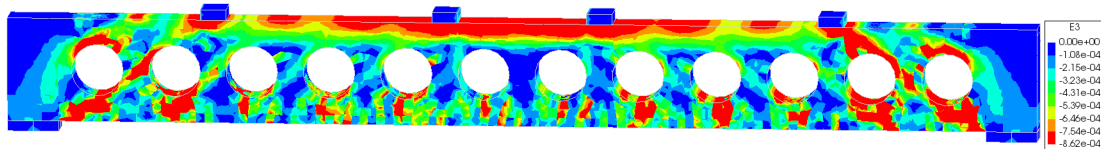


(c) Peak LS 9 (P=255 kN). Red colour= $|\epsilon_2| > |\epsilon_{cu2}|$. Blue colour= $|\epsilon_2| < |\epsilon_c|$.

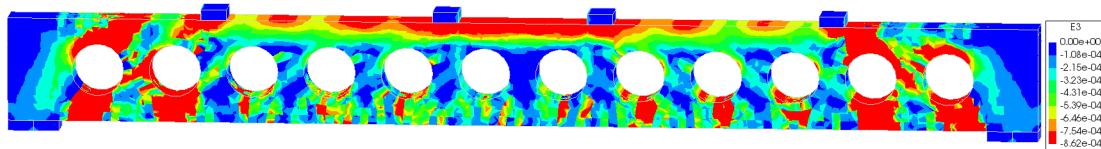
Figure 3.89: RCxcb (2D). Principal compressive strain plots from essential LSs in NLFEA with constant compressive behaviour function.



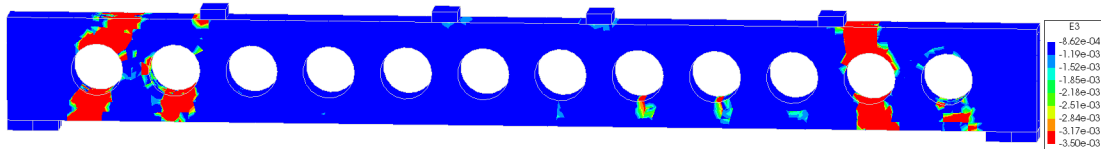
(a) LS 4 (P=161kN). Red colour= $|\epsilon_3| > |\epsilon_c|$.



(b) Peak LS 7 (P=244kN). Red colour= $|\epsilon_3| > |\epsilon_c|$.



(c) Post-peak LS 8 (P=225kN). Red colour= $|\epsilon_3| > |\epsilon_c|$.



(d) Post-peak LS 9 (P=181kN). Red colour= $|\epsilon_3| > |\epsilon_{cu2}|$. Blue colour= $|\epsilon_3| < |\epsilon_c|$.

Figure 3.90: RCxcb (3D). Principal compressive strain plots from essential LSs in NLFEA with constant compressive behaviour function.

Figures 3.91 and 3.92 show the reaction forces in the supports from Analyses 1 and 2, in the 2D and the 3D model respectively. The clear drop in all curves indicates that non of the models were able to transfer load to the supports after failure mechanisms were formed.

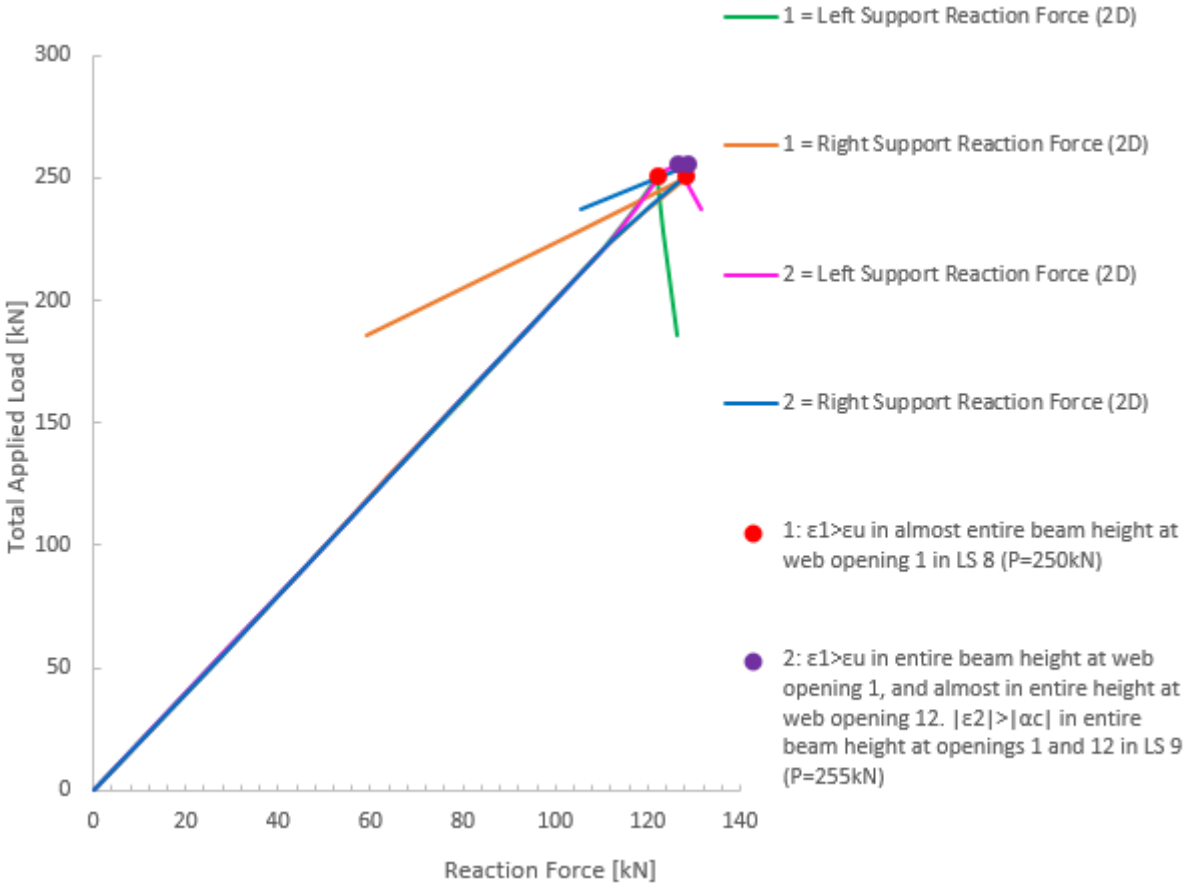


Figure 3.91: RCxcb (2D). Reaction forces from the NLFEAs with different compressive behaviour functions. The curves are marked with crack- and crushing observations.

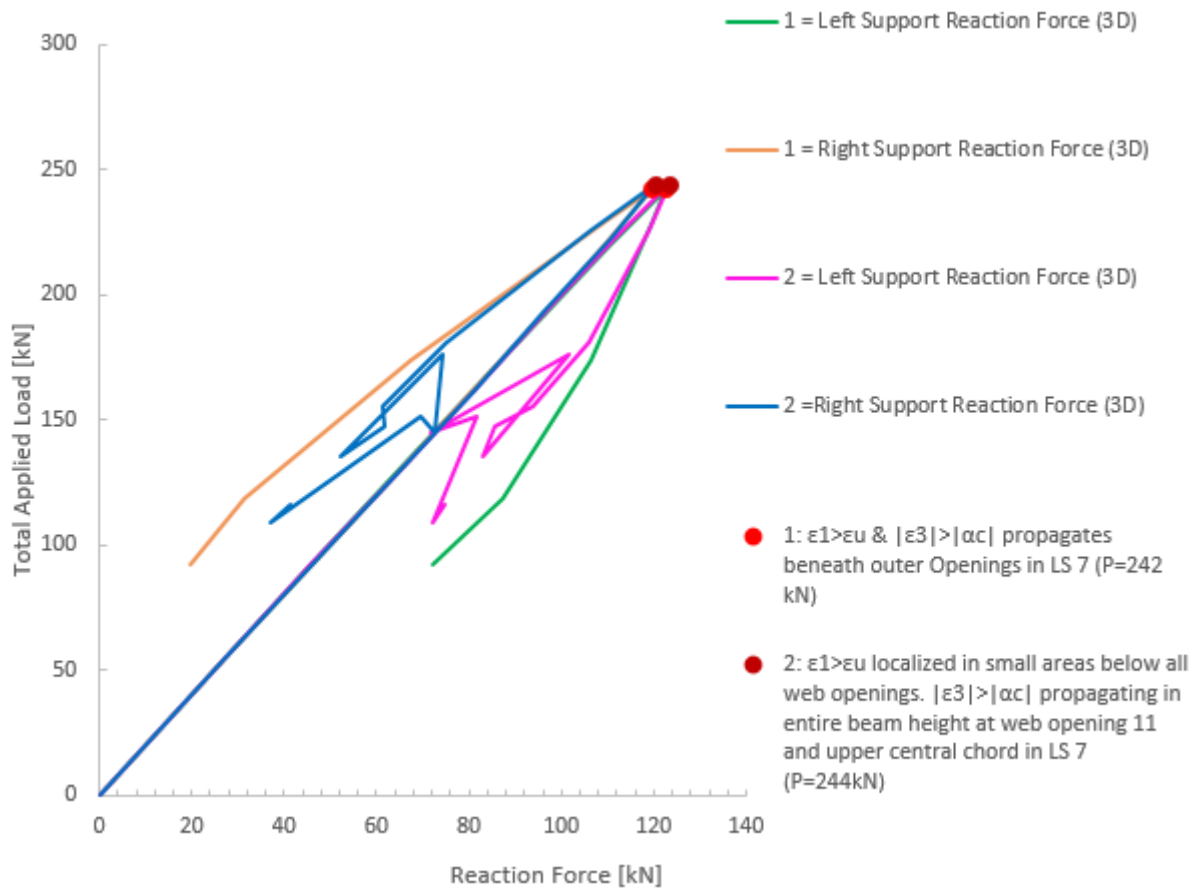


Figure 3.92: RCxcb (3D). Reaction forces from the NLFEAs with different compressive behaviour functions. The curves are marked with crack- and crushing observations.

As in Analysis 1, yielding of reinforcement was observed in the same critical areas in Analysis 2. The main longitudinal reinforcement did not yield before a failure mechanism was established.

Table 3.63 presents the obtained 2D and 3D failure modes in Analysis 1 and 2 of this sensitivity study. The two analyses yielded the same brittle failure mechanism in both models. A larger load was taken up by both the 2D and the 3D RCxcb model in Analysis 2 than in Analysis 1. Since the realistic failure load, obtained in the experiment, was underestimated in all these NLFEAs, Analysis 2 achieved a lower modelling uncertainty than Analysis 1.

Table 3.63: RCxcb. Failure mode and failure load from the NLFEAs with different compressive behaviour functions.

Analysis	Failure Mode	Failure Load	Modelling Uncertainty $(\frac{R_{exp}}{R_{NLFEA}})$
1 (2D)	Diagonal Tension Failure combined with Web Crushing Failure	250 kN	1.14
2 (2D)	Diagonal Tension Failure combined with Web Crushing Failure	255 kN	1.11
1 (3D)	Diagonal Tension Failure combined with Web Crushing Failure	242 kN	1.18
2 (3D)	Diagonal Tension Failure combined with Web Crushing Failure	244 kN	1.17

Shear Retention Model

Constant and damage based shear retention models were tested on RCxcb in order to investigate the sensitivity related to this parameter. Two shear retention factors, $\beta=0.1$ and $\beta=0.01$ were used for the constant model. Post-analysis checks for spurious tensile strength, crack pattern, crushing and load distribution were conducted.

Throughout this sensitivity study, the following designations will be used as references for the three NLFEAs of RCxcb with different shear retention approaches:

Analysis 1: Damage based shear retention model.

Analysis 2: Constant shear retention model with $\beta=0.1$.

Analysis 3: Constant shear retention model with $\beta=0.01$.

The LDCs obtained with the different shear retention models, in both 2D and 3D, are shown in Figures 3.93 and 3.94. The numerical curves are marked with dots that indicates crack observations in the concrete. The crosses indicates non-converged LSs. All analyses resulted in non-converged steps after the peak load level was exceeded.

In all analyses related to this sensitivity study for RCxcb, the same TS approach was used. Specific tensile strain values describing the concrete tensile behaviour are defined in Table 3.46. All the contour plots in Figures 3.95, 3.96, 3.97 and 3.98 are specified with these tensile strain limits, in to identify the tensile softening process in the beam.

Figure 3.95 presents the 2D model plots of the principal tensile strains from Analysis 2. Red areas represents concrete with $\epsilon_1 > \epsilon_u$, indicating completely softened material, and hence fully open cracks. In LS 11 (P=342 kN), small areas of fully open cracks were observed, as shown in Figure 3.95a. The slope of the LDC was slightly decreased in this LS. In LS 59 (P=444 kN) fully open cracks were established in the entire lower chord below openings 5,6,7 and 8, as shown in Figure 3.95b. In LS 81 (P=428kN) fully open cracks were observed through the entire height of the beam at opening 1, 2, 11 and 12, as shown in Figure 3.95c.

Figure 3.96 presents plots of the principal tensile strains in the 3D model from Analysis 2. A

similar crack pattern was observed in both the 2D and the 3D model.

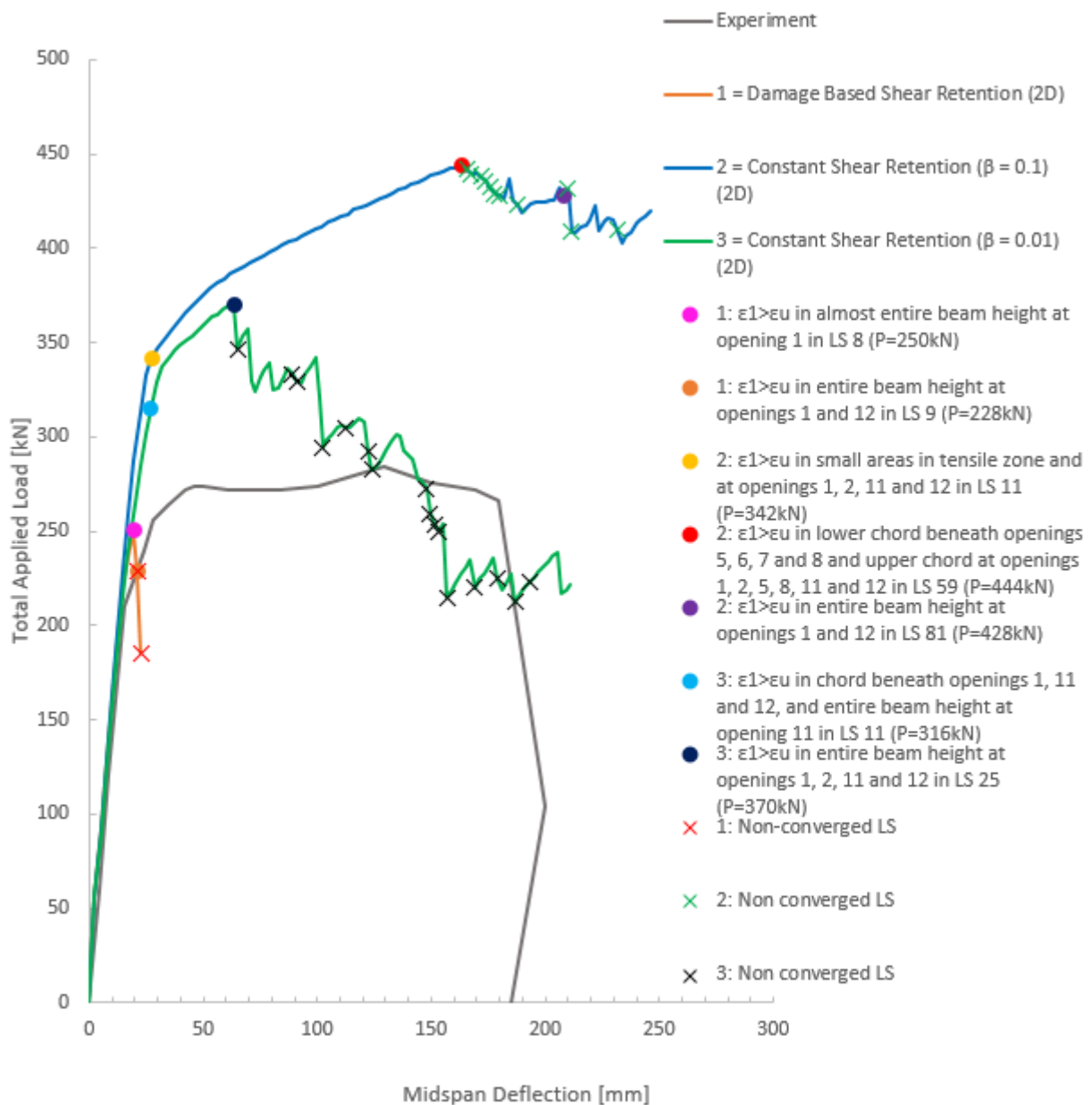


Figure 3.93: RCxcb (2D). LDCs from the NLFEAs with different shear retention models, and the experimental LDC. The numerical LDCs are marked with crack observations and non-converged LSs.

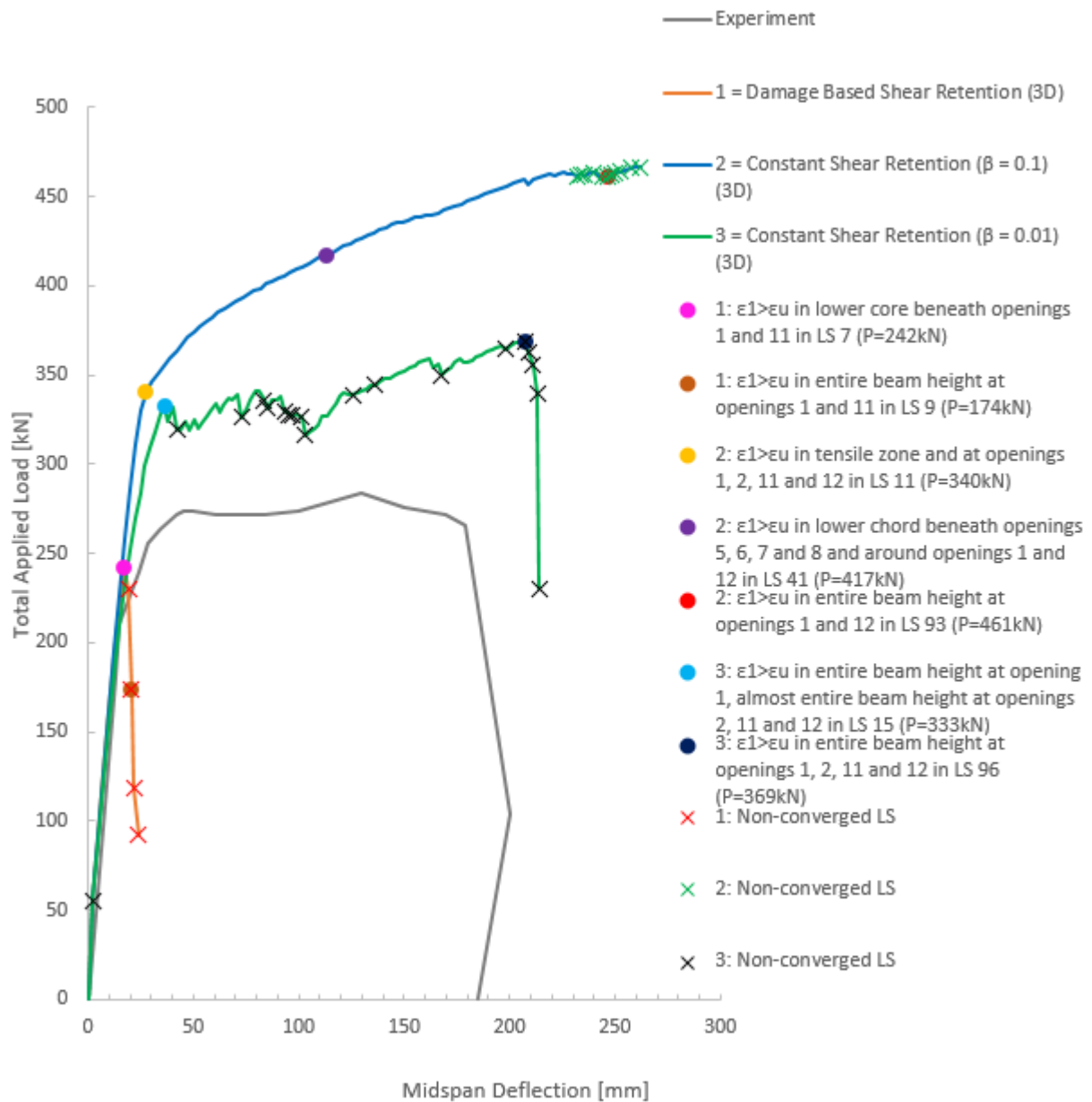


Figure 3.94: RCxcb (3D). LDCs from the NLFEAs with different shear retention models, and the experimental LDC. The numerical LDCs are marked with crack observations and non-converged LSs.

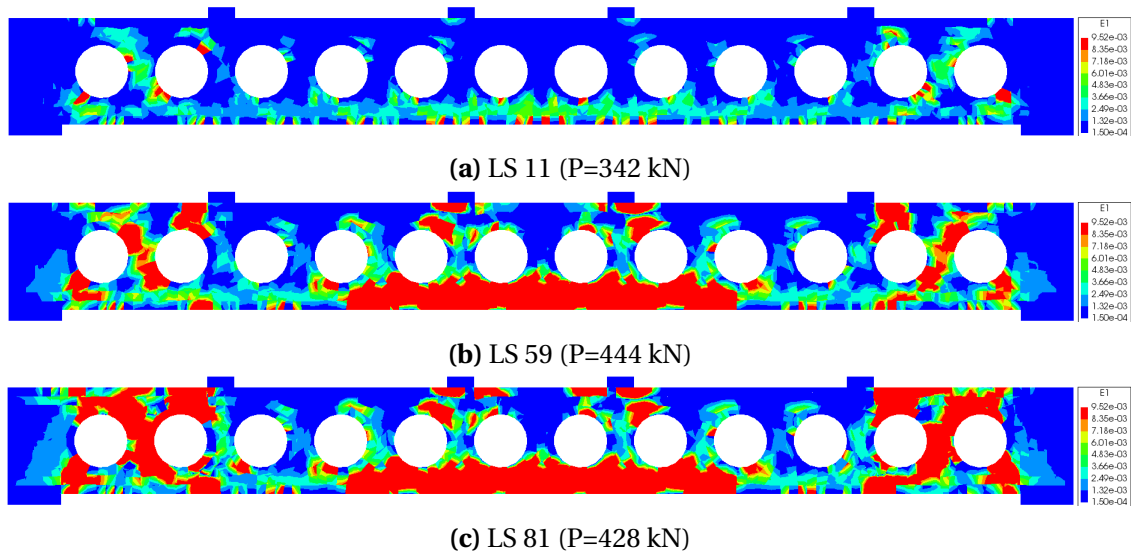


Figure 3.95: RCxcb (2D). Principal tensile strain plots from the NLFEA with constant shear retention factor $\beta=0.1$. Red colour= $\epsilon_1 > \epsilon_u$. Blue colour= $\epsilon_1 < \epsilon_{peak}$.

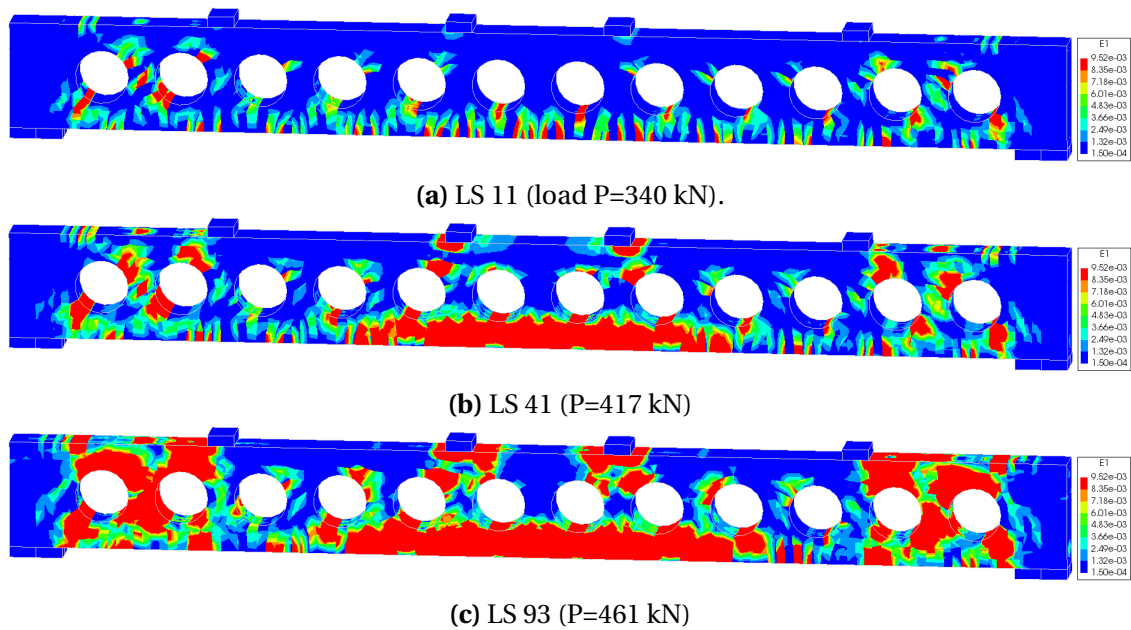


Figure 3.96: RCxcb (3D). Principal tensile strain plots from the NLFEA with constant shear retention factor $\beta=0.1$. Red colour= $\epsilon_1 > \epsilon_u$. Blue colour= $\epsilon_1 < \epsilon_{peak}$.

Figure 3.97 presents the 2D model plots of the principal tensile strains from Analysis 3. In LS 11 (P=342 kN) of this analysis, fully open cracks occurred in the entire lower chord beneath opening 1, and 12 and through the entire height of the beam at opening 11, as shown in Figure 3.97a. From LSs 11 to 25 (P=370 kN), fully open cracks were established in several parts of the beam. In LS 25, it was also observed fully open cracks through the entire height of the beam at web opening 1, 2, 3 and 12, as shown in Figure 3.97b. In addition, the lower chord beneath opening 5, 6, 7 and 8 was also fully softened in tension. In the LDC of Analysis 3, shown in Figure 3.93, it is observed a clear load drop after LS 25.

Figure 3.98 presents the 3D model plots of the principal tensile strains from Analysis 3. In LS 15 (P=333 kN) of this analysis, fully open cracks were observed through the entire height of the beam at opening 1, 2, 11 and 12, as shown in Figure 3.98a. From LS 15 to 96 (P=369 kN), the analysis suffered of several non-converged LSs, visualized in Figure 3.94. In LS 96, the concrete was completely softened in tension in the entire part of the beam from the supports to the outer load plates, as shown in Figure 3.98b.

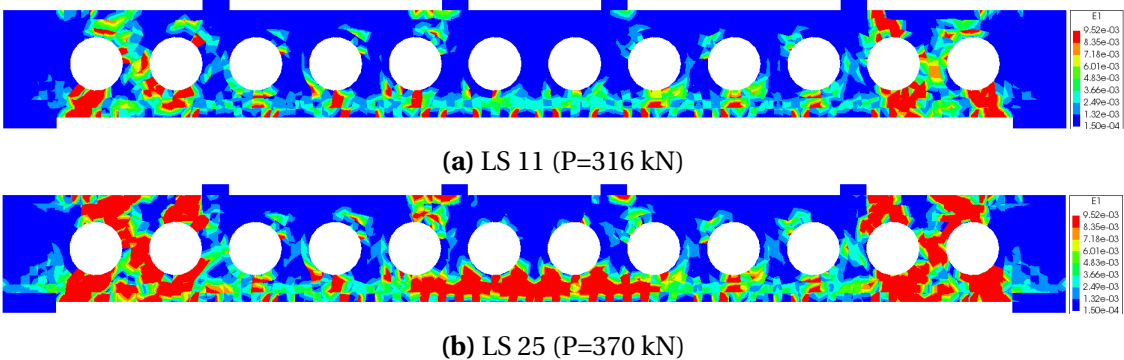


Figure 3.97: RCxcb (2D). Principal tensile strain plots from NLFEA with constant shear retention with $\beta=0.01$. Red colour= $\epsilon_1 > \epsilon_u$. Blue colour= $\epsilon_1 < \epsilon_{peak}$.

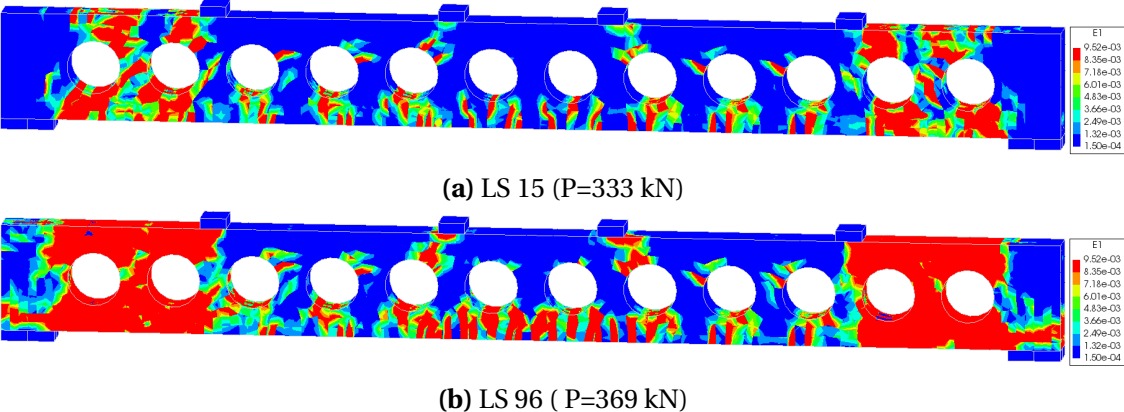


Figure 3.98: RCxcb (3D). Principal tensile strain plots from NLFEA with constant shear retention with $\beta=0.01$. Red colour= $\epsilon_1 > \epsilon_u$. Blue colour= $\epsilon_1 < \epsilon_{peak}$.

Figures 3.99 and 3.100 show the LDCs obtained with the different shear retention models, for the 2D and the 3D model respectively. The numerical curves are marked with dots that indicate specific observations related to the compressive behaviour of the concrete.

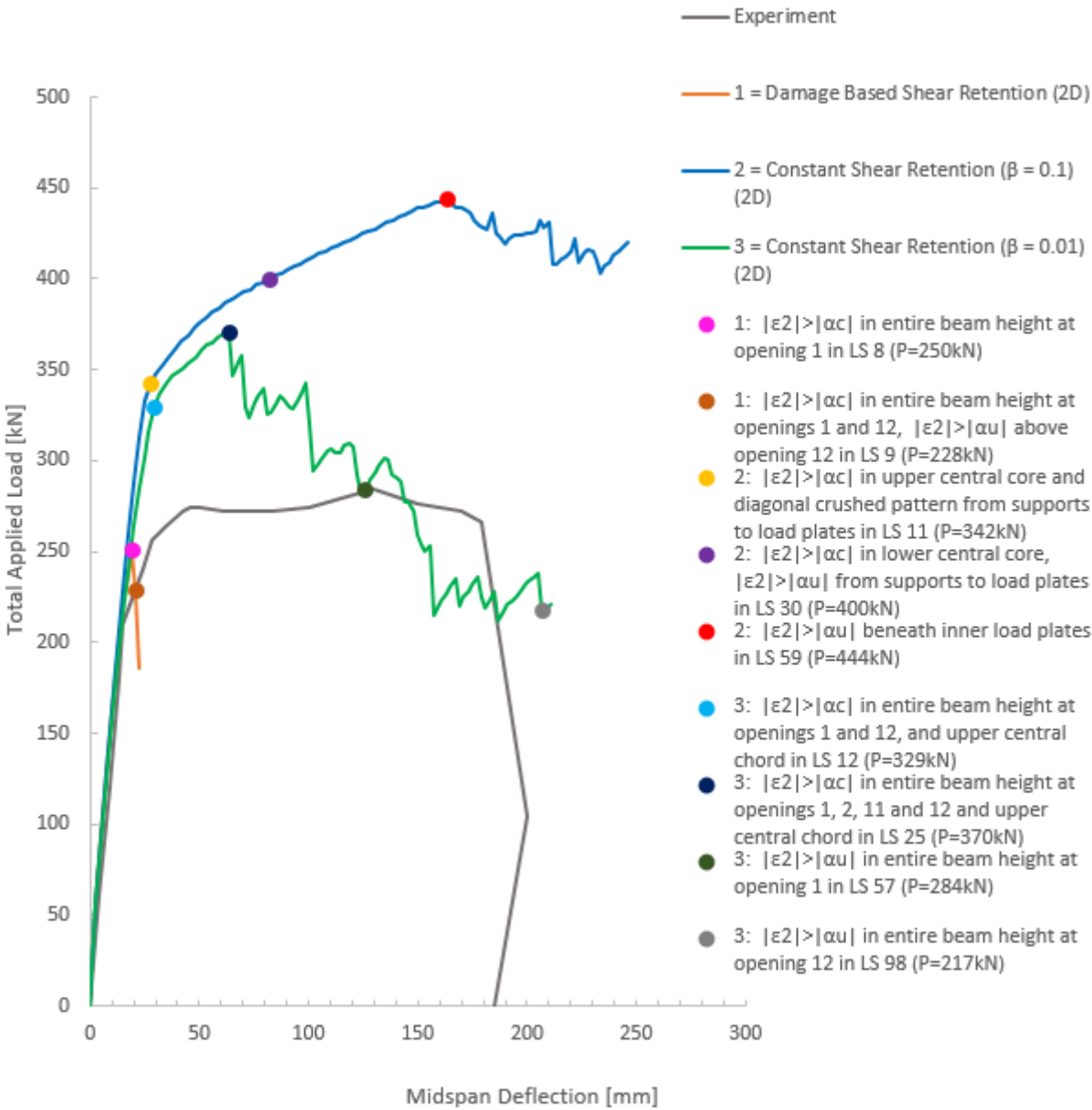


Figure 3.99: RCxcb (2D). LDCs from the NLFEAs with different shear retention models, and the experimental LDC. The numerical LDCs are marked with observations of concrete crushing.

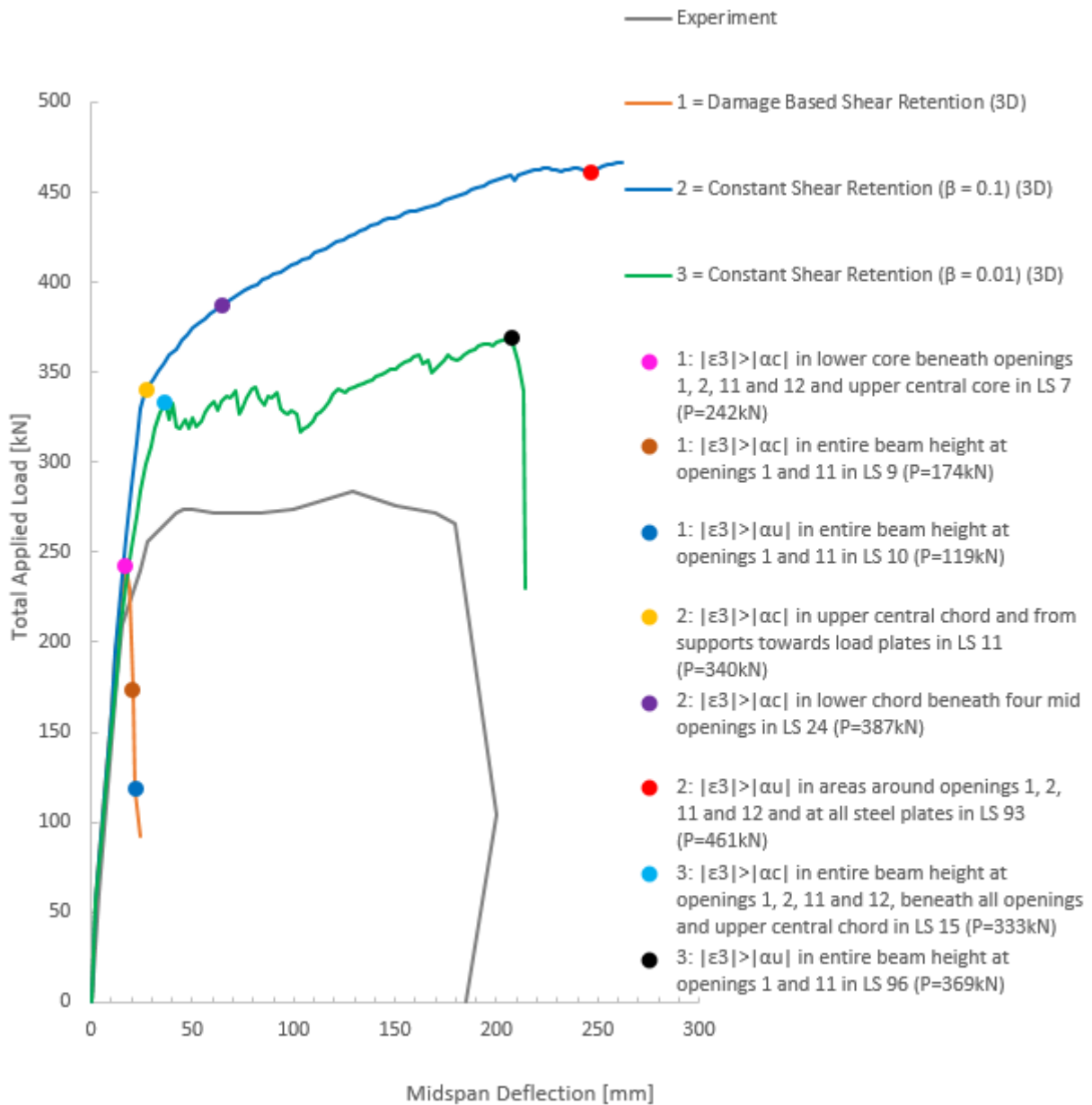


Figure 3.100: RCxcb (3D). LDCs from NLFEAs with different shear retention models, marked with observations of concrete crushing.

All analyses in this section utilizes a parabolic function for the concrete compressive behaviour. Specific compressive strain values describing the concrete compressive behaviour are defined in Table 3.50. All the contour plots shown in Figures 3.101, 3.102, 3.103 and 3.104 are specified with these compressive strain limits, in order to identify the compressive softening process in the beam. The concrete started to crush when $|\epsilon_2| > |\alpha_c|$ in the 2D model, and when $|\epsilon_3| > |\alpha_c|$ in the 3D model. Completely softened concrete was obtained when $|\epsilon_2|$ and $|\epsilon_3|$ exceeded $|\alpha_u|$.

Figure 3.101 presents the principal compressive strains plots for the 2D model in Analysis 2. In LS 11 (P=342 kN) of this analysis, crushed concrete was observed in the upper central chord, in addition to a crushed diagonal path between the supports and the outer load plates. In LS 30 (P=400 kN), this diagonal crushed path had expanded through the entire beam height, as shown in Figure 3.101b. Crushed concrete was at this stage also observed in the lower chord beneath opening 5, 6, 7 and 8. In LS 59 (P=444 kN), the concrete was completely softened in compression in a small area under the central load plates, as shown in Figure 3.101c. The pattern of crushed concrete occurred in the same path as fully open cracks were established.

Figure 3.102 presents the principal compressive strains plots for the 3D model in Analysis 2. In LS 11 (P=340 kN) of this analysis, a diagonal pattern of crushed concrete was observed, similarly as for the 2D model. This is shown in Figure 3.102a. In LS 24 (P=387 kN), larger areas of crushed concrete were observed, as shown in Figure 3.102b. This was also similar as for the 2D model, but at a lower applied load. In LS 93 (P=461 kN), large areas of the concrete were completely softened in compression, as shown in Figure 3.102. The areas of concrete that were completely softened in compression were more comprehensive in the 3D model than in the 2D model at this final stage.

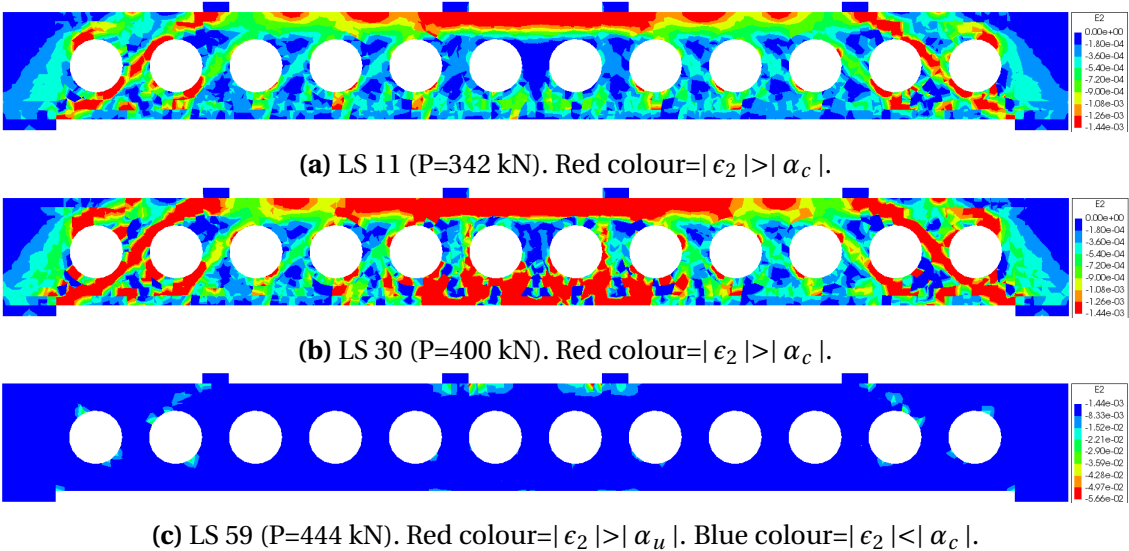


Figure 3.101: RCxcb (2D). Principal compressive strain plots from NLFEA with constant shear retention factor $\beta=0.1$.

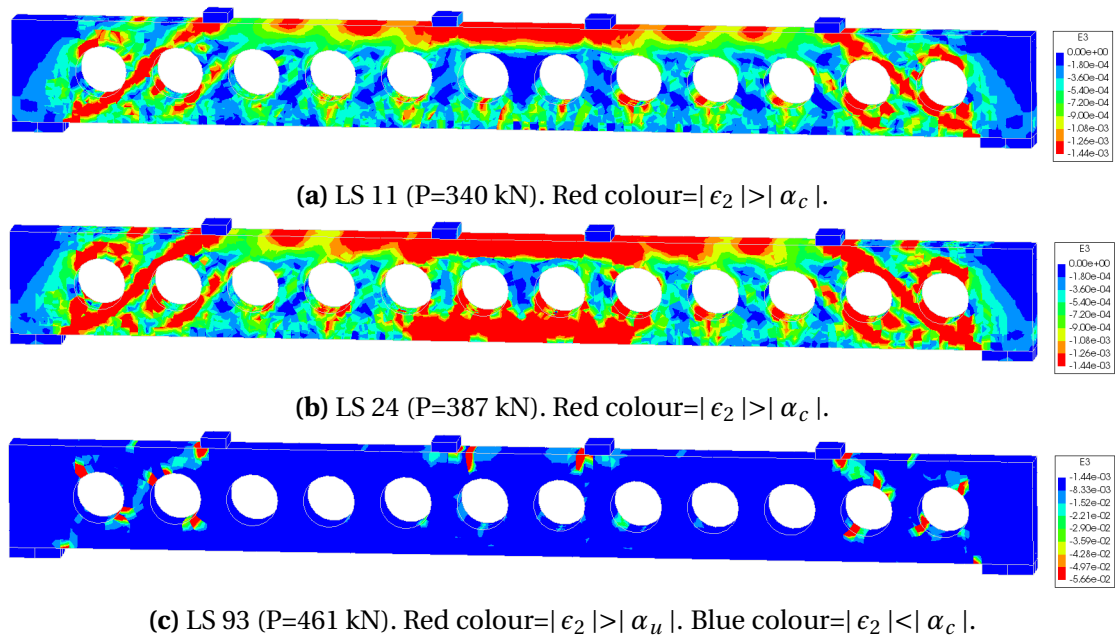
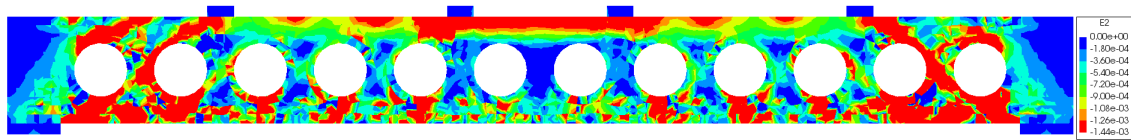


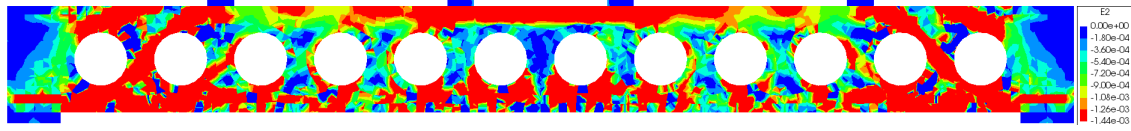
Figure 3.102: RCxcb (3D). Principal compressive strain plots from NLFEA with constant shear retention factor $\beta=0.1$.

Figure 3.103 presents the principal compressive strains plots of the 2D model from Analysis 3. In LS 12 (P=329 kN) of this analysis, it was observed crushed concrete in the upper central chord and through the entire height of the beam around the outer openings. This situation is shown in Figure 3.103a. Compared to the plot for the 2D model in Analysis 2, the crushing pattern differs at this stage. In LS 25 (P=370 kN), the concrete was crushed through the entire height of the beam at opening 1, 2, 11 and 12. In addition, crushing were prominent in the upper and lower central chord, as shown in Figure 3.103b. At this LS, a clear load drop was observed in the respective LDC. In LS 57 (P=284 kN), the concrete was completely softened in compression in the entire beam height at opening 1. In LS 98 (P=217 kN), complete compressive softening was also observed in entire beam height at opening 12, as shown in Figure 3.103d.

Figure 3.104 presents the principal compressive strains plots of the 3D model from Analysis 3. As shown in the LDC for this analysis, a peak was detected in LS 15 (P=346 kN), before the curve flattened. As shown in Figure 3.104a, the concrete was crushed through the entire height of the beam at opening 1, 2, 11 and 12 in this LS. In addition, the upper central chord and the lower chord below all openings were crushed. In LS 96 (P=369 kN), the concrete was completely softened in compression through the entire height of the beam at opening 1 and 11, as shown in Figure 3.104b.



(a) LS 12 (P=329 kN). Red colour= $|\epsilon_2| > |\alpha_c|$.



(b) LS 25 (P=370 kN). Red colour= $|\epsilon_2| > |\alpha_c|$.

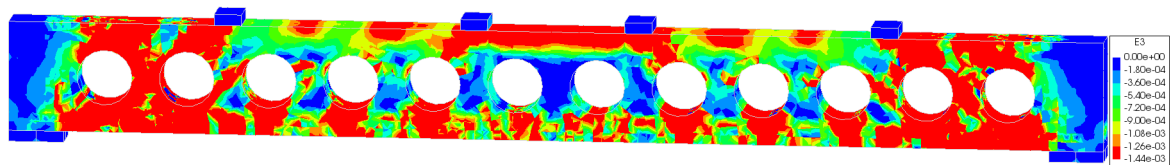


(c) LS 57 (P=284 kN). Red colour= $|\epsilon_2| > |\alpha_u|$. Blue colour= $|\epsilon_2| < |\alpha_c|$.

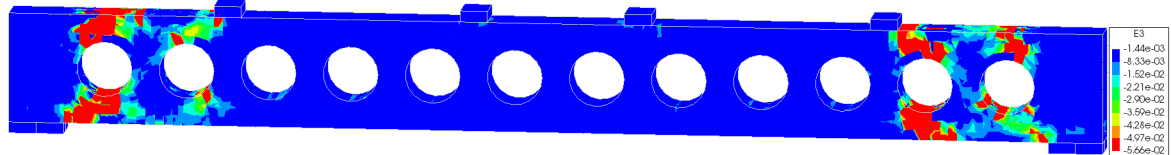


(d) LS 98 (P=217 kN). Red colour= $|\epsilon_2| > |\alpha_u|$. Blue colour= $|\epsilon_2| < |\alpha_c|$.

Figure 3.103: RCxcb (2D). Principal compressive strain plots from NLFEA with constant shear retention factor $\beta=0.01$.



(a) LS 15 (P=346 kN). Red colour= $|\epsilon_2| > |\alpha_c|$.



(b) LS 96 (P=369 kN). Red colour= $|\epsilon_2| > |\alpha_u|$. Blue colour= $|\epsilon_2| < |\alpha_c|$.

Figure 3.104: RCxcb (3D). Principal compressive strain plots from NLFEA with constant shear retention factor $\beta=0.01$.

Figures 3.105 and 3.106 present the development of the support reaction forces in both the 2D and the 3D model from Analysis 2 and 3 of this sensitivity study. These analyses yielded a ductile behaviour for both the 2D and the 3D model. The supports were able to take up more load after the concrete was fully softened in tension through the entire beam height in the areas of the load transferring struts.

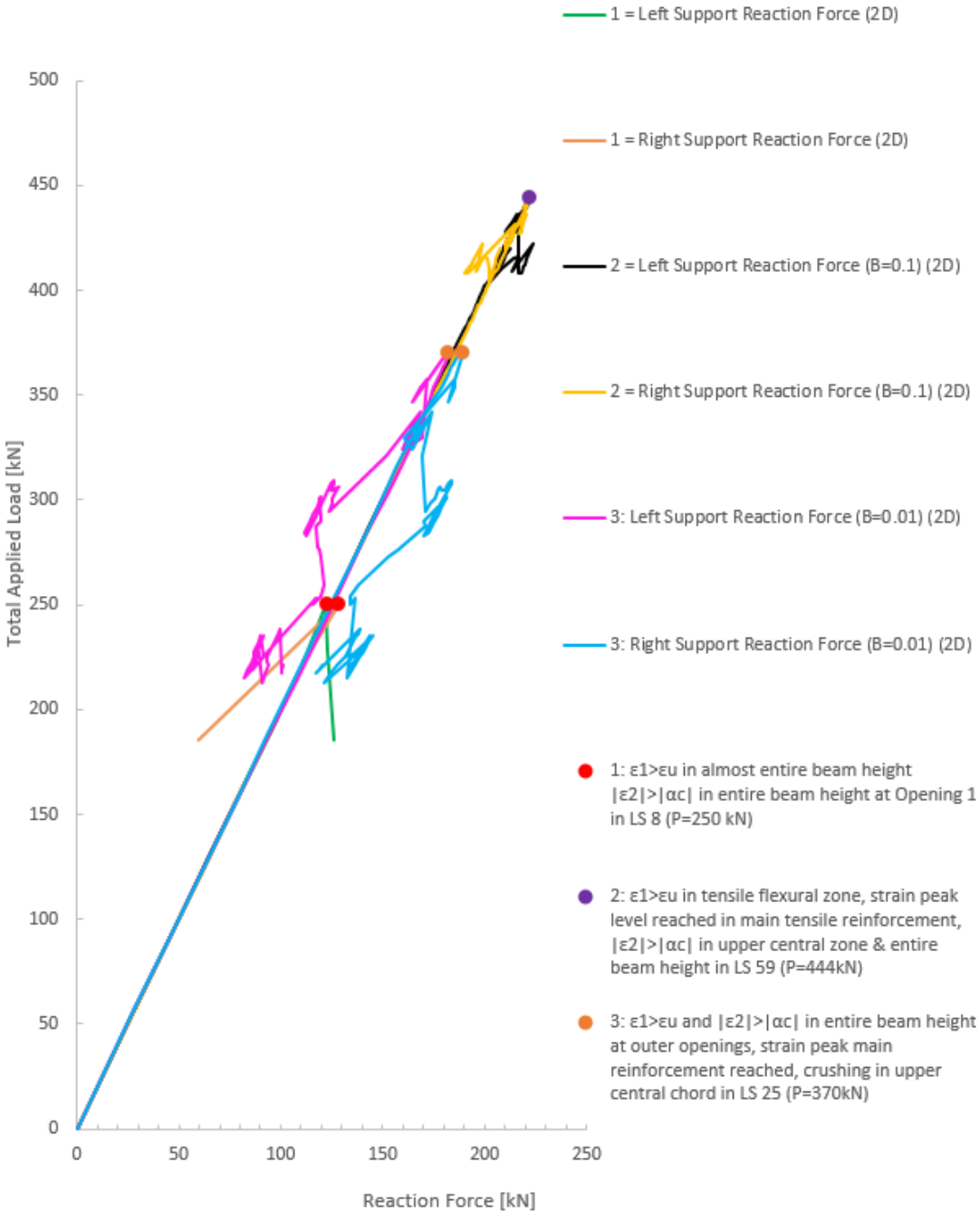


Figure 3.105: RCxcb (2D). Reaction forces from the NLFEMs with different shear retention models. The curves are marked with crack- and crushing observations.

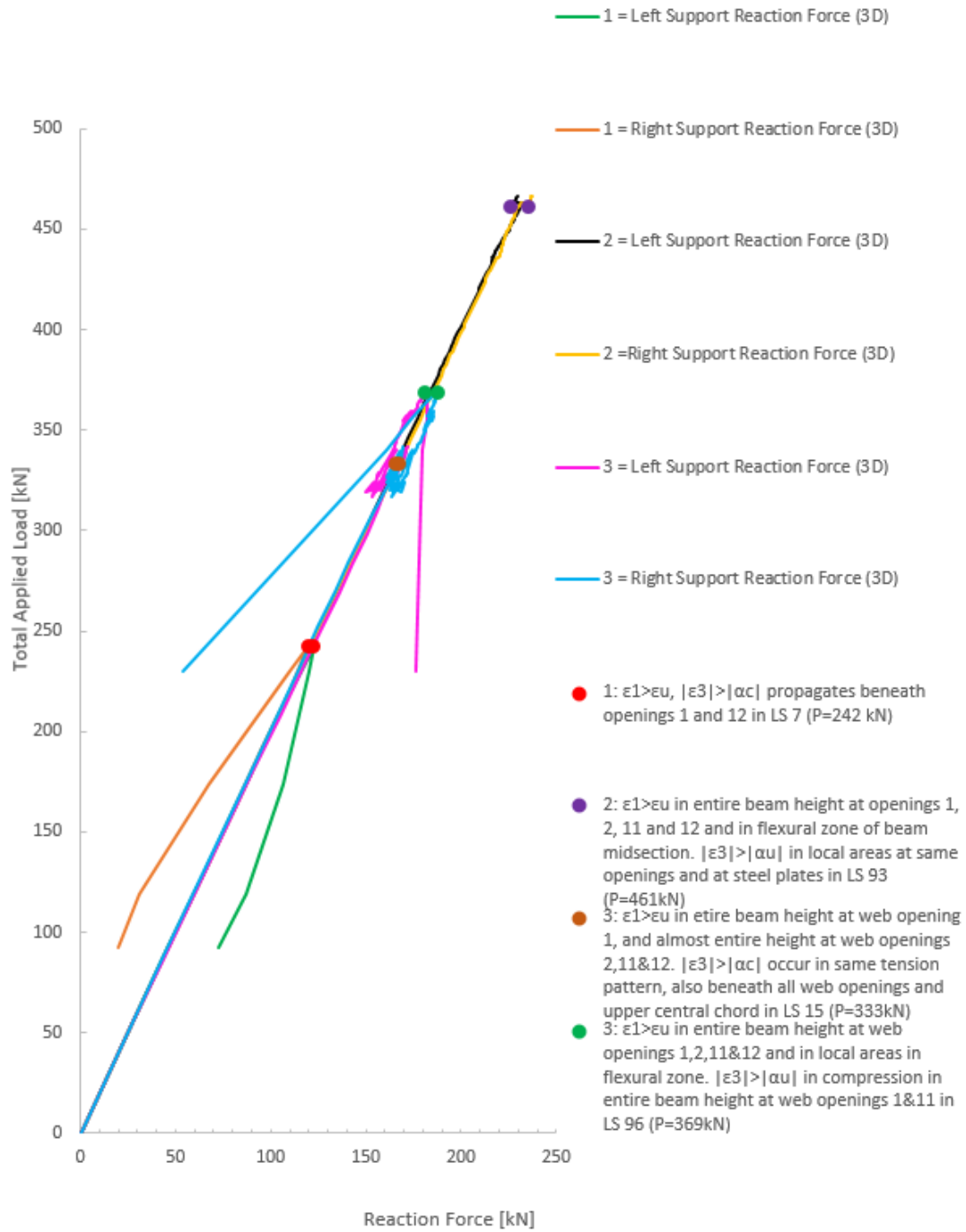


Figure 3.106: RCxcb (3D). Reaction forces from the NLFEMs with different shear retention models. The curves are marked with crack- and crushing observations.

In Analysis 2 of the 2D model, the main tensile reinforcement ($\phi 12$) reached its mean yield strain limit in nodal points in LS 10 ($P=332$ kN). The ultimate strain for the same bars, $2.75 \cdot 10^{-2}$, was exceeded in LS 30. The maximum strain obtained was $4.70 \cdot 10^{-2}$ in LS 59. The main compressive reinforcement ($\phi 12$) reached a minimum strain value of $-2.70 \cdot 10^{-3}$ in LS 59 and experienced decreased stresses afterwards. The vertical ($\phi 10$) reinforcement in the outer posts reached a maximum strain value of $4 \cdot 10^{-2}$ in LS 85. The ultimate strain, $5.73 \cdot 10^{-2}$, was never achieved in those bars. Yielding in ($\phi 4$) stirrups in the upper and lower chord was most prominent at web opening 1 and 12. These bars exceeded the yield strain of $2.60 \cdot 10^{-3}$ in LS 10. The maximum observed strain in these bars was $1 \cdot 10^{-2}$, achieved in LSs 80 and 90.

In Analysis 3 of the 2D model, the main tensile reinforcement ($\phi 12$) reached the yield strain in LS 11 ($P=316$ kN). Afterwards the strain value increased drastically until a peak strain value of approximately $1.70 \cdot 10^{-2}$ was observed in LS 25 ($P=370$ kN). The ultimate strain value, $2.75 \cdot 10^{-2}$, was never reached in the main tensile reinforcement. The main compressive reinforcement ($\phi 12$) reached a negative peak strain value of $-2.70 \cdot 10^{-3}$ in LS 25. The absolute value of the strain decreased afterwards. The vertical stirrups ($\phi 10$) in the outer posts reached a maximum strain value of $2 \cdot 10^{-2}$ in LS 60 ($P=297$ kN). Hence, the ultimate strain in these bars was never reached. Yielding of stirrups ($\phi 4$) in upper and lower chords was detected in LS 10 ($P=302$ kN) outside opening 1 and 12. The maximum strain in the respective bars was observed in LS 40, with a value of $1 \cdot 10^{-2}$.

In Analysis 2 of the 3D model, the main tensile reinforcement ($\phi 12$) started to yield in LS 10 ($P=330$ kN). The same bars reached a peak strain value of approximately $6 \cdot 10^{-2}$ in LS 80 ($P=463$ kN). The main compressive reinforcement ($\phi 12$) reached a negative peak strain value of $-9 \cdot 10^{-2}$ in LS 80 ($P=463$ kN). Afterwards the strain values stabilized. The vertical ($\phi 10$) reinforcement in the outer posts reached a maximum strain value of $3.70 \cdot 10^{-2}$ in LS 95 ($P=464$ kN). However, the respective ultimate strain value was never reached. The same bars started to yield between LSs 80 and 90. Yielding in ($\phi 4$) stirrups started in LS 10 ($P=330$ kN), and was most prominent in the upper and lower chords at web opening 1 and 12. A peak value of $8 \cdot 10^{-2}$ was reached in LS 100.

In Analysis 3 of the 3D model, the main tensile reinforcement ($\phi 12$) started to yield in LS 15 ($P=333$ kN). The strain value continued to increase until a peak strain value of approximately $1.70 \cdot 10^{-2}$ was obtained in LS 96 ($P=367$ kN). The main compressive reinforcement ($\phi 12$) reached a negative peak strain value of $-2.70 \cdot 10^{-3}$ in LS 96. The vertical reinforcement ($\phi 10$) in the outer posts reached a maximum strain value of $2 \cdot 10^{-2}$ in LS 72 ($P=355$ kN). Hence, the ultimate strain was not exceeded for these bars. Yielding of ($\phi 4$) stirrups in upper and lower chord was most prominent at openings 1 and 12. The stirrups started to yield in LS 10 ($P=302$ kN). The same bars obtained a high peak strain value of 0.7 in LS 96, which exceeded the ultimate strain value of $5 \cdot 10^{-2}$.

Table 3.64 presents the achieved failure modes for the 2D and the 3D models in the different analyses in related to this sensitivity study. It was observed a ductile behaviour of RCxcb in both Analysis 2 and 3. Analysis 1 and 3 yielded the same failure mechanism, while no failure was detected in Analysis 2. Both the 2D and the 3D model achieved the highest failure load in Analysis 3, with a constant shear retention factor $\beta=0.01$. Consequently, this analysis achieved the lowest modelling uncertainty.

Table 3.64: RCxcb. Failure mode and failure load from the NLFEAs with different shear retention models.

Analysis	Failure Mode	Failure Load	Modelling Uncertainty ($\frac{R_{exp}}{R_{NLFEA}}$)
1 (2D)	Diagonal Tension Failure combined with Web Crushing Failure	250 kN	1.14
2 (2D)	No Clear Failure		
3 (2D)	Diagonal Tension Failure combined with Web Crushing Failure	370 kN	0.77
1 (3D)	Diagonal Tension Failure combined with Web Crushing Failure	242 kN	1.18
2 (3D)	No Clear Failure		
3 (3D)	Diagonal Tension Failure combined with Web Crushing Failure	369 kN	0.77

3.4 Quantification of Modelling Uncertainty

Table 3.65 and Figure 3.107 summarize the global results from eight benchmark analyses. It resulted in a mean ratio of $\theta_m=1.06$ and standard deviation of $\sigma_\theta=0.174$. The coefficient of variation $V_\theta=16.4\%$ implies the scatter of the FE-outcome. V was based on the unbiased estimators for mean and standard deviation.

The benchmark analyses are based on the same solution strategy, with one exception. RCxcb was modelled with interfaces and different element types around the circular openings, described in Sec. 2.3.3.5. Only 2D analyses were included when calculating θ_m .

Table 3.65: The estimated modelling uncertainties

Beam specimen	Ultimate load experiment R_{exp} [kN]	Ultimate load NLFEA R_{NLFEA} [kN]	Ratio $\theta = \frac{R_{exp}}{R_{NLFEA}}$
6IT1		2565	0.85
T1-0	1452	1670	0.87
RCxcb (2D)	284	250	1.14
B-I-L	383	348	1.10
B-I-S	685	601	1.14
B-E-L	741	557	1.33
T3-3	1996	1889	1.06
T1-1	1728	1751	0.99
			$\theta_m=1.06$
			$V_\theta=16.4\%$

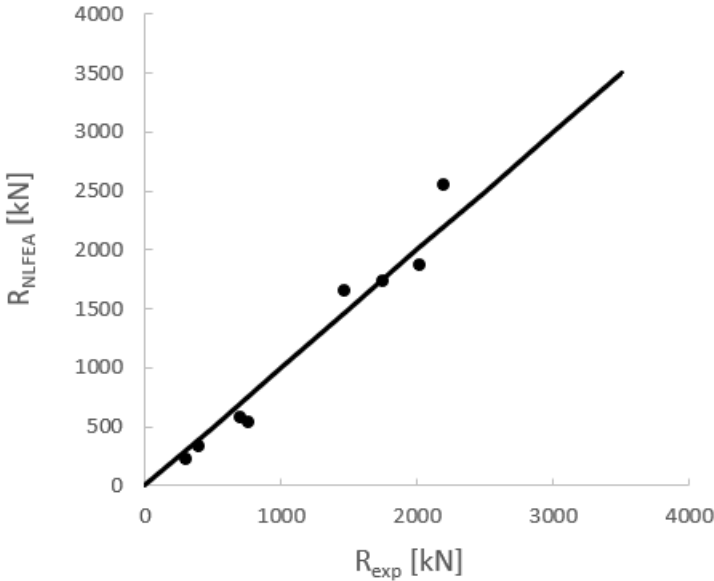


Figure 3.107: Experimental capacity and predicted capacity for nine benchmark analyses.

4. Discussion of Numerical Results

First, a general discussion regarding the modelling choices in the sensitivity study will be presented, followed by a more detailed discussion regarding the different case studies.

4.1 General Discussion

For the conducted NLFEAs where the selected solution strategy was applied, some aspects of the responses for the different FE models were similar, while some differed. This section will provide a discussion of the most prominent numerical results. The numerical response for the different FE models will be compared to the behaviour of the physical models described in the benchmark reports.

In both Case Study 1 and 2 the first microcracks appeared at a lower load in the numerical analyses than in the experiments. This was probably because cracks observed in the experiments were of a size that was visible without any instruments, while the numerical analyses detected small microcracks, that probably would not have been visible in a physical model. In Case Study 3, appearances of the first microcracks also happened at an early stage in the numerical model. However, crack development was not described in detail in the experimental report. Therefore it was not possible to determine if RCxcb generated cracks at a lower load in the NLFEA than in the physical experiment.

Common for all FE models in the case studies were that shear cracking caused failure. The failure cracks were initiated in corners of openings located in load transferring paths. The load was transferred in compressive struts from the application points and down to the supports. As the load increased, so did the the compressive stresses in these struts. Consequently, perpendicular tensile stresses and strains also increased, which led to propagation of these diagonal cracks.

Both Case Study 2 and 3 contained a great amount of shear reinforcement. Yielding of the rebars occurred in areas of reduced concrete capacity. The load transfer between reinforcement and concrete was fully utilized as embedded reinforcement was used, restricting any slip between the concrete and the reinforcement. The effect of the reinforcement was therefore introduced in the continuum elements, which described the concrete. Consequently, the reinforcement was not modelled as separate elements with separate degrees of freedom, but the strains of the rebars were determined from the displacements of the continuum elements. Due to the fact that the reinforcement had separate constitutive relations, with a higher stiffness than the concrete material had, introduction of reinforcement resulted in strengthened concrete elements in the direction of the bars. However, in reality there will always be some slip between reinforcement and concrete, due to imperfections in the materials. Consequently, the overall stiffness of the numerical models were increased compared to in the physical specimens. This could explain why the NLFEAs generated stiffer models than in the experiments, even though the same concrete strength was assigned.

Verification of the numerical models were based on comparison of the failure loads and failure modes obtained in the NLFEAs and the experiments. Published experimental studies constituted all benchmark tests. Hence, the failure modes of the physical test specimens were known. The experimental papers reported shear failure for the test specimens in Case

Study 1 and 2, while flexural crushing was crucial for the specimen in Case Study 3. However, in the experimental report for the benchmark beam in Case Study 3, tests of several beam specimens were reported. For one of the experimental test specimens with similar geometry as for the selected benchmark test, but with quadrilateral web openings instead of circular, shear failure characterized the failure mode instead of concrete crushing. Consequently, the numerical failure mode obtained in Case study 3 was prominent in one of the tested physical specimens with similar geometry.

The type of shear failure was not specified in the benchmark reports for Case Study 1 or 2. For Case Study 3 on the other hand, it was described in detail which failure modes that occurred for all the tested specimens. Consequently, in Case Study 1 and 2, the benchmark failure modes were based on the reported aspects of the response. However, this lack of information introduced uncertainties regarding the experimental type of failure. The numerical failure modes also introduced uncertainties to the verification process of the solution strategy, as the responses of the different FE models were subjectively interpreted by the analyst. The numerical failure modes were predicted based on post-analyses investigations.

For the selected solution strategy, the MC2010- and parabolic functions were used to describe the concrete tensile and compressive behaviour, respectively. For the interaction effect, Vecchio & Collins-model was applied in order to ensure a reduction of maximum allowed compressive stress in areas of large lateral tensile strains. However, these sub-models are developed independently, and are not necessarily calibrated to work well together.

As mentioned, for all the tested specimens, the global responses were highly affected by the shear behaviour. Shear loading is equivalent to a combination of both principal tensile and compressive stresses. For increased loading, and hence increased shear stresses, the principal stresses in the FE models increased. Correspondingly the principal strains increased as well. Eventually the principal tensile stresses exceeded the specified tensile strength, f_{ctm} , and cracks were initiated in the concrete. Hence, the stiffness was reduced as the tensile capacity started to follow the softening branch on the specified tensile behaviour curve. Consequently, this implied remarkably increased tensile strains.

As mentioned, the selected interaction model should provide a reduction of the compressive strength in areas of large tensile strains. To verify that this behaviour actually was provided in the numerical models, the obtained compressive stresses were checked in nodes that had achieved principal tensile strains larger than ϵ_u , hence where the concrete was completely softened in tension. If the absolute value of the compressive stresses in these points achieved a value as high as the absolute value of the specified compressive strength, this would indicate that the sub-models did not work well together.

This was carefully examined in the post-analysis investigations. For all case studies, it is proven that the compressive strength in the evaluated nodes, which had achieved large tensile strains, was reduced. Consequently, the interaction effect was achieved according to the specified interaction model.

As previously stated, for Case Study 1 and 2 the same failure modes were obtained in the numerical analyses as in the experiments. Consequently, this indicated that the selected sub-models cooperated in a way that endured a realistic concrete material behaviour in these numerical models.

In Case Study 3 it is shown that the numerical model of RCxcb yielded a brittle behaviour, while the physical model yielded a much more ductile behaviour when tested experimen-

tally. This could imply that the selected interaction model may provide a greater reduction of the compressive strength due to lateral tensile strains, than what actually was provided in the physical model. Consequently, this may indicate that the selected interaction model was not completely accurate in order to achieve a realistic concrete material behaviour for the complex failure mode in this specific FE model.

However, it was difficult to state any conclusions, as there was uncertainties related to the post-analysis checks for the crack observations. The calculated ultimate tensile strains depended on the assumed crack-band widths, which included following uncertainties:

- The crack-band width was assumed to be equal to the specified element height. However, the mesh density generated in DIANA was not consistent over the entire model. By default, the software customized the element discretization in order to generate a mesh that fitted the specific geometry. Consequently, as the crack-band width varied over the FE model, so did the ultimate tensile strain values.
- Another possible discrepancy regarding the actual crack-band width was that the elements generated in DIANA were not perfect squares. Hence, the software's definition of crack-band width, which was \sqrt{A} for higher order two-dimensional elements, did not constitute the element height, h , which was the value used in calculations of the specific strain values.
- According to DG, the equivalent length is not only based on the element dimension, but also on the crack direction. The value of the equivalent length differs based on whether cracks are generated along one of the diagonals of the element versus along one of its edges. For the value of the crack-band width used in calculations, h , cracks were considered horizontal/vertical according to this definition. For diagonal cracks the crack-band width should be estimated as the element height, h , multiplied by the square-root of two for quadratic quadrilateral elements with a square shape.

4.1.1 Sensitivity to Mesh Density

Refined mesh density generally resulted in a greater quantity of cracks. Coarser meshes resulted in wider paths of maximum tensile strains, and also larger individual crack widths. The inherent inaccuracy of the finite element method, where models discretized by coarse meshes struggle with generating smooth stress fields, affected the strain distribution. Elements and nodes may also to a larger extent have suffered from extrapolation and corresponding interpolation of stresses when larger elements were used. Hence, this may have affected the stress redistribution after crack initiation.

Another more obvious reason for the different stress fields concerns the value of the crack-band width, which was used to calculate the specific strain values. The respective strain values constituted the bounding colours in the contour plots that illustrated the distinction in path-width. Greater elements have correspondingly greater equivalent lengths. Since the denominator of the formula for ϵ_u is based on this value, larger elements result in smaller ultimate strains. Consequently, complete softening in tension occurred at lower strains for coarser mesh densities. Therefore, at specific load levels in the loading branch of the analyses, greater areas naturally achieved complete softening in tension when a coarser FE discretization was used.

The principal crack width also depended on the element size. By definition, the crack width

equals the principal strain multiplied by the element height. The peak strain, ϵ_{peak} , in the selected sub-model for the concrete tensile behaviour is consistent, and do not depend on the element size. Consequently, this justified why the width of the first initiated crack was smaller for refined meshes.

In all case studies, the NLFEAs that utilized refined mesh densities obtained the lowest failure loads. This was probably influenced by the generation of smoother stress fields, and also increased quantity of detected cracks.

The strain value that indicates complete softening in compression also depends on the crack band width and was therefore affected by the choice of mesh density. This justifies why the FE models with different element discretizations achieved different concrete compressive behaviours.

According to DG, the element size for regular 2D beams should be limited to the minimum value of $L/50$ and $H/6$. However, DG does not consider beams with web openings. Hence, the numerical solution strategy should therefore not rely solely on DG recommendations. In the NLFEAs reported in this thesis, it is shown that smaller elements did not necessarily result in more accurate results. With elements of size $L/50$, which was the finest tested mesh density for Case Study 1 and 2, one of the NLFEAs generated considerably smaller LSs than with coarser FE discretizations. In this analysis, the final LS appeared way before the load exceeded a critical level, hence no failure mechanism was formed. Consequently, element height equal to $L/50$ was not suitable for the modelling of this specific specimen.

4.1.2 Sensitivity related to choice of Tension Softening Model

In all case studies the FE models behaved differently when the concrete TS approach was changed. All NLFEAs resulted in a lower peak load for exponential TS model than for MC2010. Theoretically, the elastic branch ends at a larger strain in the MC2010 stress-strain curve than in the exponential curve. However, the differences in ϵ_{peak} -value in the curves were small for the FE models in all case studies. Consequently, the elastic branch on the LDCs obtained by use of different TS approaches was almost identical.

However, the softening branch on the LDCs differed remarkably when the TS model was changed. The ultimate strain value, ϵ_u , indicating completely softened concrete in tension is 2.5 times larger for MC2010 than for exponential TS. Hence, the area underneath the softening curve is smaller for exponential TS. This justifies why specific cracks appeared at different loads and why all FE models failed at a smaller midspan deflections when an exponential TS sub-model was used.

4.1.3 Sensitivity related to choice of Compressive Behaviour Function

Based on the numerical LDCs it was observed sensitivity related to the choice of compressive behaviour functions for the tested specimens in Case Study 1 and 2. In these case studies, the NLFEAs with concrete compressive behaviour characterized by a parabolic function, obtained a failure mode where diagonal tension cracking was combined with crushing of the concrete. Hence, the ultimate compressive strength limited the global capacity. Contrarily, when the concrete compressive behaviour was characterized by a constant function, large compressive strains did not result in reduced compressive strength. Consequently, since the original failure mode was limited by the compressive capacity in the top part of the

beams, this may explain the lack of failure in the NLFAs in Case Study 1 and 2. In Case Study 3 however, both compressive behaviour functions yielded similar LDCs. The fact that the crushing mainly occurred in the web of the model in this case study, may explain why the constant compressive function did not cause lack of failure. In the other case studies, compressive softening was crucial in flexural compression areas, where tensile strains were less prominent. The compressive strength in the beam in Case Study 3 may have been reduced by initiation of large tensile strains in the same area as where compression softening were crucial. However, due to initiation of crushing at a lower strain value when the concrete compressive behaviour was characterized by an idealized, constant function, the areas of crushed concrete was more comprehensive with this approach.

4.1.4 Sensitivity related to choice of Shear Retention Model

The results from the case studies indicate that there was sensitivity related to this aspect of the concrete constitutive model. For constant shear retention models with β different from zero, some shear capacity is always retained. In all conducted NLFAs with damage based shear retention approach, the FE models achieved some type of shear failure. With such failure modes, limited by the shear capacity, the structural response of the beam models were highly influenced by a change of shear retention approach. No clear failure load was detected in the LDCs for FE models with constant shear retention in Case Study 1 and 2. Neither was any clear failure mode identified in the post-processing of these analyses. Similarly for Case Study 3, $\beta=0.1$ did not result in a clear peak in the LDC. However, $\beta=0.01$ resulted in a clear drop in the respective LDC. The fact that all beams showed higher capacity with $\beta=0.1$ than with $\beta=0.01$ was because the percentage of retained shear capacity in the models was larger. The comparison of damage based and constant shear retention is however more complex, as the amount of retained shear stiffness with the damage based approach decreases with increased damage caused by cracking. Consequently, a damage based approach may result in greater concrete shear capacity if the FE model is not sufficiently cracked, and the β -value is relatively small. For the beam models analyzed in the case studies, cracking constituted most of the global capacity reduction. Therefore the damage based approach resulted in lowest retained shear stiffness in these NLFAs.

4.1.5 Modelling Uncertainty

The achieved modelling uncertainty for the conducted NLFAs was quantified by $\theta=1.06$ and $V_\theta=16.4\%$. This mean value, which is larger than 1, indicates that the average capacity obtained by the selected solution strategy was lower than the experimental capacity. Consequently, the numerical model underestimated the real capacity of the structure. However, as this is a mean value, the coefficient of variance is of great importance in order to be able to verify if the selected solution strategy produce accurate results. The obtained value for this coefficient, which was 16.4%, indicates that some of the NLFAs overestimated the real capacity of the structure, as the obtained mean modelling uncertainty only indicated 6% average underestimation. The fact that the analyzed RC beams had significantly different geometries probably affected the value of V_θ . More similar geometries would presumably result in a lower coefficient of variation. Additionally, the physical uncertainties, like the concrete compressive strength, presumably influenced V_θ as well. It was not given how many material tests the strength was based on in neither Case Study 1 nor 2, and the strength in Case Study 3 was only based on two material tests. As all other material parameters and depended on this uncertain value, it would implement physical uncertainty in the outcome of

the experimental capacity. Even if the value of the concrete compressive strength was based on a large number of tests, it would always remain some uncertainty related to this value due to the heterogeneous nature of the concrete material. In order to verify if the obtained value of V_θ was adequate or not, it was compared to the coefficient of variation reported in Paper IV of the PhD by Morten Engen [Engen et al., 2017a]. Based on 38 benchmark analyses which consisted of walls, beams, frames and one deep beam, Engen reported $V_\theta=10.9\%$. Hence it was obtained a lower V_θ based on a greater number of beams with a more varying geometry. Therefore, the solution strategy obtained in the PhD may be more suited for a larger range of structures. Possibly the selected solution strategy elaborated in this thesis could have accomplished a lower coefficient of variation if a more comprehensive sensitivity study was conducted, including tests of other sub-models as well. However, it is stated in recommendations by fib [du Béton, 2008] that the coefficient of variation should be less than 30%. Hence, the calculated V_θ in this thesis could also be considered as acceptable even though it was larger than the value obtained in the PhD by Morten Engen.

As the solution strategy for RCxcb deviated from the main solution strategy described in Sec.2.3.3.5, and the numerical results of this beam was included in the uncertainty-calculations, a pure modelling uncertainty was not obtained. The varying parameters, like the use of interface and different element types around the circular openings, may have influenced the results, hence had an impact on the respective modelling uncertainty. Additionally, the choice of material models may introduce uncertainty to the predicted outcome. The constitutive models that constitutes the selected solution strategy may not be accurate for all beams, as they were characterized by different failure modes. Consequently, some NLFEA results may deviate a lot from the experimental results, hence this would influence the modelling uncertainty.

The sub-models were used consistently for all analyses as the aim was to obtain a modelling uncertainty for the selected solution procedure that was as accurate as possible. For sub-models where the concrete strength was included, the specific formulas varied for the different beams, as the concrete strength differed. The specimens in Case Study 1 and 2 were characterized by high-strength concrete and therefore the formulas for tensile strength and the Young's modulus of concrete were different than for Case Study 3.

The material uncertainty, included implicitly as a physical uncertainty and explicitly through the chosen mathematical models, is the main provider of modelling uncertainty. The sensitivity study for all case studies showed that the selection of material models had a great influence on the outcome of the NLFEAs. The FE modelling especially depended on the material models for parameters that were crucial in the failure modes. The FE models from the different case studies showed similar behaviour for the various material sub-models.

The experimental results of Case Study 1 and 2 indicated unsymmetrical failure modes, which may be caused by imperfections in the geometries, loads, boundaries, materials, measuring techniques or machinery. This could have limited the local material capacity, which would influence the modelling uncertainty. Unsymmetrical failure modes also characterized most of the NLFEAs, even though the analyzed specimens were modelled symmetrically. This is probably caused by some default regulations within the software, and is therefore difficult to justify.

4.2 Case Study 1

This section presents a detailed discussion of the conducted numerical analyses associated with Case Study 1. First the results for 6IT1 obtained by the selected solution strategy will be discussed, followed by a discussion of the results obtained in the sensitivity study.

4.2.1 Selected Solution Strategy

For a five point bending test like this, the top core of the shear spans naturally achieves large compressive stresses, while the corresponding lower cores get cracked due to lateral tensile stresses. Therefore 6IT1 achieved large compressive stresses in the area beneath the load plates, while flexural cracks were generated in the lower part of the midspan. Additionally, it was shown that cracks were generated in the corners of the web openings. Due to sharp edges and angles, large stress concentrations were generated in the concrete in these areas. Complete tensile softening and fully open cracks were first achieved in the two diagonal opening corners located in the compressive strut going from the load plates to the middle support. As more load was applied, the compressive stresses in these struts increased. Consequently, so did the tensile stresses perpendicular to these compressive stresses, which led to propagation of these diagonal cracks. As these cracks constituted both the numerical and experimental failure mode of 6IT1, these observations validate the selected numerical solution strategy.

The first numerical microcrack was generated at a lower load than for the first detected crack in the experiment. As previously discussed, the first detected microcracks in the numerical model may not have been visible in a physical model. Consequently, this discrepancy not necessarily weaken the reliability of the numerical solution strategy.

As shown, the selected solution strategy resulted in a continuous crack throughout the entire height of 6IT1 after LS 74. This LS constituted the peak on the LDC. By only looking at the principal tensile strain values in the contour plots, it was hard to tell exactly when the beam was split by a continuous crack all the way through the height. Parts of the failure zone had strain values larger than ϵ_u way before failure, but they were not necessarily merged into one crack. However, as the crack was initiated in the bottom of the beam, and propagated upwards, the nodes in the upper core, at the inside of the load plates, were the least to achieve ultimate tensile strains. However, as shown, this part of the beam was highly compressed. Consequently, these areas failed when the material got completely softened in compression.

An observation that amplified that a failure mechanism was formed in LS 76, was the straight line that distinguish the blue and red parts in the contour plot in Figure 3.3d. This magnifies that the beam actually was divided into separate blocks by a shear crack that at this stage was continuous through the beam.

As shown, the top of the beam, in the areas around the inner corners of the load plates, failed in compression. It is known that concrete cracks vertically as soon as small tension stresses arise. Horizontal cracks on the other hand, or cracks with low gradients, require large compressive stresses. The direction of the cracks on the top of the beam at the point of failure implied that the failure mode was affected by large compressive stresses in these areas.

The fact that the numerical LDC showed a drastic load drop when the principal compressive

strain exceeded α_u , indicated that the ultimate capacity of the model was limited by the compressive strength. When the shear crack propagated upwards in the beam, these areas achieved increased compressive stresses. When the concrete got completely softened in these areas, there was no remaining capacity in the critical zone.

Based on the post-analysis checks for 6IT1 reported in Sec. 3.1, it was clear that the failure mechanism was provoked by a combination of diagonal tension and shear compression failure. Consequently, in order for these numerical results to be accurate, it required that the specified tension-compression interaction model initiated a realistic relation between the specified sub-models that described the concrete tensile and compressive behaviour. As proved in Sec. 3.1, the maximum compressive stress in areas that achieved large tensile strains never achieved the value of the specified compressive strength. The peak compressive stress value for the three evaluated nodes, that were highly strained in tension, seemed to be approximately -60 N/mm^2 , while the value of f_{cm} was -68.2 N/mm^2 . As previously discussed, this indicated that the interaction model worked as it should, in the way that the compressive strength got reduced due to large tensile strains.

4.2.2 Sensitivity Study

4.2.2.1 Sensitivity regarding FE Discretization

Analysis 1: Mesh density $H/12$ (50 mm)

Analysis 2: Mesh density $L/50$ (14.4 mm)

Analysis 3: Mesh density $H/6$ (100 mm)

As presented in the result section for 6IT1, a fine mesh resulted in a greater quantity of cracks compared to a coarser mesh, while the latter resulted in wider paths of maximum tensile strains, and also larger individual cracks widths. This was similar in all case studies, and is discussed in Sec. 4.1.

The formula for ϵ_{peak} does not include the value of the crack-band width, hence it is consistent, regardless of the element height. As previously discussed, the crack width equals the principal strain multiplied by the element height. Therefore, cracks with smaller widths were detected in the FE model with refined mesh density. This explains why microcracks were detected at larger applied loads for coarser mesh densities. Another theory that justifies this difference is the fact that the load step size varied with the FE discretization. Analysis 3 resulted in larger LSs than Analysis 1, which again resulted in larger LSs than Analysis 2. The incremental applied load within each LS increases with its size. Consequently, it is difficult to determine the exact load for when microcracks were generated in the analysis with large LSs. Compared to the experimental results, microcracks were generated at a larger load in Analysis 3, and at a lower load in Analysis 1 and 2. As previously discussed, the first crack in the physical model was visible to the naked eye, something that the numerical microcracks, with widths of $1.23 \cdot 10^{-5} \text{ mm}$ to $7.64 \cdot 10^{-4} \text{ mm}$, would not have been. Hence, the numerical models that generated microcracks at lower loads than the experimental cracking load were most convincing with respect to this verification check.

The fact that the size of the load steps varied with the mesh density, when no other parameters were changed, must have been due to default regulations within the software.

As discussed, due to different crack-band widths, the strain values for when the concrete got completely softened in tension and compression, α_u and ϵ_u , differed for the varying

mesh densities. This explains why the concrete tensile and compressive behaviour differed in the three analyses. The model in Analysis 3, with the greatest element sizes, achieved complete softening in tension and compression at a lower strain value than in Analysis 1 and 2. This may justify that the model in Analysis 3 achieved the largest areas of complete softening. Small elements result in complete softening at greater strains. Consequently, larger strains were required in order to achieve this in Analysis 1 than 3, and similarly even larger strains were required in order to achieve this in Analysis 2. This fact, combined with the fact that 6IT1 in Analysis 2 did not take up as large loads as in the other two analyses, the concrete did not achieve complete softening in compression in any areas with the finest FE discretization.

Increased ductility in Analysis 3, and hence larger strains, justifies the fact that this analysis achieved largest reinforcement stresses.

Non-converged steps followed if the model did not achieve convergence within the allowable number of iterations in each incremental displacement step. Consequently, this happened after large stress redistribution due to cracking. The changes within each step were limited for small LSs. Hence this explains why Analysis 2 achieved convergence after very few iterations, and had almost no non-converged LSs. Contrary, Analysis 3 generated greater changes within each LS. This was due to increased step size and larger elements, which resulted in a less smooth stress field. Consequently Analysis 3 required the largest number of iterations before convergence criteria were satisfied.

4.2.2.2 Sensitivity to choice of Constitutive Model for Concrete

Choice of Constitutive Model for Concrete - Tension Softening Model

From the sensitivity study it was clear that 6IT1 was sensitive to choice of TS model.

Analysis 1: MC2010 TS model

Analysis 2: Exponential TS model

It was shown that microcracks were initiated in the same LS and at similar load levels in both analyses. However, the distinction regarding the widths of the first microcracks may be explained by the fact that the ϵ_{peak} -value is lower for the exponential TS approach than for MC2010. Consequently, this strain value was exceeded at a corresponding lower load level.

After crack initiation, the different softening branches in the two TS curves explain why specific areas achieved complete tensile softening at different load levels. As explained, the ultimate tensile capacity was fully utilized at a strain value which was 2.5 times larger in Analysis 1 than in Analysis 2. The FE model in Analysis 1 failed due to a combination of softening in tension and compression. However, due to the fact that the tensile strength was reduced faster in Analysis 2 than 1, the tensile capacity was fully utilized at a smaller total deflection. Hence, the FE model with an exponential TS approach failed in tension before the material was fully softened in compression. The failure mode was therefore characterized by only diagonal tension failure.

Choice of Constitutive Model for Concrete - Compressive Behaviour Function

6IT1 also responded differently when the compressive behaviour function was changed.

Analysis 1: Parabolic compressive behaviour function

Analysis 2: Constant compressive behaviour function

As described, the failure mode for 6IT1 in Analysis 1 was characterized by diagonal tension cracking followed by complete softening in compression in the upper part of the beam. As shown, the shear crack propagated similarly in Analysis 2. The incremental displacement plots indicated that the beam got split into separate blocks. However, even though large compressive strains were obtained in the upper part of the beam, this did not result in a reduced compressive capacity. Due to the fact that the concrete did not soften in compression when the constant function characterized the compressive behaviour, no upper absolute strain value limited this aspect of the material capacity. Hence, this may explain why the beam did not achieve global failure in this analysis.

However, it is worth mentioning that the concrete compressive capacity may be reduced even though the selected numerical sub-model that characterizes the compressive behaviour does not yield a softening branch. As previously discussed, tension-compression interaction leads to decreased compressive strength in areas of large tensile strains. Consequently, with such a compressive behaviour approach, web crushing in the paths of tension softened concrete may become more critical. However, flexural crushing becomes less critical, as experienced for 6IT1 when the concrete compressive behaviour was characterized by a constant function.

Choice of Constitutive Model for Concrete - Shear Retention Model

6IT1 was also sensitive to choice of shear retention model.

Analysis 1: Damage based shear retention model

Analysis 2: Constant shear retention model with $\beta=0.1$

Analysis 3: Constant shear retention model with $\beta=0.01$

In Analysis 2 and 3, with constant shear retention, the FE model maintained its shear capacity throughout the analysis, while it was gradually reduced in Analysis 1, with damage based shear retention. With $\beta=0.01$, the elastic shear modulus was reduced more than with $\beta=0.1$. When the beam was adequately damaged, the LDC dropped only for Analysis 1. Due to the fact that the failure mode was characterized by shear failure, 6IT1 with a damage based shear retention approach achieved global failure at this point.

The sharp division in the contour plot of the incremental displacement for Analysis 1 may indicate that the beam was split into separate blocks in LS 76, when the upper part of the beam got completely softened in compression. The large increase in maximum crack width amplifies this assumption. The critical shear crack marked a distinction between separated blocks that moved in opposite direction of each other. Because there are no shear reinforcement in this beam, the physical model had a brittle failure behaviour. The fact that large incremental displacements were generated in one critical LS in Analysis 1 makes damage based shear retention sufficient in order to model the brittle behaviour of shear failure.

The incremental displacement plots obtained in Analysis 2 and 3 did not indicate that the beam got split into separate blocks. Neither the maximum crack widths, which increased

significantly less than in Analysis 1, indicated that a failure mechanism was formed. Even though the beam seemed to be completely softened all the way through the beam height, the brittle behaviour of shear failure was not achieved with these models. Another observation that makes these shear retention approaches inappropriate for this numerical analysis, was the fact that the beam still could transfer load in the path of the shear crack, even when the crack seemed to be fully open all the way through the beam height. This indicates that the FE model experienced spurious shear capacity. Consequently, no failure modes were identified, and no failure loads were detected in the LDCs from Analysis 2 and 3.

4.3 Case Study 2

This section presents a detailed discussion of the conducted numerical analyses associated with Case Study 2. First the results for T1-0 obtained by the selected solution strategy will be discussed, followed by a discussion of the results obtained in the sensitivity study.

4.3.1 Selected Solution Strategy

For the NLFEA of T1-0 with the selected solution strategy, cracks developed in the expected areas; flexural cracks in the tensile zone in the bottom of the beam and diagonal cracks in the critical shear zone. The crack pattern obtained in the FE model was similar as in the physical model from the experiment. As in Case Study 1, the openings disturbed the load path and weakened the cross section capacity. Consequently, the critical shear zone was located in the load path from the load plates to the supports, through the web openings.

The first cracks appeared in the same areas in the numerical analysis as in the experiment, but at lower loads. As previously discussed, this is justified by the assumption that microcracks may have been initiated before visible cracks were detected in the physical model. Correspondingly, the first detected numerical microcracks may not have been observed in the physical model. Both the numerical and experimental LDCs looked unaffected by this crack initiation, as this microcracking did not influence the behaviour of the beam. However, when fully open cracks propagated, the numerical LDC showed a small drop, while the experimental LDC did not show any load drops before failure. In the numerical model the stress distribution was updated for each incremental displacement step, while in the physical model the stress was continuously redistributing as load was applied.

The small load drop observed for LS 85 in the numerical LDC, was probably caused by an increased amount of open cracks at the outer edge of the load plates, which later on constituted the top of the path where the failure shear crack developed. The load continued to increase afterwards, indicating that the beam was not completely devastated yet. After LS 92, when the shear crack seemed to be fully open all the way through the beam height, from the right load plate to the right support, the amount of inactive cracks increased. This indicated that the beam was split into separate blocks, hence that a failure mechanism was formed.

The numerical LDC did not show any specific responses when the reinforcement started to yield, due to the fact that such a small part of only some rebars yielded at this point. As the load increased, so did the extent of yielding reinforcement. This indicated that the reinforcement contributed to the global capacity of T1-0. The load continued to increase for some LSs after some rebars reached their respective calculated ultimate strain value. However, this value is only an estimation for the strain capacity of the steel. In this NLFEA the reinforcement obtained even larger strains. Eventually, the beam failed, but this did not seem to be caused by failure of the reinforcement.

Neither initiation of crushing in the concrete affected the numerical LDC for T1-0. Even though the material had started to crush, the concrete still had compressive capacity. However, after LS 92 the concrete was completely softened in compression above the right support, and the load decreased drastically. This load drop was caused by a combination of diagonal tension cracking and complete compressive softening of concrete. The fact that the following LS did not converge within 40 iterations, indicated that the beam suffered from

large redistribution of stresses. As previously mentioned, the amount of inactive cracks as well as the crack widths increased at this point, which amplified that a failure mechanism was formed.

4.3.2 Sensitivity study

4.3.2.1 Sensitivity regarding FE Discretization

Analysis 1: Mesh density $H/12$ (50 mm)

Analysis 2: Mesh density $L/50$ (18 mm)

Analysis 3: Mesh density $H/6$ (100 mm)

The crack pattern obtained in T1-0 with all three mesh densities looked similar. However, Analysis 3 obtained a higher failure load. This may be caused by the fact that smaller elements is more suitable in detecting individual discrete cracks due to better modelling of strain localization. Consequently, after crack initiation, fine mesh densities often result in a more ductile FE model, with lower stiffness than for a coarser FE discretization. This justifies that larger element sizes result in an overestimation of the ultimate load capacity. Correspondingly, Analysis 2, with the finest mesh density, resulted in the smallest failure load, along with the greatest number of cracks.

In this case study, the finest mesh resulted in a failure load closest to the experimental failure load. This amplifies that a finer mesh density will provide more accurate result. However, in compliance with FEA theory, increased accuracy was achieved at the expense of increased computing time.

Crushing of the concrete was more concentrated for smaller elements. As discussed previously, the element height affected the crack-band width, which again affected the values of α_c and α_u . Increased element height resulted in a decrease of the absolute value of these strains. Consequently, the concrete started to crush, and achieved complete softening in compression at lower loads for larger elements. The areas of T1-0 that achieved complete softening of the concrete were also affected by the mesh density. With the coarsest mesh density, in Analysis 3, T1-0 did not experience complete softening above the right support, as for the other mesh densities. In this analysis the ultimate compressive strain was only achieved underneath the load plates. This may be caused by the inherent inaccuracy of the FEM, where large elements struggle with generation of a smooth stress field. Analysis 1 and 2, with smaller element heights, achieved complete softening in the same areas. Consequently, since this aspect of the material response constituted the last stage of the failure process, similar failure mechanism was obtained in Analysis 1 and 2.

Yielding of the reinforcement appeared mostly in the same locations for all analyses. An exception was the yielding of the horizontal bars of $\varnothing 6$ at midspan. The yielding appeared at a remarkably greater loading and at a larger deflection level for Analysis 3 than for the two other analyses, even though the crack initiation at midspan occurred simultaneously. This may be caused by less stress concentrations, as they were more evenly distributed in the concrete when a coarser mesh was used.

4.3.2.2 Sensitivity to choice of Constitutive Model for Concrete

Choice of Constitutive Model for Concrete - Tension Softening Model

Analysis 1: MC2010 TS model

Analysis 2: Exponential TS model

The two TS models resulted in different behaviours of T1-0 in Case Study 2. The crack initiation stage was equal for the two models, as the difference between the two ϵ_{peak} -values was small. The peak load, however, deviated a lot. T1-0 in Analysis 1, was able to take up larger loads than in Analysis 2, due to different softening branches in the two different TS approaches. As previously mentioned, the value of ϵ_u is 2.5 times larger for the MC2010 TS model than for the exponential one.

Yielding of the rebars were more prominent with respect to the global behaviour of T1-0 in Analysis 2 than in Analysis 1. Consequently, the LDC was more affected by this response when the TS behaviour was characterized by an exponential function. The yielding of $\varnothing 10$ -bars could explain the load drop after the final peak in the response curve for Analysis 2. The vertical stirrups, $\varnothing 6$ and $\varnothing 10$, started to yield at lower loads and smaller deflections in Analysis 2 than in Analysis 1. As mentioned, the concrete tensile strain capacity was remarkably reduced when the exponential TS approach was applied. Consequently, the material achieved complete softening in tension at a lower load and deflection level. Therefore, the reinforcement contributed more to the global capacity of T1-0 in Analysis 2. Due to the fact that the failure mode included diagonal tension cracking, a decreased concrete tensile capacity for T1-0 in Analysis 2, resulted in failure at a lower load and deflection level than in Analysis 1. Due to the fact that a lot of the reinforcement yielded at the stage of failure could also influence the shape of the softening branch of the LDC. The LDC for exponential TS in Analysis 2, showed a less brittle behaviour after failure than in Analysis 1 with MC2010.

The crack patterns were similar for T1-0 in the two analyses, where shear cracking was combined with crushing of the concrete. Due to a changed stress distribution, caused by different TS models, the concrete was completely softened in compression in another area in Analysis 2 than in Analysis 1. However, both analyses achieved crushing in the end of the main shear crack pattern. After the peak in Analysis 2, the cracks on the left side expanded, while the crack strains disappeared on the right side. This validates the assumption that the beam had failed at this stage. The failure mode was, similarly as for the selected solution strategy, characterized by a combination of shear cracking and crushing of the concrete. However, with an exponential TS model, and hence a changed stress distribution, the failure crack was developed on the left side of the beam instead of on the right side. The fact that unsymmetrical failure modes were produced in the NLFAs are discussed previously.

Choice of Constitutive Model for Concrete - Compressive Behaviour Function

Analysis 1: Parabolic compressive behaviour function

Analysis 2: Constant compressive behaviour function

The NLFEA of T1-0 with an idealized constant concrete compressive behaviour resulted in similar crack pattern as when a parabolic curve characterized the compressive behaviour of the concrete. This was as expected, due to the fact that cracks are caused by exceedance of the tensile- and/or shear strength, and both the TS- and the shear retention models were identical in the two analyses. The yielding observations were also close to identical because of this. However, due to a changed stress distribution caused by different compressive behaviour functions, there were some small differences. Yielding of $\varnothing 10$ stirrups occurred at a lower load and deflection level in Analysis 1 than in Analysis 2.

The compressive peak strain was smaller for the constant- than for the parabolic behaviour function. Consequently, this explains why T1-0 in Analysis 2 achieved crushing at a lower load level than in Analysis 1. The fact that the concrete never got completely softened in compression when the constant behaviour function was used, and that this aspect of the material capacity was crucial in Analysis 1, resulted in a lack of failure in Analysis 2. Hence, in order to be able to model the correct failure mode, which included compression failure of the concrete, a compressive behaviour function that includes a hardening-softening relation should be used. However, the failure mode is not stated specifically in the experimental report, and will be an uncertainty related to this constitutive model verification. Nevertheless, the reported crack observations, as well as the geometry of the physical model suggested that crushing contributed to the failure mode. Also, it was a reasonable assumption that a more detailed mathematical model provided more accurate numerical results, but maybe at the expense of increased computational time. Additionally, the compressive strength of real concrete structures will always have an upper strain limit. Hence the real compressive behaviour will always deviate from the numerical behaviour specified by the simplified constant function.

Choice of Constitutive Model for Concrete - Shear Retention Model

Analysis 1: Damage based shear retention

Analysis 2: Constant shear retention with $\beta=0.1$

Analysis 3: Constant shear retention with $\beta=0.01$

NLFEAs of T1-0 were also sensitive to choice of shear retention model. The linear zone in the obtained LDCs ended simultaneously for the three analyses. This was expected as the tensile peak strains were equal and the shear capacity was not reduced before cracking. For both Analysis 2 and 3, the first open cracks were flexural cracks, while in Analysis 1, shear cracks were the first to become fully open. As shown, the constant shear retention models resulted in a larger shear capacity in the diagonal crack zones for T1-0. However, the final crack patterns were quite similar for all three analyses.

Analysis 2 did not show any clear failure at the point when the shear crack seemed to be fully open all the way through the height of the specimen. As the shear stiffness was retained throughout the analysis, the reinforcement continued to take up more loads. Hence the total applied load increased throughout the analysis.

In Analysis 3, less shear stiffness was retained, which explains why T1-0 showed a stiffer global behaviour after crack initiation in Analysis 2. The LDC for Analysis 3 showed a peak

at the point when the concrete was fully softened in tension underneath the left load plate. However, as the cracks still maintained 1% shear stiffness, the beam did not fail due to this. Consequently, the applied load continued to increase after this peak. Due to maintained shear capacity, the reinforcement stresses continued to increase, hence this also contributed to increased global capacity. Consequently, no failure mechanism was detected in Analysis 3 either.

Even though T1-0 did not achieve any clear failure mechanism in Analysis 2 and 3, the obtained principal strain plots indicated that the strain distribution was similar as in Analysis 1. Consequently, when a constant shear retention approach was applied, T1-0 seemed to proceed towards a shear compression failure mode.

4.4 Case Study 3

This section presents a detailed discussion of the conducted numerical analyses associated with Case Study 3. A 2D numerical model was developed for the experimental RCxcb beam specimen. Since the obtained failure mode for this numerical model was different from the ductile experimental failure mode, an additional 3D numerical model was developed. The aim was to see if the brittle failure mode that was obtained for the 2D numerical model could be avoided by utilizing a triaxial stress state of the concrete. First, the results for RCxcb obtained by the selected solution strategy for both 2D and 3D models will be discussed, followed by a discussion of the results obtained in the sensitivity study.

A remark regarding the size of the LSs in the NLFEAs of RCxcb should be addressed. In all conducted NLFEAs, the specified prescribed deflection was divided into 100 incremental LSs. As the physical test specimen of RCxcb withstood a deflection of approximately 200 mm, this was specified as the ultimate deflection level in the corresponding NLFEAs. Consequently, by selecting a total number of 100 LSs, the incremental displacement became 2 mm. As the numerical model of RCxcb achieved a much more brittle behaviour, almost all analyses resulted in generation of a failure mechanism before LS 10. Consequently, it was difficult to distinguish the exact load and deflection level for the different observations, as large changes were generated within each LS.

4.4.1 Selected Solution Strategy

To make a good numerical model that would adapt and replicate the results from the experiments to an acceptable accuracy, was a challenging process as the different beam specimens had such different geometries.

As a result of this, the mesh for the 2D numerical modelling of RCxcb consisted of three different kinds of elements. The software input only specified that quadrilateral plane stress elements with quadratic mesh order, so called Q16-elements, should be used for this meshing. However, due to the arbitrary geometry in the areas of the circular openings, an irregular mesh, including triangular elements in addition to the Q16 specified elements were generated. Additionally, an interface element type was used between concrete and steel plates. As the aim of this thesis was to come up with a common solution strategy for a general set of beams with web openings, a mesh refinement close to openings was not an option. Hence, the irregular meshing of RCxcb could have affected the numerical outcomes.

Even though a common solution strategy was desirable, some adjustments were necessary in order to exclude obvious and destructive errors. For RCxcb, large stress concentrations were generated underneath the load plates. This may have contributed to generation of an early failure mechanism. These stress concentrations may have been caused by the fact that the connecting materials had different stiffness, which possibly caused frictional forces in these transitions as the structure was loaded. Therefore, in order to avoid these stress concentrations, an interface element with zero tangential stiffness was added between the load plates and the concrete specimen.

Another distinction between the FEAs of the beams in the other case studies and RCxcb, was as mentioned the generation of arbitrary elements around the circular openings. For the 3D numerical model of RCxcb, the concrete mesh consisted of 4 types of elements. This resulted in occurrences of error messages during post-processing due generation of two bad shaped elements, which could have affected the results.

In Case Study 3, neither the initiation of microcracks nor the first fully open crack generation affected the load carrying capacity. However, in Case Study 1 and 2, fully opening of cracks constituted a load drop in the LDCs. Compared to the beams in Case Study 1 and 2, where the corners of the quadrilateral web openings introduced large stress concentrations, the circular openings in RCxcb caused a more even stress distribution in these areas. The fact that fully open cracks were generated in areas connected to these openings in all case studies may be a reason why they caused such a large response for the beams in Case Study 1 and 2, but not in Case Study 3.

By post-processing the numerical response of RCxcb, it was observed that when the peak load level was reached, a sudden drop in the LDC for both the 2D and the 3D model occurred. This response deviated from the experimental response, where the reinforcement started to yield, and the beam achieved an additional 150 mm deflection before failing. At this load level a failure mechanism was formed in the numerical model. When investigating the cause of this brittle behaviour, it was observed that, in addition to completely softening in tension, crushing of concrete was prominent in the main load transferring struts. Due to the limited deflection, the main tensile reinforcement did not yield during the NLFEA. As shown in the result section, the specified compressive strength of the material was not reached, even though the concrete got crushed. This could be explained by the effect of the specified tension-compression interaction model, which caused a reduction of the compressive strength as a result of large lateral tensile strains. In order to investigate if this effect was applied to the model, the principal compressive stress was measured in the critical areas where completely softening in tension were prominent. As shown, the compressive capacity of the concrete was reduced in these areas, which confirmed that the effect of Vecchio & Collins-model was included in the model. However, this investigation included some significant uncertainties. The measured compressive stress values were collected from nodes and not integration points. Consequently, the obtained values may have suffered from extrapolation/interpolation of stresses in the surrounding areas.

As previously discussed, the different sub-models are developed to work independently of each other. Consequently, the effect of the specified tension-compression interaction model would depend on the specified tension and compression sub-models. For this specific FE model, one reason for the unexpected brittle behaviour could possibly be a too high decrease rate of the compressive capacity. Even though the sub-models may have introduced realistic individual aspects of the concrete material behaviour, they did presumably not work as well together for Case Study 3 as for the other case studies. A remedy for this issue could be to choose another TS sub-model for which the concrete would not soften as fast as it did for the chosen MC2010 TS model. Alternatively a higher fracture energy, in the meaning of higher tolerance of this limit, could perhaps have yielded a more ductile behaviour. This could have introduced slower development of concrete tension softening, and corresponding lower reduction rate of the compressive capacity.

When it comes to the 2D adapted model, it is known that concrete with prevented cross-sectional expansion will yield higher compressive capacity and reach higher critical strains before failure [CEN, 2004]. To investigate this effect, and utilize the reinforced concrete depth by activating more stirrups, the 3D adapted model was developed. From the numerical results, it was observed that stirrups in lateral *yy*-direction reached plastic state in a critical area below opening 11. This indicated that a triaxial stress state was achieved. However, this did not contribute to a more ductile behaviour. The main difference from the 2D approach was that the 3D model, with solid elements that included the triaxial compressive stress state,

achieved crushing in the critical areas at a lower load. This could have been due to the fact that restrained lateral expansion for plane-stress elements leads to increased compressive strength and critical strains.

However, the differences between the behaviour of the numerical 2D and 3D model were not very prominent. Even though the models had similar failure loads, the 2D model had a slightly larger load capacity. Due to the fact that both models underestimated the experimental load capacity, this resulted in a higher modelling uncertainty for the 3D model.

4.4.2 Sensitivity Study

4.4.2.1 Sensitivity regarding FE Discretization

Analysis 1: Mesh density $H/12$ (33.33 mm)

Analysis 2: Mesh density $L/50$ (76 mm)

Analysis 3: Mesh density $H/6$ (66.67 mm)

Analysis 4: Mesh density $B/6$ (25 mm)

Both the numerical 2D and 3D model yielded a less ductile behaviour when the mesh density was refined. As shown, both models resulted in a greater quantity of cracks when a fine FE discretization was assigned. Hence the largest number of cracks was obtained in Analysis 4. Additionally, the finest mesh resulted in the lowest load capacity. This was similar in all case studies, and is discussed in Sec. 4.1. As mentioned, the numerical models underestimated the load capacity. Consequently, the failure load obtained for RCxcb discretized by the finest mesh deviated most from the experimental failure load. This contradicts FE theory, which states that refined mesh density increases the accuracy of the numerical results. It was shown that the coarsest mesh densities, in Analysis 3 and 2, resulted in the most realistic failure loads for the 2D and 3D model, respectively. This implies that there is sensitivity related to mesh refinement for both 2D and 3D modelling.

All analyses yielded the same brittle behaviour as in Analysis 1, which constituted the selected solution strategy. The unsymmetrical failure mode was also obtained in all analyses, regardless of mesh density selection. The left support was able to take up more load than the right support after the peak on the LDC was reached. This indicated that fully open diagonal cracks and crushing were more prominent on the right hand side of the beam, and that a failure mechanism formed at this point.

Yielding of reinforcement was only concentrated in stirrups and cables close to outer openings where the fully open diagonal crack path was established and the concrete capacity was reduced. These areas achieved the largest strains, and due to the fact that slip between concrete and reinforcement was restrained, the largest reinforcement strains were also achieved in these areas.

Regardless of mesh density, the same combined failure mechanism was achieved. However, Analysis 1 of the 2D model was the only analysis which yielded a symmetrical crack pattern at outer openings. As previously discussed, the failure mode will typically not be symmetrical in reality. However, it is difficult to explain why the software results in an unsymmetrical failure mode when the beam geometry is symmetrical.

Similarly as in the other case studies, coarser mesh resulted in a wider spreading of the

crushed and cracked concrete in the numerical models. As previously discussed, the main reason for this was probably the fact that larger element sizes resulted in larger crack-band widths, which again resulted in lower ultimate strain values in both tension and compression. Additionally, the observed advantage of a refined mesh was a more detailed stress and strain distribution. As discussed, an inadequate inaccuracy of the FEM is that coarse meshes do not generate smooth stress fields.

When it comes to complete softening of concrete in compression, all analyses, except Analysis 1 in 2D, yielded the same softening path through the entire beam height connected to opening 11. Analysis 1 in 2D experienced the same, but connected to opening 12 instead of opening 11. However, as all 3D models achieved the same path of completely softened concrete in compression, this may indicate that 3D models are less sensitive to various mesh densities than 2D models.

4.4.2.2 Sensitivity to choice of Constitutive Model for Concrete

Choice of Constitutive Model for Concrete - Tension Softening Model

Analysis 1: MC2010 TS model

Analysis 2: Exponential TS model

As previously stated a more ductile response of the numerical model was desirable. However, neither of the two TS approaches caused a ductile behaviour of RCxcb. However, as the results show, remarkable differences were observed in the two analyses.

A larger load capacity was achieved in Analysis 1 than in Analysis 2, for both the 2D and the 3D model. As previously discussed, the 2D model had a larger compressive strength than the 3D model due to prevented lateral expansion. Consequently, this may justify why the 2D model withstood a higher applied load and larger midspan deflection than the 3D model in Analysis 1. However, in Analysis 2, the opposite result was observed. The 3D model yielded a higher peak load value and slightly higher midspan deflection than the 2D model. The reason for this outcome was not studied further in this thesis. However, it would be an interesting topic for further study.

As the exponential TS model is defined as completely softened in tension at a strain value 2.5 times lower than in the MC2010 TS model, the ultimate tensile capacity was fully utilized at an earlier stage in Analysis 2 than in Analysis 1. As the concrete tensile capacity limited the global capacity in all case studies, the exponential TS consistently resulted in lower load capacity than the MC2010 TS approach did.

In the 2D model it was shown that fully open cracks were established at a higher total applied load in Analysis 1 than in Analysis 2. As previously discussed, this was probably caused by a higher peak tensile strain value in the MC2010 stress-strain curve. Similarities obtained in the two analyses of the 2D model, were that the same crack pattern was achieved, and crushing of the concrete happened in the same LS, regardless of assigned TS approach. The only difference was that in Analysis 2, the concrete was complete softened at the stage of the peak, and not in the following LS, as it was in Analysis 1. This could possibly be explained by the fact that the concrete in Analysis 2 lost tensile capacity more rapidly than in Analysis 1, due to a shorter tension softening branch. Consequently, the compressive stresses perpendicular to these tensile strains would also increase with a higher rate. This could

explain why Analysis 2, with an exponential TS approach, resulted in complete compressive softening at an earlier stage than in Analysis 1.

Also, the 3D model resulted in earlier concrete compression softening in Analysis 2 than in Analysis 1. This was possibly caused by the same reason as for the 2D model, which is discussed above.

The 3D model also resulted in a larger load capacity in Analysis 1 than 2. For the same reasons as previously discussed, cracks were fully open at higher loads, and the concrete got completely softened in tension at higher loads with MC2010 TS compared to with exponential TS. However, for the 3D model, Analysis 2 resulted in a symmetrical failure mechanism, while Analysis 1 resulted in an unsymmetrical. As opposed to in the sensitivity study regarding FE discretization, this discrepancy related to the 3D failure mode generation may indicate that 2D models are less sensitive to various TS approaches than 3D models.

Choice of Constitutive Model for Concrete: Compressive Behaviour Function

Analysis 1: Parabolic compressive behaviour function

Analysis 2: Constant compressive behaviour function

As mentioned, a more ductile response was desirable for the numerical modelling of RCxcb. However, this was not achieved by substituting the parabolic compressive behaviour function with an idealized constant function.

During post-processing it was observed that the obtained responses was similar pre LDC-peak in both the 2D and the 3D model, regardless of assigned compressive behaviour function. However, the 2D model obtained a slightly higher load capacity in Analysis 2. This may be explained by the fact that the concrete started to crush for a higher absolute strain value with parabolic- than with constant compressive behaviour. In the parabolic hardening-softening curve, the absolute value for the peak strain is 1.67 times larger than the absolute value for the strain at when the concrete compressive strength is reached in the constant curve. Consequently, this explains why the areas of crushed concrete was more comprehensive in Analysis 2. Additionally, as previously discussed, the constant compressive approach does not introduce any compression softening branch to the concrete. Consequently, increased absolute compressive strains do not provoke a reduction of the compressive strength. As compressive softening of the concrete limited the capacity for the selected solution strategy, this lack of softening may have contributed to the increased global capacity in Analysis 2.

Choice of Constitutive Model for Concrete: Shear Retention Model

Analysis 1: Damage based shear retention

Analysis 2: Constant shear retention with $\beta=0.1$

Analysis 3: Constant shear retention with $\beta=0.01$

From the sensitivity study it was clear that the FE model was sensitive to the choice of a shear retention model.

Damage based shear retention was selected for the common solution strategy. Constant shear retention approaches were also tested in order to try to achieve a more ductile response of RCxcb. Another aim was to generate a model that was less sensitive to shear failure, as the physical test specimen failed in flexural compression and not diagonal tension failure. With the damage based shear retention model, the shear stiffness was gradually reduced to zero

as the model was damaged by cracks.

In Analyses 2 and 3, a percentage of the shear stiffness was retained in the cracked zones. Therefore, cracks maintained a certain shear capacity throughout the analyses. As the numerical models in all case studies got sufficiently cracked during the NLFEMs, this may explain why they all yielded such an increased load capacity when a constant shear retention model was used.

As previously stated, horizontal crack strains occurred when load was applied to RCxcb. This caused loss of stiffness in the orthogonal direction of these crack strain planes, which could have caused the sudden brittle failure when a damage based shear retention model was used. However, as shear stiffness was retained in Analysis 2 and 3, this response was avoided, and the FE model was able to take up a larger load. For RCxcb this increased load capacity also resulted in a more ductile behaviour. Consequently, NLFEMs of RCxcb with a non-zero β -value were the only conducted analyses to avoid the brittle response of this FE model. By looking at the obtained curves for the reaction forces, it was shown that the load transferring struts did not lose their entire capacities when lateral cracks occurred in Analysis 2 and 3. Consequently, larger shear cracks were generated, which initiated yielding in the main longitudinal reinforcement.

As mentioned, compared to Analysis 1, both Analysis 2 and 3 yielded more experimental like LDCs with respect to achieved midspan deflection. With $\beta = 0.01$, both the LDC for the 2D and the 3D model indicated a disturbed response at a certain deflection level. With $\beta = 0.1$ on the other hand, only the 2D model showed a disturbed response at the end of the analysis. The LDC for the 3D model did not show any sign of a weakened model.

For the 2D model, the LDC from Analysis 2 showed that the response was disturbed after the concrete beneath the inner load plates was completely softened in compression. However, no clear failure mechanism was detected.

For the 2D model in Analysis 3, the obtained LDC showed a disturbed response after the concrete got crushed in the entire beam height at some openings. This was at a lower deflection level than when the LDC for Analysis 2 showed a disturbed response. As previously discussed, this could be explained by the fact that a larger amount of the initial shear stiffness was retained for a larger β -value. However, no failure mechanism was detected in this analysis either. This may indicate that the models experienced spurious strength in Analysis 2 and 3, as a result of retained shear capacity.

Even though the load capacity did not show a clear drop in the LDC for the 2D model in Analysis 3, fully open shear cracks occurred and propagated through the entire beam height at the outer two web openings. In LS 98 the concrete was completely softened in compression in the entire beam height in these areas. Consequently, it looked like both Analysis 1 and 3 yielded similar failure mechanisms, even though RCxcb in Analysis 3 still had load carrying capacity afterwards. This was probably caused by the fact that 1% of the concrete shear stiffness was retained.

As discussed, the largest constant shear retention factor resulted in the largest load capacity for both the 2D and the 3D model. However, the 3D models in both Analysis 2 and 3 resulted in a larger load capacity than the 2D models. A greater deflection was also achieved before disturbed responses were observed. This distinction regarding the obtained responses for the 2D and 3D model would be an interesting topic for further study.

5. Conclusions

For the selected solution strategy, the different FE models resulted in varying modelling uncertainties. Some NLFEAs resulted in overestimation of the experimental failure loads, while others resulted in underestimation. Based on the conducted sensitivity studies, it was proven that the analyzed beams were sensitive to selection of sub-models constituting the concrete constitutive model. Selections regarding the FE-discretization also affected the accuracy of the numerical results. The different FE models did not necessarily show sensitivity to the same aspects of the solution strategy. However, for specific variations within the solution procedure, a certain consistency was observed in the numerical response spectra. Consequently, some observations from the conducted NLFEAs were qualified contributors in the justification process of the numerical solution strategy for beams with web openings.

As all the analyzed numerical models achieved shear failure combined with concrete crushing, the conducted sensitivity study proved that the most detailed mathematical models were preferable for the modelling of these specific behaviour aspects. For the most simplified sub-models tested in conjunction with this study, most of the FE models achieved spurious strengths and unrealistic stress distributions. Hence, the sub-models regarding tensile, compressive and shear behaviour should be carefully considered. Attention should also be brought to the interaction effect of concrete structures subjected to a multidimensional stress state. It was proved that the selected interaction model, according to Vecchio & Collins, included an interaction effect in the concrete, as the compressive capacity was reduced in areas that achieved large tensile strains. However, it is questionable if this interaction model was the best selection for all the FE models. For Case Study 3, the numerical failure mode deviated from the experimental one. This may be caused by a too large reduction of compressive strength, provided by the interaction model.

All conducted NLFEAs related to each FE model obtained a similar crack pattern, even though failure was not always achieved. Consequently, the respective LDCs often deviated substantially, while the post-analysis checks indicated that the stress distributions were similar prior to the ultimate states. Consequently, numerical analyses should always be accompanied by thorough post-analysis checks in order to identify if failure mechanisms form without being detected in the response curves. As proved, this may happen due to spurious strengths that provide false capacity.

Considering FE discretization, it is shown that the explicit choice of element size should be of great concern in numerical analyses. According to FE theory, a finer mesh should result in more accurate FE outcomes, but at the expense of increased computing time. However, the numerical observations reported in this thesis were not necessarily in compliance with this theory. Upon mesh refinement, neither the results from Case Study 1 nor 3 converged towards the exact solution for these boundary value problems. For Case Study 2, the obtained results were in accordance to the FE theory. However, it was proven that the density for the selected solution strategy yielded almost as realistic results as with the finest mesh density. Consequently, with respect to failure load and mode for this specific model, it was not necessary to use the fine mesh. However, for all analyzed FE models one advantage with finer mesh density was that smoother stress fields were produced. This was not obtained to the same extent when a coarser element discretization was used to mesh the

models. However, these results did not qualify for a common conclusion regarding optimal mesh density for a general set of beams with openings.

Based on the obtained results from the numerical analyses, the ability for the selected solution strategy to model various failure modes is undetected, as all conducted NLFEAs tended towards shear failure. This was however the desired failure modes in most of the NLFEAs, as it was in compliance with the experimental failure modes.

Based on the calculated modelling uncertainty, $\theta=1.06$, and coefficient of variation, $V_{\theta}=16.4\%$, the selected solution strategy is validated as adequate, as the coefficient of variation it is lower than the recommended maximum coefficient of variation of 30%.

Most of the numerical analyses resulted in an underestimation of the capacity. A solution strategy that produces conservative results is preferable in a design perspective. However, due to fact that the coefficient of variation was larger than the mean percentage of underestimation of the failure load, the selected solution strategy not necessarily provide a conservative numerical model that is safe to use as design approach. However, the geometries of the tested beams varied remarkably. Hence, the obtained coefficient of variation, which was not unacceptably high, indicate that the solution strategy may be considered as an elementary procedure to evaluate the capacity of beams with openings.

6. Suggestions for Further Research

In this thesis a solution strategy for numerical modelling of beams with web openings were developed. Limitations and inconsistencies observed in the conducted sensitivity studies should be addressed and investigated further before the selected solution strategy can be validated for a general set of beams with web openings. This section contains proposals for further research in order to justify or improve the solution strategy.

The observed sensitivity related to FE discretization for FE models with web openings should be investigated further. The reason for why the LS-size varied for different mesh densities, even though this size was explicitly specified in the software, should be addressed. The NLFEMs evaluated in this thesis showed no consistency regarding what mesh densities that resulted in larger LSs and what mesh densities that resulted in smaller LSs.

The effect related to the tension-compression interaction model for concrete should also be further investigated. Any limitations within the Vecchio & Collins-model should be addressed. In general, the correlation effect between all sub-models that constitute the concrete constitutive model should be elaborated.

Some limitations were related to the verification checks used to prove that the selected interaction-model worked as intended in these analyses. Tensile strains and compressive stresses were assessed in FE nodes. However, stresses and strains are by definition evaluated in integration points. The extent of this inaccuracy should be addressed, and validated tests that qualify for accurate investigation of the interaction effect between constitutive sub-models should be developed.

As shown in this research, shear failure characterized all obtained numerical failure modes. However, this deviated from the experimental failure mode for one of the tested specimens. This distinction should be further examined, and adjustments should be made to the solution strategy with the intention to achieve realistic numerical failure modes for all beams with openings. Therefore, proper constitutive sub-models that include realistic interaction effects, and that are able to recreate all types of failure modes should be chased.

Additionally, the numerical effect of 3D versus 2D modelling of beams with web openings should be further investigated. The intention should be to address limitations and differences related to the provided dimension of the numerical stress state.

The suggested investigations and measures intend to improve the reliability of the numerical solution strategy. The overall aim for further work is to achieve realistic numerical failure modes for a general set of beams with web openings, and also to reduce the coefficient of variation related to the mean numerical failure load.

Bibliography

- Ashour, A. F. and Rishi, G. (2000). Tests of reinforced concrete continuous deep beams with web openings. *Structural Journal*, 97(3):418–426.
- Autodesk Inc. (2018). *Autodesk Revit Structure release 18.2.0.51*. San Rafael, California, U.S. Available at <https://www.autodesk.com> (22.05.2018).
- Aykac, B., Aykac, S., Kalkan, I., Dundar, B., and Can, H. (2014). Flexural Behaviour and Strength of Reinforced Concrete Beams with Multiple Transverse Openings. *ACI Structural Journal*, 111(2):267–277.
- CEN (2003). *NS-EN ISO 3766:2003 - Construction drawings. Simplified representation of concrete reinforcement*. European Committee for Standardization, Brussels, 2. edition february 2004. edition.
- CEN (2004). *EN 1992-1-1:2004 - Design of concrete structures. General rules and rules for buildings*. European Committee for Standardization, Brussels.
- Code, M. (2010a). First complete draft, vol. 1. *fib Bulletin*, (55).
- Code, M. (2010b). First complete draft, vol. 1, paragraph 5.1.8.2. *fib Bulletin*, (55).
- COMSOL Inc, . The finite element method (fem).
- DIANA, F (2017). Diana user's manual, release 10.1.
- DIANA FEA (2014). *DIANA FEM-software release 9.4.4*. DIANA FEA BV, Delft, The netherlands. Available at <https://dianafea.com/content/DIANA> (28.11.2017).
- DIANA FEA (2018). *DIANA FEM-software release 10.2*. DIANA FEA BV, Delft, The Netherlands. Available at <https://dianafea.com/content/DIANA> (26.05.2018).
- Du, H. and CHEN, N. (2012). Detailed study of the cracking process at shear failure through fe analysis of beam experiments.
- du Béton, F. I. (2008). Practitioners guide to finite element modelling of reinforced concrete structures. *State-of-Art Report*.
- Engen, M. (2017). *Aspects of design of reinforced concrete structures using non-linear finite element analyses. Solution strategy, modelling uncertainty and material uncertainty*. PhD thesis, NTNU; 2017:149.
- Engen, M., Hendriks, M. A., Köhler, J., Øverli, J. A., and Åldstedt, E. (2017a). A quantification of the modelling uncertainty of non-linear finite element analyses of large concrete structures. *Structural Safety*, 64:1–8.
- Engen, M., Hendriks, M. A., Øverli, J. A., and Åldstedt, E. (2017b). Reliability assessment of a large concrete structure making use of non-linear finite element analyses. In *The Second Concrete Innovation Conference*, pages 6–8.

- Hendriks, M. A. N., de Boer, A., and Belletti, B. (2017). *Guidelines for Nonlinear Finite Element Analysis of Concrete Structures*. , Rijkswaterstaat Center for Infrastructure, Report RTD:1016-1:2017, Delft, The Netherlands.
- H.Zheng, D.F.Liu, C. and L.G.Tham (2005). Displacement-controlled method and its applications to material non-linearity.
- Kotsovos, M. and Pavlovic, M. (1995). *Structural Concrete: Finite-Element Analysis for Limit State Design*. Thomas Telford Services Ltd., 1 Heron Quay, London E14 4JD, 1995.
- Mancini, G. (2017). Comparison between safety formats for nlfea of rc structures - the example of rc beam with square and circular openings. PowerPoint Presentation.
- Placas, A. and Regan, P. E. Shear failure of reinforced concrete beams. In *Journal Proceedings*.
- TNO DIANA (2010a). *DIANA-9.4.3 User's Manual. First ed. 30.1.1 Iterative Procedures*. Available at <https://dianafea.com/manuals/d943/Analys/node386.html>> (24.05.2018).
- TNO DIANA (2010b). *DIANA-9.4 User's Manual. First ed. 12.4.4.2 Crack Status*. Available at <https://dianafea.com/manuals/d93/Analys/node151.html>> (10.05.2018).
- Yang, K.-H. and Ashour, A. F. Structural behaviour of reinforced concrete continuous deep beams with web openings. *ACI Structural Journal*.
- Yang, K.-H., Chung, H.-S., and Ashour, A. F. (2007). Influence of inclined web reinforcement on reinforced concrete deep beams with openings. *ACI Structural Journal*, 104(5):580.